JOURNAL OF THE AERONAUTICAL SCIENCES

VOLUME 24 APRIL, 1957 NUMBER 4

ST. LOUIS
APR 5 1957
LIBRARY

CONTENTS

Plastic Torsional Buckling Strength of Cylinders Including the Effects of Imperfections.....LAWRENCE H. N. LEE AND CLIFFORD S. ADES 241

Boundary-Layer Measurements at Supersonic Nozzle Throats....MERWIN SIBULKIN 249

Postbuckling Behavior of Circular Cylindrical Shells Under Hydrostatic Pressure...
.....JOSEPH KEMPNER, K. A. V. PANDALAI, SHARAD A. PATEL, AND JACQUES CROUZET-PASCAL 253

Theories of Strength for Combined Stresses and Nonisotropic Materials.....
.....JOSEPH MARIN 265

Plastic Stability Theory of Thin Shells.....GEORGE GERARD 269

A Method for Examination of Store Separation From Aircraft Through Dynamic Model Testing at Full-Scale Mach Number.....SEYMOUR J. DEITCHMAN 275

A Comparison of the Calculated and Observed Flutter Characteristics of a Helicopter Rotor Blade.....LEONARD GOLAND AND ABRAHAM A. PERLMUTTER 281

Plastic Buckling of Simply Supported Plates Subjected to Combined Shear and Bending or Eccentric Compression in Their Plane.....P. P. BIJLAARD 291

Readers' Forum..... 304

Published by
INSTITUTE OF THE AERONAUTICAL SCIENCES, INC.

JOURNAL OF THE AERONAUTICAL SCIENCES

Editor: W. R. SEARS
Director, Graduate School of Aeronautical Engineering, Cornell University

Associate Editor: ROBERT R. DEXTER *Managing Editor:* RITA J. TURINO
Editorial Assistant: CAROLINE TAYLOR

Editorial Committee

Aerodynamics and Fluid Mechanics
Holt Ashley
H. Julian Allen
Dean R. Chapman
Francis H. Clauser
Hugh L. Dryden
John C. Evvard
Antonio Ferri
Alexander Flax
Wallace D. Hayes
R. T. Jones
Carl Kaplan
H. W. Liepmann
C. C. Lin
H. F. Ludloff
Harold Luskin
Clark B. Millikan
C. D. Perkins
H. J. E. Reid
George S. Schairer
G. B. Schubauer
John Stack
Theodore Theodorsen
Arthur N. Tifford
Th. von Kármán

Flight Testing
R. R. Gilruth
Melvin N. Gough
W. L. Howland
W. F. Milliken, Jr.

Rotating Wing Aircraft
F. B. Gustafson
K. H. Hohenemser
Bartram Kelley
R. B. Maloy
Ralph McClarren
R. H. Miller
R. H. Prewitt
Igor I. Sikorsky

Structures
John E. Duberg
N. J. Hoff
Samuel Levy
J. F. McBrearty
W. Ramberg
E. E. Sechler
F. R. Shanley
C. R. Strang
S. Timoshenko

Meteorology
C. F. Brooks
D. M. Little
F. W. Reichelderfer
K. C. Spengler

Vibration and Flutter
Lee Arnold
M. A. Biot
R. L. Bisplinghoff
Harold A. Cheilek
I. E. Garrick
Martin Goland

Aircraft Design
W. E. Beall
E. H. Heinemann
Hall L. Hibbard
Richard Hutton
C. L. Johnson
A. A. Kartveli
E. G. Stout
F. K. Teichmann

Electronics
Welcome W. Bender
K. C. Black
M. V. Kiebert, Jr.
David S. Little
S. B. Rogers
Paul Rosenberg
L. M. Sherer

Physiologic Problems
H. G. Armstrong
Louis H. Bauer
Robert J. Benford
W. Randolph Lovelace, II
Ross A. MacFarland

Flight Propulsion
William Bollay
George W. Brady
R. P. Kroon
Frank E. Marble
Abe Silverstein
Martin Summerfield
E. S. Taylor

Instruments
Alan G. Binnie
Charles H. Colvin
Frank R. Cook
C. S. Draper
S. G. Eskin
C. F. Savage
R. C. Sylvander

SUBSCRIPTION RATES

JOURNAL OF THE AERONAUTICAL SCIENCES, Published Monthly. United States and Possessions: 1 Year, $15.00; Single Copies, $1.50. Foreign Countries Including Canada (American Currency Rates): 1 Year, $16.00; Single Copies, $1.50.

AERONAUTICAL ENGINEERING REVIEW, Published Monthly. United States and Possessions: 1 Year, $3.00; Single Copies, $0.50. Foreign Countries Including Canada (American Currency Rates): 1 Year, $3.50; Single Copies, $0.50.

Notices of change of address should be sent to the Institute at least 30 days prior to actual change of address.

Manuscripts for publication, proofs, and all correspondence should be addressed to the Editorial Office of the JOURNAL.

Publication Office, 20th and Northampton Sts., Easton, Pa. Correspondence regarding subscriptions may be addressed to the Editorial Office of the JOURNAL OF THE AERONAUTICAL SCIENCES, 2 East 64th Street, New York 21, N.Y.

© *Copyright, 1957, by the Institute of the Aeronautical Sciences, Inc.*

Entered as Second-Class Matter at the Post Office, Easton, Pa., May 1, 1937. Acceptance for mailing at a special rate of Postage provided for in the Act of August 24, 1912. Authorized April 29, 1937.

JOURNAL OF THE AERONAUTICAL SCIENCES

VOLUME 24 APRIL, 1957 NUMBER 4

Plastic Torsional Buckling Strength of Cylinders Including the Effects of Imperfections†

LAWRENCE H. N. LEE* AND CLIFFORD S. ADES**

University of Notre Dame and Bendix Aviation Corporation, Respectively

SUMMARY

The torsional buckling strength of a cylinder in the plastic range has been determined. An energy solution and a more exact solution, both based on a plastic stress-strain relationship given by the simple deformation theory, are presented. Close agreement between the two solutions is found. The effects of large deflections and imperfections on buckling strength are analyzed. For two groups of experimental results used for comparison, the effects of geometrical imperfections in the plastic range are negligible. The theoretical results are found to be in good agreement with the experimental results.

SYMBOLS

a_l	= amplitude of buckling wave
a_{0l}	= amplitude of initial deviation from perfect shape
D	= outside diameter of cylinder
d	= parameter defining buckling wave
E	= Young's modulus of elasticity
E_{sec}	= secant modulus
E_{tan}	= tangent modulus
e_l	= strain intensity defined by Eq. (4)
F	= Airy's function for membrane forces
$F_{0.7}$	= stress defined by secant line of slope $0.7E$
F_{st}	= torsional modulus of rupture
H	= nondimensional geometry factor
J	= $1/H$
K	= imperfection factor defined by Eq. (8)
L	= length of cylinder
L_x, L_s	= longitudinal and circumferential half-wave lengths
M_t	= torque
$(M_t)_{cr}$	= critical buckling torque
M_x, M_s, M_{xs}	= bending and twisting moments in cylindrical shell
m	= wave-length ratio
N	= shape factor of stress-strain curve
n	= number of circumferential waves
r	= mean radius of cylinder
T_x, T_s, T_{xs}	= membrane forces
t	= thickness of cylinder
U	= total potential
U_0	= unevenness factor
u, v, w	= displacements in axial, circumferential, and radial directions
w_0	= initial radial displacement
V	= imperfection factor
x, s, z	= coordinates in axial, circumferential, and radial directions
x, y	= rectangular coordinates in a plane
γ	= tangent of average angle of buckling waves with axial direction
γ_{xs}	= middle surface shear strain
γ'_{xs}	= average unit angle of twist
γ_{xy}	= shear strain in xy plane
δ	= second unevenness factor
E	= strain energy
ϵ_x, ϵ_s, ϵ_y	= normal strains
η	= reduced modulus factor
λ_m	= ratio of circumference to critical longitudinal wave length
μ	= Poisson's ratio
ξ	= modulus ratio
σ_x, σ_y	= normal stresses
τ_{xs}	= average shear stress
τ_{xy}	= shear stress in xy plane
$(\tau_{cr})_0$	= critical buckling shear stress for perfect cylinder
$(\tau_{cr})_V$	= critical buckling shear stress for imperfect cylinder
χ_x, χ_s, χ_{xs}	= curvatures

Received May 10, 1956.

† This work was sponsored by The Bendix Products Division at the request of the ANC-5 Panel. The purpose was to investigate the need for a revision of certain allowables appearing in Government Document ANC-5, "Strength of Metal Aircraft Elements."

* Associate Professor of Engineering Mechanics.

** Head of Structures Development, Shock Strut Engineering, Bendix Products Division.

INTRODUCTION

THE EFFECTS of large deflections and imperfections on the elastic buckling strengths of cylindrical

shells have been investigated in recent years.[1–3] It has been shown that these effects are significant and that they provide a theoretical means to explain correctly the experimental phenomena in the elastic range. These effects are comparatively small in plastic buckling as revealed by available experimental results. They may still be significant, however, especially in the region close to the elastic range. It is the purpose of this paper to provide a formula to estimate closely the torsional strength of cylinders for design and to establish the order of magnitudes of these effects so that the scattering of test results can be, at least, partly explained.

There are three groups of theories on the plastic stress-strain relationships of work hardening materials—namely, incremental theories,[4–6] slip theories,[7–8] and deformation theories.[9–11] It has been shown, however, that available experimental results for the plastic buckling of plates and shells agree best with predictions obtained by using the deformation theories.[12–14] The stress-strain relationship based on the deformation theory as suggested by Ilyushin[11] is used as a mathematical simplification to fulfill the purposes of this investigation. In addition, Shanley's concept[15] that buckling and increase in load progress simultaneously has been considered. Thus the entire cylinder may remain in a purely plastic state in the early stages of buckling.

In studying the effects of imperfections, and in comparing experimental and theoretical results, the Ramberg-Osgood representation of the uniaxial stress-strain curve[16, 17] has been adopted. Furthermore, the following two assumptions have been made: (1) the displacements are small compared to length or diameter of the cylinder, but may be of the order of magnitude of the thickness, and (2) there are no normal stresses in the radial direction, and lines originally normal to the median surface of the shell remain so after loading.

Analysis

Membrane Forces and Moments

For a thin cylindrical shell of mean radius r, length L, and thickness t, let x, s, and z denote orthogonal coordinates in the axial, tangential, and radial directions, respectively. Further, let u, v, and w (positive inward) be the corresponding components of displacement of any point in the middle surface of the shell. The average shear stress, τ_{xs}, of the cylinder subjected to an external torque, M_t, is

$$\tau_{xs} = M_t/2\pi r^2 t \tag{1}$$

If the stress is in the plastic range, the corresponding shear strain, γ_{xs}, may be determined by the simple deformation theory of Ilyushin.[11] He considers an isotropic incompressible material (Poisson's ratio $\mu = 1/2$) and assumes that

$$\sigma_i = f(e_i) \qquad \text{for} \quad d\sigma_i > 0 \tag{2}$$

In a state of plane stress, the stress intensity

$$\sigma_i = \sqrt{\sigma_x^2 + \sigma_y^2 - \sigma_x\sigma_y + 3\tau_{xy}^2} \tag{3}$$

and the strain intensity

$$e_i = (2/\sqrt{3})\sqrt{\epsilon_x^2 + \epsilon_y^2 + \epsilon_x\epsilon_y + (\gamma_{xy}^2/4)} \tag{4}$$

σ_x, σ_y, and τ_{xy} are normal and shear stresses, respectively, and ϵ_x, ϵ_y, and γ_{xy} are the corresponding strains. The functional relationship shown in Eq. (2) may be determined from the uniaxial stress-strain curve of the material. If $d\sigma_i < 0$, the relationship between σ_i and e_i becomes linear as in the elastic range. According to Eq. (2), the average shear stress and the middle surface shear strain, γ_{xs}, have the following relationship before buckling:

$$\tau_{xs} = (E_{sec}/3)\,\gamma_{xs} \tag{5}$$

where $E_{sec} = \sigma_i/e_i$ is the secant modulus of elasticity.

When buckling occurs, the stress field may be considered to be composed of membrane and bending actions. They are revealed as follows. Considering the effects of large deflections and imperfections, the strain-displacement relationships[18] are

$$\left.\begin{aligned} \epsilon_x &= (\partial u/\partial x) + (K/2)\,(\partial w/\partial x)^2 \\ \epsilon_s &= (\partial v/\partial s) + (K/2)\,(\partial w/\partial s)^2 - (w/r) \\ \gamma_{xs} &= (\partial u/\partial s) + (\partial v/\partial x) + K(\partial w/\partial x)\,(\partial w/\partial s) \end{aligned}\right\} \tag{6}$$

in which ϵ_x and ϵ_s are middle-surface normal strains. The curvature-displacement relationships are

$$\left.\begin{aligned} \chi_x &= \partial^2 w/\partial x^2 \\ \chi_s &= \partial^2 w/\partial s^2 \\ \chi_{xs} &= \partial^2 w/\partial x\,\partial s \end{aligned}\right\} \tag{7}$$

The constant K introduced by Donnell is defined as follows:

$$K = 1 + (2w_0/w) = 1 + (2a_0 t/at) = 1 + (V/a) \tag{8}$$

Here w_0 is the initial radial deviation from the perfect shape, and is assumed to be proportional to the buckling shape w. The quantities $a_0 t$ and at are the amplitudes of w_0 and w, respectively. V is the imperfection factor.

According to the deformation theory,[12] the additional membrane forces, T_x, T_s, and T_{xs} per unit length of section, occurring as a result of the plastic torsional buckling, are

$$\left.\begin{aligned} T_x &= (4/3)\,E_{sec}\,t[\epsilon_x + (1/2)\epsilon_s] \\ T_s &= (4/3)\,E_{sec}\,t[\epsilon_s + (1/2)\epsilon_x] \\ T_{xs} &= (1/3)\,E_{tan}\,t\gamma_{xs} \end{aligned}\right\} \tag{9}$$

The bending moments per unit length of section are

$$\left.\begin{aligned} M_x &= -(E_{sec}\,t^3/9)\,[\chi_x + (\chi_s/2)] \\ M_s &= -(E_{sec}\,t^3/9)\,[\chi_s + (\chi_x/2)] \\ M_{xs} &= (E_{tan}\,t^3/18)\,\chi_{xs} \end{aligned}\right\} \tag{10}$$

where $E_{tan} = d\sigma_i/de_i$ is the tangent modulus of elasticity.

Membrane Force Function

Let the Airy function $F(x, s)$ be defined as follows:

$$\left.\begin{aligned} T_x &= t(\partial^2 F/\partial s^2) \\ T_s &= t(\partial^2 F/\partial x^2) \\ T_{xs} &= -t(\partial^2 F/\partial x\,\partial s) \end{aligned}\right\} \quad (11)$$

Then the condition of equilibrium for an element in the plane of the cylinder wall will be approximately satisfied if no body force is considered. The compatibility equation, in terms of the strains and the radial displacement, may next be obtained by eliminating u and v between Eqs. (6). Substituting from Eqs. (9) and (11) into the compatibility equation, the following relationship between the force function F and the radial displacement w is obtained:

$$\begin{aligned}(\partial^4 F/\partial x^4) + (3\xi - 1)\,(\partial^4 F/\partial x^2 \partial s^2) + (\partial^4 F/\partial s^4) &= KE_{sec}[(\partial^2 w/\partial x\,\partial s)^2 - (\partial^2 w/\partial x^2)\,(\partial^2 w/\partial s^2)] - (E_{sec}/r)\,(\partial^2 w/\partial x^2) \quad (12)\end{aligned}$$

where $\xi = E_{sec}/E_{tan}$.

From the nature of the problem, it appears that T_x, T_s, and T_{xs} will be harmonic functions, except for a constant component of T_{xs} equal to $t\tau_{xs}$ which exists prior to buckling. To satisfy this physical condition, the general solution of F from the homogeneous equation corresponding to Eq. (12) (when $w = 0$) is

$$F = -\tau_{xs} xs \quad (13)$$

The harmonic terms of the force function F may be obtained if the deflection surface is known or assumed. The deflection surface used in the elastic range[2] is in good agreement with the buckling phenomena and is assumed to be of the same shape in the plastic range. The deflection shape is

$$w = at\{\sin\,[n(s + \gamma x)/r]\,\sin\,(\pi x/L_x) + (d/2)\,[\cos\,(2\pi x/L_x) - 1]\} \quad (14)$$

Thus, $$w_0 = (a_0/a)\,w$$

Here a, n, γ, and d are arbitrary constants, and L_x is the longitudinal half-wave length. For the case of pure torsion, $L_x = L$.

Substituting from Eq. (14) into Eq. (12), the Airy force function is found to be

$$\begin{aligned} F = \frac{KE_{sec}(at)^2 m^2}{32}\Bigg[&\frac{1}{\gamma^4 + (3\xi - 1)\gamma^2 + 1}\cos\frac{2n(s + \gamma x)}{r} + \left(\frac{1}{m}\right)^4 \cos\frac{2\pi x}{L} + \frac{16d}{\alpha_1^4 + (3\xi - 1)\alpha_1^2 + 1} \times \\ &\cos\frac{n(s + \alpha_1 x)}{r} - \frac{16d}{\beta_1^4 + (3\xi - 1)\beta_1^2 + 1}\cos\frac{n(s + \beta_1 x)}{r} + \frac{16d}{\beta_3^4 + (3\xi - 1)\beta_3^2 + 1} \times \\ &\cos\frac{n(s + \beta_3 x)}{r} - \frac{16d}{\alpha_3^4 + (3\xi - 1)\alpha_3^2 + 1}\cos\frac{n(s + \alpha_3 x)}{r}\Bigg] + \frac{E_{sec}at}{2r}\left(\frac{r}{n}\right)^2 \times \\ &\left[\frac{\alpha_1^2}{\alpha_1^4 + (3\xi - 1)\alpha_1^2 + 1}\cos\frac{n(s + \alpha_1 x)}{r} - \frac{\beta_1^2}{\beta_1^4 + (3\xi - 1)\beta_1^2 + 1}\cos\frac{n(s + \beta_1 x)}{r} + \frac{d}{4m^2}\cos\frac{2\pi x}{L}\right] \quad (15)\end{aligned}$$

where $\alpha_1 = \gamma - m$ $\quad \beta_1 = \gamma + m$
$\alpha_3 = \gamma - 3m$ $\quad \beta_3 = \gamma + 3m$

Here m is the ratio between the circumferential and longitudinal half-wave length, or $m = L_s/L_x = \pi r/nL$. The parameters a, n, γ, and d are to be determined by minimizing the total potential with respect to these parameters.

Work and Strain Energy

The total strain energy in the cylinder may be considered to be composed of two parts. The first part is due to ordinary torsion, and the second is the strain energy, in terms of the membrane forces, and moments, caused by buckling. This latter may be expressed as

$$\mathrm{E} = (1/2)\iint (T_x\epsilon_x + T_s\epsilon_s + T_{xs}\gamma_{xs} + M_x\chi_x + M_s\chi_s + 2M_{xs}\chi_{xs})\,dx\,ds \quad (16)$$

Substituting Eqs. (6), (7), (9), (10), and (11) in Eq. (16), the strain energy due to buckling is obtained.

$$\begin{aligned}\mathrm{E} = \frac{t}{2E_{sec}}\int_0^L\int_0^{2\pi r}\Bigg[&\left(\frac{\partial^2 F}{\partial x^2}\right)^2 - \frac{\partial^2 F}{\partial x^2}\frac{\partial^2 F}{\partial s^2} + \left(\frac{\partial^2 F}{\partial s^2}\right)^2 + 3\xi\left(\frac{\partial^2 F}{\partial x\,\partial s}\right)^2\Bigg]dx\,ds + \frac{E_{sec}t^3}{18}\int_0^L\int_0^{2\pi r}\Bigg[\left(\frac{\partial^2 w}{\partial x^2}\right)^2 + \\ &\frac{\partial^2 w}{\partial x^2}\frac{\partial^2 w}{\partial s^2} + \left(\frac{\partial^2 w}{\partial s^2}\right)^2 + \frac{1}{\xi}\left(\frac{\partial^2 w}{\partial x\,\partial s}\right)^2\Bigg]dx\,ds \quad (17)\end{aligned}$$

In these integrations, it is assumed that no part of the cylinder is being unloaded, and E_{sec} and E_{tan} are considered to be independent of the position of an element. In other words, it is assumed that E_{sec} and E_{tan} of the middle surface element corresponding to an average shear stress are independent of the amplitude at of the deflection surface. This is approximately true for small values of a, and the peak buckling stress will not be greatly affected by this assumption.

Similarly, the work done by the external torque may also be considered to consist of two parts. The first part is related to the angular displacement caused by the ordinary torsion; and the second part is related to the additional angular displacement caused by the wave formations of the middle surface during buckling. The total work done by the external torque may be represented by the expression

$$\int_0^L\int_0^{2\pi r}\left[t\int_0^{\gamma_{xs}}\tau_{xs}\,d\gamma'_{xs}\right]dx\,ds \quad (18)$$

where $d\gamma'_{xs}$ is the total average strain increment. The product $\gamma'_{xs}\,(L/r)$ gives the value of the total angle of twist of one end with respect to the other.

Determination of Parameters

The total potential, U, is given by the sum of the strain energies and the potential of the external torque.

The partial derivatives of U with respect to the parameters a, n, γ, and d must be simultaneously zero. To simplify the solution, the approximate formulas for γ and n developed by Donnell[19] for the elastic range are adopted, since it has been assumed that the deflection surface in the plastic range is the same as that in the elastic range. These respective approximate formulas are as follows:

$$\gamma = -(1.732/H) \tag{19}$$

and

$$n = (\pi r/L)\,(H/0.722) \tag{20}$$

where

$$H = [L^2/rt]^{1/4}$$

Knowing the values of γ and n, the relationship between τ_{xs} and γ'_{xs} may next be established. γ'_{xs}, as previously defined, is actually the nonperiodic term in the expression $[(\partial u/\partial s) + (\partial v/\partial x)]$ of Eq. (6). Substituting from Eqs. (19), (20), and (14) into Eq. (6), and equating the nonperiodic terms on both sides of the equation, it is found that

$$(L/t)^2\,\gamma'_{xs} = (L/t)^2\,(3\tau_{xs}/E_{sec}) + 8.1979Ha(a + V) \tag{21}$$

The parameters a and d can then be determined by carrying out the differentiations

$$\partial U/\partial a = 0 \qquad \partial U/\partial d = 0 \tag{22}$$

These lead to the simultaneous equations

$$a\left\{a^2 + \frac{3}{2}Va + \frac{1}{2}V^2\right\}\left\{\frac{1}{9J^4 + 3(3\xi - 1)J^2 + 1} + \frac{H^4}{0.2718}\right\} + a\left\{0.08213\,H^8 \times \left[\frac{1}{0.0276H^4 + 0.1660(3\xi - 1)H^2 + 1} + \frac{1}{0.9608H^4 + 0.9802(3\xi - 1)H^2 + 1}\right] + 3.2704H^4\left[37.3063J^4 + 7.0422\left(1 + \frac{1}{\xi}\right)J^2 + 2\right]\right\} + d^2a\left\{16\left[a^2 + \frac{3}{2}Va + \frac{1}{2}V^2\right] \times \left[\frac{1}{36.2657J^4 + 6.0221(3\xi - 1)J^2 + 1} + \frac{1}{1.0406J^4 + 1.0201(3\xi - 1)J^2 + 1} + \frac{1}{0.0355J^4 + 0.1884(3\xi - 1)J^2 + 1} + \frac{1}{230.8698J^4 + 15.1944(3\xi - 1)J^2 + 1}\right] + 0.08213H^8 + 14.2222\right\} + 0.6079daH^4\left\{a + \frac{2}{3}V\right\}\left\{\frac{24.0884J^2}{36.2657J^4 + 6.0221(3\xi - 1)J^2 + 1} + \frac{4.0804J^2}{1.0406J^4 + 1.0201(3\xi - 1)J^2 + 1} + \frac{H^2}{0.5213}\right\} - 3.5910H\left\{\frac{L}{t}\right\}^2\left\{\frac{3\tau_{xs}}{E_{sec}}\right\}\left\{a + \frac{V}{2}\right\} = 0 \tag{23}$$

$$d\left\{1.7777 + 0.01026H^8 + [a + V]^2\left[\frac{1}{36.2657J^4 + 6.0221(3\xi - 1)J^2 + 1} + \frac{1}{1.0406J^4 + 1.0201(3\xi - 1)J^2 + 1} + \frac{1}{0.0355J^4 + 0.1884(3\xi - 1)J^2 + 1} + \frac{1}{230.8698J^4 + 15.1944(3\xi - 1)J^2 + 1}\right]\right\} + 0.02533H^4[a + V] \times \left[\frac{24.0884J^2}{36.2657J^4 + 6.0221(3\xi - 1)J^2 + 1} + \frac{4.0804J^2}{1.0406J^4 + 1.0201(3\xi - 1)J^2 + 1} + \frac{H^2}{0.5213}\right] = 0 \tag{24}$$

where $J = 1/H$.

For a cylinder of known geometry, the values of a and d may be calculated by assigning a value for V and a value for τ_{xs}. The quantities E_{sec} and ξ are functions of τ_{xs} which may be determined from the uniaxial stress-strain curve. It has been shown that the stress-strain relationship of ductile materials can be represented by a nondimensional equation of the form[16-17]

$$(\epsilon E/F_{0.7}) = (\sigma/F_{0.7})\,[1 + (3/7)\,(\sigma/F_{0.7})^{N-1}] \tag{25}$$

where E is Young's modulus, $F_{0.7}$ is the stress defined by the secant line of slope $0.7E$, N is a shape parameter, and σ and ϵ are stress and strain, respectively. The values of E, $F_{0.7}$, and N which define the shape of the stress-strain curve can be obtained experimentally. The quantity ξ can then be expressed in terms of τ_{xs} as

$$\xi = \frac{1 + (3/7)N(\sqrt{3}\tau_{xs}/F_{0.7})^{N-1}}{1 + (3/7)\,(\sqrt{3}\tau_{xs}/F_{0.7})^{N-1}} \tag{26}$$

Perfect Cylinder

In the perfect case—i.e., $V = 0$—the values of a and d determined from Eqs. (23) and (24) approach zero up to the peak buckling stress. Thus the peak buckling stress for a perfect cylinder, $(\tau_{cr})_0$, can be reduced from Eq. (23) to the following form:

$$3.5910H\left[\frac{L}{t}\right]^2\left[\frac{3(\tau_{cr})_0}{E_{sec}}\right] = 3.2704H^4 \times \left[37.3063J^4 + 7.0422\left(1 + \frac{1}{\xi_{cr_0}}\right)J^2 + 2\right] + 0.08213H\left[\frac{1}{0.0276H^4 + 0.1660(3\xi_{cr_0} - 1)H^2 + 1} + \frac{1}{0.9608H^4 + 0.9802(3\xi_{cr_0} - 1)H^2 + 1}\right] \quad (27)$$

Here ξ_{cr_0} is the modulus ratio corresponding to $(\tau_{cr})_0$.

In calculating the buckling strength in the plastic range, a factor, η, defined as[12]

$$(\tau_{cr})_{\text{plastic}} = \eta(\tau_{cr})_{\text{elastic}} \quad (28)$$

may be conveniently used. The elastic buckling stress may be computed by the usual equations, or may be computed from Eq. (27) by placing $\xi_{cr_0} = 1$ and $E_{sec} = E$. Poisson's ratio of necessity here would be equal to 1/2 for both the elastic and plastic cases. The exact expression for η is too lengthy and time consuming for practical use. It has been found by a cut-and-try process that

$$\eta = [1 - (0.06 + 0.114H - 0.006H^2) \times (1 - \xi_{cr_0}^{-1.5/H})](E_{sec}/E) \quad (29)$$

is a good approximation. It is believed that little error will be introduced if Eq. (29) is used along with some value of μ less than 1/2. The maximum deviation of the buckling stress computed using Eq. (29) as compared to that of the exact expression has been found to be less than one per cent for cylinders of ordinary metals. The value of η for all possible cases varies from $0.5(E_{sec}/E)$ to E_{sec}/E.

The buckling stresses for perfect cylinders of aluminum alloys computed by Eq. (27) or Eq. (28) are shown in Fig. 1 in a nondimensional form. $N = 10$ is used in the computation, as it has been shown[20] that the stress-strain curves of almost all of the aluminum alloys ordinarily used in aircraft structures can be approximated by a curve having this shape parameter.

Effects of Imperfections

When there are imperfections—i.e., $V \neq 0$—the values of a and d corresponding to a shear stress τ_{xs} may also be determined from Eqs. (23) and (24). Substituting a sequence of values of a in Eq. (21), a curve showing the variation of $\sqrt{3}\tau_{xs}/F_{0.7}$ against $(L/t)^2\,\gamma'_{xs}$ may be drawn. Such curves for the respective values of the dimensionless factors H, V, N, and $(L/t)^2(F_{0.7}/E)$ are shown in Figs. 2 through 10. These show that the effects of the imperfections (revealed through the drop-off peaks) depend upon the combinations of the various factors. The most pronounced result is that the effects of the imperfections decrease rapidly as the factor $\sqrt{3}\tau_{xs}/F_{0.7}$ increases. These effects therefore are much less in the plastic range than in the elastic range.

Summing up the results shown in Figs. 2 through 10

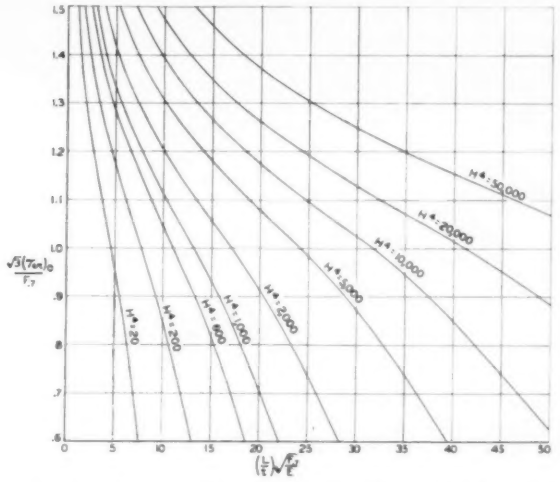

FIG. 1. Critical torsional buckling stresses for perfect aluminum-alloy cylinders.

the effects of the imperfections may be obtained by the following approximate formula found by cut and-try methods:

$$(\tau_{cr})_V/(\tau_{cr})_0 = 1 - (2/3)\,[V/\xi_{cr_0}^{3/2}(L^2/rt)^{0.3}]^{0.6} \quad (30)$$

Here $(\tau_{cr})_V$ is the drop-off peak value of buckling stress corresponding to a given imperfection factor V. In the elastic range, the formula established by Loo,[2]

$$(\tau_{cr})_V/(\tau_{cr})_0 = 1 - (3/4)\,[V/(L^2/rt)^{0.3}]^{0.6} \quad (31)$$

should be used. The apparent difference between these two equations [let $\xi_{cr_0} = 1$ in Eq. (30)] is due mainly to the difference in the values of Poisson's ratio used.

It has been suggested[1, 2] that the imperfection factor V can be related to the half-wave lengths L_x and L_s of the deflection surface by the equation

$$V = 2a_0 = 2U_0[L_xL_s/(L_x + L_s)]\cdot(1/t)^\delta \quad (32)$$

where U_0 and δ are experimentally determined unevenness factors. For the case of pure torsion, $L_x \cong L$ and $L_s = mL_x \cong mL$. In deriving Eq. (32), the geometric deviation has been considered the major part of the initial imperfection.

Donnell and Wan[1] have shown that, with $\delta = 2.0$, the unevenness factor U_0 varies from 1.5 to 3.0×10^{-5} for machined tubes, from 3.0 to 5.0×10^{-5} for cylinders carefully rolled from well-flattened sheet, and from 5.0 to 10.0×10^{-5} for cylinders rolled from unflattened sheet.

Exact Solution

The energy solution given in the preceding sections involves some simplifications and approximations. To check its accuracy, the exact solution for the case of a perfect, very long cylinder subject to torsion has been carried out. No attempt has been made to obtain the effects of end restraint by an exact solution because of the immense amount of work involved. The method used in the derivation of the fundamental equations in the plastic range is similar to that used by Timoshenko[21]

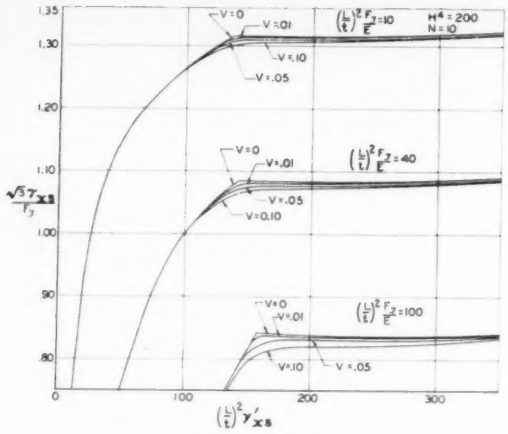

FIG. 2. Effects of imperfections.

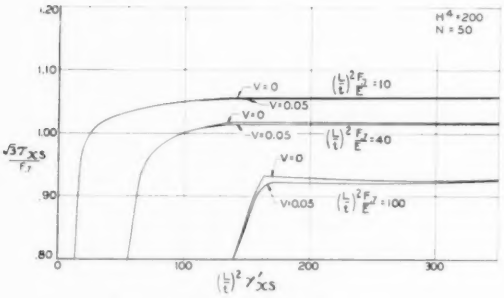

FIG. 4. Effects of imperfections.

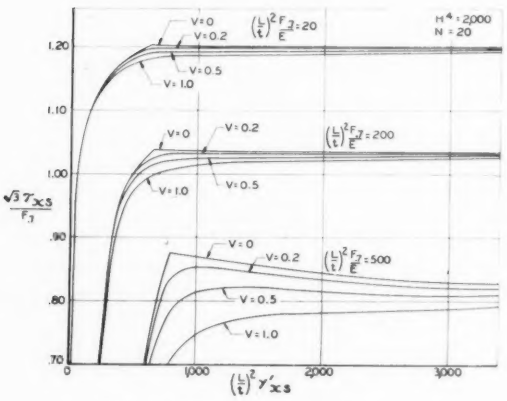

FIG. 6. Effects of imperfections.

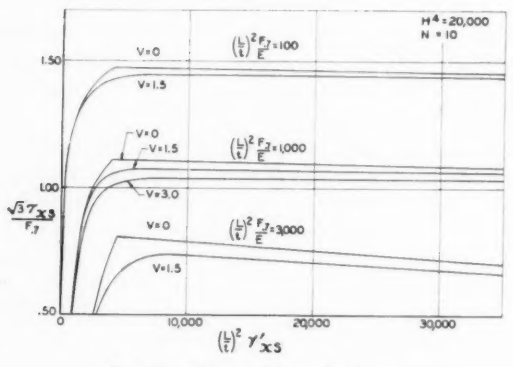

FIG. 8. Effects of imperfections.

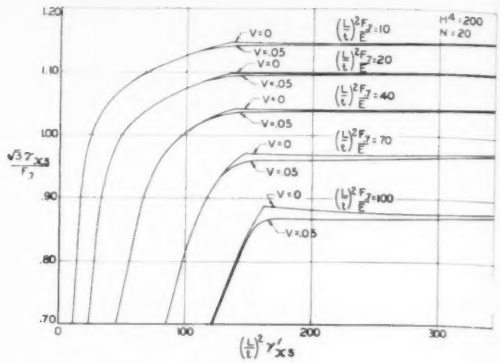

FIG. 3. Effects of imperfections.

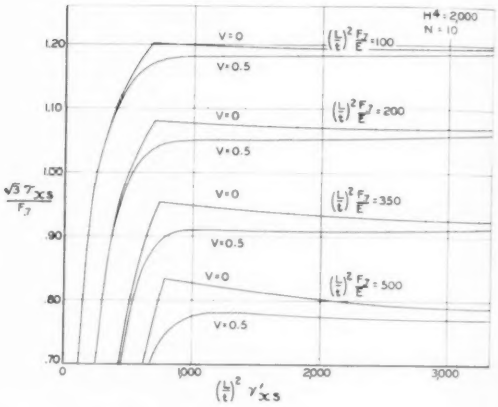

FIG. 5. Effects of imperfections.

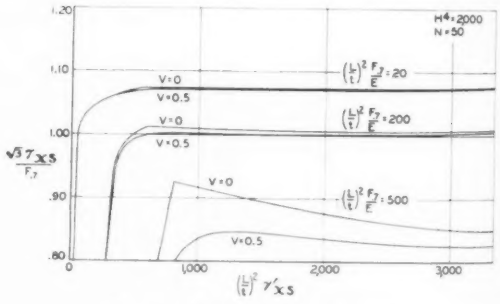

FIG. 7. Effects of imperfections.

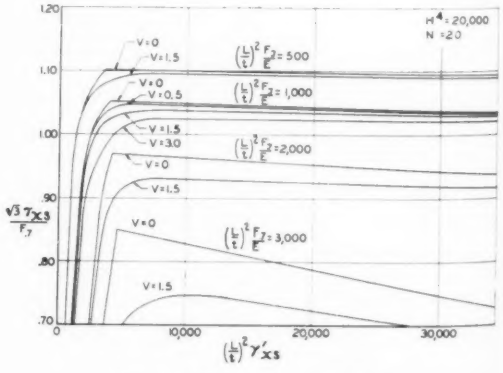

FIG. 9. Effects of imperfections.

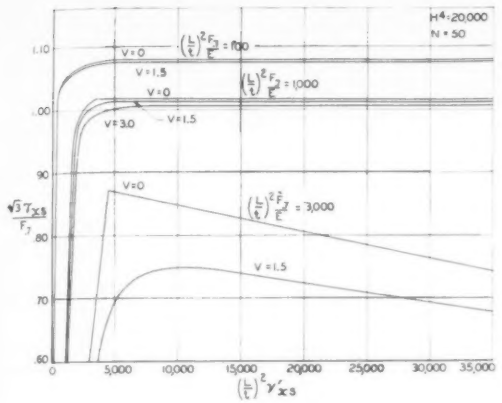

FIG. 10. Effects of imperfections.

for the same problem in the elastic range. From a consideration of the conditions of equilibrium of the membrane forces and bending moments and their relations to the displacements, three differential equations in terms of displacements are obtained. Assuming the deflection surface to be the same as that used by Timoshenko, the buckling stress is found to be

$$\tau_{cr} = \frac{E_{tan}}{12} \cdot \frac{3\xi\lambda_m^4 + 1.33[t/r]^2\,[(27\xi^2 + 10.5)\lambda_m^2 + 36\xi]}{(9\xi - 2)\lambda_m^3 + 12\lambda_m} \tag{33}$$

Here λ_m is the ratio of the circumference to the critical longitudinal wave length, and is equal to the least positive root of the equation

$$3\xi[9\xi - 2]\lambda^6 + [108\xi - 1.33(t/r)^2 \times (9\xi - 2)\,(27\xi^2 + 10.5)\,]\lambda^4 + 192[(1/12)\,(t/r)^2\,(27\xi^2 + 10.5) - 9\xi(9\xi - 2)\,]\lambda^2 - 6912\xi = 0 \tag{34}$$

ξ as used just above is the modulus ratio corresponding to the buckling stress τ_{cr}.

A comparison of the energy solution with the more exact solution has been made for cylinders of heat-treated steel having the following properties:[22] F_{tu} (ultimate tensile strength) = 90,000 psi, $E = 29 \times 10^6$ psi, F_{ty} (0.2 per cent offset yield stress) = 70,000 psi, $F_{0.7}$ = 67,700 psi, and $N = 17.6$. The results are shown in Fig. 11, where the quantity F_{st} is the torsional modulus of rupture as determined by the well-known elementary torsional formula

$$F_{st} = (M_t)_{cr} D/2I_0 \tag{35}$$

Here $(M_t)_{cr} = (\tau_{cr})_0\, 2\pi r^2 t$, D is the outside diameter of the cylinder, and I_0 is the polar moment of inertia. The theoretical curves given in Fig. 11 are for perfect cylinders. The curve $L/D = 0$ is based on the assumption that the complete section is subjected to the ultimate shear stress. The energy solution gives good agreement with the exact solution in the plastic range.

Comparison with Experimental Results

In Fig. 11, a total of 81 test results are also shown. The cylinders used in the tests were made of nominally 90,000 psi heat-treated steel,[23–27] and the recorded ultimate strengths varied from 88,400 psi to 122,700 psi. For comparison purposes, a shape factor $N = 17.6$ is assumed, and the experimental buckling stresses are reduced by direct ratio to those corresponding to 90,000 psi ultimate strength. Investigation of tubing torsional strength test data shows this to be feasible. The average ratio of experimental to theoretical buckling stress for the group is 1.070 (excluding test results of $D/t < 10$). It is believed that the higher values of the experimental results were due to (a) the additional strength developed by excess deformation after buckling (see Figs. 2–10) and (b) the loading function for the plastic stress-strain relationship.

A comparison of the experimental results of 24 aluminum-alloy tubes with the theoretical buckling stresses by Eq. (27) is shown in Table 1. Specimens 1 through 10 were machined from 75S-T6 2-in. diameter round rods,[28] and specimens 11 through 24 were made of 61S-T6 round tubing.[29] $N = 10$ was used in the calculations. $F_{0.7}$ was taken equal to 0.2 per cent offset yield stress.[30] For the 75S-T6 tubes, the longitudinal yield stress was 76,100 psi and the transverse yield stress was 70,000 psi; the average value of 73,050 psi was used in the computations. Only one set of yield stresses is given for the second group, and presumably they were longitudinal properties. The average ratio of experimental to theoretical buckling stress for the 24 cylinders is 0.930.

In an attempt to account for this relatively lower ratio of experimental to theoretical results for the aluminum cylinders, the effects of imperfections were considered. If the unevenness factors of $\delta = 2.0$, $U_0 = 3 \times 10^{-5}$ for machined tubes are substituted in Eq. (32) and then into Eq. (30), it is found that

$$(\tau_{cr})_V/(\tau_{cr})_0 = 1 - (0.00132/\xi_{cr_0}{}^{0.9}) \times (\{H/[1 + (0.722/H)]^{2.5}\}\,(r/t)^{1.25})^{0.48} \tag{36}$$

The computed effects of imperfections are shown in Table 1, and are found to be practically negligible. Another explanation is that the aluminum alloys are considerably anisotropic as indicated by the difference in the longitudinal and transverse properties. If the

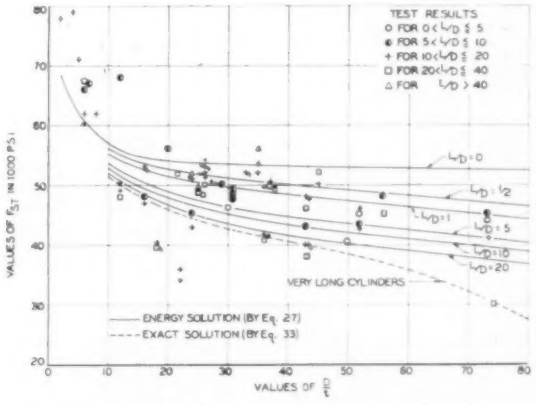

FIG. 11. Comparison of theory with experimental results—steel cylinders.

TABLE 1
Comparison of Theory With Experimental Results—Aluminum-Alloy Cylinders

Specimen	D/t	L/D	$F_{0.7}$, psi	$(\tau_{cr})_{exp}$, psi	$(\tau_{cr})_0$, psi by Eq. (27)	$(\tau_{cr})_V/(\tau_{cr})_0$ by Eq. (36)	$(\tau_{cr})_{exp}/(\tau_{cr})_0$
1	9.9	6.41	73,050	53,400	54,400	0.9991	0.982
2	15.1	6.94	73,050	50,000	50,900	0.9985	0.982
3	20.0	7.21	73,050	43,600	48,200	0.9978	0.904
4	20.1	6.55	73,050	44,800	48,100	0.9979	0.932
5	24.9	6.69	73,050	41,900	46,400	0.9971	0.904
6	30.1	6.78	73,050	41,700	44,400	0.9961	0.938
7	40.2	6.91	73,050	38,600	40,500	0.9932	0.953
8	48.9	6.98	73,050	36,200	37,300	0.9887	0.971
9	57.4	7.03	73,050	33,100	33,700	0.9822	0.982
10	80.6	7.09	73,050	20,600	23,800	0.9680	0.866
11	80.6	5.70	40,500	19,100	21,300	0.9867	0.897
12	58.8	5.70	38,000	18,600	22,600	0.9935	0.823
13	58.8	17.0	38,000	17,400	19,800	0.9853	0.878
14	39.4	5.70	38,500	22,700	25,100	0.9965	0.904
15	39.4	17.0	38,500	22,300	22,800	0.9933	0.978
16	39.4	27.6	38,500	22,000	21,600	0.9906	1.018
17	19.8	5.70	39,800	25,400	29,000	0.9983	0.876
18	19.8	17.1	39,800	25,100	27,000	0.9974	0.929
19	19.8	27.7	39,800	25,900	26,200	0.9968	0.988
20	10.0	17.1	39,700	28,600	30,500	0.9988	0.937
21	80.6	11.5	40,700	15,400	17,600	0.9713	0.875
22	60.6	11.5	40,000	20,200	21,200	0.9875	0.952
23	40.4	11.5	41,500	23,900	24,800	0.9941	0.963
24	20.1	11.5	38,600	24,500	27,200	0.9979	0.901
						Ave.	0.930

transverse yield strength and proper values of Poisson's ratio were used in the calculations, it is probable that better agreement between the experimental and theoretical results would be found.

Concluding Remarks

The effects of imperfections on the buckling strength of cylinders in the plastic range are relatively small. They may still be significant, however, depending on the combination of geometry, method of fabrication, stress-strain relationships, and the intensity of stress. Eqs. (30) and (32) can be used in estimating the reduction in buckling strength due to imperfections.

The results of this analysis indicate that the plastic stress-strain relationship given by the deformation theory again leads to a fairly accurate prediction of buckling strength. This shows that the deformation theory is at least adequate for solving buckling problems.

Acknowledgment

The lengthy computations required for this paper were done on digital computers at Wright Air Development Center. The writers are therefore indebted to G. M. Goldman, Air Force member of the ANC-5 Panel, for sponsoring the computer project; and to D. C. Zonars, F. W. Bauer, and R. S. Graham of the Systems Dynamic Analysis Branch for setting up the problem and running it off on the computers. Thanks are also due to J. N. Herrmann of The Bendix Products Division for his checking of the theory for very long cylinders; and his extensive work checking and plotting the test data, some of which were used in this paper.

References

[1] Donnell, L. H., and Wan, C. C., *Effects of Imperfections on Buckling of Thin Cylinders and Columns Under Axial Compression*, Trans. ASME, Vol. 72, pp. 73–83, 341–343, 1950.

[2] Loo, T. T., *Effects of Large Deflections and Imperfections on the Elastic Buckling of Cylinders Under Torsion and Axial Compression*, Proceedings of the Second U.S. National Congress of Applied Mechanics, pp. 345–357, 1954.

[3] Nash, W. A., *Effect of Large Deflections and Initial Imperfections on the Buckling of Cylindrical Shells Subject to Hydrostatic Pressure*, Journal of the Aeronautical Sciences, Vol. 22, No. 4, pp. 264–269, April, 1955.

[4] Saint-Venant, B., *Mémoire sur l'établissement des equations différentielles des mouvements intérieurs opérés dans les corps solides ductiles . . .*, Compt. rend. acad. sci. Paris, Vol. 70, p. 473, 1870.

[5] Handelman, G. H., Lin, C. C., and Prager, W., *On the Mechanical Behavior of Metals in the Strain-Hardening Range*, Quarterly Appl. Math., Vol. IV, No. 4, pp. 397–407, January, 1947.

[6] Drucker, D. C., *A More Fundamental Approach to Plastic Stress-Strain Relations*, Proceedings of the First U.S. National Congress of Applied Mechanics, pp. 487–491, 1951.

[7] Batdorf, S. B., and Budiansky, B., *A Mathematical Theory of Plasticity Based on the Concept of Slip*, NACA TN 1871, April, 1949.

[8] Lin, T. H., *A Proposed Theory of Plasticity Based on Slips*, Proceedings of the Second U.S. National Congress of Applied Mechanics, pp. 461–468, 1954.

[9] Hencky, H., *Über langsame stationäre Strömungen in plastischen Massen mit Rucksicht auf die Vorgänge beim Walzen, Pressen und Ziehen von Metallen*, Z.f.a.M.M., Bd. 5, Heft 2, p. 115, 1925.

[10] Nádai, A., *Theory of Flow and Fracture of Solids;* McGraw-Hill Book Company, Inc., New York, 1950.

[11] Ilyushin, A. A., *Stability of Plates and Shells Stressed Beyond the Elastic Limit*, NACA TM 1116, October, 1947. (Translated from Prikl. Mat. Mekh., Vol. 8, No. 5, pp. 337–360, Moscow, 1944.)

[12] Stowell, E. Z., *A Unified Theory of Plastic Buckling of Columns and Plates*, NACA Report 898, 1948.

[13] Bijlaard, P. P., *Theory and Tests on the Plastic Stability of Plates and Shells*, Journal of the Aeronautical Sciences, Vol. 16, No. 9, pp. 529–541, September, 1949. Discussions of the paper: Vol. 16, No. 9, pp. 567–568, September, 1949; Vol. 17, No. 6, pp. 378–379, June, 1950; and Vol. 17, No. 11, pp. 742–743, November, 1950.

[14] Batdorf, S. B., *Theories of Plastic Buckling*, Journal of the Aeronautical Sciences, Vol. 16, No. 7, pp. 405–408, July, 1949.

[15] Shanley, F. R., *Inelastic Column Theory*, Journal of the Aeronautical Sciences, Vol. 14, No. 5, pp. 261–268, May, 1947.

(*Continued on page 264*)

Boundary-Layer Measurements at Supersonic Nozzle Throats†

MERWIN SIBULKIN*
California Institute of Technology

Summary

Wall-static-pressure measurements and boundary-layer pitot-pressure surveys were made near the throat of a flexible-wall supersonic-wind-tunnel nozzle at three settings having throat radii of curvature from 33 to 59 in. It is found that the longitudinal static-pressure gradient at the nozzle throat calculated from one-dimensional flow theory agreed with the measured wall-static-pressure gradient.

The boundary-layer velocity profiles at the nozzle throat are presented and discussed. The boundary layers were turbulent and 0.046 to 0.107 in. thick. It is found that the boundary-layer momentum thickness at the nozzle throat calculated using the momentum integral equation and several approximations agrees with the values determined from the measured boundary-layer profiles. Finally, it is noted that, in spite of the different static-pressure gradients, the boundary-layer velocity profiles for the different nozzle settings are similar, and it is shown analytically that this similarity is to be expected.

Symbols

H = δ^*/θ
L^* = radius of curvature at nozzle throat $\equiv 2/(d^2t/dx^2)^*$
M = Mach Number
M_e = nozzle exit Mach Number
N = constant in equation $(u/u_1) = (y/\delta)^{1/N}$
p = static pressure
p_0 = supply pressure
p_0' = pitot pressure
t = local height of nozzle
T = temperature
T_e = equilibrium temperature
T_0 = (1) total temperature; (2) supply temperature
$\bar{T}$ = defined by Eq. (3)
u = velocity in x direction
u^* = shearing stress velocity $= \sqrt{\tau/\rho_w}$
x = distance parallel to wall
y = distance perpendicular to wall
β = free-stream velocity gradient at nozzle throat
γ = ratio of specific heats
δ = boundary-layer thickness
δ_{log} = boundary-layer parameter defined in text
δ^* = displacement thickness
θ = momentum thickness
ν = kinematic viscosity
ρ = static density
τ = wall shearing stress

Subscripts

1 = local value at boundary-layer edge
w = local value at wall

Superscripts

* = value at $M = 1$ (except δ^* and u^*)
$(\bar{})$ = mean value (evaluated at $\bar{T}$)

Introduction

The use of the momentum-integral-equation method for calculating the boundary-layer thickness corrections for wind-tunnel nozzle contours is widely known and has been partially confirmed by experiment. More recently, the boundary-layer integral equations have been used to calculate the heat transfer to wind-tunnel and rocket nozzle walls.[1] In these cases, the region of greatest interest is the nozzle throat since the heat-transfer rates are greatest there. An intermediate step in calculating local heat-transfer rates is the determination of the local boundary-layer momentum thickness. Consequently, measurements were made at several supersonic-nozzle throats to study the boundary layers there and to test the values of throat momentum thickness predicted by reference 1.

Experimental Technique

Measurements were made near the throat of the Jet Propulsion Laboratory's 12-in. supersonic wind tunnel of the pitot-tube pressure p_0' across the boundary layer and of the static pressure p along the nozzle wall. Because of the undesirability of drilling holes in the highly stressed nozzle flexible plate, a boundary-layer pitot probe was developed which could be supported from the tunnel test section.‡ A schematic drawing and photograph of the probe are shown in Fig. 1. The pitot tube is fixed to a cantilever beam which is free to move inside the body of the probe when the beam deflection cable is pulled. The deflection of the beam is sensed by a pair of strain gages glued to the beam and is measured by a self-balancing bridge (using a modified Brown Electronik precision indicator). The bridge was set so that one instrument division equalled 0.0002 in., as determined by calibrating the indicator reading against the movement of a micrometer screw; contact with the micrometer was determined by a sensitive electrical fouling circuit. The position of the wall was

Received June 11, 1956.

† This paper presents the results of one phase of research carried out at the Jet Propulsion Laboratory, California Institute of Technology, under joint sponsorship of the Department of the Army, Ordnance Corps (under Contract No. DA-04-495-Ord 18), and the Department of the Air Force.

* Formerly, Research Engineer, Jet Propulsion Laboratory. Now, Staff Scientist, Scientific Research Laboratory, Convair, San Diego, A Division of General Dynamics Corporation.

‡ The instrumentation was designed by Carl Thiele and built by J. A. Irving and D. E. Griffith of the Jet Propulsion Laboratory.

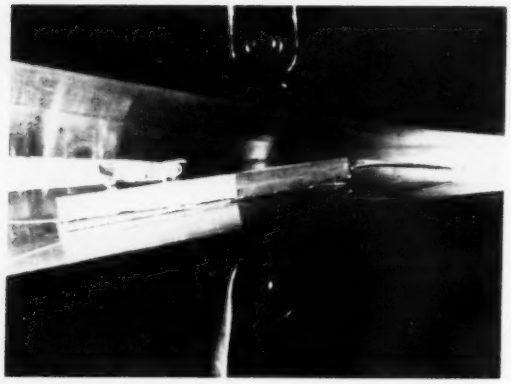

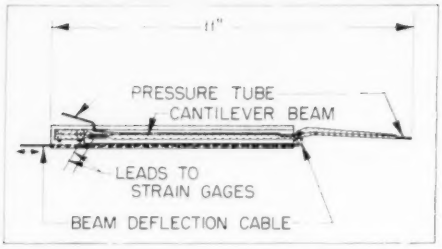

FIG. 1. Boundary-layer pitot probe. (*Top*). Probe in wind tunnel. (*Bottom*). Side view (schematic).

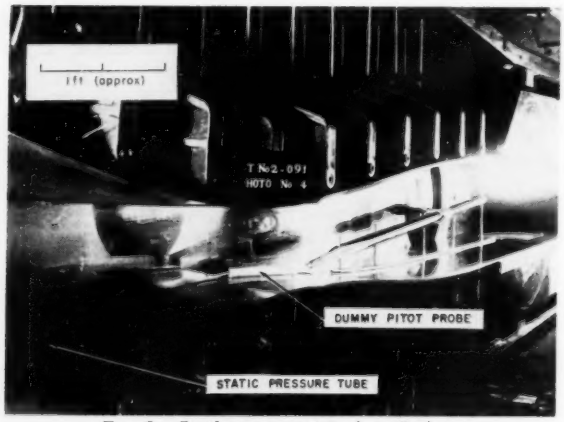

FIG. 2. Static-pressure-tube installation.

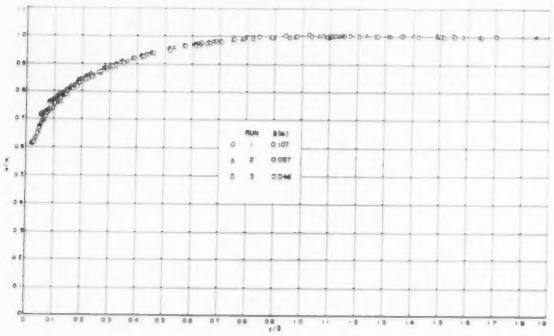

FIG. 5. Boundary-layer velocity distribution.

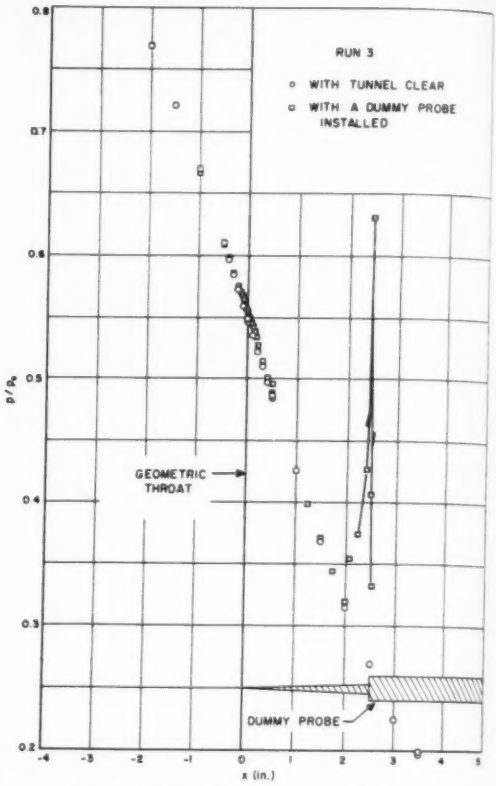

FIG. 3. Wall-static-pressure distribution.

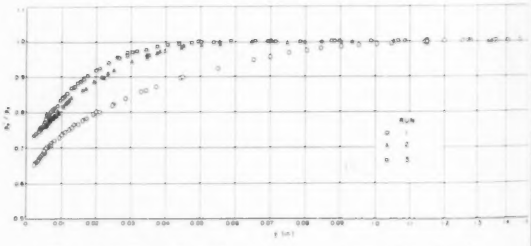

FIG. 4. Boundary-layer pitot-pressure distribution.

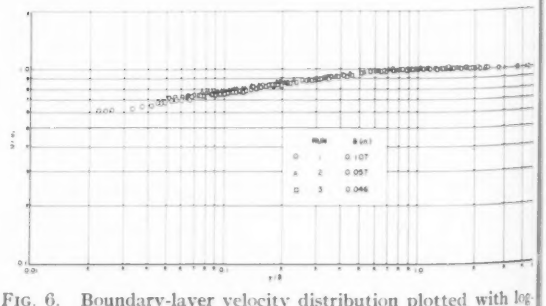

FIG. 6. Boundary-layer velocity distribution plotted with log-log coordinates.

TABLE 1
Tunnel Operating Conditions and Boundary-Layer Parameters

Run	M_s	L^* (in.)	L (in.)	p_0 (psia)	T_0 (°F)	u_1	
1	2.2	4.34	59	27.1	119	1.010	
2	3.3	1.45	34	27.1	102	0.984	
3	3.8	0.88	33	27.1	100	0.967	

Run	β (sec^{-1})		β (sec^{-1}) Eq. 6	δ (in.)	δ_{log} (in.)	θ (in.)	δ^* (in.)	$\frac{u_1\delta}{\nu}$
1	742		730	0.107	0.082	0.0077	0.0130	4220
2	1615		1649	0.057	0.042	0.0037	0.0064	2010
3	2140		2160	0.046	0.036	0.0031	0.0054	1720

Run	H	H Ref. 2	θ/δ	θ/δ_{log}	θ/δ Ref. 2	δ^*/δ	δ^*/δ_{log}	δ^*/δ Ref. 2
1	1.69	1.74	0.072	0.094	0.091	0.122	0.158	0.158
2	1.74	1.72	0.064	0.088	0.091	0.112	0.153	0.157
3	1.72	1.70	0.068	0.087	0.091	0.118	0.150	0.156

chosen as that probe deflection reading at which further movement of the beam toward the wall gave no corresponding decrease in the measured pressure, a result which showed that, although the cable was bending the flexible beam, the tip of the pitot tube was at a fixed position in the flow (i.e., at the wall). The tip of the pitot tube was made of flattened hypodermic tubing and had an external height of 0.0044 in. and a width of 0.025 in. The minimum probe Reynolds Number was 1,600 (based on a length of 0.0044 in.), which was large enough to avoid errors due to viscous effects.

The wall static pressure was measured by moving a 0.050-in. tube having four coplanar 0.008-in. holes along the nozzle wall (Fig. 2). The tube was moved by a simple screw and nut arrangement, and its position was read to 0.01 in. Measurements were made (1) with the tunnel clear and (2) with a dummy pitot probe installed over the tube to check the extent to which the probe disturbed the flow field.

Discussion of Measurements

Measurements were made at three nozzle settings corresponding to test-section Mach Numbers M_s of 2.2, 3.3, and 3.8. The nozzle shape parameters and tunnel supply conditions are given in Table 1. Previous hot-wire and pitot-pressure measurements made about 30 in. upstream from the nozzle throat had shown that the boundary layer was turbulent at that point. A typical static-pressure ratio, p/p_0, survey is shown in Fig. 3 where p_0 is the tunnel supply pressure and $x = 0$ is the nozzle geometric throat. It can be seen that the change in pressure due to the dummy pitot probe is small upstream from the probe body. The measured throat boundary-layer pitot-pressure ratio, p_0'/p_0, is plotted versus distance perpendicular to the wall y in Fig. 4. Each profile represents three or more traverses of the boundary layer. The minimum distance y at which data were obtained for run 2 is greater than for runs 1 and 3 because of a misalignment of the pitot-probe tip during run 2.

The velocity u in the boundary layer was calculated using the assumptions p = constant and T_0 = constant across the boundary layer. The value of p was taken from the static tube survey, and T_0 was taken as the wind-tunnel supply temperature. The values of p/p_0' and u/u_1 versus y/δ have been tabulated as Table III of reference 5, and the values of u/u_1 versus y/δ, log u/u_1 versus log y/δ, and u/u_1 versus log y/δ are plotted in Figs. 5, 6, and 7. The value of δ was chosen from Fig. 4 as the distance y at which $p_0'/p_0 = 0.995$.

A straight line faired through the velocity data plotted on the log-log basis (Fig. 6) gives a slope of about 1/7.0 to 1/7.5. This shows that the throat boundary layers were turbulent and suggests that assuming a 1/7-power velocity profile in applying the momentum integral equation to the calculation of boundary-layer thickness at a nozzle throat should give good results.

Theoretical values of u/u_1 versus y/δ were calculated from the incompressible turbulent velocity distribution of von Kármán

$$u/u_1 = 5.75\,(u^*/u_1)\log(y/\delta) + (u^*/u_1)\,[5.75\log(u^*\delta/\nu_w) + 5.5] \quad (1)$$

evaluated for $u^* = \sqrt{\tau/\rho_w}$. The shearing stress τ was calculated from

$$\tau/\bar{\rho}u_1^2 = 0.0126\,(\bar{\nu}/u_1\theta)^{1/4} \quad (2)$$

which is the incompressible turbulent skin-friction relation of Blasius modified by the evaluation of $\bar{\rho}$ and $\bar{\nu}$ at a mean temperature

$$\bar{T} \equiv (T_1 + T_r)/2 \quad (3)$$

The value of T_r was calculated using a turbulent recovery factor of 0.9. Combining Eqs. (1) and (2) gives u as a function of y for the known values of the

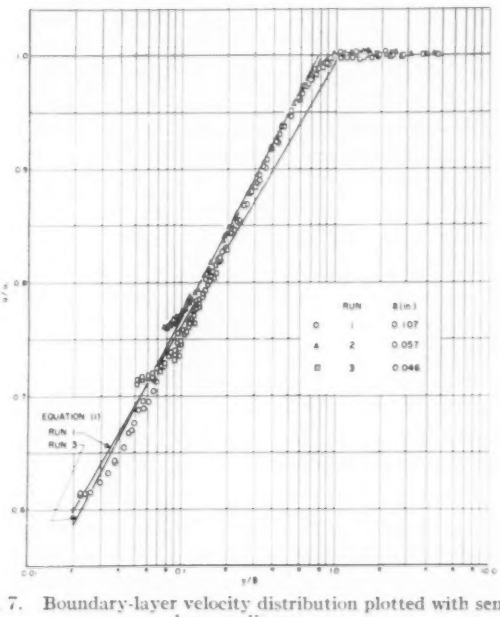

FIG. 7. Boundary-layer velocity distribution plotted with semi-log coordinates.

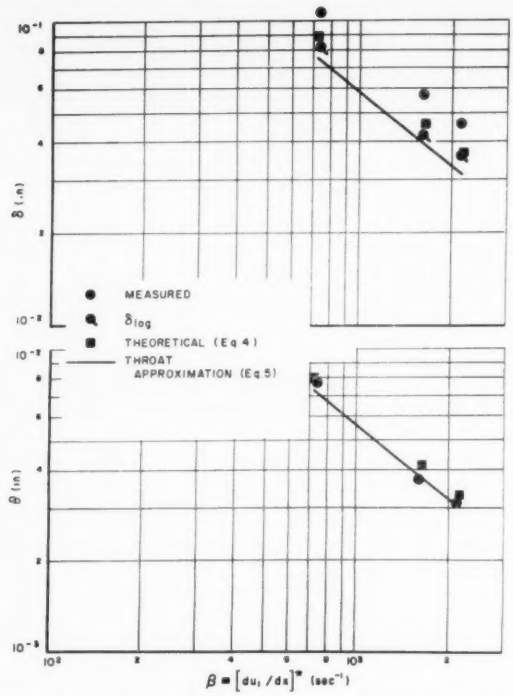

FIG. 8. Comparison of measured and calculated boundary-layer thicknesses.

constants δ, θ, u_1, ρ_w, $\bar{p}$, and $\bar{\nu}$. The computed curves for runs 1 and 3 (Fig. 7) bracket the data, and, although the measured flow was not incompressible, it is believed that this agreement implies that the wall shearing stress did not differ greatly from the values computed from Eq. (2).

The tunnel operating conditions and the measured boundary-layer parameters are summarized in Table 1. A boundary-layer thickness δ_{log} has been defined as the value of y at $u/u_1 = 1$ given by a straight line drawn through the data on a plot of log u/u_1 versus log y. From Fig. 6 it can be seen that for these measurements $\delta_{log}/\delta \cong 0.8$. Table 1 shows that the boundary-layer parameters were nearly constant for the three runs. This agreement would indicate (as do Figs. 5–7) that the boundary-layer profiles had a similar shape in spite of their having different static-pressure gradients. This similarity will be discussed in the next section. From Table 1 it can be seen that the measured values of the boundary-layer shape parameter H agreed with the theoretical values tabulated by Tucker[2] for $N = 7$. A comparison of the measured and calculated values of θ/δ and δ^*/δ shows that the measured physical boundary-layer thickness δ is greater than that given by theory. However, if the measured value of δ_{log} is used, the agreement is improved.

Comparison With Theory

A theoretical calculation of boundary-layer growth along the wind-tunnel nozzle was made by means of the boundary-layer momentum integral equation.

$$(d\theta/dx) + (H + 2 - M_1^2)\,(du_1/dx)\,(\theta/u_1) = \tau/\rho_1 u_1^2 \quad (4)$$

using values of τ given by Eq. (2) and values of H and θ/δ from reference 2 for $N = 7$. The calculation was started from a point about 30 in. upstream from the nozzle throat where previous measurements had shown the boundary layer to be turbulent and about 1/4-in. thick.

The boundary-layer thickness at the nozzle throat was also estimated by the "throat approximation" formula (Eq. 35 and Section IV-C of reference 1)

$$\delta = 0.052\,[(\bar{\nu}^*)^{1/5}\,(t^*L^*)^{2/5}/T_0^{1/10}], \qquad \theta = (7/72)\delta \quad (5)$$

The calculated and measured values of θ and δ are plotted on Fig. 8 against the measured values of the velocity-gradient parameter β. The calculated values of β were obtained (assuming one-dimensional, isentropic flow; cf. Appendix B of reference 1) from

$$\beta \equiv (du_1/dx)^* = 41.0\,\sqrt{T_0/t^*L^*} \quad (6)$$

Eq. (6) gave values of β which agreed within 2 per cent (Table 1) with the experimental values of β determined from the measured wall-static-pressure gradient (Fig. 3). It can be seen that the "throat approximation" for θ agrees with the more exact calculation and that both calculations agree with the measured values. The measured values of δ are higher than those calculated, while the measured values of δ_{log} are in closer agreement with those calculated, as might be expected from the behavior of θ/δ.

It has been noted that the nondimensional boundary-layer velocity profiles from the different nozzles are similar. It has been suggested[3] that, for incompressible flow, the shape of the velocity profile depends on a parameter of the form $(\theta/\tau)\,(dp/dx)$, which is the ratio of pressure to the viscous forces acting on the boundary layer [cf. Eq. (4)]. Consideration of the "throat approximation" analysis of reference 1, which is based on a linear-velocity gradient $u_1 = \beta x$, shows (cf. Appendix A of reference 5) that, for a particular nozzle, $(\theta/\tau)\,(dp/dx)$ does not vary with x; and, furthermore, that this constant value of $(\theta/\tau)\,(dp/dx)$ is independent of nozzle shape and supply conditions. The calculated numerical value of this parameter is

$$(\theta/\tau)\,(dp/dx) = -0.26 \quad (7)$$

This result implies (1) that, neglecting the effects of compressibility and within the accuracy of the "throat approximation" analysis, the turbulent boundary layers near supersonic nozzle throats are equilibrium layers, in the sense of reference 3, and (2) that the profiles should be similar since they have the same value of the equilibrium parameter. Since τ was not measured, it is not possible to check Eq. (7) directly.

Although no other equilibrium boundary-layer profiles having favorable pressure gradients, $(\theta/\tau)\,(dp/dx) < 0$, are available with which to compare these throat profiles, a comparison can be made with the turbulent-pipe-flow profile for which $(\theta/\tau)(dp/dx) \cong -0.19$

(Continued on page 264)

Postbuckling Behavior of Circular Cylindrical Shells Under Hydrostatic Pressure†

JOSEPH KEMPNER,* K. A. V. PANDALAI,** SHARAD A. PATEL,*** AND JACQUES CROUZET-PASCAL§

Polytechnic Institute of Brooklyn

Summary

The postbuckling behavior of initially perfect, thin-walled, circular cylindrical shells under hydrostatic pressure is investigated with the aid of the principle of stationary potential energy together with appropriate approximate deflection functions. Calculations show that postbuckling equilibrium configurations exist for loads greater than as well as loads slightly less than the critical load calculated from small-deflection theory. Loads less than the critical load are obtained only for a finite range of a parameter indicative of shell geometry. For loads corresponding to radial displacements of the order of the shell thickness, it is found that the number of circumferential waves remain essentially constant with increasing deflection and equal to the number of waves developed at buckling.

Symbols

A_j	$= \alpha^5/(1 + j\alpha)^2$
B	$= (\pi^4/48)(Rt/L^2)^2/(1 - \nu^2)$
C_j	$= A_j(\alpha + A_j^{1/2})$
D	$= (1/12)Et^3/(1 - \nu^2)$
E	= modulus of elasticity
$F(x, y)$	= Airy stress function
L	= shell length
R	= mean shell radius
U	$= (2\pi^3R^3/EtL^5)(W_1 + W_2 + W_3 + W_4)$
W_1, W_2, W_3, W_4	= extensional strain energy, bending strain energy, potential of applied axial load, and potential of applied lateral load, respectively
a, b, c	= deflection parameters
f	= stress-function parameter
g	= parameter appearing in stress function
k_p	$= \pi^2R^2p/EtL^2$
k_p'	= hydrostatic-pressure parameter corresponding to small deflection theory
$k_{p\ crit}$	= critical hydrostatic-pressure parameter
$k_{p\ min}$	= minimum value of k_p in postbuckling region
n	= number of circumferential waves
p	= external hydrostatic pressure
t	= wall thickness
u, v, w	= axial, circumferential, and inward radial displacements, respectively
$\bar{w}$	= uniform radial deflection of prebuckling state
x, y	= axial and circumferential coordinates on median surface of shell, respectively
α	$= (\lambda_y/L)^2$
α_{crit}	= value of α corresponding to critical pressure ($k_{p\ crit}$)
$\gamma_{xy}, \epsilon_x, \epsilon_y$	= median surface shear, axial, and circumferential strains, respectively
η	$= (t/R)n^2$
λ_y	= circumferential half-wave length
ν	= Poisson's ratio (0.3)
ξ	= deflection parameter
$\sigma_x, \sigma_y, \tau_{xy}$	= axial, circumferential, and shear median surface stresses, respectively
$\bar{\sigma}_x, \bar{\sigma}_y$	= average axial and circumferential compressive stresses, respectively
ω	$= \xi\eta$
∇^4	$= (\partial^4/\partial x^4) + 2(\partial^4/\partial x^2\partial y^2) + (\partial^4/\partial y^4)$

Received February 10, 1956. Revised and received July 12, 1956.

† This paper is based upon a dissertation submitted by K. A. V. Pandalai to the Polytechnic Institute of Brooklyn in partial fulfillment of the requirements for the degree of Doctor of Philosophy. The work reported on was sponsored by the Office of Naval Research under Contract No. Nonr 839(14), Project No. NRO64-167.

* Associate Professor of Aeronautical Engineering.

** Formerly, Research Associate. Now, Assistant Professor of Aeronautical Engineering, Madras Institute of Technology, Madras, India.

*** Research Associate.

§ Research Assistant.

Introduction

THE INABILITY of the classical small-deflection theory to predict critical loads in agreement with experimentally determined collapse loads for axially compressed circular cylindrical shells has led Donnell as well as several later investigators to consider the problem as one requiring an analysis based upon finite-deflection theory.[1–8] These investigators applied the principle of stationary potential energy together with suitably assumed deflection functions. With such an analysis, stable postbuckling equilibrium configurations corresponding to axial loads as low as 30 per cent of small-deflection critical loads have been obtained.[8] In reference 2, the average of published experimental data on failing loads of axially compressed cylinders is shown to be approximately 25 per cent of the critical load predicted by classical theory.

In view of the success of finite-deflection theory in revealing equilibrium states of deformation at loads considerably less than the critical load for axially compressed cylinders, the present investigation was initiated in the belief that similar results would be obtained from a finite-deflection analysis of cylinders under external hydrostatic pressure. In reference 9, Batdorf has compared the theoretical critical hydrostatic pressures of simply supported circular cylinders with test results of Windenburg and Trilling[10] and of Sturm.[11] The critical pressures were determined with the small-deflection Donnell equations of reference 12, which yielded results almost identical with those of von Mises.[13] This comparison indicated that, for

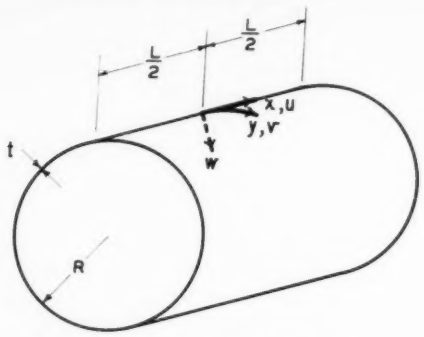

FIG. 1. Coördinates and components of displacement of a point on the median surface of the cylinder.

fixed values of the radius and thickness, good agreement between theory and experiment was obtained for relatively long cylinders, whereas for relatively short cylinders the experimentally determined collapse pressures were appreciably below the theoretically predicted critical pressures. Since the behavior of cylinders under external hydrostatic pressure is of considerable interest, it is important that this discrepancy be investigated. In the present report the postbuckling behavior of initially perfect cylinders is analyzed with the aid of the techniques applied in references 1, 3, and 5 to 8, appropriately modified to account for hydrostatic pressure loading. Calculations are performed with the aid of deflection functions chosen in such a way that critical loads obtained for vanishingly small wave amplitudes correspond to those derived from classical small-deflection theory (see for example, references 1 and 3). In the present case this consideration requires that at the ends of the cylinder no changes in curvature be permitted other than that caused by a uniform radial displacement. With the deflection functions considered, finite-deflection equilibrium configurations were found to exist for pressures greater than as well as less than the critical pressure determined from small-deflection theory. Pressures less than the critical pressure were found to exist only for a finite range of a parameter indicative of shell geometry.

BASIC RELATIONS

The present analysis is based upon the same relations among the strains, displacements, and stresses as the analyses of references 1, 3, 5, 6, and 8.

Strain-Displacement Relations—The axial and circumferential median-surface strains ϵ_x and ϵ_y and the corresponding shear strain γ_{xy} of a thin-walled circular cylindrical shell of radius R are taken as

$$\left.\begin{aligned} \epsilon_x &= (\partial u/\partial x) + (1/2)(\partial w/\partial x)^2 \\ \epsilon_y &= (\partial v/\partial y) + (1/2)(\partial w/\partial y)^2 - (w/R) \\ \gamma_{xy} &= (\partial u/\partial y) + (\partial v/\partial x) + (\partial w/\partial x)(\partial w/\partial y) \end{aligned}\right\} \quad (1)$$

in which u, v, and w are displacements of a point of the median surface in the axial, circumferential, and inward radial directions, respectively; x is the axial and y the circumferential coordinate of a point on the median surface (see Fig. 1).

Stress-Displacement Relations—The axial, circumferential, and shear stresses in the median surface are from Eqs. (1) and the usual form of Hooke's law for thin shells,

$$\left.\begin{aligned} \sigma_x &= [E/(1-\nu^2)]\{(\partial u/\partial x) + (1/2)(\partial w/\partial x)^2 + \nu[(\partial v/\partial y) + (1/2)(\partial w/\partial y)^2 - (w/R)]\} \\ \sigma_y &= [E/(1-\nu^2)]\{(\partial v/\partial y) + (1/2)(\partial w/\partial y)^2 - (w/R) + \nu[(\partial u/\partial x) + (1/2)(\partial w/\partial x)^2]\} \\ \tau_{xy} &= [E/2(1+\nu)]\{(\partial u/\partial y) + (\partial v/\partial x) + (\partial w/\partial x)(\partial w/\partial y)\} \end{aligned}\right\} \quad (2)$$

in which σ_x and σ_y are positive in tension; E is the modulus of elasticity; and ν is Poisson's ratio (0.3 in subsequent calculations).

Strain-Energy Expressions—The strain-energy expressions corresponding to median-surface and bending stresses, respectively, are (see, for example, reference 3)

$$W_1 = (t/2E)\int_{-L/2}^{L/2}\int_0^{2\pi R} [(\sigma_x + \sigma_y)^2 - 2(1+\nu)(\sigma_x\sigma_y - \tau_{xy}^2)]\,dx\,dy \quad (3)$$

$$W_2 = (D/2)\int_{-L/2}^{L/2}\int_0^{2\pi R} \{[(\partial^2 w/\partial x^2) + (\partial^2 w/\partial y^2)]^2 - 2(1-\nu)[(\partial^2 w/\partial x^2)(\partial^2 w/\partial y^2) - (\partial^2 w/\partial x \partial y)^2]\}\,dx\,dy \quad (4)$$

in which L is the length of the shell, t the wall thickness, and $D = (1/12)Et^3/(1-\nu^2)$.

Potential of External Loads—The potential energy of axial stresses applied symmetrically to the ends of the shell can be expressed as[3]

$$W_3 = -t\int_0^{2\pi R} (\sigma_x)_{x=L/2}\,dy \int_{-L/2}^{L/2} (\partial u/\partial x)\,dx \quad (5)$$

The potential energy of an applied external lateral pressure p is chosen to be consistent with the well known approximate large-deflection equations given below.

$$W_4 = -\int_{-L/2}^{L/2}\int_0^{2\pi R} pw\,dx\,dy \quad (6)$$

Variation of the total potential $W = W_1 + W_2 + W_3 + W_4$ with respect to the displacements u, v, and w yields three equilibrium equations (see, for example, reference 8). These equations together with Eq. (2) yield the equilibrium equation and the compatibility equation, respectively, given by

$$(D/t)\nabla^4 w = (\partial^2 F/\partial y^2)(\partial^2 w/\partial x^2) - 2(\partial^2 F/\partial x \partial y)(\partial^2 w/\partial x \partial y) + (\partial^2 F/\partial x^2) \times (\partial^2 w/\partial y^2) + (1/R)(\partial^2 F/\partial x^2) + (p/t) \quad (7)$$

and

$$\nabla^4 F = E[(\partial^2 w/\partial x \partial y)^2 - (\partial^2 w/\partial x^2)(\partial^2 w/\partial y^2) - (1/R)(\partial^2 w/\partial x^2)] \quad (8)$$

in which the Airy stress function $F(x, y)$ is defined by the relations

$$\sigma_x = (\partial^2 F/\partial y^2), \quad \tau_{xy} = -(\partial^2 F/\partial x \partial y), \quad \sigma_y = (\partial^2 F/\partial x^2) \tag{9}$$

and

$$\nabla^4 = (\partial^4/\partial x^4) + 2(\partial^4/\partial x^2 \partial y^2) + (\partial^4/\partial y^4)$$

Deflection and Stress Functions

As mentioned previously, the present analysis is based upon the procedure described in references 1, 3, and 5 to 8. In the present calculations, the deflection function is chosen as

$$\left.\begin{aligned} w &= \xi t_1^1 [a - \cos(\pi y/\lambda_y)][\cos(\pi x/L) + b\cos(3\pi x/L)] + e t_1^1 \\ &= \xi t[-\cos(\pi x/L)\cos(\pi y/\lambda_y) - b\cos(3\pi x/L)\cos(\pi y/\lambda_y) + a\cos(\pi x/L) + ab\cos(3\pi x/L) + e] \end{aligned}\right\} \tag{10}$$

in which x is measured from the center of a generator; ξ, a, b, and e are undetermined coefficients, λ_y is the circumferential half-wave length; and t and L, respectively, are the wall thickness and length of the cylinder. Thus at $x = \pm(L/2)$, the edge moment $M_x = -D[(\partial^2 w/\partial x^2) + \nu(\partial^2 w/\partial y^2)]$ vanishes, while the deflection corresponds to a uniform radial displacement (ξte). The latter deflection component was included in Eq. (10) to account for the uniform radial contraction prior to buckling assumed in the classical solutions.[9, 13] This term together with the first term of Eq. (10) in its expanded form are consistent with the small-deflection buckling solutions of references 9 and 13. The remaining terms were introduced to impart to the deflection function additional degrees of freedom in approximating the deflected shape in the postbuckling region. The additional degree of freedom obtained by allowing the coefficient of the cos $(3\pi x/L)$ term to be completely arbitrary could improve the solution but would entail a significant amount of additional computational labor. As in the previously cited references, in order to avoid an unwieldy number of deflection parameters, the remaining boundary conditions on u and v (or σ_x and τ_{xy}) are not stipulated; they are replaced by conditions of overall equilibrium explicitly applied to the stress function F.

For external hydrostatic pressure loading, the stress function satisfying Eq. (8) and consistent with the assumed deflection function of Eq. (10) is taken as

$$\begin{aligned} F = -(Et^2/\alpha\eta^2)[&f_{1,1}\cos(\pi x/L)\cos(\pi y/\lambda_y) + f_{2,2}\cos(2\pi x/L)\cos(2\pi y/\lambda_y) - f_{2,1}\cos(2\pi x/L)\cos(\pi y/\lambda_y) + \\ &f_{3,1}\cos(3\pi x/L)\cos(\pi y/\lambda_y) - f_{4,1}\cos(4\pi x/L)\cos(\pi y/\lambda_y) + f_{4,2}\cos(4\pi x/L)\cos(2\pi y/\lambda_y) - \\ &f_{6,1}\cos(6\pi x/L)\cos(\pi y/\lambda_y) - f_{1,0}\cos(\pi x/L) + f_{2,0}\cos(2\pi x/L) - f_{3,0}\cos(3\pi x/L) + f_{4,0}\cos(4\pi x/L) + \\ &f_{6,0}\cos(6\pi x/L) - f_{0,1}\cos(\pi y/\lambda_y) + f_{0,2}\cos(2\pi y/\lambda_y)] - (1/2)[\bar{\sigma}_x y^2 + (\bar{\sigma}_y + g)x^2] \end{aligned} \tag{11}$$

in which g is a parameter to be determined subsequently,

$$\bar{\sigma}_x = (pR/2t) \qquad \bar{\sigma}_y = (pR/t) \tag{12}$$

$$\begin{aligned} f_{1,1} &= A_1\omega & f_{1,0} &= \omega a \\ f_{2,2} &= (1/4)A_1\omega^2 b & f_{2,0} &= (1/32)\omega^2(1 + 2b) \\ f_{2,1} &= (1/2)A_4\omega^2 a(1 + 10b) & f_{3,0} &= (1/9)\omega ab \\ f_{3,1} &= 9A_9\omega b & f_{4,0} &= (1/64)\omega^2 b \\ f_{4,1} &= 5A_{16}\omega^2 ab & f_{6,0} &= (1/288)\omega^2 b^2 \\ f_{4,2} &= (1/16)A_4\omega^2 b & f_{0,1} &= (1/2)\alpha^2\omega^2 a(1 + 9b^2) \\ f_{6,1} &= (9/2)A_{36}\omega^2 ab^2 & f_{0,2} &= (1/32)\alpha^2\omega^2(1 + 9b^2) \\ \alpha &= (\lambda_y/L)^2 & \eta &= (\pi^2 Rt/\alpha L^2) = (t/R)n^2 \\ \omega &= \xi\eta = (\pi^2 Rt/L^2)(\xi/\alpha) & A_j &= \alpha^2/(1 + j\alpha)^2 \end{aligned}$$

and n is the number of circumferential waves.

The expression for the stress function F given in Eq. (11) satisfies the conditions that the average shear stress is zero and that overall equilibrium in the axial direction is satisfied. The parameter g can be related to the deflection parameters with the aid of the condition that the circumferential displacement v be periodic in y (see reference 3). From the first two of Eqs. (2) and Eqs. (9),

$$(\partial v/\partial y) = (1/E)[(\partial^2 F/\partial x^2) - \nu(\partial^2 F/\partial y^2)] - (1/2)(\partial w/\partial y)^2 + (w/R)$$

This relation together with Eqs. (10) to (12) and the periodicity requirement on v yields

$$\pi^2(gR^2/EL^2) = \alpha\omega e - (1/8)\alpha\omega^2(1 + b^2) - (1/2)(2 - \nu)k_p \tag{13}$$

in which the hydrostatic-pressure parameter k_p is defined as

$$k_p = \pi^2 R^3 p/EtL^2 \tag{14}$$

Determination of Deflection Parameters

The approximate analysis of the postbuckling behavior of cylinders under hydrostatic pressure can be performed with the use of Eqs. (10) and (11) and the principle that for equilibrium the total potential energy must have a stationary value for any small variation of the independent undetermined parameters appearing in the assumed deflection function. It may be noted that each parameter in Eqs. (10) and (11) can be expressed in terms of a, b, e, α, and ω.

Because considerable cancellation of terms is effected, it is simpler to calculate $W_1 + W_3$ rather than the individual quantities. W_1 can be determined from Eqs. (3), (9), and (11) to (14), while W_3 requires the consideration of the first two of Eqs. (2) and Eqs. (5) and (9) to (14). The result can be expressed as

$$U_1 + U_3 = (1/64)\alpha^2\omega^4\{648(2\alpha^2 + A_{36})a^2b^4 + 32(9\alpha^2 + 25A_4 + 25A_{16})a^2b^2 + 160A_4a^2b + 3(1 + 27\alpha^2)b^4 + 2(6 + 9\alpha^2 + 16A_1 + A_4)b^2 + 4b + 8(2\alpha^2 + A_4)a^2 + 3 + \alpha^2\} + (4/\pi)\alpha^2\omega^3\{(1/9)(1 + 162A_{36})ab^3 - (1/35)(27 + 420A_4 + 1200A_{16} + 162A_{36})ab^2 - (1/15)(3 + 118A_4 - 80A_{16})ab - (1/3)(1 + 2A_4)a - (\pi/8)(1 + b^2)e\} + (1/2)\alpha^2\omega^2\{(2 - 9k_p)a^2b^2 + (2 - k_p)a^2 + [81A_9 - (1/2\alpha)(9\alpha + \nu)k_p]b^2 + (16/3\pi)a(3 - b)e + 4e^2 + A_1 - (1/2\alpha)(\alpha + \nu)k_p\} + 2\nu k_p\alpha\omega\{(2/3\pi)a(3 - b) + e\} - (1/2)(1 - \nu^2)k_p^2 \quad (15)$$

in which

$$U_1 = (2\pi^3R^3/EtL^5)W_1, \text{ etc.} \qquad B = (\pi^4/48)(Rt/L^2)^2/(1 - \nu^2) \quad (16)$$

Also Eqs. (4) and (10), and (6) and (10), respectively, yield

$$U_2 = 2B\alpha^2\omega^2\{162a^2b^2 + 2a^2 + (1/A_9)b^2 + (1/A_1)\} \quad (17)$$

$$U_4 = -4k_p\alpha\omega\{(2/3\pi)a(3 - b) + e\} \quad (18)$$

Equations for the determination of the deflection parameters can now be derived by enforcing the condition that for equilibrium $U = U_1 + U_2 + U_3 + U_4$ must have a stationary value with respect to a, b, e, ω, and α. Calculations are facilitated if this is done first for e. Thus, from Eqs. (15), (17), and (18), $(\partial U/\partial e) = 0$ yields

$$e = (1/8)\omega(1 + b^2) - (2/3\pi)a(3 - b) + (1/2\,\alpha\omega)(2 - \nu)k_p \quad (19)$$

which can also be written as

$$\xi e = (1/8)(\pi^2Rt/L^2)(\xi^2/\alpha)(1 + b^2) - (2/3\pi)\xi a(3 - b) + (1/2)(L^2/\pi^2Rt)(2 - \nu)k_p \quad (19a)$$

From the boundary conditions considered, the prebuckling state of the shell must correspond to the degenerate form of the deflection function of Eq. (10), for which no wave-like deformation can exist. Such a form is obtained for the limiting conditions given by

$$\xi, a, b \to 0 \qquad (w/t) \to \xi e$$

Eq. (19a), together with these conditions, yields

$$\bar{w}/t = \{[1 - (\nu/2)]/[48(1 - \nu^2)B]^{1/2}\}k_p \quad (20)$$

in which the bar over the w indicates the uniform radial deflection of the prebuckling state. The relation between deflection and load given in Eq. (20) is identical to that obtained from elementary analysis of the uniform contraction of an infinitely long thin-walled circular cylindrical shell under external hydrostatic pressure.

With the aid of Eq. (19), the parameter e can be eliminated from Eqs. (15) and (18), and the total nondimensional potential U can be expressed as

$$U = (1/64)\alpha^2\omega^4\{648(2\alpha^2 + A_{36})a^2b^4 + 32(9\alpha^2 + 25A_4 + 25A_{16})a^2b^2 + 160A_4a^2b + (1 + 81\alpha^2)b^4 + 2(4 + 9\alpha^2 + 16A_1 + A_4)b^2 + 4b + 8(2\alpha^2 + A_4)a^2 + 1 + \alpha^2\} + (1/\pi)\alpha^2\omega^2a\{(1/9)(1 + 648A_{36})b^3 - (1/35)(73 + 1680A_4 + 4800A_{16} + 648A_{36})b^2 - (1/15)(17 + 472A_4 - 320A_{16})b - (1/3)(1 + 8A_4)\} + (1/2)\alpha^2\omega^2\{[2 - (16/9\pi^2) + 648B - 9k_p]a^2b^2 + (32/3\pi^2)a^2b + [2 - (16/\pi^2) + 8B - k_p]a^2 + [81A_9 + (4B/A_9) - (1/2\alpha)(2 + 9\alpha)k_p]b^2 + A_1 + (4B/A_1) - (1/2\alpha)(2 + \alpha)k_p\} - (1/2)(5 - 4\nu)k_p^2 \quad (21)$$

With this expression, the following four relations among the deflection parameters are obtained by enforcing the condition that, for equilibrium, U must have a stationary value with respect to a, b, ω, and α, respectively.

$$(1/32)\omega^2a\{648(2\alpha^2 + A_{36})b^4 + 32(9\alpha^2 + 25A_4 + 25A_{16})b^2 + 160A_4b + 8(2\alpha^2 + A_4)\} + (1/\pi)\omega\{(1/9) \times (1 + 648A_{36})b^3 - (1/35)(73 + 1680A_4 + 4800A_{16} + 648A_{36})b^2 - (1/15)(17 + 472A_4 - 320A_{16})b - (1/3)(1 + 8A_4)\} + a\{[2 - (16/9\pi^2) + 648B - 9k_p]b^2 + (32/3\pi^2)b + 2 - (16/\pi^2) + 8B - k_p\} = 0 \quad (22)$$

$$(1/16)\omega^2\{648(2\alpha^2 + A_{36})a^2b^3 + 16(9\alpha^2 + 25A_4 + 25A_{16})a^2b + 40A_4a^2 + (1 + 81\alpha^2)b^3 + (4 + 9\alpha^2 + 16A_1 + A_4)b + 1\} + (1/\pi)\omega a\{(1/3)(1 + 648A_{36})b^2 - (2/35)(73 + 1680A_4 + 4800A_{16} + 648A_{36})b - (1/15)(17 + 472A_4 - 320A_{16})\} + (16/3\pi^2)a^2 + b\{[2 - (16/9\pi^2) + 648B - 9k_p]a^2 + 81A_9 + (4B/A_9) - (1/2\alpha)(2 + 9\alpha)k_p\} = 0 \quad (23)$$

$$(1/16)\omega^2\{648(2\alpha^2 + A_{36})a^2b^4 + 32(9\alpha^2 + 25A_4 + 25A_{16})a^2b^2 + 160A_4a^2b + (1 + 81\alpha^2)b^4 + 2(4 + 9\alpha^2 + 16A_1 + A_4)b^2 + 4b + 8(2\alpha^2 + A_4)a^2 + 1 + \alpha^2\} + (3/\pi)\omega a\{(1/9)(1 + 648A_{36})b^3 - (1/35)(73 + 1680A_4 + 4800A_{16} + 648A_{36})b^2 - (1/15)(17 + 472A_4 - 320A_{16})b - (1/3)(1 + 8A_4)\} + [2 - (16/9\pi^2) + 648B - 9k_p]a^2b^2 + (32/3\pi^2)a^2b + [2 - (16/\pi^2) + 8B - k_p]a^2 + [81A_9 + (4B/A_9) - (1/2\alpha)(2 + 9\alpha)k_p]b^2 + A_1 + (4B/A_1) - (1/2\alpha)(2 + \alpha)k_p = 0 \quad (24)$$

$$(1/32)\omega^2\{648(4\alpha^3 + C_{36})a^2b^4 + 32(18\alpha^3 + 25C_4 + 25C_{16})a^2b^2 + 160C_4a^2b + \alpha(1 + 162\alpha^2)b^4 + 2(4\alpha + 18\alpha^3 + 16C_1 + C_4)b^2 + 4\alpha b + 8(4\alpha^3 + C_4)a^2 + \alpha(1 + 2\alpha^2)\} + (2/\pi)\omega a\{(1/9)(\alpha + 648C_{36})b^3 - (1/35)(73\alpha + 1680C_4 + 4800C_{16} + 648C_{36})b^2 - (1/15)(17\alpha + 472C_4 - 320C_{16})b - (1/3)(\alpha + 8C_4)\} + \alpha[2 - (16/9\pi^2) + 648B - 9k_p]a^2b^2 + (32/3\pi^2)\alpha a^2b + \alpha[2 - (16/\pi^2) + 8B - k_p]a^2 + [36B(1 + 9\alpha) + 81C_9 - (1/2)(1 + 9\alpha)k_p]b^2 + 4B(1 + \alpha) + C_1 - (1/2)(1 + \alpha)k_p = 0 \quad (25)$$

in which $C_j = A_j(\alpha + A_j^{1/2})$

Thus, for specified values of the cylinder parameter B and pressure parameter k_p, the simultaneous solution of the nonlinear algebraic equations (22) to (25) determines the deflection parameters a, b, α, and ω such that the corresponding potential has a stationary value.

For vanishingly small wave-amplitudes, the following relations between load and wave-length ratio corresponding to the small-deflection asymmetrical buckling theory of reference 9 can be obtained from Eqs. (24) and (25), respectively, if ω, a, and b are permitted to vanish.

$$\left.\begin{aligned} k_p' &= 2[\alpha^4 + 4B(1 + \alpha)^4]/\alpha(2 + \alpha)(1 + \alpha)^2 \\ k_p' &= 2[\alpha^3(2 + \alpha) + 4B(1 + \alpha)^4]/(1 + \alpha)^4 \end{aligned}\right\} \quad (26)$$

in which the prime on the load indicates the limiting case of small-deflection theory. Elimination of k_p' from Eqs. (26) yields the following polynomial for the determination of α such that k_p' corresponds to the critical hydrostatic pressure:

$$2\alpha^5 + 3\alpha^4 - 4B(1 + \alpha)^4 = 0 \quad (27)$$

Since Eq. (27) corresponds to small-deflection theory, it can also be obtained from the first of Eqs. (26) if k_p' is minimized with respect to α therein.[9]

Application of Descarte's rule of signs to Eq. (27) shows that there exists at most one positive real root for α. Eq. (27) and either of Eqs. (26) can be combined to yield

$$k_{p\,crit} = 4\alpha_{crit}^3/(1 + \alpha_{crit})^2 \quad (28)$$

in which $k_{p\,crit}$ is the critical hydrostatic-pressure parameter and α_{crit} is the corresponding wave-length parameter determined by Eq. (27).

In Fig. 2 the variation of $k_{p\,crit}$ and α_{crit} with the cylinder parameter B is shown. It may be noted that these results, obtained with Eqs. (27) and (28), are identical to those of reference 9.

Approximate axially symmetric buckling loads corresponding to cylinders with free edges can also be obtained from Eqs. (22) and (23). These loads together with corresponding deflection functions and limiting conditions on the parameters appearing in Eq. (10) are

$$\left.\begin{aligned} k_{p\,crit_1} &= 2[1 - (8/\pi^2)] + 8B \\ w &= \xi t[a\cos(\pi x/L) + e]; \qquad (\xi, b \to 0;\ \xi a, \xi e \neq 0) \end{aligned}\right.$$

$$\left.\begin{aligned} k_{p\,crit_2} &= (2/9)[1 - (8/9\pi^2)] + 72B \\ w &= \xi t[ab\cos(3\pi x/L) + e]; \qquad (\xi, \xi a, \xi b \to 0;\ \xi ab, \xi e \neq 0) \end{aligned}\right.$$

$$\left.\begin{aligned} k_{p\,crit_{1,2}} &= (1/2)\{k_{p\,crit_1} + k_{p\,crit_2} - [(k_{p\,crit_1} - k_{p\,crit_2})^2 + (1024/81\pi^4)]^{1/2}\} \\ w &= \xi t[a\cos(\pi x/L) + ab\cos(3\pi/L) + e]; \qquad (\xi, \xi b \to 0;\ \xi a, \xi ab, \xi e \neq 0) \end{aligned}\right.$$

These results are also indicated in Fig. 2. It can be shown that buckling loads corresponding to $k_{p\,crit_{1,2}}$ afford good approximations to those determined from exact solution of the axially symmetric, small-deflection differential equations in the region considered. Fig. 2 shows that when $B > 7.2 \times 10^{-2}$, $k_{p\,crit_{1,2}} < k_{p\,crit_1}$ and hence, buckling is initiated in an axially symmetric fashion. Calculations also show that when $B > 7.96 \times 10^{-2}$, $k_{p\,crit_1} < k_{p\,crit}$ (see also Fig. 2). The primary concern of the present analysis of postbuckling behavior is with equilibrium configurations initiated by asymmetrical buckling.

Numerical Solutions and Discussion of Results

Because of the complicated nature of the set of simultaneous equations (22) to (25), which corresponds to the assumed deflection function of Eq. (10), it was expedient first to solve four simpler sets of equations based upon approximations to Eq. (10) before considering the more complete solution. This served the double purpose of producing, with relatively simple computations, first approximations for subsequent calculations and of indicating the suitability of the assumed deflection function.

First Approximation $a = b = 0$

The deflection function corresponding to small-deflection theory affords a simple first approximation. Since this function corresponds to that of Eq. (10) when a and b are fixed as zero, the related set of equations for determination of the remaining deflection parameters α and ω is given by Eqs. (24) and (25) with $a = b = 0$. Manipulation of the resulting

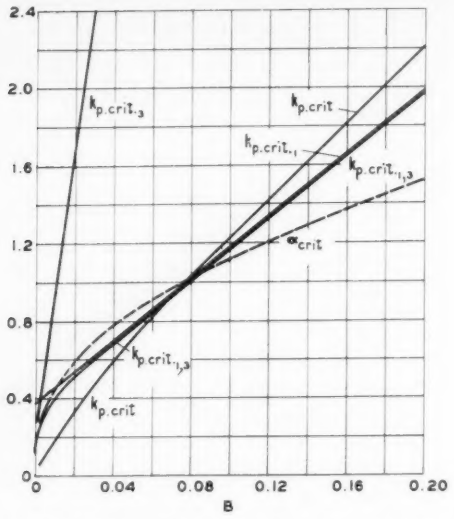

FIG. 2. Variation of buckling parameters with B.

equations yields

$$k_p = [2/\alpha^2(1 - 2\alpha)(1 + \alpha)^3][\alpha^4(3 + \alpha + 2\alpha^2) - 4B(1 + \alpha)^4(1 - \alpha + 2\alpha^2)] \quad (29)$$

Thus, for a given value of the cylinder parameter B, α can be determined for any specified value of k_p. It is, of course, much simpler to choose α and solve for k_p. In either case only positive values of α are admissible, since $\alpha = (\lambda_y/L)^2$. Furthermore once a set of values for k_p and α is determined, the parameter ω can be calculated from Eqs. (24) or (25). If ω and α constitute a solution of these equations then so does the set $-\omega$, α. Obviously, values of k_p and α must be restricted to that range in which ω is real. Hence, enforcement of the condition that ω^2 must be greater than or equal to zero yields from Eq. (24) (with $a = b = 0$)

$$k_p \geq 2[\alpha^4 + 4B(1 + \alpha)^4]/\alpha(2 + \alpha)(1 + \alpha)^2$$

The smallest value of k_p from this expression is k_p', where k_p' is given by the first of Eqs. (26). It has been shown previously that the minimum value of k_p' is $k_{p\ crit}$. Thus, within the present approximation the least permissible value of the postbuckling pressure is the critical pressure computed from small-deflection theory, and hence in Eq. (29) $k_p \geq k_{p\ crit}$.

Since the deflection coefficient ξ appearing in Eq. (10) is related to α, ω, and B by the expression

$$\xi = \alpha\omega/[48(1 - \nu^2)B]^{1/2}$$

and since e is given by Eq. (19), the amplitudes and wave-length ratio ($\alpha^{1/2}$) of the deflection function of Eq. (10) with $a = b = 0$ are readily determined for all admissible values of k_p.

The postbuckling region was investigated with the aid of Eqs. (29) and (25) (with $a = b = 0$) for $\nu = 0.3$ and $B = 3 \times 10^{-4}$, 2×10^{-3}, 2×10^{-2}, and 2×10^{-1}. These values of B were chosen because they correspond to the region within which reference 9 indicates large discrepancies between small-deflection buckling theory and experiments. In Fig. 3, curves are presented showing the variation of α, ω, ξ, and ξe with k_p for the aforementioned values of B. It may be noted from Eq. (29) that as $\alpha \to 1/2$, $k_p \to \infty$, provided $B \neq 1/81$. When $\alpha = 1/2$ and $B = 1/81$, k_p is found to be negative and hence from Eq. (24) (with $a = b = 0$), ω is imaginary. From Eq. (29) it can also be shown that for $B = 1/81$ the parameter k_p is negative for all α; thus Eq. (24) yields only imaginary values for ω. This analysis shows that the present solution is unsuitable for the investigation of the postbuckling region when $B = 1/81$. However, for this value of B Eqs. (27) and (28) yield $k_{p\ crit} = 2/9$ and $\alpha_{crit} = 1/2$, and thus a singular solution is obtained.

From Eq. (10) (with $a = b = 0$), it may be noted that, since ξe is always positive [see Eq. (19a)], the maximum radial deflection is given by $t(|\xi| + \xi e)$. The variation of k_p with $(w_{max}/t) = (|\xi| + \xi e)$ is shown by the solid lines in Fig. 4. Thus, according to the present approximation the postbuckling behavior is characterized by a relation between pressure and maximum radial deflection such that k_p increases monotonically with w_{max}, has its least value $k_{p\ crit}$ at α_{crit}, and grows indefinitely large as α approaches one half. The latter two conditions correspond to $w_{max} \to (\bar{w})_{kp\ crit}$ and $w_{max} \to \infty$, respectively. The initial straight line portion of each curve lies in the prebuckling region defined by $0 \leq k_p \leq k_{p\ crit}$, and hence the relation between pressure and deflection in this region is given in Eq. (20).

Although the analysis shows that the wave-length parameter α assumes values between α_{crit} and one half, the calculations indicate that for loads corresponding to radial displacements of the order of the shell thickness, α is almost identical to α_{crit} (see Fig. 3). Hence, in this region the number of circumferential waves remains essentially constant. If the present approximation is simplified by fixing $\alpha = \alpha_{crit}$, Eqs. (24), (27), and (28) yield

$$\omega^2 = 8[(2 + \alpha_{crit})/\alpha_{crit}(1 + \alpha_{crit}^2)](k_p - k_{p\ crit}) \quad (30)$$

which satisfies the requirement that $k_p \to k_{p\ crit}$ as $\omega \to 0$. When the results stemming from Eq. (30) are plotted in the region covered in Fig. 4, the curves obtained cannot be distinguished from the corresponding curves determined by the unsimplified first-approximation solution. However, when $B = 1/81$, Eq. (30) yields results in the postbuckling region, whereas Eq. (29) did not (see Fig. 4).

An investigation of the state of equilibrium of the postbuckling configurations determined with the first-approximation solution and the simplified first-approximation solution was performed with the aid of the second variation of the total potential (see for example, reference 8). This analysis showed that the results correspond to states of stable equilibrium.

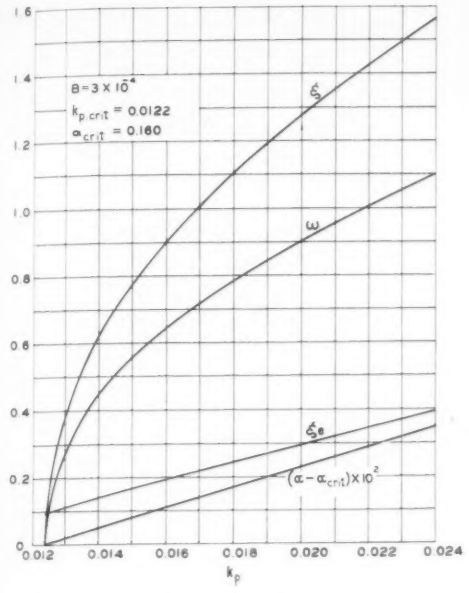

FIG. 3(a). Variation of deflection parameters with k_p (first approximation; $a = b = 0$).

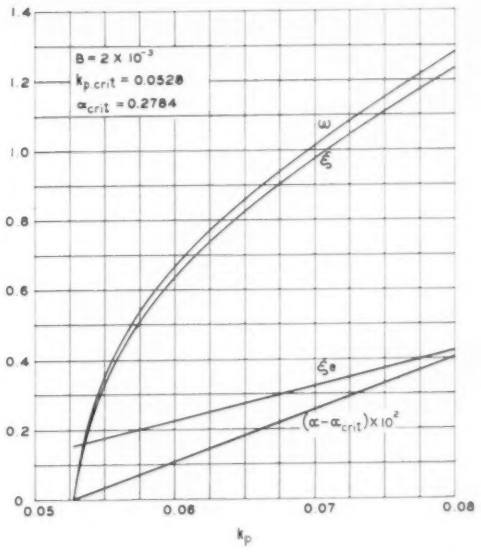

FIG. 3(b). Variation of deflection parameters with k_p (first approximation; $a = b = 0$).

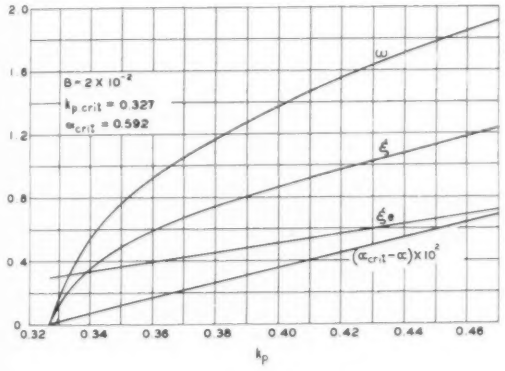

FIG. 3(c). Variation of deflection parameters with k_p (first approximation; $a = b = 0$).

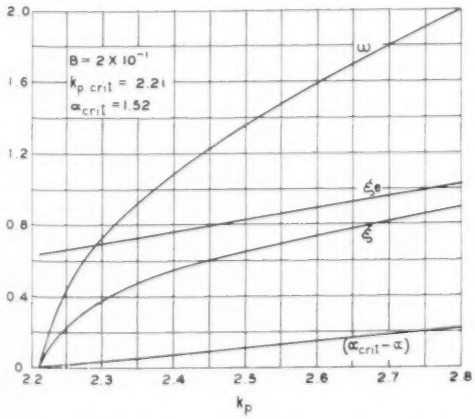

FIG. 3(d). Variation of deflection parameters with k_p (first approximation; $a = b = 0$).

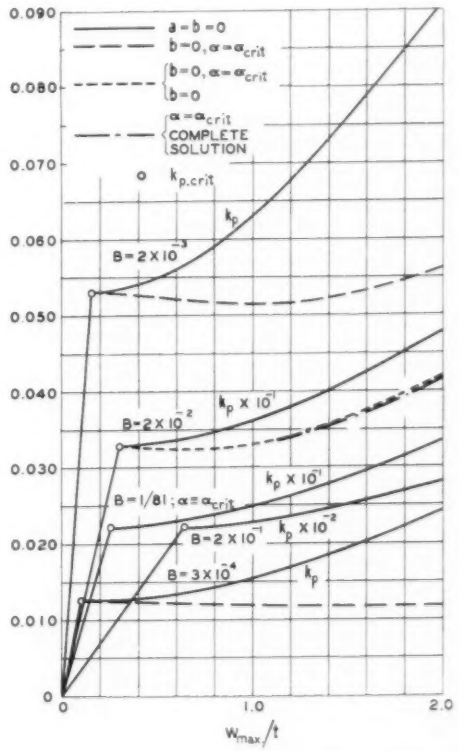

FIG. 4. Variation of k_p with maximum displacement.

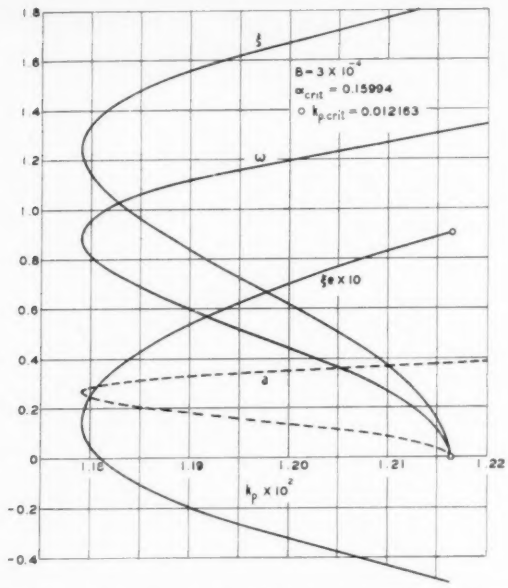

FIG. 5(a). Variation of deflection parameters with k_p (simplified second approximation; $b = 0$, $\alpha = \alpha_{crit}$).

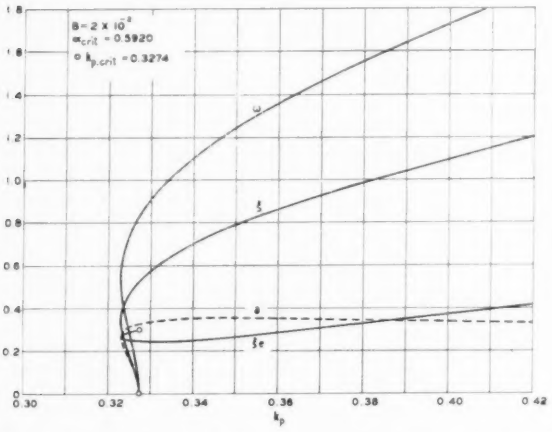

FIG. 5(c). Variation of deflection parameters with k_p (simplified second approximation; $b = 0$, $\alpha = \alpha_{crit}$).

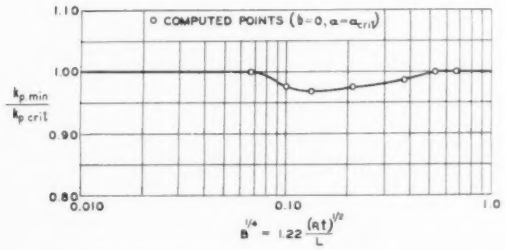

FIG. 7. Ratio of minimum pressure to critical pressure as a function of cylinder parameter B.

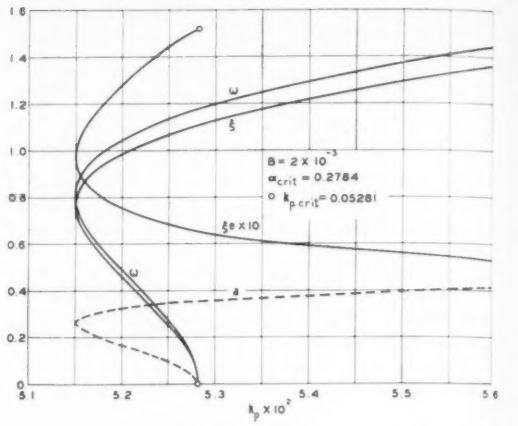

FIG. 5(b). Variation of deflection parameters with k_p (simplified second approximation; $b = 0$, $\alpha = \alpha_{crit}$).

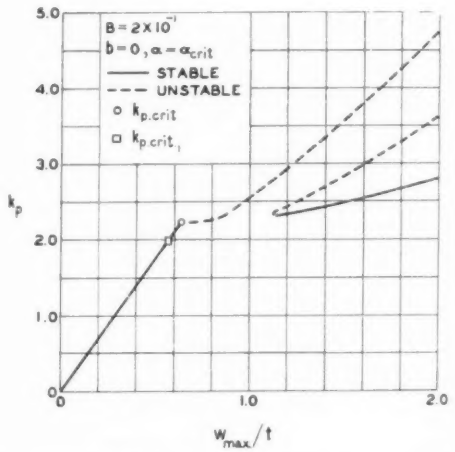

FIG. 6. Variation of k_p with maximum displacement ($B = 2 \times 10^{-1}$).

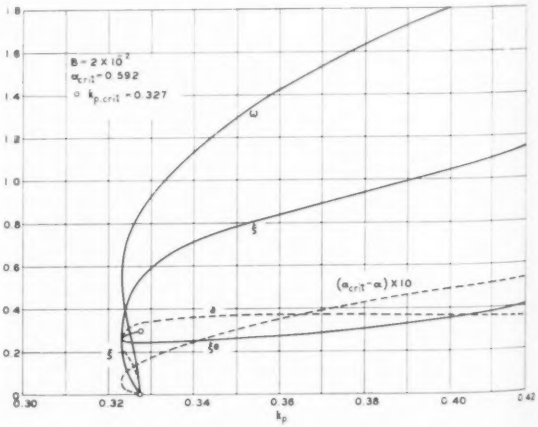

FIG. 8. Variation of deflection parameters with k_p (second approximation; $b = 0$).

Second Approximation $b = 0$ and Simplified Second Approximation $b = 0$, $\alpha = \alpha_{crit}$

A second approximation to the radial deflection function is obtained if only b is fixed as zero in Eq. (10). The resulting function allows one more degree of freedom in the circumferential direction than the first approximation. The corresponding equations for the determination of the deflection parameters a, ω, and α are obtained from Eqs. (22), (24), and (25) (with $b = 0$). These equations can be written as

$$a = (4/3\pi)\omega(1 + 8A_4)/\{\omega^2(2\alpha^2 + A_4) + 4[2 - (16/\pi^2) + 8B - k_p]\} \quad (31)$$

$$\omega^2[8(2\alpha^2 + A_4)a^2 + 1 + \alpha^2] - (16/\pi)\omega a(1 + 8A_4) + 16\{[2 - (16/\pi^2) + 8B - k_p]a^2 + A_1 + (4B/A_1) - (1/2\alpha)(2 + \alpha)k_p\} = 0 \quad (32)$$

$$\omega^2[8(4\alpha^3 + C_4)a^2 + \alpha(1 + 2\alpha^2)] - (64/3\pi)\omega a(\alpha + 8C_4) + 16\{2\alpha[2 - (16/\pi^2) + 8B - k_p]a^2 + 2C_1 + 8B(1 + \alpha) - (1 + \alpha)k_p\} = 0 \quad (33)$$

It may be noted that if a, ω, and α constitute a solution of Eqs. (31) to (33) then so does the set $-a$, $-\omega$, and α. The two sets differ only in the location of the origin of the circumferential coordinate.

Because of the complicated nature of the simultaneous nonlinear algebraic Eqs. (31) to (33), solutions were determined with a numerical iteration procedure. The results of the previous calculations ($a = b = 0$ and $a = b = 0$, $\alpha = \alpha_{crit}$) suggest starting such a calculation with an investigation of Eqs. (31) to (33), simplified by fixing $\alpha = \alpha_{crit}$. For fixed values of k_p, Eqs. (31) and (32) then reduce to two equations in the variables ω and a. However, for purposes of computation, it was found convenient to consider ω as given, with a and k_p to be determined. Thus, for a fixed value of ω, Eq. (31) was used to eliminate a from Eq. (32), yielding a cubic in k_p. After k_p was found, a was computed with Eq. (31). This procedure was repeated for successive values of ω until curves of ω and a vs. k_p were determined for prescribed values of the cylinder parameter B. In the solution of the cubic in k_p all three roots were investigated. Calculations were performed for $B = 2 \times 10^{-5}$, 10^{-4}, 3×10^{-4}, 2×10^{-3}, 2×10^{-2}, and 2×10^{-1} (see, for example, Figs. 4, 5, and 6). Except for the case $B = 2 \times 10^{-1}$, the cubic always yielded three real positive roots, the two higher ones of which were found to correspond to unstable equilibrium states. Postbuckling load-deflection curves for these latter roots started at the load corresponding to the axially symmetric buckling load $k_{p\ crit_1}$, while similar curves for the lowest root started at the asymmetric buckling load $k_{p\ crit}$. Since for the calculations under discussion $B < 7.96 \times 10^{-2}$ and, hence, $k_{p\ crit} < k_{p\ crit_1}$ (see Fig. 2), it is to be expected that the solutions corresponding to buckling initiated in an axially symmetric manner correspond to states of unstable equilibrium. Typical results of the calculations for the asymmetrical buckling solutions are presented in Figs. 4 and 5. For the approximation under consideration ($b = 0$, $\alpha = \alpha_{crit}$), the abscissa in Fig. 4 is [see Eq. (10)]

$$w_{max}/t = |\xi|(1 + |a + e|)$$

The three dashed curves in Fig. 4 and the curves in Fig. 5 show that for $B = 3 \times 10^{-4}$, 2×10^{-3}, and 2×10^{-2}, postbuckling equilibrium configurations exist for loads less than the critical load of small-deflection theory. Stability calculations (see reference 8) also show that these configurations are unstable in the region of decreasing k_p with increasing w_{max}/t (see Fig. 4); thereafter, they are stable. Similar results were obtained for $B = 2 \times 10^{-5}$ and 10^{-4}. The dashed load-deflection curves of Fig. 4 differ significantly from those obtained with the first-approximation solution ($a = b = 0$). The latter solution does not reveal the existence of postbuckling loads lower than $k_{p\ crit}$.

For the case $B = 2 \times 10^{-1}$, the cubic in k_p exhibited only one real root for small values of ω; for other values of ω, three real roots were obtained. The corresponding load-deflection relation shown in Fig. 6 differs considerably from those discussed previously. In the present case, the postbuckling configuration which corresponded to the asymmetrical buckling load $k_{p\ crit}$ was found to be unstable. This is to be expected since for $B > 7.96 \times 10^{-2}$, the axially symmetric buckling load $k_{p\ crit_1}$ is less than $k_{p\ crit}$ (see Figs. 2 and 6). The only stable branch of the load-deflection relation is shown as a solid line in Fig. 6. This curve starts with a horizontal tangent at a load k_p greater than $k_{p\ crit}$. Thus the present calculations indicate a gap in the solution—i.e., a region $k_p > k_{p\ crit}$ in which no stable finite deflection configurations exist. This result may be due to the fixing of $\alpha = \alpha_{crit}$ in the calculations, since buckling must start at $k_p = k_{p\ crit_1} < k_{p\ crit}$ and, hence, α_{crit} can have no physical significance. Because the present investigation is concerned primarily with buckling initiated at $k_p = k_{p\ crit_1}$, no further investigations were undertaken for $B > 7.96 \times 10^{-2}$.

In order to investigate the manner in which the postbuckling load-deflection curves depend upon the cylinder parameter B, further calculations were performed. Each dashed curve of Fig. 4 shows that, for the value of B considered, k_p equals $k_{p\ crit}$ at the outset of buckling ($\xi = 0$) as well as for some finite deflection ($\xi > 0$). This condition can exist only if the minimum value of the postbuckling load is less than $k_{p\ crit}$. If a load-deflection curve exhibits only an increase in the load after buckling, only one value of ξ (namely, $\xi = 0$) can correspond to $k_p = k_{p\ crit}$. In order to determine B corresponding to such a condition, k_p was set equal to $k_{p\ crit}$ in Eqs. (31) and (32) [see Eq. (28)], B was expressed in terms of α_{crit} with the aid of Eq. (27), and the expression obtained for a from Eq. (31) was used to eliminate a from Eq. (32). The resulting expression relates ω to α_{crit} and reduces to a biquadratic in ω. From this relation, which

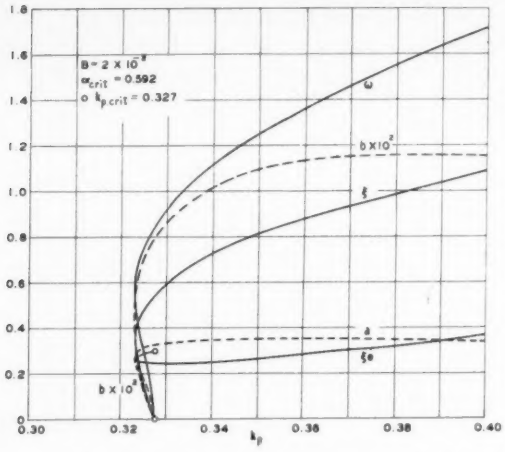

FIG. 9. Variation of deflection parameters with k_p (complete solution with $\alpha = \alpha_{crit}$).

corresponds to $k_p = k_{p\,crit}$, it was found that a and, hence, ξ could have nonvanishing values only if α_{crit} were such that $1.86 \times 10^{-5} < B < 7.96 \times 10^{-2}$. The latter limit on B coincides with that obtained previously for $k_{p\,crit_1} = k_{p\,crit_2}$; for $B > 7.96 \times 10^{-2}$, $k_{p\,crit_1} < k_{p\,crit_2}$. The calculations fixing the range of B for which two values of the deflection exist when $k_p = k_{p\,crit}$ together with load calculations in this range and outside this range are summarized in Fig. 7. In this diagram the ratio of the minimum value of the postbuckling load to the asymmetrical critical load is plotted against $B^{1/4}$. The curve obtained shows that the lowest value of the postbuckling load is 97 per cent of the corresponding critical load. This occurs when $B \simeq 3 \times 10^{-4}$.

The results obtained thus far correspond to a simplified second approximation, since α has been assumed equal to α_{crit}. This requirement corresponds to the assumption that the number of circumferential waves obtained throughout the postbuckling region is identical to that obtained at the outset of buckling. The iteration procedure required for the solution based upon the complete second approximation [Eqs. (31) to (33)] was facilitated by the knowledge of the preceding results. The parameters a, α, and k_p were chosen as the unknowns in Eqs. (31) to (33), while, once again, ω was considered fixed. For assumed values of α, Eqs. (31) and (32) were solved as described previously for corresponding values of a and k_p until a set of values for a, α, and k_p was determined which, together with the fixed value of ω, satisfied Eq. (33). These calculations were repeated for successive values of ω until curves of ω, a, and α vs. k_p were determined for a prescribed value of the cylinder parameter B. Such calculations were performed for $B = 2 \times 10^{-2}$. Since for this case $k_{p\,crit_1} < k_{p\,crit_2}$, only those results corresponding to asymmetrical buckling were considered. They are shown in Figs. 4 and 8. The curve indicating the variation of α with k_p (see Fig. 8) shows that in the range considered α differs only slightly from α_{crit}, particularly in the region of $k_{p\,min}$. The remaining curves are almost identical to those obtained previously for $\alpha = \alpha_{crit}$ [see Fig. 5(c)]. Within the accuracy of the scales used, the dashed curve for $B = 2 \times 10^{-2}$ in Fig. 4 represents the load-deflection characteristics determined from the present calculations as well as the previous calculations ($\alpha = \alpha_{crit}$). Thus, the differences in the results of the second approximation ($b = 0$) and the simplified second approximation ($b = 0$, $\alpha = \alpha_{crit}$) are insignificant.

Complete Solution With and Without $\alpha = \alpha_{crit}$

The analysis corresponding to the complete deflection function of Eq. (10) involves the laborious task of solving four nonlinear algebraic Eqs. (22) to (25) for the four deflection parameters a, b, ω, and α. If a, b, ω, and α constitute a solution to these equations, then it can be seen that the set $-a$, b, $-\omega$, and α is also a solution differing from the first set only in the location of the origin of the circumferential coordinate. Solutions to Eqs. (22) to (25) include one more degree of freedom than those obtained with the second approximation ($b = 0$).

In view of the preceding results, computations were first performed with $\alpha = \alpha_{crit}$. Hence, the calculations consisted of the solution of a set of three simultaneous nonlinear equations [Eqs. (22) to (24)] for the determination of a, b, and k_p for fixed values of ω. The iteration procedure used was the same as that described previously except that Eqs. (22) and (24) replaced Eqs. (31) and (32), respectively, Eq. (23) replaced Eq. (33), and values of b were assumed rather than values of α. The results of calculations corresponding to $B = 2 \times 10^{-2}$ are presented in Figs. 4 and 9. Comparison of the curves of Fig. 9 with those of Figs. 5(c)

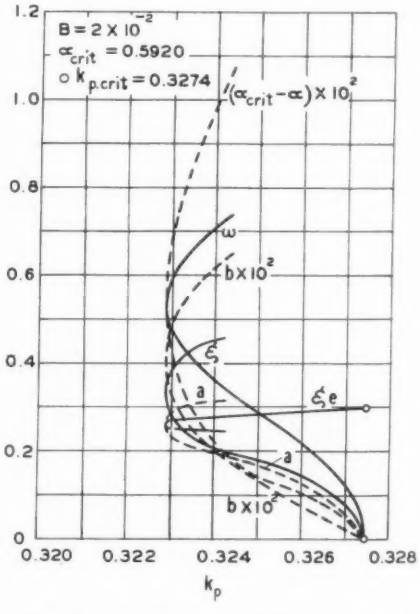

FIG. 10. Variation of deflection parameters with k_p (complete solution).

and 8 reveals little difference among the results of the three sets of calculations represented. The parameter b, neglected in the previous approximations, is seen to be small compared to a and, hence, does not contribute significantly to the solution. The load-deflection diagram determined from the present results differs but slightly from the curve obtained earlier (see the dash-dot curve of Fig. 4). For the present approximation the abscissa in Fig. 4 is

$$w_{max}/t = |\xi|\,[1 + b + |a(1 + b) + c|\,]$$

The results of this analysis facilitated the computations required for the complete solution [Eqs. (22) to (25)]. In the iteration procedure applied to the solution of Eqs. (22) to (25), the parameters a, b, α, and k_p were considered as the unknowns. For a fixed value of ω, several values of α were assumed, and Eqs. (22) to (25) were solved as described previously for corresponding values of a, b, and k_p until a set of values for a, b, α, and k_p was found which, together with the fixed value of ω, satisfied Eq. (25). The results of such calculations performed in the neighborhood of $k_{p\,min}$ are shown in Fig. 10 for $B = 2 \times 10^{-2}$. Once again it is seen that in the region considered α differs only slightly from α_{crit}, and the remaining results hardly differ from those obtained with $\alpha = \alpha_{crit}$ (see also Fig. 4).

The present results together with those of the several approximations considered earlier indicate that the simplified second approximation ($b = 0$, $\alpha = \alpha_{crit}$) gives satisfactory accuracy within the analysis afforded by the use of the deflection function of Eq. (10). Of course, application of deflection functions omitting the terms found to be insignificant here and inclusion of additional degrees of freedom might yield somewhat different quantitative results. In addition, consideration of the effect of initial imperfections in cylinder construction could also materially affect the numerical results (see, for example, reference 7).

The present solution may be considered summarized in Fig. 7. The curve shown indicates that, in the range of the parameter B in which buckling is initiated in an asymmetric manner ($B^{1/4} < 0.531$), a closed region exists in which the analysis yields postbuckling loads less than the corresponding critical loads. The comparison between experiment and small-deflection theory made by Batdorf (see Fig. 6 of reference 9) indicates that in the region $0.12 < B^{1/4} < 0.37$ experimentally determined collapse pressures were appreciably less than theoretically determined critical pressures. For values of B greater than 0.37, no experimental data were given and, hence, this value of B cannot be considered as significant. The region described is seen to lie within the range predicted by the present analysis to be that in which postbuckling loads less than the theoretical critical load exist (see Fig. 7). However, the 3 per cent maximum decrease in load obtained with the present analysis hardly accounts for the large discrepancies between classical theory and experiment which were shown by Batdorf to be as much as 60 per cent.

Conclusions

The results of an approximate analysis of the postbuckling behavior of hydrostatically loaded, initially perfect, thin-walled, circular cylindrical shells indicate that stable postbuckling equilibrium configurations exist for pressures greater than as well as pressures less than the critical pressure determined from small deflection theory. Pressures less than the critical pressure were found to exist only for a finite range of a parameter indicative of shell geometry. This range is approximately that found by Batdorf to be one in which considerable discrepancy between experiment and theory is exhibited. However, the calculated minimum value of the postbuckling load was found to be only 3 per cent less than the corresponding classical linear critical load, while experimental collapse pressures are as little as 60 per cent of the theoretical pressures. Achievement of better quantitative agreement might require the application of more accurate nonlinear strain-displacement relations, the consideration of edge conditions more closely approximating those realized in tests, the use of more extensive assumed deflected shapes, the inclusion of terms accounting for initial imperfections, and the consideration of inelastic behavior.

It was also found that for loads corresponding to maximum radial displacements of the order of the shell thickness the number of circumferential waves remains essentially constant with increasing deflection and equal to the number obtained at buckling.

References

[1] Donnell, L. H., *A New Theory for the Buckling of Thin Cylinders Under Axial Compression and Bending*, Trans. ASME, Vol. 56, p. 795, 1934.

[2] von Kármán, Th., Dunn, Louis, G., and Tsien, Hsue-Shen, *The Influence of Curvature on the Buckling Characteristics of Structures*, Journal of the Aeronautical Sciences, Vol. 7, No. 7, p. 276, May, 1940.

[3] von Kármán, Th., and Tsien, Hsue-Shen, *The Buckling of Thin Cylindrical Shells Under Axial Compression*, Journal of the Aeronautical Sciences, Vol. 8, No. 8, p. 303, June, 1941.

[4] Tsien, Hsue-Shen, *A Theory for the Buckling of Thin Shells*, Journal of the Aeronautical Sciences, Vol. 9, No. 10, p. 373, August, 1942.

[5] Leggett, D. M. A., and Jones, R. P. N., *The Behavior of a Cylindrical Shell Under Axial Compression When the Buckling Load Has Been Exceeded*, A.R.C. R&M No. 2190, August, 1942.

[6] Michielsen, Herman F., *The Behavior of Thin Cylindrical Shells after Buckling Under Axial Compression*, Journal of the Aeronautical Sciences, Vol. 15, No. 12, p. 738, December, 1948.

[7] Donnell, L. H., and Wan, C. C., *Effect of Imperfections on Buckling of Thin Cylinders and Columns Under Axial Compression*, J. Appl. Mech., Vol. 17, No. 1, p. 73, March, 1950.

[8] Kempner, Joseph, *Postbuckling Behavior of Axially Compressed Circular Cylindrical Shells*, Journal of the Aeronautical Sciences, Vol. 21, No. 5, p. 329, May, 1954. (Formerly PIBAL Report No. 212, Polytechnic Institute of Brooklyn, December, 1952.)

[9] Batdorf, S. B., *A Simplified Method of Elastic-Stability*

Analysis for Thin Cylindrical Shells. I—Donnell's Equation, NACA TN 1341, June, 1947.

[10] Windenburg, Dwight F., and Trilling, Charles, *Collapse by Instability of Thin Cylindrical Shells under External Pressure*, Trans. ASME, Vol. 56, No. 11, p. 819, November, 1934.

[11] Sturm, Rolland G., *A Study of the Collapsing Pressure of Thin-Walled Cylinders*, Eng. Exp. Sta. Bull. No. 329, Univ. Ill., 1941.

[12] Donnell, L. H., *Stability of Thin-Walled Tubes under Torsion*, NACA TR 479, 1933.

[13] von Mises, R., *Der kritische Aussendruck für allseits belastete zylindrische Rohre*, Fest. zum 70 Geburstag von Prof. A. Stodola, Zurich, pp. 418–430, 1929. Translated and annotated by D. F. Windenburg under the title *The Critical External Pressure of Cylindrical Tubes under Uniform Radial and Axial Load*, U.S. Experimental Model Basin, Report No. 366, August, 1933.

Plastic Torsional Buckling Strength of Cylinders . . .

(*Continued from page 248*)

[16] Ramberg, W., and Osgood, W. R., *Description of Stress-Strain Curves by Three Parameters*, NACA TN 902, July, 1943.

[17] Ramberg, W., and Miller, J. A., *Determination and Presentation of Compressive Stress-Strain Data for Thin Sheet Metal*, Journal of the Aeronautical Sciences, Vol. 13, No. 11, pp. 569–580, November, 1946.

[18] Donnell, L. H., *A New Theory for the Buckling of Thin Cylinders under Axial Compression and Bending*, Trans. ASME, Vol. 56, pp. 795–806, 1934.

[19] Donnell, L. H., *Stability of Thin-Walled Tubes under Torsion*, NACA Report 479, 1933.

[20] Cozzone, F. P., and Melcon, M. A., *Non-dimensional Buckling Curves—Their Development and Application*, Journal of the Aeronautical Sciences, Vol. 13, No. 10, pp. 511–517, October, 1946.

[21] Timoshenko, S., *Theory of Elastic Stability*, pp. 480–490; McGraw-Hill Book Company, Inc., New York, 1936.

[22] ANC-5, *Strength of Metal Aircraft Elements*, March, 1955.

[23] Otey, N. S., *Torsional Strength of Nickel Steel Tubing as Affected by the Ratio of Diameter to Gage Thickness*, NACA TN 189, April, 1924.

[24] Stang, A. H., Ramberg, W., and Back, G., *Torsion Tests of Tubes*, NACA Report 601, 1937.

[25] *The Torsional and Tensile Strength of Chromium-Molybdenum Tubing*, Boeing Aircraft Co., Engineering Section Memorandum, Report M-56-2622, July, 1935.

[26] *Bending, Torsion, Tension, and Crushing Test of H. T. Steel Tubes*, Boeing Aircraft Co., Test Report T-25032, 1943.

[27] *Boeing Document No. D-5935*, 1944.

[28] Moore, R. L., and Clark, J. W., *Torsion, Compression, and Bending Tests of Tubular Sections Machined from 75S-T6 Rolled Round Rod*, NACA RM 52125, November, 1952.

[29] Moore, R. L., and Holt, M., *Beam and Torsion Tests of Aluminum-Alloy 61S-T Tubing*, NACA TN 867, 1942.

[30] Gatewood, B. E., and Williams, E. L., *Allowable Compressive Stresses in Aircraft Structures*, Journal of the Aeronautical Sciences, Vol. 18, No. 10, pp. 657–664, October, 1951.

Boundary-Layer Measurements at Supersonic Nozzle Throats

(*Continued from page 252*)

(cf. Appendix B of reference 5). It can be seen (Fig. 7) that, for the throat profiles, u is linear with log y almost to the outer edge of the boundary layer, which is also a well-known characteristic of the pipe-flow profile.[4] For flat-plate flow, $(\theta/\tau)(dp/dx) = 0$, and, for equilibrium flows with positive pressure gradients, the semilogarithmic profile departs from linearity well within the boundary layer (Fig. 18 of reference 3).

References

[1] Sibulkin, M., *Heat Transfer to an Incompressible Turbulent Boundary Layer and Estimation of Heat-Transfer Coefficients at Supersonic Nozzle Throats*, Journal of the Aeronautical Sciences, Vol. 23, No. 2, pp. 162–172, February, 1956.

[2] Tucker, M., *Approximate Calculation of Turbulent Boundary-Layer Development in Compressible Flow*, NACA TN 2337, 1951.

[3] Clauser, F. H., *Turbulent Boundary Layers in Adverse Pressure Gradients*, Journal of the Aeronautical Sciences, Vol. 21, No. 2, pp. 91–108, February, 1954.

[4] Goldstein, S., *Modern Developments in Fluid Dynamics*, 1st Ed., Vol. 1, Fig. 93; Oxford University Press, London, England, 1938.

[5] Sibulkin, M., *Boundary-Layer Measurements at Supersonic Nozzle Throats*, Jet Propulsion Laboratory Report 20-97, May, 1956.

Theories of Strength for Combined Stresses and Nonisotropic Materials

JOSEPH MARIN*

The Pennsylvania State University

SUMMARY

Many theories of failure for defining yield and ultimate strengths of materials have been proposed during the past 100 years. One of the inadequacies of these theories is that they are not applicable for materials with different tensile strengths in various directions, nor are they suitable for materials with different strengths in simple tension and compression. Theories to provide for these limitations are proposed in this paper.

DISCUSSION

(1) Conventional Theories of Failure for Yield Strength in Isotropic Ductile Materials

THE TWO MAIN THEORIES used for defining failure by yielding for ductile materials are the *maximum shear stress* and *distortion energy or Von Mises-Hencky theories*.[1] The equations defining these theories are, respectively,

$$\left.\begin{aligned}\sigma_1 - \sigma_2 &= \pm\sigma_{yp}\\ \sigma_2 - \sigma_3 &= \pm\sigma_{yp}\\ \sigma_3 - \sigma_1 &= \pm\sigma_{yp}\end{aligned}\right\} \tag{1}$$

$$\sigma_1^2 + \sigma_2^2 + \sigma_3^2 - \sigma_1\sigma_2 - \sigma_2\sigma_3 - \sigma_3\sigma_1 = \sigma_{yp}^2 \tag{2}$$

where σ_{yp} = the yield stress in simple tension.

Fig. 1 shows a graphical representation of both the maximum shear and distortion energy theories for biaxial stresses obtained by placing $\sigma_3 = 0$ in Eqs. (1) and (2). Most biaxial-stress test results on ductile metals show that the distortion energy theory is in best agreement with these test results.

(2) Conventional Theories of Failure for Ultimate or Fracture Strength in Isotropic Materials

Various theories of failure for ultimate strength in isotropic materials have been proposed.[3] It is usually recommended that for ductile materials the *maximum shear theory*[2] be used while for brittle materials the *maximum stress theory* is often used. For the case of triaxial stresses, the equations defining these theories are, respectively,

$$\left.\begin{aligned}\sigma_1 - \sigma_2 &= \pm\sigma_u\\ \sigma_2 - \sigma_3 &= \pm\sigma_u\\ \sigma_3 - \sigma_1 &= \pm\sigma_u\end{aligned}\right\} \tag{3}$$

$$\left.\begin{aligned}\sigma_1 &= \pm\sigma_u\\ \sigma_2 &= \pm\sigma_u\\ \sigma_3 &= \pm\sigma_u\end{aligned}\right\} \tag{4}$$

In Eqs. (3) and (4), σ_u is the ultimate or fracture stress in simple tension or compression. For two-dimensional stresses, $\sigma_3 = 0$. Then Eqs. (3) and (4) can be plotted as shown in Fig. 2.

(3) Theories of Failure for Materials with Different Strengths in Tension and Compression

The strengths in simple tension and compression are not equal for some materials. Two of the main theories that have been recommended for such materials are the *Mohr theory*[5] and the *maximum stress theory*. These theories are plotted in Fig. 3 for two-dimensional stresses. The equations defining failure for biaxial stresses are, by these theories, as follows:

(a) For the Mohr theory:

$$\left.\begin{aligned}\sigma_1 &= \sigma', \quad \sigma_2 = \sigma'\\ \sigma_1 &= -\sigma'', \quad \sigma_2 = -\sigma''\\ \sigma_2 &- (\sigma''/\sigma')\sigma_1 = -\sigma''\\ \sigma_1 &- (\sigma''/\sigma')\sigma_2 = -\sigma''\end{aligned}\right\} \tag{5}$$

where σ' = the yield, ultimate, or fracture strength in simple tension and σ'' = the yield, ultimate, or fracture strength in simple compression.

(b) For the maximum stress theory:

$$\left.\begin{aligned}\sigma_1 &= \sigma', \quad \sigma_2 = \sigma'\\ \sigma_1 &= -\sigma'', \quad \sigma_2 = -\sigma''\end{aligned}\right\} \tag{6}$$

It has been recommended[6] that the Mohr theory be used for most materials since the few available test results indicate that this theory is conservative.

(4) Combined Static Stresses—A Generalized Theory of Strength

The conventional theories of failure described by Eqs. (1) to (6) have the following limitations:

(a) Different theories have been recommended for different materials and for yield and ultimate strengths. It would, of course, be desirable to have one theory

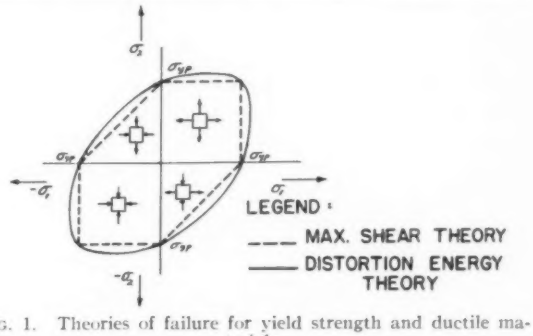

FIG. 1. Theories of failure for yield strength and ductile materials.

Received April 20, 1956. Revised and received September 28, 1956.

* Professor and Head, Department of Engineering Mechanics.

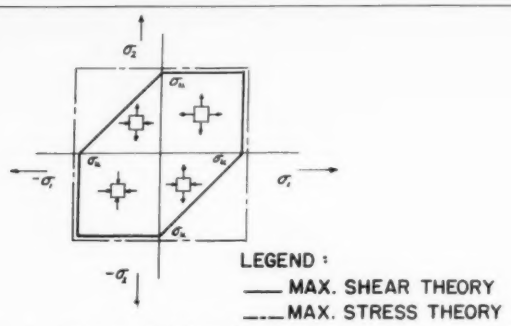

FIG. 2. Theories of failure for ultimate strength and ductile materials.

which expresses the behavior for all materials and for both yield and ultimate strengths.

(b) The Mohr theory only approximately defines failure in materials with different strengths in tension and compression. A theory which could more accurately express strengths for such materials is desired.

(c) The conventional theories described in these equations do not provide for materials with different uniaxial strengths in various directions.

A theory which eliminates the foregoing limitations will be developed in this article. It will be referred to as a *generalized theory of strength*. For an element subjected to triaxial stresses, it will be assumed that failure is a function of the second stress invariant.[7] Then, for isotropic materials without directional properties and with the same strength in simple tension and compression, failure for combined stresses according to the requirement of stress invariancy, is defined by

$$(\sigma_1 - \sigma_2)^2 + (\sigma_2 - \sigma_3)^2 + (\sigma_3 - \sigma_1)^2 = 2\sigma_t^2 \quad (7)$$

where σ_t is the failure strength (yield or ultimate) in simple tension. It can be shown that Eq. (7) is identical with the relation representing failure by the distortion energy or Von Mises-Hencky criterion of failure [Eq. (2)] provided that σ_t in Eq. (7) represents the yield strength in simple tension. If failure is assumed to be a function of the octahedral shear stress, Eq. (7) is also obtained.[3] It is found, furthermore, that Eq. (7) is the relation corresponding to the statistical average of the shear stresses on all slip planes of a polycrystalline aggregate.[8] Eq. (7) is also obtained (for biaxial stresses of opposite sign) if failure is assumed to be a function of internal friction. That is, if the failure shear stress τ is considered to be a quadratic function of the normal stress σ_n on the critical plane—namely, $\tau^2 = a\sigma_t^2 - b\sigma_n^2$—Eq. (7) is obtained. Moreover, it is of interest to note that Eq. (7) represents the expression for the effective or significant stress used in formulating the stress-strain relations in the plastic range according to the simple deformation theory.[1, 2, 9, 10]

Although the foregoing observations in themselves provide strong support to the selection of Eq. (7) as a basis of failure, the most important consideration supporting Eq. (7) is the fact that most available test data for ductile and isotropic materials agree with the values predicted by this equation.[3, 4]

Eq. (7) requires that the material have equal strengths in simple tension and compression and that each of these strengths be the same in all directions. For materials in which these restrictions do not apply, the following modifications can be made in Eq. (7):

(a) *Strength Theory for Anisotropic Materials (materials with different strengths in different directions)*—To provide for materials which have different simple tensile strengths σ_t in different directions, Eq. (7) can be modified as follows:

$$[K_a(\sigma_1 - \sigma_2)]^2 + [K_b(\sigma_2 - \sigma_3)]^2 + [K_c(\sigma_3 - \sigma_1)]^2 = 2\sigma^2 \quad (8)$$

For two-dimensional stresses, $\sigma_3 = 0$, and Eq. (8) becomes

$$a^2\sigma_1^2 + b^2\sigma_1\sigma_2 + c^2\sigma_2^2 = 1 \quad (9)$$

where

$$a^2 = (K_a^2 + K_c^2)/(2\sigma^2), \qquad b^2 = -K_a^2/\sigma^2$$
$$c^2 = (K_a^2 + K_b^2)/(2\sigma^2) \quad (10)$$

The values of a, b, and c in Eq. (9) can be obtained from three simple strength properties of the material. Various possible strengths might be considered. In the present determination, values of a, b, and c will be found from the simple tensile strengths in the σ_1 and σ_2 directions and the simple torsional strengths—that is, using the conditions that $\sigma_1 = \sigma_{t1}$ for $\sigma_2 = 0$, $\sigma_2 = \sigma_{t2}$ for $\sigma_1 = 0$ and for $\sigma_1 = -\sigma_2$, and that $\sigma_1 = -\sigma_2 = \tau_s$, then values of a, b, and c can be determined. When these are substituted in Eq. (9), the failure relation becomes

$$\sigma_1^2 + [1 + (\sigma_{t1}/\sigma_{t2})^2 - (\sigma_{t1}/\tau_s)^2]\sigma_1\sigma_2 + (\sigma_{t1}/\sigma_{t2})^2\sigma_2^2 = \sigma_{t1}^2 \quad (11)$$

Eq. (11) reduces to Eq. (7) or the distortion energy theory for $\sigma_3 = 0$, $\sigma_{t1} = \sigma_{t2} = \sigma_t$, and $\tau_s = \sigma_{t1}/\sqrt{3}$. A plot of Eq. (11) for $\sigma_{t1}/\sigma_{t2} = 0.75$ and $\sigma_{t1}/\tau_s = 1.5$ is

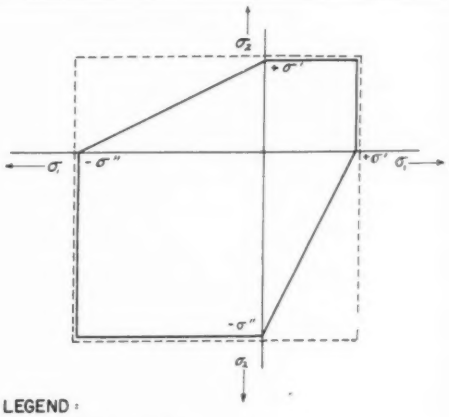

FIG. 3. Theories of failure for brittle materials.

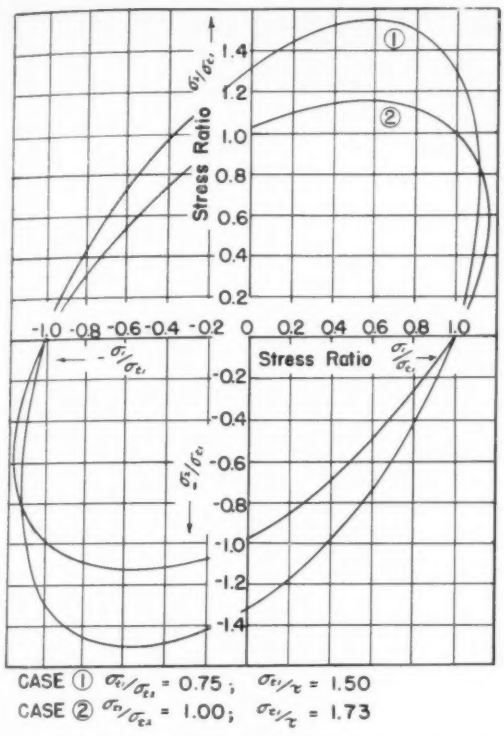

FIG. 4. Theory of failure for nonisotropic materials with directional properties.

shown in Fig. 4. For purposes of comparison, the special case of Eq. (11) representing the distortion energy theory is also shown—that is, the case for which $\sigma_{t1}/\sigma_{t2} = 1$ and $\sigma_{t1}/\tau_s = 1.73$. An examination of Fig. 4 shows that the method of formulation of this theory requires that the simple tension and compression strengths in a given direction be equal. It should also be noted that a modification in Eq. (11) is necessary when the directions of the principal stresses do not coincide with the directions for which the strengths σ_{t1} and σ_{t2} are known.

(b) *Generalized Strength Theory*—For materials with different strengths in tension and compression and for materials with simple tensile and compressive strengths that vary in different directions, a more general relation than that given by Eq. (8) must be found. For this purpose, Eq. (7) can be replaced by the equation

$$(\sigma_1 - a)^2 + (\sigma_2 - b)^2 + (\sigma_3 - c)^2 + q[(\sigma_1 - a)(\sigma_2 - b) + (\sigma_2 - b)(\sigma_3 - c) + (\sigma_3 - c)(\sigma_1 - a)] = \sigma^2 \quad (12)$$

Values of a, b, and c can be found, based on various requirements. For example, for biaxial stresses, if the simple tensile strengths in the σ_1 and σ_2 directions are, respectively, σ_{t1} and σ_{t2}, the simple compressive strength in the σ_1 direction is σ_c, and the strength for $\sigma_1 = -\sigma_2$ is τ_s, then it can be shown that Eq. (12) becomes

$$\sigma_1^2 + K_1\sigma_1\sigma_2 + \sigma_2^2 + K_2\sigma_1 + K_3\sigma_2 = K_4 \quad (13)$$

or

$$\sigma_1^2 + \left[2 - \frac{\sigma_{c1}\sigma_{t1} - \tau_s^2}{\tau_s^2}\{\sigma_{c1} - \sigma_{t1} = \sigma_{c1}(\sigma_{t1} - \sigma_{t2}) + \sigma_{t2}\}\right] \times \sigma_1\sigma_2 + \sigma_2^2 + (\sigma_{c1} - \sigma_{t1})\sigma_1 + [\sigma_{c1}(\sigma_{t1} - \sigma_{t2}) - \sigma_{t2}]\sigma_2 = \sigma_{c1}\sigma_{t1} \quad (14)$$

For an isotropic material, $\sigma_{c1} = \sigma_{t1} = \sigma_{t2} = \sigma_t$, and Eq. (14) reduces to

$$\sigma_1^2 - [2 - (\sigma_t/\tau_s)^2]\sigma_1\sigma_2 + \sigma_2^2 = \sigma_t^2 \quad (15)$$

If the shear strength τ_s is taken as $\sigma_t/\sqrt{3}$, Eq. (15) reduces to the equation for the distortion energy theory. Fig. 5 gives a plot of Eq. (14) for the case where $\sigma_{t2} = 0.8\sigma_{t1}$, $\sigma_{c1} = 1.20\sigma_{t1}$, and $\tau_s = 0.8\sigma_{t1}$. For a material with these strength properties, Eq. (14) becomes

$$x^2 - 0.5xy + y^2 + 0.2x + 0.7y = 1.2 \quad (16)$$

where $x = \sigma_1/\sigma_{t1}$ and $y = \sigma_2/\sigma_{t2}$.

The generalized theories described in this article may be adapted to both ductile and brittle materials. This is made possible by the flexibility introduced by the experimental constant τ_s in both Eqs. (11) and (14).

(5) *Design for Combined Static Stresses*

In Sections 1–4, theories of failure which give the strength of an element subjected to combined stresses were defined. The failure relations were in all cases expressed in terms of strengths in simple tension and compression. Working stress relations corresponding to these failure relations can be obtained by using the equations given above, provided that the failure

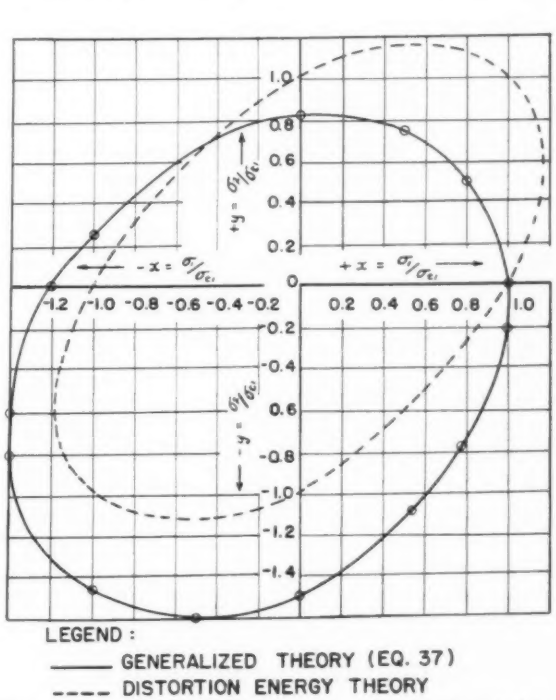

FIG. 5. Generalized theory of failure for nonisotropic materials.

strengths in simple tension, compression, and shear are replaced by the allowable values. Working stress equations for combined stresses are formulated in various codes as, for example, those given in references 5 and 6. By the generalized theory as given in Eq. (16), the working stress relation becomes

$$\sigma_1 - 0.5\sigma_1\sigma_2 + \sigma_2^2 + 0.2\sigma_1\sigma_{w1} + 0.7\sigma_2\sigma_{w1} = 1.2\sigma_{w1}^2 \quad (17)$$

where σ_{w1} = the working tensile stress for the σ_1 direction. In using Eq. (17) for the determination of the dimensions of a member, it is often necessary to determine the principal stresses from the stress components, as illustrated in the following example.

Example: Shaft Subjected to Torsion and Bending—It is required to determine the diameter of a circular shaft d for a combined loading consisting of a twisting moment M_t and bending moment M, using the working strength relation as given by Eq. (17).

For a shaft subjected to torsion and bending the critical element is on the outer fiber where the stress components both have the maximum values of

$$\sigma_x = Mr/I = 32M/\pi d^3, \qquad \tau_{xy} = M_t r/I_p = 16M_t/\pi d^3 \quad (18)$$

The principal stresses σ_1 and σ_2 produced by stress components σ_x and τ_{xy} are

$$\left.\begin{aligned}\sigma_1 &= (\sigma_x/2) + \sqrt{(\sigma_x^2/4) + \tau_{xy}^2}\\ \sigma_2 &= (\sigma_x/2) - \sqrt{(\sigma_x^2/4) + \tau_{xy}^2}\end{aligned}\right\} \quad (19)$$

Placing the values of σ_1 and σ_2 from Eqs. (19) in Eq. (17), the working stress relation becomes

$$0.75\,\sigma_x^2 + 0.5(\sigma_x - \sigma_{w1})\sqrt{(\sigma_x^2/4) + \tau_{xy}^2} + 1.5\tau_{xy}^2 + 0.45\sigma_{w1}\sigma_x = 1.2\sigma_{w1}^2 \quad (20)$$

The value of the shaft diameter can be determined from Eq. (20) by substituting σ_x and τ_{xy} from Eq. (18) in Eq. (20).

In some design problems the critical element cannot be selected by inspection. In such cases the stress components and the principal stresses at a point in the member are expressed in terms of the loads, dimensions, and the coordinates of the point. The expressions for the principal stresses are then substituted in a working stress equation such as Eq. (17). To determine the location of the critical element, the left-hand side of Eq. (17) is considered as an equivalent tensile stress. Differentiating with respect to the variable coordinate and equating to zero gives an equation which defines the position of the critical element. With the position of the critical element known, Eq. (17) is then used to find the required dimension of the element.

(6) *Design for Static Stress Concentration*

It is well known that, at areas of stress concentration such as fillets, grooves, holes, and keyways, the state of stress is not that of simple tension or compression but is a state of combined stress. This is true not only for complex loadings but also for such members as cylindrical bars with circumferential grooves subjected to axial tension. For certain types of members, loadings, and types of discontinuities, theoretical stress-concentration factors based on the theory of elasticity have been obtained.[11] In some cases, stress-concentration factors have been obtained by using methods of experimental stress analysis including photoelasticity and electric strain gages. These stress-concentration factors are nominally determined for the maximum normal stress.

A consideration of stress concentrations in design has often been made by simply correcting the maximum normal stress for stress concentration. This procedure amounts to design based on the maximum stress theory. A more rational procedure is to consider the combined stress effect—that is, to apply a theory of failure to the particular problem. For example, in a cylindrical bar with a circumferential groove subjected to axial tension, let σ_1 be the axial stress and σ_2 the circumferential stress at the edge of the groove. Then, by the Von Mises or distortion energy theory, the strength is defined by

$$\sigma_1^2 - \sigma_1\sigma_2 + \sigma_2^2 = \sigma_t^2 \quad (21)$$

where σ_t = the yield strength in simple tension. If σ_n is the nominal axial stress (the axial yield load divided by the net area), then Eq. (21) can be expressed as

$$(\sigma_1/\sigma_n)\sqrt{1 - c + c^2} = (\sigma_t/\sigma_n)$$

where $c = \sigma_2/\sigma_1$

or

$$K_t\sqrt{1 - c + c^2} = K_{t1} \quad (22)$$

In Eq. (22), $K_t = \sigma_1/\sigma_n$ is called the *stress-concentration factor* while K_{t1} is the *combined stress-concentration factor*. The factor K_t is the usual factor applied in design while the factor K_1, considers both stress concentration and the combined stress effect. Values of both K_t and K_{t1} [as calculated by Eq. (22)] have been determined by Peterson[12] for a variety of members and types of stress concentration. Charts are plotted in reference 12 in such a manner that the combined stress-concentration factors can be selected easily by the designer.

Stress concentration as treated above does not include effects of plastic flow. In some cases, designers may consider loads which produce plastic flow of the material. It is known that, at points of stress concentration, loading in the plastic range produces a redistribution of stress and reduction in the stress-concentration factors. The theoretical determination of stress-concentration factors in the plastic range presents a difficult problem. Some attempts have been made to determine the plastic stress-concentration factors experimentally.[13]

Conclusion

This paper develops theories of failure for defining strength for various states of combined stresses as

(*Continued on page 274*)

Plastic Stability Theory of Thin Shells

GEORGE GERARD*
New York University

Symbols

A_i	= plasticity coefficients
B	= axial rigidity, $B = E_s t/(1 - \nu^2)$
D	= bending rigidity, $D = E_s t^3/12(1 - \nu^2)$, also diameter
e_i	= strain intensity
E	= modulus of elasticity
E_s	= secant modulus
E_t	= tangent modulus
k	= buckling coefficient, $k = \sigma t L^2/\pi^2 D$
L	= length of cylinder
m	= number of longitudinal half wave lengths
M	= bending moment per unit width
n	= number of circumferential wave lengths
N	= loading per unit width
p	= external pressure
R	= radius
t	= thickness
u, v, w	= displacements
x, y, z	= coordinates
Z	= cylinder curvature parameter, $Z = (L^2/Rt)\ (1 - \nu^2)^{1/2}$
α	= $(3/\sigma_i^2)\ (1 - E_t/E_s)$
β	= wave-length parameter
γ	= shear strain
ϵ	= axial strain
η	= plasticity reduction factor
ν	= Poisson's ratio
ν_e	= elastic value of Poisson's ratio, $\nu_e = 0.3$
σ	= axial stress
σ_i	= stress intensity
τ	= shear stress
χ	= curvature
∇^4	= differential operator $\nabla^4 = (\partial^2/\partial x^2 + \partial^2/\partial y^2)^2$

Subscripts

x, y, xy	= coordinate orientation
$1, 2, 3$	= variations which arise during buckling in ϵ and χ
cr	= critical
$'$	= variations which arise during buckling, such as M' and N'

Introduction

Considerable interest is currently centered on the role of deformation and flow types of plasticity theories in the solution of stability problems. For thin flat plates, deformation theory combined with classical stability theory appears to yield results which are in substantially good agreement with test data. On the other hand, flow or incremental theories appear to require the introduction of initial imperfections in order to obtain a satisfactory degree of correlation with tests.†

Thus, in view of the current state of development of plastic stability theory, it appears fruitful to exploit the mathematical simplicity inherent in deformation theory in the investigation of the plastic stability of thin shells. Although there may be theoretical objections to deformation theories as a class, test data on flat plates do suggest the predictive value of the results obtained from this theory.

In this paper, a set of equilibrium differential equations for the plastic buckling of thin shells of constant unequal radii is derived. This set of three equations applies to flat plates, cylinders, and spheres under any loading system leading to buckling. For particular problems such as buckling of cylinders under axial compression, torsion or lateral pressure, and spheres under external pressure, the set of equations can be reduced to a single eighth-order partial differential equation of the Donnell type in terms of the radial displacement only. These Donnell-type equations are used to obtain solutions for plastic buckling of spheres under external pressure and long and moderate length cylinders under lateral pressure or torsion loads. The limiting cases of a simply supported flat plate under compression or shear, represent the solutions for short cylinders under lateral pressure or torsion, respectively.

Derivation of Equilibrium Equations

Plasticity Considerations

A fundamental hypothesis of plasticity theory is that the stress intensity, σ_i, is a uniquely defined, single-valued function of the strain intensity, e_i, for a given material, when the stress intensity increases (loading) and is elastic when it decreases (unloading). For the octahedral shear law, the stress and strain intensities can be defined as follows:

$$\sigma_i = (\sigma_x^2 + \sigma_y^2 - \sigma_x\sigma_y + 3\tau^2)^{1/2} \tag{1}$$

$$e_i = [2/(3)^{1/2}]\ (\epsilon_x^2 + \epsilon_y^2 + \epsilon_x\epsilon_y + \gamma^2/4)^{1/2} \tag{2}$$

With the assumption that the principal axes of stress and strain coincide, the secant modulus can be defined as

$$E_s = \sigma_i/e_i \tag{3}$$

Furthermore, by use of deformation-type stress-strain laws together with the assumption of plastic isotropy and the idealization that Poisson's ratio is equal to 1/2 for both the elastic and plastic region, the following simplified two-dimensional stress-strain relations are obtained:

$$\epsilon_x = (1/E_s)\ [\sigma_x - (1/2)\sigma_y] \tag{4}$$

Received March 1, 1956.

* Assistant Director, Research Division, College of Engineering.

† For a recent summary of the relation of theory and test data on plastic buckling of plates, see reference 5.

$$\epsilon_y = (1/E_s)\,[\sigma_y - (1/2)\sigma_x] \tag{5}$$

$$\gamma = 3\tau/E_s \tag{6}$$

Equilibrium Considerations

Donnell's equation[1, 2] for elastic buckling of thin-wall circular cylinders has been used with a considerable degree of success in elastic stability problems. Recently, Becker[3] has extended the Donnell type of equation to thin shells of constant unequal radii and has demonstrated the simplicity of its use by obtaining a solution for elastic buckling of a sphere under external pressure.

By employing the strain-displacement relations and force equilibrium equations of Donnell[1] in conjunction with the equations derived by Stowell[4] for the force and moment variations which arise during buckling, Gerard[5] derived a set of equilibrium differential equations for plastic buckling of cylinders. These equations were used to investigate compressive and torsional buckling of long cylinders. Thus, the Donnell-type equations have been used to investigate the elastic and plastic stability of cylinders and elastic stability of spheres. In the following, a general set of equations for the plastic stability of thin shells of unequal radii are derived.

The middle-surface strain variations and curvature changes that occur during buckling of a shell with constant unequal radii are related to the displacements as follows:

$$\left.\begin{aligned} \epsilon_1 &= \partial u/\partial x + w/R_x & \chi_1 &= \partial^2 w/\partial x^2 \\ \epsilon_2 &= \partial v/\partial y + w/R_y & \chi_2 &= \partial^2 w/\partial y^2 \\ \epsilon_3 &= (1/2)\,[(\partial u/\partial y) + (\partial v/\partial x)] & \chi_3 &= \partial^2 w/\partial x \partial y \end{aligned}\right\} \tag{7}$$

These equations are the same as those used by Donnell, with the exception of the w/R_x term in the ϵ_1 relation.

The following simplified equilibrium equations as derived by Donnell neglect certain terms which are of small magnitude when the circular cross section of the shell is distorted during buckling. In cases in which the cross section retains its circular shape during buckling the neglected terms are generally of some importance.

$$(\partial N_x'/\partial x) + (\partial N_{xy}'/\partial y) = 0 \tag{8}$$

$$(\partial N_y'/\partial y) + (\partial N_{xy}'/\partial x) = 0 \tag{9}$$

$$\begin{aligned} -(\partial^2 M_x'/\partial x^2) - 2(\partial^2 M_{xy}'/\partial x \partial y) - (\partial^2 M_y'/\partial y^2) + \\ (N_x'/R_x) + (N_y'/R_y) + N_x(\partial^2 w/\partial x^2) + \\ 2N_{xy}(\partial^2 w/\partial x \partial y) + N_y(\partial^2 w/\partial y^2) + p = 0 \end{aligned} \tag{10}$$

In Eq. (10), the additional term N_x'/R_x accounts for the thin shell behavior. The remainder of the equation is that used by Donnell for cylinders.

Inelastic Buckling Considerations

From the standpoint of classical stability theory, the equilibrium differential equations are formulated on the basis that at the buckling load an exchange of stable equilibrium configuration occurs between the straight form and the slightly bent form. Since the load remains constant during this exchange, a strain reversal must occur on the convex side, and, therefore, the buckling model leading to the reduced modulus concept for columns is correct within this framework.

Practical columns and plates invariably contain initial imperfections and therefore axial loading and bending proceed simultaneously. Since in the presence of relatively large axial compressive stresses the bending stresses are generally small, no strain reversal would be expected to occur, and the incremental bending stresses in the inelastic range are given by the tangent modulus model. However, the bent form is the only stable configuration in this case, and, therefore, use of equilibrium equations based on perfect columns, plates, or shells is clearly unjustified.

Partially to remove this difficulty, Stowell[4] has assumed that the straight form of the plate or column is stable until buckling occurs. At buckling, infinitesimal bending is assumed to proceed simultaneously with a corresponding infinitesimal increase in axial loading so that the plate is not subjected to a strain reversal and remains plastic. Again this model poses an essential difficulty, since classical stability theory is based on the assumption that the axial loading remains constant during the buckling process. Therefore, some justification is necessary in order to use equilibrium equations based on constant external loads for plastic buckling problems in which the external load must increase slightly.

It is assumed that in the buckling process the external loads increase slightly. Denoting this increment by δN, the external loads are increased as follows: $N_x + \delta N_x$, $N_{xy} + \delta N_{xy}$, $N_y + \delta N_y$ and $p + \delta p$. The terms containing a prime ($'$) in Eqs. (8) to (10) are the middle-surface force and bending moment variations arising from bending and twisting of the plate at buckling. Therefore, the slight increase in external load represented by δN can have only a negligible influence upon the primed terms in Eqs. (8) and (10).

In Eq. (10), the external loads N_x, N_{xy}, N_y and p appear. If these loads are replaced by $N_x + \delta N_x, \ldots, p + \delta p$, then terms such as $\delta N_x(\partial^2 w/\partial x^2)$ and δp appear which are clearly of higher order than those terms appearing in Eq. (10) and can be neglected. Thus, it appears permissible to conclude that the slight increase in load required for the plate to remain plastic during buckling is compatible with the use of equilibrium equations based on classical stability concepts.

Incremental Forces and Moments

When buckling occurs, the displacements vary slightly from their values before buckling. The resulting strain variations arise partly from variations of middle-surface strains and partly due to bending strains. These resulting variations of stresses have been considered by Stowell.[4] Using the assumption that no part of the plate is unloaded, Stowell has derived the variations of the moments during the buckling process. The variations of the middle-surface forces can be derived directly from this work.

Denoting the variations of the forces and moments by primes ($'$), the following relations apply to fully plastic plates during buckling.

$$N_x' = B[A_1\epsilon_1 + (1/2)\,A_{12}\epsilon_2 - (1/2)A_{13}\epsilon_3] \quad (11)$$

$$N_y' = B[A_2\epsilon_2 + (1/2)\,A_{21}\epsilon_1 - (1/2)A_{23}\epsilon_3] \quad (12)$$

$$N_{xy}' = (B/2)\,[A_3\epsilon_3 - (1/2)\,A_{31}\epsilon_1 - (1/2)A_{32}\epsilon_2] \quad (13)$$

$$M_x' = -D[A_1\chi_1 + (1/2)\,A_{12}\chi_2 - (1/2)\,A_{13}\chi_3] \quad (14)$$

$$M_y' = -D[A_2\chi_2 + (1/2)\,A_{21}\chi_1 - (1/2)\,A_{23}\chi_3] \quad (15)$$

$$M_{xy}' = -(D/2)\,[A_3\chi_3 - (1/2)\,A_{31}\chi_1 - (1/2)\,A_{32}\chi_2] \quad (16)$$

In Eqs. (11) to (16), ϵ_1 and ϵ_2 are middle-surface normal strain variations and ϵ_3 is the middle-surface shear strain variation; χ_1 and χ_2 are the changes in curvature and χ_3 is the change in twist. Furthermore, the plasticity coefficients are defined as follows:

$$A_1 = 1 - \alpha\sigma_x^2/4 \quad (17)$$

$$A_2 = 1 - \alpha\sigma_y^2/4$$

$$A_3 = 1 - \alpha\tau^2$$

$$A_{21} = A_{12} = 1 - \alpha\sigma_x\sigma_y/2$$

$$A_{31} = A_{13} = \alpha\sigma_x\tau$$

$$A_{32} = A_{23} = \alpha\sigma_y\tau$$

where $\alpha = (3/\sigma_i^2)\,(1 - E_t/E_s)$

The axial rigidity $B = 4E_st/3$ (18)

The bending rigidity $D = E_st^3/9$ (19)

In the elastic region, $\alpha = 0$ and, therefore, $A_1 = A_2 = A_3 = A_{12} = 1$, and $A_{13} = A_{23} = 0$. By replacing the definitions of Eqs. (18) and (19) which are for a fully plastic plate by $B = Et/(1 - \nu_e^2)$ and $D = Et^3/12(1 - \nu_e^2)$, respectively, and replacing the coefficient (1/2) by ν_e, Eqs. (11) to (16) reduce to the familiar relations for the elastic plate.

Equilibrium Equations

By use of the force and moment variations, Eqs. (11) to (16), and the strain-displacement relations, Eqs. (7), the equilibrium relations, Eqs. (8) to (10), can be written in terms of the displacements u, v, w and their derivatives.

$$A_1(\partial^2u/\partial x^2) - (A_{13}/2)\,(\partial^2u/\partial x\partial y) + (A_3/4)\,(\partial^2u/\partial y^2) - (A_{13}/4)\,(\partial^2v/\partial x^2) + [(A_{12}/2) + (A_3/4)]\,(\partial^2v/\partial x\partial y) - (A_{23}/4)\,(\partial^2v/\partial y^2) + [(A_1/R_x) + (A_{12}/2R_y)]\,(\partial w/\partial x) - [(A_{13}/4R_x) + (A_{23}/4R_y)]\,(\partial w/\partial y) = 0 \quad (20)$$

$$A_2(\partial^2v/\partial y^2) - (A_{23}/2)\,(\partial^2v/\partial x\partial y) + (A_3/4)\,(\partial^2v/\partial x^2) - (A_{13}/4)\,(\partial^2u/\partial x^2) + [(A_{12}/2) + (A_3/4)]\,(\partial^2u/\partial x\partial y) - (A_{23}/4)\,(\partial^2u/\partial y^2) + [(A_2/R_y) + (A_{12}/2R_x)]\,(\partial w/\partial y) - [(A_{23}/4R_y) + (A_{13}/4R_x)]\,(\partial w/\partial x) = 0 \quad (21)$$

$$D[A_1(\partial^4w/\partial x^4) - A_{13}(\partial^4w/\partial x^3\partial y) + (A_{12} + A_3)\,(\partial^4w/\partial x^2\partial y^2) - A_{23}(\partial^4w/\partial x\partial y^3) + A_2(\partial^4w/\partial y^4)] + (B/R_x)\,\{A_1[(\partial u/\partial x) + (w/R_x)] + (A_{12}/2)\,[(\partial v/\partial y) + (w/R_y)] - (A_{13}/4)\,[(\partial u/\partial y) + (\partial v/\partial x)]\} + (B/R_y)\,\{(A_{12}/2)\,[(\partial u/\partial x) + (w/R_x)] + A_2[(\partial v/\partial y) + (w/R_y)] - (A_{23}/4)\,[(\partial u/\partial y) + (\partial v/\partial x)]\} + N_x(\partial^2w/\partial x^2) + 2N_{xy}(\partial^2w/\partial x\partial y) + N_y(\partial^2w/\partial y^2) + p = 0 \quad (22)$$

Eqs. (20) to (22) constitute a basic set of equilibrium differential equations for plastic stability of thin shells. Because of the appearance of cross-product derivative terms in these equations it is not possible to reduce, Eq. (22) to a single eighth-order equation of the Donnell type in w only. However, as will be shown subsequently, it is possible to accomplish this desirable objective in specific problems.

Sphere Under External Pressure

For a sphere under external pressure, the following parameters are pertinent to Eq. (17):

$$\left.\begin{aligned} &R = R_x = R_y \\ &\sigma = \sigma_x = \sigma_y = pR/2t \\ &\tau = 0 \end{aligned}\right\} \quad (23)$$

From Eq. (1), $\sigma_i = \sigma$

Therefore, $\alpha = (3/\sigma^2)\,(1 - E_t/E_s)$

For this value of α, the plasticity coefficients are:

$$\left.\begin{aligned} A_1 &= (1/4) + (3/4)\,E_t/E_s \\ A_2 &= A_1 \\ A_3 &= 1 \\ A_{12} &= (3/2)\,(E_t/E_s) - 1/2 \\ A_{13} &= A_{23} = 0 \end{aligned}\right\} \quad (24)$$

By inserting these values into Eqs. (20) to (22), the latter reduce to

$$\left.\begin{aligned} &A_1\frac{\partial^2u}{\partial x^2} + \frac{1}{4}\frac{\partial^2u}{\partial y^2} + \left(\frac{A_{12}}{2} + \frac{1}{4}\right)\frac{\partial^2v}{\partial x\partial y} + \left(\frac{A_1}{R} + \frac{A_{12}}{2R}\right)\frac{\partial w}{\partial x} = 0 \\ &A_1\frac{\partial^2v}{\partial y^2} + \frac{1}{4}\frac{\partial^2v}{\partial x^2} + \left(\frac{A_{12}}{2} + \frac{1}{4}\right)\frac{\partial^2u}{\partial x\partial y} + \left(\frac{A_1}{R} + \frac{A_{12}}{2R}\right)\frac{\partial w}{\partial y} = 0 \\ &D\left[A_1\frac{\partial^4w}{\partial x^4} + (A_{12} + 1)\,\frac{\partial^4w}{\partial x^2\partial y^2} + A_1\frac{\partial^4w}{\partial y^4}\right] + \frac{B}{R}\left(A_1 + \frac{A_{12}}{2}\right)\left[\frac{\partial u}{\partial x} + \frac{\partial v}{\partial y} + 2\,\frac{w}{R}\right] + \sigma t\left(\frac{\partial^2w}{\partial x^2} + \frac{\partial^2w}{\partial y^2}\right) + p = 0 \end{aligned}\right\} \quad (25)$$

By suitable manipulation of Eqs. (25), they can be put in the following form:

$$\nabla^4u = -(3/2A_1R)\,(E_t/E_s)\,[(\partial^3w/\partial x^3) + (\partial^3w/\partial x\partial y^2)] \quad (26)$$

$$\nabla^4 v = -(3/2A_1R)\,(E_t/E_s)\,[(\partial^3 w/\partial y^3) + (\partial^3 w/\partial x^2 \partial y)] \quad (27)$$

$$\nabla^4[DA_1\nabla^4 w + \sigma t\nabla^2 w + (E_t t/A_1 R^2)w] = 0 \quad (28)$$

It can be noted that Eq. (28) is a Donnell-type equation in terms of the radial displacement, w, only. A suitable solution is

$$w = w_m \sin mx \sin my \quad (29)$$

By substitution of Eq. (29) into Eq. (28) and minimizing the nontrivial solution in the form $\partial\sigma/\partial m = 0$, the following results are obtained:

$$\sigma_{cr} = [3\,(1 - \nu_e^2)]^{-1/2}\,\eta E(t/R) \quad (30)$$

where

$$\eta = [(1 - \nu_e^2)/(1 - \nu^2)]^{1/2}\,(E_s/E)\,(E_t/E_s)^{1/2} \quad (31)$$

In obtaining Eq. (30), a value of $D = Et^3/12(1 - \nu^2)$ was used in place of the fully plastic value given by Eq. (19). It has been found that this method affords a reasonable approach for including Poisson ratio effects in the yield region where the transition from the elastic to plastic value is most pronounced.

By taking $\eta = 1$ in Eq. (30), the familiar critical stress equation for an elastic sphere is obtained. It is well known, however, that initial imperfections and large deflection effects are significant in this case. Therefore, it is suggested that the value of η given by Eq. (31), which is equivalent to that presented by Bijlaard,[6] be applied to a modified Eq. (30) which has a coefficient less than $[3(1 - \nu_e^2)]^{-1/2}$ and derived from large deflection theory.

Circular Cylinder Under External Lateral Pressure

For a circular cylinder under external lateral pressure, the parameters pertinent to Eqs. (17) are:

$$\left.\begin{aligned} & R = R_y;\quad R_x = \infty \\ & \sigma_y = pR/t \\ & \sigma_x = \tau = 0 \\ \text{From Eq. (1),}\quad & \sigma_i = \sigma_y \\ \text{Therefore,}\quad & \alpha = (3/\sigma_y^2)\,(1 - E_t/E_s) \end{aligned}\right\} \quad (32)$$

The plasticity coefficients have the following values:

$$\left.\begin{aligned} A_1 &= A_3 = A_{12} = 1 \\ A_2 &= (1/4) + (3/4)\,E_t/E_s \\ A_{13} &= A_{23} = 0 \end{aligned}\right\} \quad (33)$$

By inserting these values into Eqs. (20) to (23), and manipulating suitably, the following set of equations is obtained:

$$\nabla_2{}^4 u = -(1/2R)\,(\partial^3 w/\partial x^3) + (A_2/R)\,(\partial^3 w/\partial x \partial y^2) \quad (34)$$

$$\nabla_2{}^4 v = -(1/R)\,(4A_2 - 3/2)\,(\partial^3 w/\partial x^2 \partial y) - (A_2/R)\,(\partial^3 w/\partial y^3) \quad (35)$$

$$[D\nabla_1{}^4 + \sigma_y t + (\partial^2/\partial y^2)]\nabla_2{}^4 w + (E_t t/R^2)\,(\partial^4 w/\partial x^4) = 0 \quad (36)$$

where $\nabla_1{}^4 = \nabla^4 + (3/4)\,[(E_t/E_s) - 1]\,(\partial^4/\partial y^4)$

$$\nabla_2{}^4 = \nabla_1{}^4 + 3[(E_t/E_s) - 1]\,(\partial^4/\partial x^2 \partial y^2)$$

A suitable solution to Eq. (36) which satisfies the boundary conditions of simple support is

$$w = w_{mn} \sin (\pi x/L) \sin (ny/R) \quad (37)$$

Upon substituting the appropriate derivatives of Eq. (37) into Eq. (36), the nontrivial solution is obtained:

$$k_y = \frac{(\beta^2 + 1)^2 + (3/4)\,[(E_t/E_s) - 1]\,\beta^4}{\beta^2} + \frac{12Z^2 E_t/E_s}{\pi^4\beta^2\{(\beta^2 + 1)^2 + 3[(E_t/E_s) - 1]\beta^2 + (3/4)\,[(E_t/E_s) - 1]\beta^4\}} \quad (38)$$

where $k_y = \sigma_y t\,L^2/\pi^2 D$

$\beta = nL/\pi R$

Moderate Length Cylinders

For cylinders of moderate length it can be assumed that $\beta^2 \gg 1$, and, therefore, Eq. (38) reduces to the following:

$$k_y = \beta^2[(1/4) + (3/4)\,(E_t/E_s)] + (12Z^2/\pi^4\beta^6)\,(E_t/E_s)/[(1/4) + (3/4)E_t/E_s] \quad (39)$$

Upon minimizing, $\partial k_y/\partial\beta = 0$, and substituting for β into Eq. (39),

$$k_y = 1.038Z^{1/2}\,(E_t/E_s)^{1/4}\,[(1/4) + (3/4)\,(E_t/E_s)]^{1/2} \quad (40)$$

In the elastic case $E_t/E_s = 1$, and therefore Eq. (40) becomes

$$k_y = 1.038\,Z^{1/2} \quad (41)$$

It is interesting to note that Eq. (41) follows directly from the assumption that $\beta^2 \gg 1$. Batdorf[2] obtained the same result by fitting a curve to the results of his calculations and found that it applied in the range $100t/R < (L/R)^2 < 5R/t$.

In an alternate form, Eq. (41) becomes

$$\sigma_{ycr} = 0.855\,[\eta_y E/(1 - \nu_e^2)^{3/4}]\,(t/L)\,(t/R)^{1/2} \quad (42)$$

where

$$\eta_y = [(1 - \nu_e^2)/(1 - \nu^2)]^{3/4}\,(E_s/E)\,(E_t/E_s)^{1/4} \times [(1/4) + (3/4)\,(E_t/E_s)]^{1/2} \quad (43)$$

Long Cylinders

Cylinders which are long, $(L/R)^2 > 5R/t$, buckle with two circumferential waves. Therefore, $\beta = 2L/\pi R \gg 1$, and Eq. (38) reduces simply to

$$k_y = (4L^2/\pi^2 R^2)\,[(1/4) + (3/4)\,(E_t/E_s)] \quad (44)$$

or

$$\sigma_y = [\eta_y E/3(1 - \nu^2)]\,(t/R)^2 \quad (45)$$

TABLE 1
Plasticity Reduction Factors for Shells

(1) Cylinder—axial compression,[5] and Sphere—external pressure	$\eta = \left[\frac{1-\nu_e^2}{1-\nu^2}\right]^{1/2} \frac{E_s}{E}\left(\frac{E_t}{E_s}\right)^{1/2}$
(2) Cylinder—torsion	
(a) moderate length, $50\,t/R < (L/R)^2 < 10\,R/t$	$\eta_s = \left[\frac{1-\nu_e^2}{1-\nu^2}\right]^{5/8} \frac{E_s}{E}$
(b) long $(L/R)^2 > 10\,R/t$	$\eta_s = \left[\frac{1-\nu_e^2}{1-\nu^2}\right]^{3/4} \frac{E_s}{E}$
(3) Cylinder—lateral pressure	
(a) moderate length, $100\,t/R < (L/R)^2 < 5\,R/t$	$\eta_y = \left[\frac{1-\nu_e^2}{1-\nu^2}\right]^{3/4} \frac{E_s}{E}\left(\frac{E_t}{E_s}\right)^{1/4}\left(\frac{1}{4}+\frac{3}{4}\frac{E_t}{E_s}\right)^{1/2}$
(b) long, $(L/R)^2 > 5\,R/t$	$\eta_y = \left[\frac{1-\nu_e^2}{1-\nu^2}\right] \frac{E_s}{E}\left(\frac{1}{4}+\frac{3}{4}\frac{E_t}{E_s}\right)$

where

$$\eta_y = [(1-\nu_e^2)/(1-\nu^2)]\,(E_s/E)\,[(1/4) + (3/4)\,(E_t/E_s)] \quad (46)$$

Eq. (46) is a result equivalent to that presented by Bijlaard.[6] The only case of those investigated by Batdorf[2] that results in an error due to the basic assumptions of the Donnell equations is the long cylinder under external pressure. Here $n = 2$, and since the equations are based upon the assumption that $n^2 \gg 1$, this result is not unexpected. More exact solutions of elastic buckling of long cylinders under lateral pressure indicate that the coefficient 3 in Eq. (45) should be replaced by 4, as discussed in reference 2.

Circular Cylinder Under Torsion

For a circular cylinder under torsion, the following parameters are pertinent to Eqs. (17):

$$\left.\begin{aligned} & R = R_y;\quad R_x = \infty \\ & \sigma_x = \sigma_y = 0 \\ \text{From Eq. (1),}\quad & \sigma_i = (3)^{1/2}\tau \\ \text{Therefore,}\quad & \alpha = \tau^{-2}(1 - E_t/E_s) \end{aligned}\right\} \quad (47)$$

The plasticity coefficients have the following values:

$$\left.\begin{aligned} A_1 &= A_2 = A_{12} = 1 \\ A_3 &= E_t/E_s \\ A_{13} &= A_{23} = 0 \end{aligned}\right\} \quad (48)$$

By inserting these values into Eqs. (20) to (23), and manipulating suitably, the following set of equations is obtained:

$$\nabla_2^4 u = -(1/2R)\,(\partial^3 w/\partial x^3) + (1/R)\,(\partial^3 w/\partial x \partial y^2) \quad (49)$$

$$\nabla_2^4 v = -(1/R)\,[(3/A_3) - (1/2)] \times (\partial^3 w/\partial x^2 \partial y) - (1/R)\,(\partial^3 w/\partial y^3) \quad (50)$$

$$[D\nabla_1^4 + 2\tau t\,(\partial^2/\partial x \partial y)]\nabla_2^4 w + (E_s t/R^2)\,(\partial^4 w/\partial x^4) = 0 \quad (51)$$

where $\nabla_1^4 = \nabla^4 - (1 - E_t/E_s)\,(\partial^4/\partial x^2 \partial y^2)$

$\nabla_2^4 = \nabla^4 + 3(E_s/E_t)\,[1 - (E_t/E_s)]\,(\partial^4/\partial x^2 \partial y^2)$

Long Cylinders

A long cylinder under torsion, $(L/R)^2 > 10R/t$, buckles in two circumferential waves. Since the boundary conditions are insignificant for a long cylinder, the following solution to Eq. (51) is satisfactory.

$$w = w_{mn} \sin\,[m\pi(x/L) + (2y/R)] \quad (52)$$

Upon substituting the appropriate derivatives of Eq. (52) into Eq. (51), the following nontrivial solution is obtained:

$$\tau = \frac{D[(\beta^2+4)^2 - 4(1 - E_t/E_s)\beta^2]}{4R^2 t\,\beta} + \frac{E_s\beta^3}{4[(\beta^2+4)^2 + 12(E_s/E_t)\,(1 - E_t/E_s)\beta^2]} \quad (53)$$

where $\beta = m\pi R/L$

For a long cylinder, the angle between the generator and the helical buckle pattern is small. Consequently, $\beta^2 \ll 1$, and Eq. (53) can be reduced to

$$\tau = (4D/R^2 t\beta) + E_s(\beta/4)^3 \quad (54)$$

Upon minimization of Eq. (54), $\partial\tau/\partial\beta = 0$, and substituting for β,

$$\tau_{cr} = 0.272\,(1 - \nu_e^2)^{-3/4}\,\eta_s E\,(t/R)^{3/2} \quad (55)$$

where $\eta_s = [(1-\nu_e^2)/(1-\nu^2)]^{3/4}\,(E_s/E)$ (56)

For $\eta_s = 1$, Eq. (55) is the well-known elastic solution for torsional buckling of a cylinder. The plasticity reduction factor given by Eq. (56) was previously obtained in reference 5 by solving Eqs. (20) to (22) directly for this case.

Moderate Length Cylinders

For cylinders of moderate length, Eq. (52) is not satisfactory, since the boundary conditions are not satisfied. Elastic solutions for torsional buckling of moderate-length cylinders indicate that the buckling stress with clamped edges is a constant 10 per cent higher than for simply supported edges. Thus, in reference 7 it was suggested that an approximate solution would satisfy the single boundary condition $w = 0$ but not necessarily any boundary conditions on the slope $\partial w/\partial n = 0$ (clamping) or moment $\partial^2 w/\partial n^2 = 0$ (simple support) because of the small difference in buckling stress between the simply supported and clamped edge solutions for elastic cylinders.

In reference 8, the following solution was used for an elastic cylinder of moderate length, and excellent agree-

ment was obtained with the simply supported cylinder solution of Batdorf.[2]

$$w = w_{mn}(\sin [(m\pi x/L) + (ny/R)] - \sin \{[(m + 2)\pi x/L] + (ny/R)\}) \quad (57)$$

Note that Eq. (57) is a sum of solutions of the type of Eq. (52) and satisfies the boundary condition $w = 0$ at $x = 0, L$.

By substituting the appropriate derivatives of Eq. (57) into Eq. (51), and utilizing the assumptions that $\beta_1^2 \ll 1$ and $\beta_2^2 \ll 1$ as shown in reference 8, the following is obtained:

$$\tau = [D(n/R)^2/t(\beta_1 + \beta_2)] + [E_s(\beta_1^4 + \beta_2^4)/2R^2(n/R)^2(\beta_1 + \beta_2)] \quad (58)$$

where $\beta_1 = m\pi R/nL$

$$\beta_2 = (m + 2)\,\pi R/nL$$

Upon minimization of Eq. (58) in the form $\partial\tau/\partial m = 0$, $\partial\tau/\partial n = 0$, the critical shear stress can be obtained in the form

$$\tau_{cr} = 0.701\,(1 - \nu_e^2)^{-5/8}\,\eta_s E(t/R)^{5/4}\,(R/L)^{1/2} \quad (59)$$

where $\eta_s = [(1 - \nu_e^2)/(1 - \nu^2)]^{5/8}\,(E_s/E)$

For $\eta_s = 1$, Eq. (59) is identical to the elastic solution presented by Batdorf[2] in which his results for moderate length cylinders under torsion were obtained by curve fitting. The moderate-length cylinder range in this case is defined by $50t/R < (L/R)^2 < 10R/t$.

Conclusion

The plasticity reduction factors obtained herein, as well as that obtained in reference 5 for a circular cylinder under axial compression, are summarized in Table 1 for convenience.

References

[1] Donnell, L. H., *Stability of Thin-Walled Tubes Under Torsion*, NACA Report No. 479, 1933.

[2] Batdorf, S. B., *A Simplified Method of Elastic-Stability Analysis for Thin Cylindrical Shells: I—Donnell's Equation*, NACA TN 1341, 1947.

[3] Becker, H., *Donnell's Equation for Thin Shells*, Readers' Forum, Journal of the Aeronautical Sciences, Vol. 24, No. 1, p. 79, January, 1957.

[4] Stowell, E. Z., *A Unified Theory of Plastic Buckling of Columns and Plates*, NACA Report 898, 1948.

[5] Gerard, G., *Compressive and Torsional Buckling of Thin-Wall Cylinders in the Yield Region*, NACA TN 3726, August, 1956.

[6] Bijlaard, P. P., *Theory and Tests on the Plastic Stability of Plates and Shells*, Journal of the Aeronautical Sciences, Vol. 16, No. 9, pp. 529–541, September, 1949.

[7] Gerard, G., *Torsional Instability of a Long Sandwich Cylinder*, Proceedings, First U. S. National Congress of Applied Mechanics, pp. 391–394, June, 1951.

[8] Becker, H., and Gerard, G., *Torsional Buckling of Moderate Length Cylinders*, Jour. Appl. Mech., Vol. 23, No. 4, pp. 647–648, December, 1956.

Theories of Strength for Combined Stresses . . .

(*Continued from page 268*)

applied to materials with different strengths in different directions. A theory is also developed for defining strengths under combined strengths in the case of materials with different strengths in tension and compression.

References

[1] Von Mises, R., Nachr. Ges. Wiss. Gottingen, Math-Physik Klasse, p. 582, 1913.

[2] Navies, M., *Résumé des leçons*, 1er partie, "Sur la resistance des materiaux," p. 126, 1833.

[3] Nadai, A., *Theory of Flow and Fracture of Materials*, Vol. 1; McGraw-Hill Book Company, Inc., New York, 1950. (See also Timoshenko, S., *Strength of Materials*, Part 2; D. Van Nostrand Company, Inc., New York, 1956.)

[4] Marin, J., *Mechanical Properties of Materials and Design;* McGraw-Hill Book Company, Inc., New York, 1942.

[5] Mohr, O., *Die Elastizitatsgrenze und der Brucheines Materials*, VDI, Vol. 44, p. 1530, 1900.

[6] Hetenyi, M. (Ed.), *Handbook for Experimental Stress Analysis*, Soderberg, C. R., "Working Stresses," Chap. 10, p. 148; John Wiley & Sons, Inc., New York, 1950.

[7] Timoshenko, S., and Goodier, N., *Theory of Elasticity*, 2nd Ed.; McGraw-Hill Book Company, Inc., New York, 1951.

[8] Sachs, G., *Zur Ableitung einer Fliessbedingung*, Z. Ver. deut. Ing., Vol. 72, p. 734, 1928.

[9] Hill, R., *The Mathematical Theory of Plasticity;* Oxford University Press, 1950.

[10] Prager, W., and Hodge, P. G., *Theory of Perfectly Plastic Solids;* John Wiley & Sons, Inc., New York, 1951.

[11] Neuber, N., *Kerbspannungslehre;* Springer, Berlin, 1937 (translation, *Theory of Notch Stresses;* J. W. Edwards Bros., Ann Arbor, Mich., 1946).

[12] Peterson, R. E., *Stress Concentration Design Factors*, John Wiley & Sons, Inc., New York, 1953.

[13] Fitchie, J. W., *Some Experiments into the Behavior of Plain and Notched Steel Specimens under Static and Fatigue Loadings*, Inst. of Mech. Engrs., London, 1955.

A Method for Examination of Store Separation From Aircraft Through Dynamic Model Testing at Full-Scale Mach Number†

SEYMOUR J. DEITCHMAN*

Cornell Aeronautical Laboratory, Inc.

SUMMARY

The need for study of the motion of stores after launch or jettison from high-speed aircraft has led the designer to resort to dynamic model testing at full-scale Mach Numbers as a direct analytical technique. Accordingly, it has been found useful to formulate a set of similarity laws for such testing for the cases most commonly encountered—i.e., freely falling bodies and fin or spin stabilized powered projectiles. Consideration has also been given to obtaining model to full-scale similarity of the jet of a powered projectile, for study of its effect on the launching aircraft. Requirements for simulation of the effects of fuel in a full or partially full tank have been examined qualitatively. Some simulation errors that may be encountered have been examined and evaluated.

SYMBOLS

A	= cross-section area
d	= maximum diameter
x, y, z	= body axes; a right-hand system, positive with x forward, which pitches and yaws but does not roll with the body
$X\ Y\ Z$ $L\ M\ N$	= forces along and moments about, respectively, the corresponding axes
$C_X\ C_Y\ C_Z$ $C_l\ C_m\ C_n$	= corresponding aerodynamic coefficients
I_x, I_y, I_z	= moments of inertia about the subscript axes
l	= length
$\bar{l}$	= nondimensional length
M	= Mach Number
m	= mass; mass flow of exhaust gases
p	= static pressure
r	= body radius
T	= thrust; jet absolute temperature
t	= time
U	= air-stream velocity
U_0	= initial air-stream velocity
V	= volume; velocity
V_x, V_y, V_z	= perturbation velocities along the subscript axes
α_v, ψ_v	= aerodynamic angles of attack and yaw, respectively; defined in the text
Γ	= circulation
γ	= gas constant
ζ	= damping factor
λ	= scale factor; refers to length without subscript number
ρ	= air-stream or exhaust gas density
σ	= body density
ϕ	= spin of the body about its x axis in the x, y, z system
ψ, θ	= rotations of x, y, z axes relative to reference X_e, Y_e, Z_e axes fixed in the launching airplane, taken in the order shown (ψ = rotation about Z_e; θ = rotation about Y_e)
Ω	= ratio of full-scale to model stream velocity, U_{0fs}/U_{0m}
$\omega_x, \omega_y, \omega_z$	= angular velocities about the subscript axes

Subscripts

a	= surrounding air stream
j	= jet
fs	= full scale
M	= Magnus force
m	= model

INTRODUCTION

ALL PRESENT-DAY military aircraft are required to jettison or launch stores of various types—fuel tanks, bombs, rockets, missiles, etc. High operational speeds lead to special problems in predicting and analyzing the behavior of these stores immediately after launch or jettison, because the presence of the aircraft distorts the flow over the stores and induces on them interference air loads that are large relative to their mass and inertia. The induced initial motions may cause the stores to endanger the aircraft or suffer serious degradation of required ballistic properties. In seeking solutions to these problems the designer has turned to dynamic model testing. This testing may use wind-tunnel, high-speed sled, or reduced scale free-flight techniques; in any case, the tests have the following characteristics in common: (a) reduced scale models of the stores are dropped or launched from exactly or partially simulated models of the aircraft; (b) the model stores must exhibit motion that is considered similar, by some applicable similarity criteria, to the full-scale motion; and (c) because of the high air speeds involved, model and full-scale Mach Numbers must be equal.

These characteristics lead to the requirement that, in addition to geometric scale reduction, the properties of the air stream, and store mass and inertia, must be reduced in such a way that motion similarity is maintained as defined. Such scale reduction criteria

Received May 8, 1956. Revised and received October 30, 1956.

† This work was completed as a part of studies sponsored by the Armament Laboratory, WADC, and Air Munitions Development Laboratory, AFAC, of the U.S. Air Force, under Contract AF33(616)-2394.

The author is indebted to H. Lawrence, formerly Assistant Head, Theoretical Aerodynamics Department, and A. Flax, Assistant Director, Cornell Aeronautical Laboratory, Inc., for their suggestions regarding the basic approach to the similarity laws as derived herein.

* Principal Aeronautical Engineer.

have been derived in the past for specific cases of interest—e.g., references 1 and 2.* It appears that a set of similarity laws applying to most configurations encountered in practice can serve a useful purpose by collecting some scattered results and examining the similarities and differences for various cases. Consequently, similarity criteria are defined herein, and similarity laws for examination of store separation from aircraft through dynamic model testing are derived for several types of stores.

Specifically, free-fall and powered model testing are considered. The first category includes bombs and tanks, and the second, rockets and missiles—either fin or spin stabilized. The general equations of motion are modified for each category to permit derivation of the scale reduction criteria required for the particular definition of motion similarity. Some discussion of simulation errors and their consequence is also given. The magnitude of the errors, which will define the regions of validity of the similarity laws, is indicated.

General Approach

The six degree of freedom equations of motion for an axisymmetric body in a modified body axis system that does not roll, but within which the body may roll about its axis, are

$$\left.\begin{aligned}
\dot{V}_x &= (X/m) - g\sin\theta + V_y\omega_z - V_z\omega_y \\
\dot{V}_y &= (Y/m) - V_x\omega_z\tan\theta - V_x\omega_z \\
\dot{V}_z &= (Z/m) + g\cos\theta + V_x\omega_y + \\
&\qquad V_y\omega_x\tan\theta \\
\dot{\omega}_x &= L/I_x \\
\dot{\omega}_y &= (M/I_y) - \omega_z^2\tan\theta - (I_x/I_y)\omega_x\omega_z \\
\dot{\omega}_z &= (N/I_y) + \omega_y\omega_z\tan\theta + (I_x/I_y)\omega_x\omega_y
\end{aligned}\right\} \quad (1)$$

Aerodynamic forces and moments are expressed in the standard coefficient form, and the aerodynamic angles of attack and yaw are[3]

$$\left.\begin{aligned}
\tan\alpha_u &= \frac{U_0\cos\psi\sin\theta + V_z}{U_0\cos\psi\cos\theta + V_x} \\
\sin\psi_v &= (U_0\sin\psi - V_y)/U
\end{aligned}\right\} \quad (2)$$

These angles can be approximated by

$$\left.\begin{aligned}
\alpha_u &= [\theta + (V_z/U_0)]/[1 + (V_x/U_0)] \\
\psi_v &= [\psi - (V_y/U_0)]/[1 + (V_x/U_0)]
\end{aligned}\right\} \quad (3)$$

and these approximate expressions will be acceptable for even moderately large values of θ and ψ (up to 20 or 30 degrees) and V/U_0 (up to about 0.3).

The similarity laws in a particular case will be derived by specifying the similarity criteria; simplifying the equations of motion in keeping with those criteria and the characteristics of the stores being considered; assuming certain scale transformations that will be required; and determining all of these transformations in terms of the scale factor of length alone. This procedure will be illustrated for the case of a free-fall body, and the derivation of similarity laws for powered projectiles follows the same scheme.

Certain assumptions are made in deriving the similarity laws. Because of the powerful influence of Mach Number on aerodynamic characteristics, it is assumed that the model tests must be performed at the full-scale Mach Number. The need for duplicating the effects of Reynolds Number is not unique to this problem, and in many cases of model testing it is found that the Reynolds Number resulting from the test conditions and apparatus can be accepted. In cases where Reynolds Number effects are expected to be significant, some experimental accounting for these effects can be made, in either static or dynamic test situations, by such methods as the use of roughness strips to cause boundary-layer transition. Therefore, no Reynolds Number effects are considered herein.

Since the model tests are performed at the full-scale Mach Number, model and full-scale aerodynamic coefficients are considered equal. This assumption remains valid in the practical case as long as errors of angle of attack and yaw that may result from application of the similarity laws derived do not lead to coefficient errors of larger order than the accuracy with which the coefficients are known. For the initial formulation of the similarity laws damping forces are neglected, since in general they are much smaller than static forces. The effects of the scale transformations on damping are then considered for simplified one degree of freedom motions.

The application of constant forces throughout the trajectory to produce vertical acceleration simulating a scaled effect of gravity, without introducing extraneous effects in other directions, is considered a practical impossibility. Therefore, no transformations of the acceleration of gravity are permitted.

Free-Fall Bodies

Bombs

Freely falling bodies are characterized, near the start of fall, by velocities V_x, V_y, V_z that are small relative to U_0. Therefore, aerodynamic coefficients may be based on U_0 only, and velocity errors will not lead to initially large errors in α_u and ψ_v. The motion similarity criteria will therefore be based on attitude and position only.

$$\left.\begin{aligned}
\bar{l}_{fs} &= \bar{l}_m \\
(\psi, \theta, \phi)_{fs} &= (\psi, \theta, \phi)_m
\end{aligned}\right\} \quad (4)$$

Now assume the scale transformations

$$\left.\begin{aligned}
l_{fs} &= \lambda\, l_m \\
t_{fs} &= \lambda_2 t_m \\
m_{fs} &= \lambda_3 m_m \\
I_{fs} &= \lambda_4 I_m \\
(\rho U_0^2)_{fs} &= \lambda_5(\rho U_0^2)_m
\end{aligned}\right\} \quad (5)$$

* Most of the aircraft companies, and many agencies such as the NACA, have analyzed various aspects of the problem.

Mass is given by

$$m = \sigma V$$

where σ is the body density and V is the body volume, so that, immediately,

$$\lambda_3 = \lambda^3(\sigma_{fs}/\sigma_m) \tag{6}$$

and, similarly,

$$\lambda_4 = \lambda^5(\sigma_{fs}/\sigma_m) \tag{7}$$

Now solve the first of Eqs. (1) for C_X, equate C_{Xm} and C_{Xfs}, and substitute scale transformations (5) into the side of the equation representing C_{Xfs}:

$$\begin{aligned}[(\dot{V}_x - V_y\omega_z + V_z\omega_y)_m + g\sin\theta] \times \\ [m_m/(1/2)\,(\rho U_0^2)_m A_m] = \\ [(\dot{V}_x - V_y\omega_z + V_z\omega_y)_m \lambda/\lambda_2^2 + g\sin\theta] \times \\ [\lambda^3(\sigma_{fs}/\sigma_m) m_m/(1/2)\lambda_5(\rho U_0^2)_m \lambda^2 A_m]\end{aligned} \tag{8}$$

By inspection of the two sides of Eq. (8),

$$[\lambda(\sigma_{fs}/\sigma_m)/\lambda_5] = 1 = [\lambda^2(\sigma_{fs}/\sigma_m)/\lambda_5\lambda_2^2]$$

whence

$$\lambda_2 = \sqrt{\lambda} \tag{9}$$

$$\lambda_5 = \lambda(\sigma_{fs}/\sigma_m) \tag{10}$$

Eqs. (6), (7), (9), and (10), when substituted into any of Eqs. (1), with equal full-scale and model aerodynamic coefficients, will satisfy similarity criteria (4). Summarizing, therefore, the following conditions must be obtained for trajectory position and attitude similarity of free-fall models to the full-scale objects:

$$\left.\begin{aligned} l_{fs}/l_m &= \lambda \\ m_{fs}/m_m &= \lambda^3(\sigma_{fs}/\sigma_m) \\ I_{fs}/I_m &= \lambda^5(\sigma_{fs}/\sigma_m) \\ (\rho U_0^2)_{fs}/(\rho U_0^2)_m &= \lambda(\sigma_{fs}/\sigma_m) \end{aligned}\right\} \tag{11}$$

giving (since $t_{fs} = \sqrt{\lambda} t_m$)

$$\left.\begin{aligned} \bar{l}_{fs}/\bar{l}_m &= (\psi, \theta, \phi)_{fs}/(\psi, \theta, \phi)_m = 1 \\ (V_x, V_y, V_z)_{fs}/(V_x, V_y, V_z)_m &= \sqrt{\lambda} \\ (\omega_x, \omega_y, \omega_z)_{fs}/(\omega_x, \omega_y, \omega_z)_m &= 1/\sqrt{\lambda} \\ (\dot{V}_x, \dot{V}_y, \dot{V}_z)_{fs}/(\dot{V}_x, \dot{V}_y, \dot{V}_z)_m &= 1 \\ (\dot{\omega}_x, \dot{\omega}_y, \dot{\omega}_z)_{fs}/(\dot{\omega}_x, \dot{\omega}_y, \dot{\omega}_z)_m &= 1/\lambda \end{aligned}\right\} \tag{12}$$

It will be observed that, while trajectory similarity exists, according to the present definition, the model and full-scale linear velocity perturbations and angular velocities differ by a factor $\sqrt{\lambda}$ or $1/\sqrt{\lambda}$, respectively. Whether this makes a significant difference in simulation depends on whether the condition on (ρU_0^2) was fulfilled by reducing ρ, or U_0, or both. Ordinarily, at subsonic or low supersonic Mach Numbers in the wind tunnel, it will be necessary to keep $U_{0fs} \leftrightarrows U_{0m}$ and reduce ρ to maintain $M_{fs} = M_m$. At high supersonic speed, it may be that $U_{0m} < U_{0fs}$. The consequences of these differences can be examined through some further simple analyses.

Conditions (11) were derived with damping forces neglected. Since the pitch (or yaw) aerodynamic damping moments are the only ones of consequence, consider the effect of conditions (11) on them through the single degree of freedom case of pitch only, with $\theta \approx \alpha_w$. Let the equation of motion for free oscillation be

$$\ddot{\theta} + M_{\dot{\theta}}\,\dot{\theta} + M_\theta\theta = 0 \tag{13}$$

Define $M_{\dot{\theta}}$ by

$$M_{\dot{\theta}} = -[K_H(1/2)\rho U d^4/I_y] \tag{14}$$

where

$$K_H = \text{damping moment}/\rho U d^4\dot{\theta}$$

and $K_{Hfs} = K_{Hm}$ since K_H can be shown to depend on geometry only, within the limits of Mach Number and Reynolds Number requirements discussed previously.

Then, substituting the similarity conditions,

$$M_{\dot{\theta}_{fs}} = (1/\Omega) M_{\dot{\theta}_m} \tag{15}$$

where

$$\Omega = U_{0fs}/U_{0m}$$

and, similarly,

$$M_{\theta_{fs}} = (1/\lambda) M_{\theta_m} \tag{16}$$

where

$$M_\theta = (dC_m/d\theta)\,[(1/2)\rho U^2 A d/I_y] \tag{17}$$

Now, from the solution of Eq. (13), for critical damping,

$$\sqrt{(M_{\dot{\theta}})^2 - 4M_\theta} = 0 \tag{18}$$

and since the damping factor is given by

$$\zeta = M_{\dot{\theta}}/(M_{\dot{\theta}})_{cr} \tag{19}$$

substituting Eqs. (15) and (16) in Eqs. (18) and (19) yields

$$\zeta_{fs}/\zeta_m = \sqrt{\lambda}/\Omega \tag{20}$$

The ratio of successive amplitudes is given by

$$\theta_2/\theta_1 = e^{-\delta}$$

where, for small damping,

$$\delta = 2\pi\zeta$$

so that, from Eq. (20),

$$(\theta_2/\theta_1)_{fs}/(\theta_2/\theta_1)_m = e^{-2\pi\zeta_{fs}[1-(\Omega/\sqrt{\lambda})]} \tag{21}$$

Thus, for $\Omega = \sqrt{\lambda}$ the damping rate will be simulated exactly, while as $\Omega \to 1$ (the more usual case in subsonic wind-tunnel testing) the model will be more lightly damped than the full-scale body. Fig. 1 shows how large this damping error will be for some typical values of ζ and $\Omega/\sqrt{\lambda}$. A value of ζ of 0.01 is reasonably typical of many stores. If major interest centers on the motion immediately after release (say, the first half oscillation) damping rate errors of the magnitude shown will probably not be important.

Having $\Omega/\sqrt{\lambda} \neq 1$ also leads to erroneous angles of

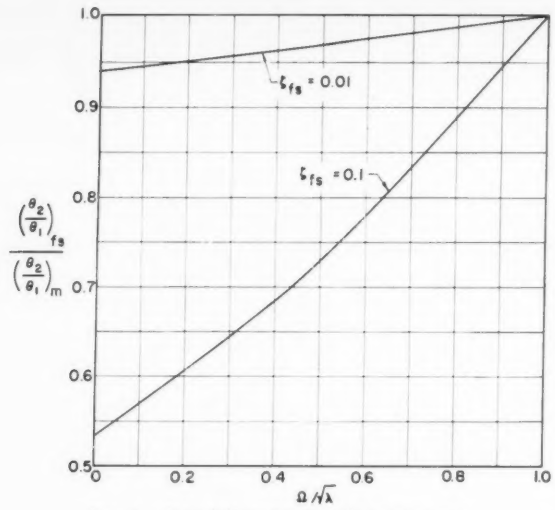

FIG. 1. Free-fall model damping rate error.

attack and yaw. For example, applying the appropriate part of Eqs. (12) to the first of Eqs. (3) will give

$$\alpha_{um} = \frac{\theta + (V_z/U_0)_{fs}(\Omega/\sqrt{\lambda})}{1 + (V_x/U_0)_{fs}(\Omega/\sqrt{\lambda})} \tag{22}$$

whence the ratio α_{um}/α_{ufs} can be determined for various values of $\Omega/\sqrt{\lambda}$. This ratio is shown plotted in Fig. 2 for typical values of $(V_z/U_0)_{fs}$ and $(V_x/U_0)_{fs}$. The smaller values of the latter correspond to the free-fall body, while larger values correspond to powered projectiles (see below). Fig. 2 shows that, for smaller ratios of V/U_0, such as those experienced by a free-fall body near the launching aircraft, and large pitch angles (θ), the α error is never larger than about 10 per cent. The error will be relatively smaller when the store is more highly disturbed, and that case is of greater importance to the experimenter.

Again, the error will be reduced as $\Omega \to \sqrt{\lambda}$, but this may not be practicable at any but high supersonic or very low Mach Numbers. If the air speed is so low that Mach Number effect is of no consequence, then adjustment of U_0^2 such that $\Omega/\sqrt{\lambda} = 1$ is possible, thereby eliminating the errors in damping rate and angles of attack and sideslip.

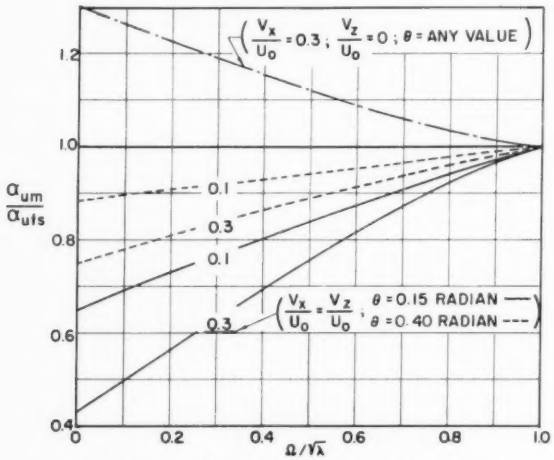

FIG. 2. Free-fall model angle of attack error.

Fuel Tanks

The preceding formulation of similarity laws for freely falling bodies applies equally well to heavy bodies such as bombs or light ones such as empty fuel tanks. It may be desired, however, to perform model jettison tests on full or partially full fuel tanks. The theoretical problem of defining the motion of such a tank is difficult, and has not been completely solved.[4, 5] It may be possible, however, to examine simulation requirements from some highly simplified considerations. It is assumed that mass will be scaled according to Eq. (11).

Consider, first, a stable configuration. It is shown in reference 5 that, for pitch oscillations of "a few degrees," appreciable damping due to the fuel occurs only during steady forced oscillations, but does not appear immediately after application of a step function to start oscillations. Since the latter motion corresponds more to the motion after release, it is implied that only inertia (and mass) considerations are important.

The effective fuel inertia is shown[5] to be related to the "solid" inertia about the fuel centroid, for an ellipsoid of revolution, by

$$I_{eff} = I_{solid}\left\{[(a/b)^2 - 1]/[(a/b)^2 + 1]\right\} \tag{23}$$

where (a/b) is the ratio of radii of the ellipse. It is also shown experimentally that this relationship is substantially independent of the amount of fuel in the tank (from full to 10 per cent full); and that viscosity has no effect on the tank motion, within the viscosity range of aircraft fuels. Thus, Eq. (23) shows that the inertia requirement will be, as for a solid store, $I_{eff_{fs}} \div I_{eff_m} = \lambda^5\sigma_{fs}/\sigma_m$, and the model geometry will simply be scaled directly.

To examine inertia simulation requirements for an unstable partially full tank, consider the tank to be a right circular cylinder in either horizontal or vertical positions (see Fig. 3). Then in the horizontal posi-

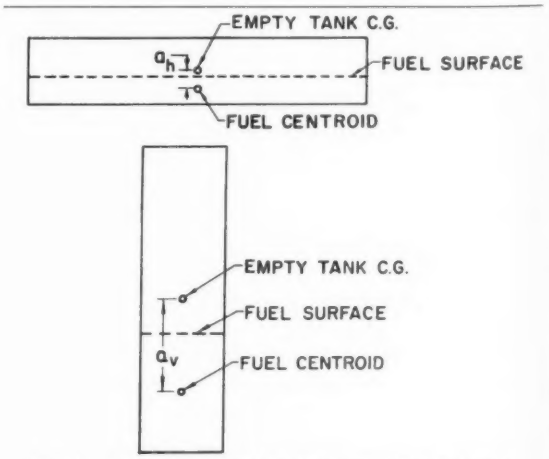

FIG. 3. Model for a partially filled, tumbling fuel tank.

tion

$$I_h = I_{c.g.} + m_f a_h^2 + I_{eff_h} \tag{24}$$

and in the vertical position

$$I_v = I_{c.g.} + m_f a_v^2 + I_{eff_v} \tag{25}$$

where I_h or I_v are total moments of inertia about the empty tank c.g. in the horizontal or vertical positions, respectively; $I_{c.g.}$ is the moment of inertia of the empty tank; m_f is mass of fuel; a_h and a_v are defined in Fig. 3; and I_{eff_h} or I_{eff_v} are represented by Eq. (23) which is shown in reference 5 to be nearly true for a cylindrical tank.

After initial tipoff the unstable tank will diverge in pitch and tumble, so that it is a reasonable assumption that the actual moment of inertia oscillates harmonically between Eqs. (24) and (25), where for a long tank $I_v > I_h$:

$$I = I_h + (I_v/2)\,(1 + \sin \omega t) \tag{26}$$

From Eqs. (9) and (12), $(\sin \omega t)_{fs}/(\sin \omega t)_m = 1$, and all the full-scale and model inertia terms will be related by $\lambda^5\, \sigma_{fs}/\sigma_m$ as before.

This highly simplified qualitative analysis did not include the effects of wave motion in the fluid, phase effects due to distortion of the fuel volume during violent motion, etc. Yet it clearly implies that the similarity laws derived for solid freely falling bodies [Eqs. (11)] may apply to tanks with liquid as well.

Powered Projectiles

Fin Stabilized Projectiles

Fig. 2 shows that for larger values of V_x/U_0 the error between model and full-scale angle of attack becomes quite large at small scale and $\Omega = 1$. It will therefore be required that angle of attack and yaw similarity be obtained (through velocity simulation) in addition to position similarity.

$$\left.\begin{aligned} &\bar{l}_{fs} = \bar{l}_m \\ &(\psi, \theta, \phi)_{fs} = (\psi, \theta, \phi)_m \\ &\left(\frac{V_x}{U_0}, \frac{V_y}{U_0}, \frac{V_z}{U_0}\right)_{fs} = \left(\frac{V_x}{U_0}, \frac{V_y}{U_0}, \frac{V_z}{U_0}\right)_m \end{aligned}\right\} \tag{27}$$

Since powered projectiles have comparatively large forward acceleration (20 to 50 g or more full-scale) the effect of gravity for the initial part of such a trajectory is negligible, and the g terms of Eqs. (1) can be neglected. The force X now contains a thrust term, T, and aerodynamic coefficients will be based on actual forward velocity, approximated by $U_0 + V_x = U_0(1 + V_x/U_0)$.

Let the scale transformations be

$$\left.\begin{aligned} l_{fs} &= \lambda l_m \\ t_{fs} &= \lambda_6 t_m \\ m_{fs} &= \lambda_7 m_m \\ I_{fs} &= \lambda_8 I_m \\ T_{fs} &= \lambda_9 T_m \end{aligned}\right\} \tag{28}$$

Operating with these transformations on Eqs. (1), as for the bomb case, leads to the following similarity laws for fin-stabilized powered projectiles:

$$\left.\begin{aligned} &l_{fs}/l_m = \lambda \\ &m_{fs}/m_m = \lambda^3(\sigma_{fs}/\sigma_m) \\ &I_{fs}/I_m = \lambda^5(\sigma_{fs}/\sigma_m) \\ &T_{fs}/T_m = \lambda^2[(\rho U_0^2)_{fs}/(\rho U_0^2)_m] \\ &(\sigma_{fs}/\sigma_m)\,(\rho_m/\rho_{fs}) = 1 \end{aligned}\right\} \tag{29}$$

giving [since $t_{fs} = (\lambda/\Omega)t_m$]

$$\left.\begin{aligned} &\frac{\bar{l}_{fs}}{\bar{l}_m} = \frac{(\psi, \theta, \phi)_{fs}}{(\psi, \theta, \phi)_m} = \frac{\left(\frac{V_x}{U_0}, \frac{V_y}{U_0}, \frac{V_z}{U_0}\right)_{fs}}{\left(\frac{V_x}{U_0}, \frac{V_y}{U_0}, \frac{V_z}{U_0}\right)_m} = 1 \\ &\frac{(\omega_x, \omega_y, \omega_z)_{fs}}{(\omega_x, \omega_y, \omega_z)_m} = \frac{\Omega}{\lambda} \\ &\frac{(\dot{V}_x, \dot{V}_y, \dot{V}_z)_{fs}}{(\dot{V}_x, \dot{V}_y, \dot{V}_z)_m} = \frac{\Omega^2}{\lambda} \\ &\frac{(\dot{\omega}_x, \dot{\omega}_y, \dot{\omega}_z)_{fs}}{(\dot{\omega}_x, \dot{\omega}_y, \dot{\omega}_z)_m} = \frac{\Omega^2}{\lambda^2} \end{aligned}\right\} \tag{30}$$

Examining the pitch damping case in a similar manner to that used for bombs yields for the ratio of successive amplitudes in pitch (or yaw)

$$(\theta_2/\theta_1)_{fs}/(\theta_2/\theta_1)_m = 1 \tag{31}$$

Thus, the similarity laws of Eqs. (29) permit motion simulation within the limitations of the present assumptions, including damping effects. It is possible, from Eqs. (29), to reduce thrust to manageable values by reducing the dynamic pressure of the tests (desirable for wind-tunnel testing). However, the last of requirements (29) necessitates a corresponding reduction of model density. This is unlike the case of bombs, where an increase of model density is desirable to avoid unattainably low dynamic pressures for high-altitude simulation.

Spin-Stabilized Projectiles

As for the fin-stabilized projectile, the g terms in Eqs. (1) can be neglected. The major part of the stability comes from the terms $(I_x/I_y)\omega_x\omega_z$ and $(I_x/I_y)\omega_x\omega_y$, where ω_x is given by

$$\omega_x = \dot{\phi} - \omega_z \tan \theta \tag{32}$$

and $\dot{\phi}$ is the spin of the projectile about its axis of symmetry. Now, the similarity criteria for the fin-stabilized projectiles will hold here and the similarity laws and motion similarity of Eqs. (29) and (30) will be true for this case. Thus it will be required, for correct model stability, that

$$\omega_{xfs}/\omega_{xm} = \Omega/\lambda \tag{33}$$

However, the Magnus forces and moments may be large, and, if so, they must also be correctly scaled.

The Magnus forces will be given by

$$\left.\begin{aligned} Z_M &= \rho V_y \Gamma \\ Y_M &= -\rho V_z \Gamma \end{aligned}\right\} \tag{34}$$

and they will act at centers of pressure determined by the projectile geometry. If $\dot{\phi}$ in Eq. (32) is very large, then the term $\omega_z \tan\theta$ can be neglected. Assuming the projectile to be a long right circular cylinder of radius r, and neglecting the end shapes, Eqs. (34) become

$$\left.\begin{aligned} Z_M &= 2\pi\rho V_y r^2 \dot{\phi} \\ Y_M &= -2\pi\rho V_z r^2 \dot{\phi} \end{aligned}\right\} \tag{35}$$

or, in coefficient form,

$$\left.\begin{aligned} C_{Z_M} &= 4\pi(V_y/U_0) r^2\dot{\phi}/U_0[1 + (V_x/U_0)]^2 A \\ C_{Y_M} &= -\left\{4\pi(V_z/U_0) r^2\dot{\phi}/U_0[1 + (V_x/U_0)]^2 A\right\} \end{aligned}\right\} \tag{36}$$

Letting $(C_{Z_M})_{fs} = (C_{Z_M})_m$ and $(C_{Y_M})_{fs} = (C_{Y_M})_m$ leads to the requirements that either $\dot{\phi}_{fs} = \dot{\phi}_m$ or $\Omega = \lambda$.

The first of these requirements is incompatible with Eq. (33), and the second is probably impossible to obtain for any substantially reduced scale unless Mach Number effects are neglected.

Thus it does not appear possible to use models to simulate the motion of spin-stabilized projectiles unless either Mach Number or Magnus force effects can be neglected.

Jet Similarity

It is shown in reference 6 that the angle of spread of a supersonic jet depends on the ratio between average jet and free-stream Mach Numbers, $M_{j_{avg}}/M_{a_{vg}}$. Thus, for geometric similarity of model and full-scale jets, it will be required that

$$\left.\begin{aligned} M_{j_{fs}} &= M_{j_m} \\ A_{j_{fs}} &= \lambda^2 A_{j_m} \end{aligned}\right\} \tag{37}$$

Thrust is given by

$$T = mV_j + A_j(p_j - p_a) = A_j[\rho_j V_j^2 + (p_j - p_a)] \tag{38}$$

and combining the thrust requirement of Eq. (29) with Eq. (37) and $q = (\gamma/2)p_a M^2$,

$$\frac{p_{a_{fs}}}{p_{a_m}} = \frac{p_{j_{fs}}}{p_{j_m}} = \frac{(\rho U_0^2)_{fs}}{(\rho U_0^2)_m} \tag{39}$$

Eqs. (37) and (39) together constitute the conditions for combined jet and thrust (motion) similarity in model testing.

It is implied that $V_{j_{fs}} = V_{j_m}$ and $T_{j_{fs}} = T_{j_m}$, in view of Eqs. (38), (39), and $V_j = M_j\sqrt{\gamma p/\rho}$. Since the model and full-scale jets are geometrically similar and have the same Mach Number, the pressure and temperature distributions in the model jet, with starting values given above, will also be scaled geometrically, and will act on a particular part of the launching aircraft model for a time $t_m = t_{fs}\,\Omega/\lambda$. Further, since from Eqs. (37) and (38)

$$m_{fs}/m_m = (\rho U_0^2)_{fs}/(\rho U_0^2)_m$$

and from Eq. (39) the stream flow past a given model cross-section area will be reduced identically, the ratio of exhaust gas to stream air in any local nondimensional volume near the model will duplicate the full-scale ratio.

It should be noted that the design of a model motor to give the desired thrust may call for a nozzle design and chamber pressure that preclude simultaneous fulfillment of the conditions for thrust and jet similarity.

Concluding Remarks

Motion similarity between model and full-scale stores at full-scale Mach Numbers has been defined and the similarity laws have been formulated for freely falling bodies and fin- or spin-stabilized powered projectiles near a launching aircraft. Certain simulation errors have been examined and evaluated. It has been found that testing models of freely falling bodies at full-scale Mach Numbers will probably lead to errors in damping rate and aerodynamic angles of attack and yaw, which can be kept under 10 per cent in most test situations. Simulation of the motion of powered projectiles without attitude or damping errors is possible if forward acceleration is large with respect to gravity. The motion of spin-stabilized powered projectiles can be simulated only if either Mach Number or Magnus force effects can be neglected.

It has also been found that in addition to motion simulation the jet effects of powered projectiles can be simulated, for study of their effect on the launching aircraft. Qualitative examination of the requirements for reproducing at reduced scale the motion of a tank with fuel after release indicates that the similarity laws derived for a solid free-fall body will apply.

References

[1] Fort, M. K., Jr., *Scale Factors for Model Bomb Tests*, BRL Memorandum Report 387, August, 1945.

[2] Neihouse, A. I., and Pepoon, P. W., *Dynamic Similitude Between a Model and a Full-Scale Body for Model Investigation at full-scale Mach number*, NACA TN 2062, March, 1950.

[3] Hopgood, R. C., *A Proposed Revision of American Standard Letter Symbols for Aeronautical Sciences*, Aeronautical Engineering Review, Vol. 12, No. 1, pp. 41–55, January, 1953.

[4] Luskin, H., and Lapin, E., *An Analytical Approach to the Fuel Sloshing and Buffeting Problems of Aircraft*, Journal of the Aeronautical Sciences, Vol. 19, No. 4, pp. 217–228, April, 1952.

[5] Widmayer, E., Jr., and Reese, J. R., *Moment of Inertia and Damping of Fluid in Tanks Undergoing Pitching Oscillations*, NACA RM L53E01a, June, 1953.

[6] Wilder, J. G., Jr., and Hindersinn, K., *Spreading of Supersonic Jets in Supersonic Streams*, Institute of the Aeronautical Sciences, IAS Preprint No. 421; Presented at the Annual Summer Meeting, IAS, July, 1953.

A Comparison of the Calculated and Observed Flutter Characteristics of a Helicopter Rotor Blade†

LEONARD GOLAND* AND ABRAHAM A. PERLMUTTER**

Princeton University

SUMMARY

The results of a series of rotor blade flutter tests[1] in hovering flight are compared with corresponding values predicted by analysis. The rotor tested possessed nonuniform flexible blades as well as flexibility in the blade pitch-control system. The predicted values are based on a Rayleigh-type analysis quite similar to that developed for fixed-wing flutter predictions with, however, the additional effects due to the rotation of the blades taken into account.

While only a limited amount of experimental data is available, a number of interesting observations are made regarding the accuracy of the theoretical calculations. Considering the nature of the phenomenon and the simplifying assumptions made, the results show that the calculated values compare favorably with the test data. For the rotor tested, the effects of unsteady aerodynamics are found to have a major influence on the flutter speed and frequency.

(1) SYMBOLS

A_1, A_2, etc.	= coefficients of the flapping equation
a	= distance of elastic axis from mid-chord in per cent semichord, positive toward trailing edge
a_0	= two-dimensional lift curve slope, per rad.
B_1, B_2, etc.	= coefficients of the pitching equation
b	= semichord, $= c/2$
c	= chord, ft.
$C(k)$	= $F + iG$, Theodorsen's coefficient
F	= real part of $C(k)$
g	= coefficient of structural damping
G	= imaginary part of $C(k)$
(GJ)	= torsional stiffness, lbs.-ft.^{2}
I_{rr}	= mass moment of inertia about blade flapping axis, slug-ft.^{2}
I_{yy}	= mass moment of inertia about the elastic axis of the blade, slug-ft.^{2} = $\int_{\text{blade}} (y^2 + z^2)dm$
I'_{yy}	= mass moment of inertia about the elastic axis per unit span, slug-ft.
k	= reduced frequency, $\omega b/V$
K_θ	= control stiffness, ft.-lbs./rad.
L'	= lift per unit span, lbs./ft.
M'	= stalling moment per unit span, ft.-lbs./ft.
$m(r)$	= mass per unit span at section r, slug/ft.
Q_β, Q_{θ_t}	= generalized force in flapping and torsion, respectively, ft.-lbs.
Q' , Q'_{θ_t}	= generalized forces per unit span, ft.-lbs./ft.
$Q_{\beta\beta}$, $Q_{\beta\theta}$, etc.	= coefficients of the generalized forces in flapping and torsion
r, y, z	= rotating coordinate system, with origin at center of rotation (see Fig. 1)
R	= radius of the blade, ft.
S_θ	= Southwell coefficient
t	= time, sec.
T	= kinetic energy, ft.-lbs.
U	= potential energy, ft.-lbs.
V	= forward velocity of airfoil, ft./sec.
x_1, y_1, z_1	= fixed coordinate system with origin at the center of rotation (see Fig. 1)
x, x_i	= r/R, r_i/R, nondimensional spanwise distance
y_{cg}	= distance of section center of gravity from the 1/4 chord position, ft.
y_{sc}	= distance of section shear center from the 1/4 chord position, ft.
$\bar{\beta}$	= flapping angle, rad.
$\bar{\theta}$	= pitch angle, rad.
β_0, θ_0	= equilibrium angles, rad.
β, θ	= changes from equilibrium position, rad.
θ_t	= torsional deflection of blade tip, rad.
Φ	= first torsional mode shape
Ω	= angular velocity of the blade, rad./sec.
Ψ	= azimuth angle = Ωt, rad. (see Fig. 1)
ρ	= air density, slugs/ft.^{3}
μ	= $V/\Omega R$, tip-speed ratio
Ω_f	= rotor rotational speed at flutter, rad./sec.
ω_f	= flutter frequency, rad /sec.
ω_{θ_0}	= fundamental torsional frequency of the nonrotating blade, rad./sec.
ω_θ	= fundamental torsional frequency of the rotating blade, rad./sec.
ϵ	= distance between the a.c. and the 1/4 c in per cent chord, positive toward the leading edge

Received June 27, 1956.

† The results presented in this paper were obtained in the course of research sponsored jointly by the Office of Naval Research and the Department of the Army under Contract No. N6 onr-27015.

* Formerly, Chief Project Engineer, James Forrestal Research Center. Now, Director of Research, Kellett Aircraft Corporation.

** Formerly, Research Assistant, James Forrestal Research Center. Now, Senior Aerodynamicist, Kellett Aircraft Corporation.

(2) INTRODUCTION

EXPERIENCE IN THE DESIGN and operation of helicopter rotor blades has indicated a need for a reliable analytical method for the prediction of classical-type rotor blade flutter. Consequently, to aid the designer concerned with this type of instability, a practical method for the prediction of rotor blade flutter is presented herein. The method is based on a Rayleigh-type analysis and is similar to that developed for fixed-wing flutter predictions with, however, certain effects due to the rotation of the blades taken into account. Unsteady aerodynamics is considered and, in fact, is found to have a major influence on the calculated flutter speeds. While this method is based upon a conven-

tional approach, a number of assumptions had to be made due to lack of an adequate aerodynamic theory and to simplify the analysis so as to result in a method that could be effectively used.

Recently, the NACA[1] released the results of a series of flutter tests on a thirteen-ft. diameter, two-bladed helicopter rotor. The rotor, being of practical design, possessed blade pitch-control system flexibility as well as significant blade flexibility. The blades had rather large spanwise variations of mass, inertia, and structural characteristics. To check the accuracy of the analytical method, the predicted flutter characteristics are accordingly compared to those presented in reference 1. In that reference, tests are described at zero initial collective pitch angle for both the hovering and forward flight conditions. The results of the investigation showed, "that the flutter speed of the blades was increased as the blade-pitch-control stiffness was increased and indicated that the structural blade modes of primary significance with respect to flutter were the first torsion mode and the flapping mode. Motion pictures and visual observations of the flutter showed that the motion of the various blade elements during flutter consisted of a combination of translation in the flapping plane and torsion and that a large part of the translation of the blade elements was due to blade flapping. The oscillograph records of the flutter showed that some elastic bending of the blade was also present; however, the structural modes which primarily affected the flutter characteristics of the blade were the first torsional mode and the flapping mode." The method presented herein is restricted to hovering flight. It should be noted, however, that for the blades tested, the effect of forward flight (blades tested up to $\mu = 0.2$) on the flutter speed was small.

The analysis which follows is divided into two major parts. In the first part [Section (3)] it is assumed that (a) the elastic axis coincides with the 25 per cent chord line, (b) structural damping can be neglected, (c) the initial collective pitch angle setting is equal to zero, and (d) the inertia effects of finite blade thickness can be neglected. In the second part [Section (4)] the effects of the above restrictions are analyzed.

(3) Method of Analysis

The forces acting on a rotor blade in operation are of three types: (1) inertia forces, (2) structural restraining forces, and (3) air forces. Although a rigorous solution of the dynamic and structural aspects of the problem is theoretically feasible, it does present certain computational difficulties. As to the air forces, no rotating wing aerodynamic theory of proven accuracy exists at present. Hence, it is apparent that an approximate solution of the subject problem will have to suffice, and, consequently, a number of simplifying assumptions must be made.

It has been shown in the case of fixed-wing analysis that a fair representation of the flutter characteristics can be obtained by considering the motion of the system at flutter to be a superposition of the fundamental bending and torsion modes. In addition, it was shown in the experimental investigation[1] that "the motion of the various blade elements during flutter consisted of a combination of translation in the flapping plane and torsion and that a large part of the translation of the blade elements was due to blade flapping." Consequently, following the fixed-wing approach, the present analysis is confined to two degrees of freedom corresponding to the fundamental bending and the first torsional modes of the blade.

Major emphasis is placed upon a hinged-type rotor blade whose fundamental vertical deflection mode is rigid blade flapping. However, the analysis could be readily adapted to other types of rotor systems. Torsional flexibility is assumed to arise from both the control system and the blade itself. The effects of blade lagging motion and chordwise bending are neglected. The fundamental torsional mode is obtained by use of a standard Holzer analysis[2] which is quite familiar to the vibration analyst.

The problem as considered herein is three-dimensional only to the extent that the spanwise variation of mass, geometry, and blade vibration mode shape is taken into account. The aerodynamic forces and moments are those given by strip theory. Hence, use is made of the two-dimensional potential theory for oscillating thin airfoils.[3] Furthermore, the simplifying assumption is made that Theordorsen's unsteady aerodynamic factor, $C(k)$, which actually varies over the span, can be averaged out if evaluated at a representative blade section. As the 75 per cent spanwise station is found to be representative for most other aerodynamic rotor investigations, it is also adopted herein. It is also assumed that the elastic axis coincides with the 25 per cent chord line and that the initial collective pitch angle is equal to zero degrees.

In deriving the equations governing the motions of the blade, use is made of Lagrange's equations of motion.[4]

(*a*) *Lagrange's Equations of Motion*

As previously discussed, the flutter of an articulated blade may be treated by considering two degrees of freedom—namely, rigid blade flapping,

$$\bar{\beta} = \beta_0 + \beta$$

and blade torsional deflection,

$$\bar{\theta} = \theta_0 + \theta$$

where β_0 and θ_0 are the equilibrium angles and β and θ are small changes from the equilibrium angles. For zero initial collective pitch $\bar{\beta} = \beta$ and $\bar{\theta} = \theta$. θ can be expressed as $\theta_t \Phi(r)$ where θ_t is the blade tip torsional deflection about the elastic axis and $\Phi(r)$ is the normalized first torsional mode shape of the flexible blade with control system flexibility. Choosing β and θ_t as the two generalized coordinates, the equations of motion become

Flapping

$$\frac{d}{dt}\left(\frac{\partial T}{\partial \dot{\beta}}\right) - (\partial T/\partial \beta) + (\partial U/\partial \beta) = Q_\beta \qquad (1)$$

Pitching

$$\frac{d}{dt}\left(\frac{\partial T}{\partial \dot{\theta}_t}\right) - (\partial T/\partial \theta_t) + (\partial U/\partial \theta_t) = Q_{\theta t} \qquad (2)$$

where T is the kinetic energy of the system, U is the potential energy of the system, and Q_β and $Q_{\theta t}$ are the generalized forces.

(b) *Kinetic Energy Terms of the Lagrange Equations*

In the derivation of the kinetic energy terms, two sets of coordinates are used, as shown in Fig. 1.

A fixed coordinate system, x_1, y_1, z_1, is defined with the origin at the rotor center of rotation. The x_1 y_1-plane is perpendicular to the shaft and the z_1-axis is along the shaft, positive upward. The azimuth position of the blade is given by the angle Ψ and is measured from the x_1-axis in a counterclockwise direction.

A rotating coordinate system r, y, and z is chosen for each blade element with the origin at the rotor center of rotation. The r-axis points in the spanwise direction of the blade and passes through the 25 per cent chord position of the element. The y-axis lies along the chord of the element, positive toward the leading edge, and the z-axis, perpendicular to the ry-plane, is positive when pointing upward.

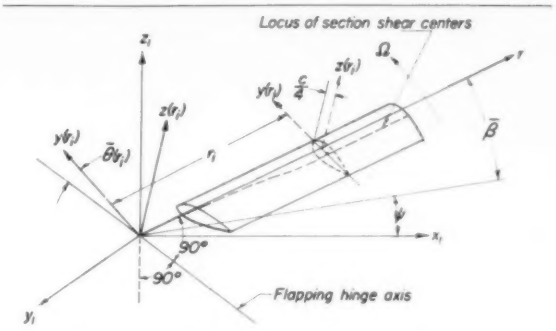

FIG. 1. The coordinates of a blade element at section r_1.

The coordinates x_1, y_1, z_1 of a point on the blade may be developed as functions of r, y, z and the angular deflections of the blade in pitch, flapping, and azimuth position, θ, β, and Ψ, respectively.

$$\left.\begin{aligned} x_1 &= (r\cos\beta - z\cos\theta\sin\beta - y\sin\theta\sin\beta)\cos\Psi - (y\cos\theta - z\sin\theta)\sin\Psi \\ y_1 &= (r\cos\beta - z\cos\theta\sin\beta - y\sin\theta\sin\beta)\sin\Psi + (y\cos\theta - z\sin\theta)\cos\Psi \\ z_1 &= z\cos\theta\cos\beta + y\sin\theta\cos\beta + r\sin\beta \end{aligned}\right\} \qquad (3)$$

The kinetic energy of the blade is, therefore, given by

$$\begin{aligned} T &= (1/2)\int_{\text{blade}} (\dot{x}_1^2 + \dot{y}_1^2 + \dot{z}_1^2)dm \\ &= (1/2)\int_{\text{blade}} [\{r^2 + z^2\cos^2(\theta_t\Phi) + y^2\sin^2(\theta_t\Phi) + yz\sin(2\theta_t\Phi)\}\dot{\beta}^2 + \{(z^2+y^2)\Phi^2\}\dot{\theta}_t^2 + \\ &\quad \{-rz\,\Phi\sin(\theta_t\Phi) + ry\,\Phi\cos(\theta_t\Phi)\}2\dot{\beta}\dot{\theta}_t - \{-yz\cos\beta\cos(2\theta_t\Phi) + (1/2)(z^2-y^2)\sin(2\theta_t\Phi)\times \\ &\quad \cos\beta - ry\sin\beta\cos(\theta_t\Phi) + rz\sin\beta\sin(\theta_t\Phi)\}2\Omega\dot{\beta} - \{-(y^2+z^2)\Phi\sin\beta + ry\Phi\cos\beta\sin(\theta_t\Phi) + \\ &\quad rz\Phi\cos\beta\cos(\theta_t\Phi)\}2\Omega\dot{\theta}_t + \{r^2\cos^2\beta + y^2\cos^2(\theta_t\Phi) + z^2\sin^2(\theta_t\Phi) + y^2\sin^2\beta\sin^2(\theta_t\Phi) + \\ &\quad z^2\sin^2\beta\cos^2(\theta_t\Phi) - rz\sin(2\beta)\cos(\theta_t\Phi) - ry\sin(2\beta)\sin(\theta_t\Phi) - yz\cos^2\beta\sin(2\theta_t\Phi)\}\Omega^2]dm \end{aligned} \qquad (4)$$

where dm is a mass particle and the integral is evaluated over the whole blade. $(\dot{})$ denotes differentiation with respect to time.

Since in the prediction of flutter the sole attempt is to specify one or more conditions of instability, only small oscillations about the position of equilibrium need be considered. Thus, angular deflections β and θ_t are considered small, and, hence, any products of these deflections are negligible. Further simplifications may be obtained by neglecting relatively small terms. The resulting expressions are

$$\frac{d}{dt}(\partial T/\partial\dot{\beta}) - (\partial T/\partial\beta) = \int_{\text{blade}} (r^2\ddot{\beta} + ry\Phi\ddot{\theta}_t + r^2\Omega^2\beta + ry\Omega^2\Phi\theta_t)dm \qquad (5a)$$

$$\frac{d}{dt}(\partial T/\partial\dot{\theta}_t) - (\partial T/\partial\theta_t) = \int_{\text{blade}} \{(y^2+z^2)\Phi^2\ddot{\theta}_t + ry\Phi\ddot{\beta} + \Omega^2(y^2-z^2)\Phi^2\theta_t + \Omega^2 ry\Phi\beta\}dm \qquad (5b)$$

(c) *The Potential Energy of the Blade*

The potential energy of the rotating blade can be considered as a superposition of nonrotational and rotational effects.

The potential energy stored in the nonrotating blade, when the blade is deflected, is the strain energy of torsion of the blade and control system. This strain energy may be written as

$$U = (1/2)\int_0^R GJ(r)\left\{\frac{\partial}{\partial r}[\theta_t\Phi(r)]\right\}^2 dr + (1/2)K_\theta[\theta_t\Phi(0)]^2 \qquad (6)$$

The above expression for potential energy contains quantities which generally are not easily calculable. However, this potential energy may be related to the torsional frequency since

$$(1/2)\theta_t^2\omega_{\theta_0}^2\int_0^R I'_{yy}(r)[\Phi(r)]^2dr = (1/2)\theta_t^2\left\{\int_0^R GJ(r)\left[\frac{\partial}{\partial r}\Phi(r)\right]^2dr + K_\theta[\Phi(0)]^2\right\} \tag{7}$$

where $I_{yy}(r)$ is the mass moment of inertia about the elastic axis of a blade section at spanwise station r, and, therefore,

$$U = (1/2)\omega_{\theta_0}^2\left[\int_0^R I'_{yy}(r)\{\Phi(r)\}^2dr\right]\theta_t^2 \tag{8}$$

The rotational effects on the potential energy of the blade are introduced due to the action of the centrifugal force field. Similar to the above, the total potential energy of the rotating blade can be written as

$$U = (1/2)\omega_\theta^2\left[\int_0^R I'_{yy}(r)\{\Phi(r)\}^2dr\right]\theta_t^2 \tag{9}$$

where ω_θ is the rotational frequency of the first torsional mode. ω_θ^2 can be written as[1]

$$\omega_\theta^2 = \omega_{\theta_0}^2 + S_\theta\Omega^2 \tag{10}$$

where S_θ is commonly referred to as the Southwell coefficient. Hence S_θ determines the contribution due to rotation and is a function of the chordwise and axial components of the centrifugal force as well as of the manner in which the blade is mounted on the hub.

The contribution of the chordwise component of the centrifugal force to S_θ is approximately equal to 1 and has already been accounted for by the kinetic energy terms, as shown by the third term on the right-hand side of Eq. (5b). The axial component of the centrifugal force contributes to S_θ because of its tendency to straighten the fibers of the deflected blade. Reference 1 discusses the effect and evaluates this contribution as 0.17 for the blades tested. The contribution to S_θ due to the manner in which the blade is mounted on the hub is essentially zero if thrust bearings are used. However, the blades for which experimental data were obtained were attached to the hub by means of blade-retention straps and, therefore, significantly contributed to S_θ. The total Southwell coefficient including the effects of this particular type of attachment is presented in reference 1 as a function of ω_{θ_0}.

(d) *Generalized Forces*

The generalized forces may be obtained by use of two-dimensional potential flow theory. The expression for the lift of an airfoil oscillating in bending and torsion can be written as[3]

$$L' = a_0\rho Vb C(k)\{V\theta - \dot z + b[(1/2) - a]\dot\theta\} + \pi\rho b^2[V\dot\theta - \ddot z - ba\ddot\theta] \tag{11}$$

In this expression $C(k)$ is a complex function (equal to $F + iG$, where F and G are real) whose real and imaginary parts are functions of the reduced frequency, $k = \omega b/V$, where ω is the frequency of oscillation. The last two terms, which are independent of forward velocity V and dependent on accelerations $\ddot z$ and $\ddot\theta$, are the so-called "apparent mass" terms and account for the effective inertia of the air surrounding the airfoil.

Similarly, the stalling moment about the shear center is

$$M' = a_0\rho Vb^2[a + (1/2)]C(k)\{V\theta - \dot z + b[(1/2) - a]\dot\theta\} - \pi\rho b^2\{[(1/2) - a]Vb\dot\theta + b^2[(1/8) + a^2]\ddot\theta + ba\ddot z\} \tag{12}$$

where the last two terms dependent on $\ddot\theta$ and $\ddot z$ are the "apparent mass" contributions. The oscillatory aerodynamic lift and moment expressions per unit span can be obtained from Eqs. (11) and (12) by replacing θ by $\theta_t\Phi$ and z by $r\beta$. Thus,

$$L' = a_0\rho VbC(k)\{V\Phi\theta_t - r\dot\beta + b[(1/2) - a]\Phi\dot\theta_t\} + \pi\rho b^2[V\Phi\dot\theta_t - r\ddot\beta - ba\Phi\ddot\theta_t] \tag{13}$$

$$M' = a_0\rho Vb^2[a + (1/2)]C(k)\{V\Phi\theta_t - r\dot\beta + b[(1/2) - a]\Phi\dot\theta_t\} - \pi\rho b^2\{[(1/2) - a]Vb\Phi\dot\theta_t + b^2[(1/8) + a^2]\Phi\ddot\theta_t + bar\ddot\beta\} \tag{14}$$

The generalized force in the θ degree of freedom, Q'_{θ_t}, is determined from the work done by the air forces, δW, in displacing the structure by a virtual displacement $\delta\theta$, all other degrees of freedom being held constant during the displacement. Thus,

$$\delta W = M'\Phi(r)\delta\theta_t \tag{15}$$

so that

$$Q'_{\theta_t} = \delta W/\delta\theta_t = M'\Phi(r) \tag{16}$$

similarly,

$$Q'_\beta = \delta W/\delta\beta = L'r \tag{17}$$

Now, since $V = \Omega r$,

$$Q'_\beta = a_0\rho\Omega bC(k)\{\Omega r^3\Phi(r)\theta_t - r^3\dot\beta + b[(1/2) - a]\Phi(r)r^2\dot\theta_t\} + \pi\rho b^2[\Omega r^2\Phi(r)\dot\theta_t - r^2\ddot\beta - ba\Phi(r)r\ddot\theta_t] \tag{18}$$

Letting $c = 2b$, $C(k) = F + iG$, integrating over the blade span, and letting the resultant coefficient of β be designated by $Q_{\beta\beta}$, the coefficient of $\dot\beta$ by $Q_{\beta\dot\beta}$, etc., there results

$$\left.\begin{aligned}
Q_{\beta\beta} &= 0\\
Q_{\beta\dot\beta} &= -(1/8)a_0\rho\Omega cR^4(F + iG)\\
Q_{\beta\ddot\beta} &= -(1/12)\pi\rho c^2R^3\\
Q_{\beta\theta_t} &= (1/2)a_0\rho\Omega^2c(F + iG)\int_0^R r^3\Phi(r)dr\\
Q_{\beta\dot\theta_t} &= (1/4)a_0\rho\Omega c^2[(1/2) - a](F + iG)\times\int_0^R r^2\Phi(r)dr + (1/4)\pi\rho c^2\Omega\int_0^R r^2\Phi(r)dr\\
Q_{\beta\ddot\theta_t} &= -(1/8)\pi\rho c^3a\int_0^R r\Phi(r)dr
\end{aligned}\right\} \tag{19}$$

Similarly,

$$Q'_{\theta_t} = a_0\rho\Omega b^2[a + (1/2)]C(k)\{\Omega r^2\Phi^2(r)\theta_t - r^2\Phi(r)\dot{\beta} + b[(1/2) - a]r\Phi^2(r)\dot{\theta}_t\} - \pi\rho b^2\{[(1/2) - a]\Omega br\Phi^2(r)\dot{\theta}_t + b^2[(1/8) + a^2]\Phi^2(r)\ddot{\theta}_t + bar\Phi(r)\ddot{\beta}\} \quad (20)$$

and

$$\left.\begin{aligned}
Q_{\theta_t\beta} &= 0 \\
Q_{\theta_t\dot{\beta}} &= -(1/4)a_0\rho\Omega c^2[a + (1/2)](F + iG)\int_0^R r^2\Phi(r)dr \\
Q_{\theta_t\ddot{\beta}} &= -(1/8)\pi\rho c^2 a\int_0^R r\Phi(r)dr \\
Q_{\theta_t\theta_t} &= (1/4)a_0\rho\Omega^2 c^2[a + (1/2)](F + iG)\int_0^R r^2\Phi^2(r)dr \\
Q_{\theta_t\dot{\theta}_t} &= (1/8)a_0\rho\Omega c^3[a + (1/2)](F + iG)[(1/2) - a]\int_0^R r\Phi^2(r)dr - (1/8)\pi\rho c^3\Omega[(1/2) - a]\int_0^R r\Phi^2(r)dr \\
Q_{\theta_t\ddot{\theta}_t} &= -(1/16)\pi\rho c^4[(1/8) + a^2]\int_0^R \Phi^2(r)dr
\end{aligned}\right\} \quad (21)$$

(e) *Flutter Equations*

Using the previously presented results, the equations of motion for the two degree of freedom system under discussion can be written as

flapping equation

$$A_1\beta + A_2\theta_t + A_3\dot{\beta} + A_4\dot{\theta}_t + A_5\ddot{\beta} + A_6\ddot{\theta}_t = 0 \quad (22)$$

pitching equation

$$B_1\beta + B_2\theta_t + B_3\dot{\beta} + B_4\dot{\theta}_t + B_5\ddot{\beta} + B_6\ddot{\theta}_t = 0 \quad (23)$$

where

$$\begin{aligned}
A_1 &= \Omega^2 I_{rr} \\
A_2 &= \Omega^2\int_0^R mry_{cg}\Phi dr - (1/2)a_0\Omega^2\rho c R^4(F + iG)\int_0^R x^3\Phi(x)dx \\
A_3 &= (1/8)a_0\rho c\Omega R^4(F + iG) \\
A_4 &= -(1/4)[(1/2) - a]a_0\rho c^2\Omega R^3(F + iG)\int_0^1 x^2\Phi(x)dx - (1/4)\pi\rho c^2\Omega R^3\int_0^1 x^2\Phi(x)dx \\
A_5 &= I_{rr} + (1/12)\pi\rho c^2 R^3 \\
A_6 &= \int_0^R mry_{cg}\Phi(r)dr + (1/8)a\pi\rho c^3 R^2\int_0^1 x\Phi(x)dx
\end{aligned}$$

and where

$$\begin{aligned}
B_1 &= \Omega^2\int_0^R mry_{cg}\Phi(r)dr \\
B_2 &= (\omega_{\theta_0}^2 + S_\theta\Omega^2)\int_0^R I'_{yy}\Phi^2(r)dr - (1/4)[a + (1/2)]a_0\rho c^2\Omega^2 R^3(F + iG)\int_0^1 x^2\Phi^2(x)dx \\
B_3 &= (1/4)[a + (1/2)]a_0\rho c^2\Omega R^3(F + iG)\int_0^1 x^2\Phi(x)dx \\
B_4 &= -(1/8)[(1/4) - a^2]a_0\rho c^3\Omega R^2(F + iG)\int_0^1 x\Phi^2(x)dx + (1/8)\pi\rho c^3\Omega R^2[(1/2) - a]\int_0^1 x\Phi^2(x)dx \\
B_5 &= \int_0^R mry_{cg}\Phi(r)dr + (1/8)\pi\rho c^3 aR^2\int_0^1 x\Phi(x)dx \\
B_6 &= \int_0^R I'_{yy}\Phi^2(r)dr + (1/16)\pi\rho c^4 R[(1/8) + a^2]\int_0^1 \Phi^2(x)dx
\end{aligned}$$

In the above, m is the mass per unit span, y_{cg} is the chordwise distance between the section center of gravity and the elastic axis, and $x = r/R$.

The aerodynamic terms in the above coefficients are, as previously stated, derived by use of thin airfoil potential theory which stipulates that the a.c. be located at the 1/4 chord. With the finite thickness of the airfoil taken into account, the a.c. may not be located exactly at the 1/4 chord. This effect may be approximately evaluated by modifying the coefficients B_2, B_3, and B_4 to account for the resulting aerodynamic moments about the 25 per cent c as follows:

$$B_2 = (\omega_{\theta_0}^2 + S_\theta\Omega^2)\int_0^R I'_{yy}\Phi^2(r)dr - (1/4)[a + (1/2)]a_0\rho c^2\Omega^2R^3(F + iG)\int_0^1 x^2\Phi^2(x)dx - (1/2)\epsilon a_0\rho c^2\Omega^2R^3\int_0^1 x^2\Phi^2(x)dx$$

$$B_3 = (1/4)[a + (1/2)]a_0\rho c^2\Omega R^3(F + iG)\int_0^1 x^2\Phi(x)dx + (1/2)\epsilon a_0\rho c^2\Omega R^3\int_0^1 x^2\Phi(x)dx$$

$$B_4 = -(1/8)[(1/4) - a^2]a_0\rho c^3\Omega R^2(F + iG)\int_0^1 x\Phi^2(x)dx - (1/4)\epsilon[(1/2) - a]a_0\rho c^3\Omega R^2\int_0^1 x\Phi^2(x)dx + (1/8)\pi\rho c^3\Omega R^2[(1/2) - a]\int_0^1 x\Phi^2(x)dx$$

where ϵ is the distance in per cent chord from the 1/4 chord line to the a.c., positive toward the leading edge.

The method used for solving the equations for the flutter speed and frequency is presented in the Appendix and is similar to that used in previous papers.[3, 5]

(4) Effects of Initial Pitch Angles, Finite Blade Thickness, Shear Center Variation, and Structural Damping

(a) Influence of Initial Pitch Angle Settings and Inertia Effect of Finite Blade Thickness

To examine the effects of an initial pitch angle setting and finite blade thickness a similar approach can be used as in the previous analysis. As before, angular deflections are defined by rigid blade flapping,

$$\bar{\beta} = \beta_0 + \beta$$

and blade torsional deflection,

$$\bar{\theta} = \theta_0 + \theta$$

The significant terms containing the initial angles, β_0 and θ_0, and the blade thickness coordinate, z, are retained. Using the development and the notation of Section (3), the flutter coefficients are obtained as

$$A_1 = \Omega^2 I_{rr}$$

$$A_2 = \Omega^2\int_0^R mry_{cg}\Phi(r)dr - (1/2)a_0\rho c\Omega^2R^4(F + iG)\int_0^1 x^3\Phi(x)dx$$

$$A_3 = (1/8)a_0\rho c\Omega R^4(F + iG)$$

$$A_4 = -2\Omega\int_{\text{blade}}\Phi(z^2 + \theta_0\beta_0ry)dm - (1/4)a_0\rho c^2\Omega R^3(F + iG)[(1/2) - a]\int_0^1 x^2\Phi dx - (1/4)\pi\rho c^2\Omega R^3\int_0^1 x^2\Phi dx$$

$$A_5 = I_{rr} + (1/12)\pi\rho c^2R^3$$

$$A_6 = \int_0^R mry_{cg}\Phi dr + (1/8)\pi\rho c^3R^2a\int_0^1 x\Phi dx$$

$$B_1 = \Omega^2\int_0^R mry_{cg}\Phi dr$$

$$B_2 = (\omega_{\theta_0}^2 + S_\theta\Omega^2)\int_{\text{blade}}(y^2 + z^2)\Phi^2dm - \Omega^2\int_{\text{blade}}(2z^2 + \theta_0\beta_0ry)\Phi^2dm - (1/4)a_0\rho c^2\Omega^2R^3(F + iG)[a + (1/2)]\int_0^1 x^2\Phi^2dx$$

$$B_3 = 2\Omega\int_{\text{blade}}(z^2 + ry\theta_0\beta_0)\Phi dm + (1/2)\rho a_0c^2\Omega R^3(F + iG)[a + (1/2)]\int_0^1 x^2\Phi dx$$

$$B_4 = -(1/8)\rho a_0c^3\Omega R^2(F + iG)[(1/4) - a^2]\int_0^1 x\Phi^2dx + (1/8)\pi\rho c^3\Omega R^2[(1/2) - a]\int_0^1 x\Phi^2dx$$

$$B_5 = \int_0^R mry_{cg}\Phi dr + (1/8)\pi\rho c^3R^2a\int_0^1 x\Phi dx$$

$$B_6 = \int_{\text{blade}}(y^2 + z^2)\Phi^2dm + (1/16)\pi\rho c^4R[(1/8) + a^2]\int_0^1\Phi^2dx$$

The relationship between θ_0 and β_0 is obtained using the standard equations for hovering flight.[6] The resulting expression is

$$\beta_0 = \frac{(1/2)a_0\rho cR^3}{I_{rr}}\left[\frac{R\theta_0}{4} - \frac{1}{3}\left\{-\frac{a_0c}{8\pi} + \sqrt{\left(\frac{a_0c}{8\pi}\right)^2 + \frac{a_0cR\theta_0}{6\pi}}\right\}\right] \quad (24)$$

(b) Effect of a Spanwise Variation of the Location of the Section Shear Center

The effect of a shear center variation is treated in a previous paper.[7] Briefly, the technique is as follows. Assume that a mass particle of the blade is located at a spanwise section r and a distance y from the location of the 1/4 chord and that the tip of the blade twists

through angle θ_t. Hence, section r will have twisted through an angle $\Phi(r)\theta_t$ with respect to the flapping-hinge axis (see Fig. 1). If the location of the section shear center is constant along the blade, the particle will have described an arc $y\Phi(r)\theta_t$. However, if the chordwise location of the section shear center varies along the span, each section will revolve about a different point, and the arc described by the mass particle will no longer be $y\Phi(r)\theta_t$. In effect, the motion of the mass particle can be considered as a superposition of the relative motions of all blade elements from the root to section r. As the root of the blade twists through an angle $\Phi(0)\theta_t$ all outboard blade elements can be considered to move with the root section as a rigid blade, and, hence, the particle in question will have rotated through an arc $\{y(r) - y_{sc}(0)\}\Phi(0)\theta_t$, where y_{sc} is the chordwise distance between the section shear center and the 1/4 chord position. The blade element at r_1, immediately outboard of the root section, will move through an angle $\Delta\Phi(r_1)\theta_t = \{\Phi(r_1) - \Phi(0)\}\theta_t$ relative to the root about its shear center, and again the rest of the blade is considered to move with the r_1 element as a rigid blade. The contribution of this rotation to the motion of the mass particle will be $\{y(r) - y_{sc}(r_1)\}$ $\Delta\Phi(r_1)\theta_t$. This process continues and each blade element up to the r section will contribute to the motion of the particle (see Fig. 2). The total motion of the particle can thus be written as

$$\left[\{y(r) - y_{sc}(0)\}\Phi(0) + \int_0^r \{y(r) - y_{sc}(r_i)\}\frac{d\Phi(r_i)}{dr_i}\,dr_i\right]\theta_t \quad (25)$$

Letting $$y_{sc}(r_i) = -(c/2)[(1/2) + a]_{r_i} \quad (26)$$

$$x = r/R \quad \text{and} \quad x_t = r_t/R$$

where a is the chordwise distance in per cent semichord between the shear center and the semichord position, positive when aft of the semichord position, expression (25) may be written as

$$\left[\left\{y(x) + \frac{c}{2}\left(\frac{1}{2} + a\right)_0\right\}\Phi(0) + \int_0^x \left\{y(x) + \frac{c}{2}\left(\frac{1}{2} + a\right)_{x_i}\right\}\frac{d\Phi(x_i)}{dx_i}\,dx_i\right]\theta_t \quad (27)$$

The flutter equations are then obtained through a summation of "generalized forces." A generalized force is defined here as the derivative—with respect to a virtual displacement of the blade tip—of the energy expended due to the virtual displacement. These generalized forces are obtained by proper determination of velocities, the points of application of the acting forces, and the distances traveled by these forces when the blade is deflected. As an illustration, the derivation of one of the pertinent terms—the inertia part of the generalized flapping force due to pitch—is given below.

Due to a tip deflection, θ_t, the centrifugal force of a blade element, $mr\Omega^2 dr$, will act with a moment arm equal to the distance between the flapping hinge axis and the plane perpendicular to the shaft containing the section center of gravity of the element. Using expres-

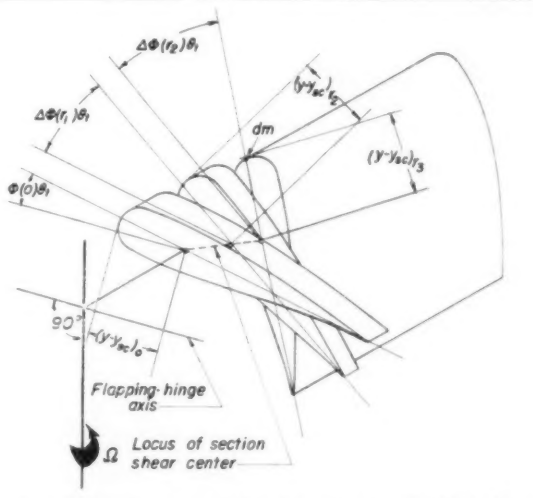

FIG. 2. Motion of a mass particle due to torsion of a blade having spanwise variation of the section shear center location

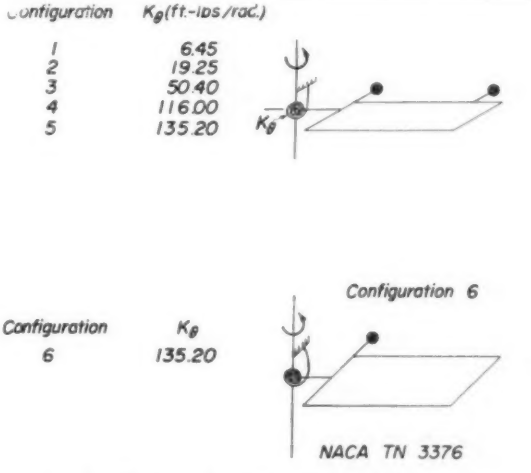

FIG. 3. Blade configurations used in this report.

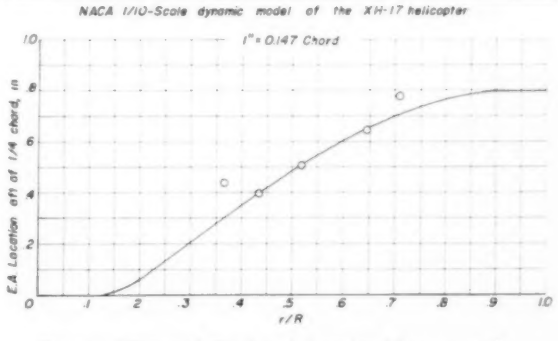

FIG. 4. Measured elastic axis location (shear center).

sion (27), the moment produced is

$$mr\Omega^2 dr\left[\left\{y_{c_g}(x)+\frac{c}{2}\left(\frac{1}{2}+a\right)_0\right\}\Phi(0)+\int_0^x\left\{y_{c_g}(x)+\frac{c}{2}\left(\frac{1}{2}+a\right)_{x_i}\right\}\frac{d\Phi}{dx_i}dx_i\right]\theta_t \quad (28)$$

The energy expended by this moment due to a virtual tip deflection $\delta\beta$ is, therefore,

$$mr\Omega^2 dr\cdot(\text{moment arm})\cdot\delta\beta \quad (29)$$

Integrating over the whole span and differentiating with respect to $\delta\beta$, the generalized flapping force due to pitch is

$$\theta_t\Omega^2R^2\int_0^1 m(x)x\left[\left\{y_{c_g}(x)+\frac{c}{2}\left(\frac{1}{2}+a\right)_0\right\}\Phi(0)+\int_0^x\left\{y_{c_g}(x)+\frac{c}{2}\left(\frac{1}{2}+a\right)_{x_i}\right\}\frac{d\Phi}{dx_i}dx_i\right]dx \quad (30)$$

Using the same technique, the coefficients of the flutter equations are as follows:

$$A_1 = \Omega^2 I_{rr}$$

$$A_2 = \Omega^2R^2\int_0^1 m(x)x\left[\left\{y_{c_g}(x)+\frac{c}{2}\left(\frac{1}{2}+a\right)_0\right\}\Phi(0)+\int_0^x\left\{y_{c_g}(x)+\frac{c}{2}\left(\frac{1}{2}+a\right)_{x_i}\right\}\frac{d\Phi}{dx_i}dx_i\right]dx - (F+iG)\frac{1}{2}a_0\rho c\Omega^2R^4\int_0^1 x^3\Phi dx$$

$$A_3 = \frac{1}{8}(F+iG)a_0\rho c\Omega R^4$$

$$A_4 = -\frac{1}{4}(F+iG)a_0\rho c^2\Omega R^3\left[\left(\frac{1}{2}-a\right)_0\frac{\Phi(0)}{3}+\int_0^1 x^2\left\{\int_0^x\left(\frac{1}{2}-a\right)_{x_i}\frac{d\Phi}{dx_i}dx_i\right\}dx\right]-\frac{1}{4}\pi\rho c^2\Omega R^2\int_0^1 x^2\Phi dx$$

$$A_5 = I_{rr}+\frac{\pi}{12}\rho c^2R^3$$

$$A_6 = R^2\int_0^1 m(x)x\left[\left\{y_{c_g}(x)+\frac{c}{2}\left(\frac{1}{2}+a\right)_0\right\}\Phi(0)+\int_0^x\left\{y_{c_g}(x)+\frac{c}{2}\left(\frac{1}{2}+a\right)_{x_i}\right\}\frac{d\Phi}{dx_i}dx_i\right]dx + \frac{1}{8}\pi\rho c^3R^2\left[\frac{a(0)}{2}\Phi(0)+\int_0^1 x\left\{\int_0^x a(x_i)\frac{d\Phi}{dx_i}dx_i\right\}dx\right]$$

$$B_1 = \Omega^2R^2\int_0^1 m(x)x\left[\left\{y_{c_g}(x)+\frac{c}{2}\left(\frac{1}{2}+a\right)_0\right\}\Phi(0)+\int_0^x\left\{y_{c_g}(x)+\frac{c}{2}\left(\frac{1}{2}+a\right)_{x_i}\right\}\frac{d\Phi}{dx_i}dx_i\right]dx$$

$$B_2 = (\omega_{\theta_0}^2+S_\theta\Omega^2)\int_0^R I'_{\nu\nu}\Phi^2dr-\frac{1}{4}(F+iG)a_0\rho c^2\Omega^2R^3\left[\int_0^1 x^2\Phi\left\{\left(\frac{1}{2}+a\right)_0\Phi(0)+\int_0^x\left(\frac{1}{2}+a\right)_{x_i}\frac{d\Phi}{dx_i}dx_i\right\}dx\right]$$

$$B_3 = \frac{1}{4}(F+iG)a_0\rho c^2\Omega R^3\int_0^1 x^2\left\{\left(\frac{1}{2}+a\right)_0\Phi(0)+\int_0^x\left(\frac{1}{2}+a\right)_{x_i}\frac{d\Phi}{dx_i}dx_i\right\}dx$$

$$B_4 = -\frac{1}{8}(F+iG)a_0\rho c^3\Omega R^2\int_0^1 x\left[\left(\frac{1}{2}-a\right)_0\Phi(0)+\int_0^x\left(\frac{1}{2}-a\right)_{x_i}\frac{d\Phi}{dx_i}dx_i\right]\left[\left(\frac{1}{2}+a\right)_0\Phi(0)+\int_0^x\left(\frac{1}{2}+a\right)_{x_i}\frac{d\Phi}{dx_i}dx_i\right]dx+\frac{1}{8}\pi\rho c^3\Omega R^2\int_0^1 x\Phi\left\{\left(\frac{1}{2}-a\right)_0\Phi(0)+\int_0^x\left(\frac{1}{2}-a\right)_{x_i}\frac{d\Phi}{dx_i}dx_i\right\}dx$$

$$B_5 = R^2\int_0^1 m(x)x\left[\left\{y_{c_g}(x)+\frac{c}{2}\left(\frac{1}{2}+a\right)_0\right\}\Phi(0)+\int_0^x\left\{y_{c_g}(x)+\frac{c}{2}\left(\frac{1}{2}+a\right)_{x_i}\right\}\frac{d\Phi}{dx_i}dx_i\right]dx + \frac{1}{8}\pi\rho c^3R^2\int_0^1 x\left\{a(0)\Phi(0)+\int_0^x a(x_i)\frac{d\Phi}{dx_i}dx_i\right\}dx$$

$$B_6 = \int_0^R I'_{\nu\nu}\Phi^2dr+\frac{1}{16}\pi\rho c^4R\left[\int_0^1\frac{\Phi^2}{8}dx+\int_0^1\left\{a(0)\Phi(0)+\int_0^x a(x_i)\frac{d\Phi}{dx_i}dx_i\right\}^2dx\right]$$

(c) *Structural Damping*

As is quite common, structural damping can be introduced as a function of the flexibility of the blade and control system—but leading the flexibility term by 90 degrees.[2] Hence, the structural damping in torsion is

$$\left\{ig\omega_{\theta_0}^2\int_0^R I'_{\nu\nu}\Phi^2(r)dr\right\}\theta_t \quad (31)$$

where g is of the order of 0.02 to 0.08.

(5) Correlation With Experimental Data and Conclusion

As previously stated, an experimental flutter study of a 1/10 scale dynamic model of the XH-17 two-blade jet-driven helicopter rotor is described in reference 1. The rotor had a diameter of 13 ft. and a solidity of 0.055. The blades were of rectangular plan form, untwisted, and had a chord of 6.8 in. The airfoil was an NACA 23018. Spanwise variations of mass, inertia, and stiffness characteristics are shown in Figs. 2 to 5 of the above reference. The blades were attached to the hub by means of blade-retention straps. Six blade configurations were tested. The configurations differed in control stiffness and/or the attachment of counter weights and are shown in Fig. 3. The spanwise variation of the chordwise location of the section shear center is shown in Fig. 4.

In Table 1 the experimental values of Ω_f and ω_f/Ω_f for the six blade configurations are compared with those obtained by means of the theory of Section (3), using a lift curve slope of 6/rad. In addition, the values of the Southwell coefficient, S_θ, and the torsional frequency, ω_{θ_0}, are indicated.

The effect of control system stiffness on the rotor flutter speed Ω_f is demonstrated by configurations 1 thru 5. It is noted that, as the stiffness is increased, the flutter speed increases. While the calculated values are in agreement with this fact, the theory tends to exaggerate the effect. In the case of a very flexible control system (configuration 1), the theoretical value is in error in a conservative sense. However, as the control system stiffness is increased and blade flexibility becomes more significant (configurations 2 through 5), the error becomes nonconservative. The calculated value of the frequency ratio ω_f/Ω_f is, however, in general agreement throughout. It should be noted that in the theory presented herein, the flutter speed is directly proportional to the nonrotating torsional frequency, ω_{θ_0}.

The effect of mass distribution of the blades is demonstrated by configurations 5 and 6, in which the control stiffness was held constant at 135.2 ft.-lbs./rad. Configuration 6 was essentially the same as configuration 5 with the outboard counterweight (forward of the elastic axis) removed. As would be expected, the flutter speed is reduced by removal of the counterweight, but again the theory tends to exaggerate this effect.

The effects of unsteady aerodynamics, the effective slope of the lift curve of the blade, and the location of

TABLE 1
Experimental and Calculated Values of Ω_f and ω_f/Ω_f

Configuration	S_θ	$\omega_{\theta_0}^2$	Calculated		Experimental	
			Ω_f(rad./sec.)	ω_f/Ω_f	Ω_f(rad./sec.)	ω_f/Ω_f
1	4.71	1,250	27.1	1.95	32–35	1.70–1.72
2	4.32	3,120	33.7	1.99	32–36	1.84–1.97
3	3.51	7,420	40.5	2.02	35–37	2.02–2.06
4	2.50	13,400	45.2	2.03	39–40	1.94–2.02
5	2.28	14,800	46.8	2.01	41–42	2.02–2.09
6	2.00	17,200	36.5	2.37	38–40	2.10–2.22

TABLE 2
Effects of a_0, ϵ, and $C(k)$ on Ω_f and ω_f/Ω_f

Configuration	a_0	ϵ	Aerodynamic Theory	Ω_f (rad./sec.)	ω_f/Ω_f
1 experimental	...	...	.....	32–35	1.70–1.72
calculated	6.0	0	quasi-steady	16.1	2.59
"	6.0	0	unsteady	27.1	1.95
"	5.7	0	unsteady	30.9	1.87
2 experimental	...	...	.....	32–36	1.84–1.97
calculated	6.0	0	quasi-steady	22.6	2.67
"	6.0	0	unsteady	33.7	1.99
"	5.7	0	unsteady	36.5	1.92
3 experimental	...	...	.....	35–37	2.02–2.06
calculated	6.0	0	quasi-steady	29.9	2.75
"	6.0	0	unsteady	40.5	2.02
"	5.7	0	unsteady	42.7	1.95
"	6.0	0.01	unsteady	35.4	2.20
"	6.0	0.02	unsteady	32.7	2.31
4 experimental	...	...	.....	39–40	1.94–2.02
calculated	6.0	0	quasi-steady	36.1	2.74
"	6.0	0	unsteady	45.2	2.03
"	5.7	0	unsteady	47.2	1.95
5 experimental	...	...	.....	41–42	2.02–2.09
calculated	6.0	0	quasi-steady	37.3	2.74
"	6.0	0	unsteady	46.8	2.01
"	5.7	0	unsteady	48.5	1.94
6 experimental	...	...	.....	38–40	2.10–2.22
calculated	6.0	0	quasi-steady	27.0	3.99
"	6.0	0	unsteady	36.5	2.37
"	5.7	0	unsteady	37.6	2.28

TABLE 3
Influence of Measured Elastic Axis Position and Structural Damping

Configuration	g	Measured e.a.		e.a. at 25% chord		Experimental	
		Ω_f(rad./sec.)	ω_f/Ω_f	Ω_f(rad./sec.)	ω_f/Ω_f	Ω_f(rad./sec.)	ω_f/Ω_f
1	0	27.3	1.95	27.3	1.95	32–35	1.70–1.72
1	0.03	28.2	1.91				
2	0	32.2	2.01	33.7	1.99	32–36	1.84–1.97
3	0	38.7	2.01	40.5	2.02	35–37	2.02–2.06
3	0.03	40.2	1.96				
4	0	43.0	2.01	45.2	2.03	39–40	1.94–2.02
5	0	43.5	2.01	46.8	2.01	41–42	2.02–2.09
6	0	35.6	2.48	36.5	2.37	38–40	2.10–2.22

the aerodynamic center are shown in Table 2. It is noted that the assumption of $C(k) = 1$ (quasi-steady assumption) results in rather large discrepancies between the calculated and experimental values for configurations 1, 2, 3, and 6, while for configurations 4 and 5 the discrepancies are mainly confined to the frequency ratio. Also, it is seen that a decrease in the lift curve slope, a_0, results in an increase of the flutter speed. A forward shift of the aerodynamic center (see configuration 3) results in a decrease of Ω_f and an increase of ω_f/Ω_f.

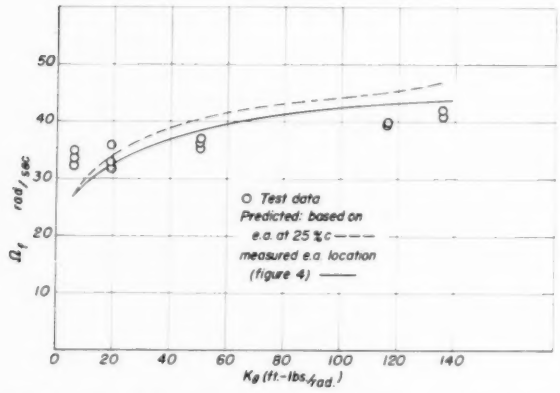

FIG. 5. Flutter speed vs. pitch-control stiffness (configurations 1–5).

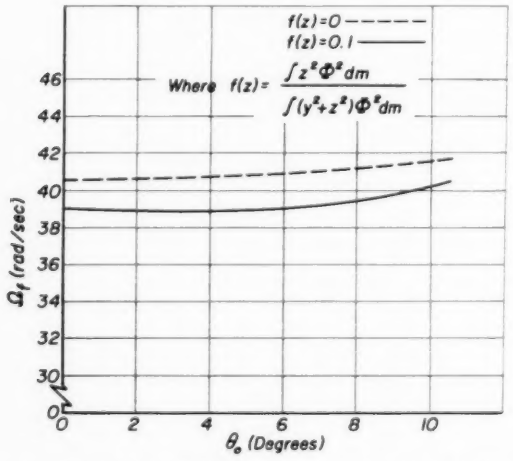

FIG. 6. Effect of initial pitch angle settings and blade thickness on the flutter speed of configuration 3.

Table 3 and Fig. 5 demonstrate the effects of a spanwise variation of the location of the section shear center and structural damping. It is noted that increased accuracy is obtained by inclusion of the measured shear center variation into the analysis. The influence of structural damping is seen to be small.

Fig. 6 shows the influence of initial pitch angle settings and inertia effect of finite blade thickness. As expected, the effects of initial pitch angle settings are found to be small. Finally, the flutter speed is seen to decrease with an increase of the inertia effect of finite blade thickness,

$$\int_{\text{blade}} z^2\Phi^2 dm$$

Although the above results are based upon the rather limited amount of available experimental data, it appears that the method presented herein could be effectively used for the prediction of classical-type rotor blade flutter. It is recommended, however, that further comparisons with experimental data be conducted.

APPENDIX—METHOD OF SOLUTION FOR THE FLUTTER CHARACTERISTICS

The method of solution is similar to that used for fixed-wing analysis. However, for those unacquainted with the technique, a brief outline of the method is given below.

The uncoupled first torsional mode shape is obtained by one of the standard tabular schemes, such as the Holzer method. The integrals appearing in the flutter coefficients can be evaluated by tabular integration. A value is chosen for the reduced frequency, and the corresponding values for F and G are obtained (see Fig. 4 of reference 5). The coefficients are calculated and the solution at flutter is assumed to be of the form

$$\left.\begin{aligned} \beta &= \beta_1 e^{i\omega_f t} \\ \theta_t &= \theta_1 e^{i\omega_f t} \end{aligned}\right\} \qquad \text{(A-1)}$$

where β_1 and θ_1 may be complex quantities. Substituting Eqs. (A-1) into the flutter equations, there results

$$\left.\begin{aligned} (-A_5\omega_f^2 + iA_3\omega_f + A_1)\beta_1 + \\ \qquad (-A_6\omega_f^2 + iA_4\omega_f + A_2)\theta_1 = 0 \\ (-B_5\omega_f^2 + iB_3\omega_f + B_1)\beta_1 + \\ \qquad (-B_6\omega_f^2 + iB_4\omega_f + B_2)\theta_1 = 0 \end{aligned}\right\} \qquad \text{(A-2)}$$

(Continued on page 320)

Plastic Buckling of Simply Supported Plates Subjected to Combined Shear and Bending or Eccentric Compression in Their Plane†

P. P. BIJLAARD*
Cornell University

SUMMARY

Formulas are derived for computing the plastic buckling stress of long simply supported plates that are subject to a combination of shear and longitudinal bending in their plane. The energy method and oblique coordinates are used. The integration in the plastic regions is carried out partially by using Simpson's rule. The more general case of combined shear and eccentric compression is also considered.

After evaluating these computations for some definite cases, simple design formulas are presented for computing the plastic reduction factor, with which the elastic buckling stress for the so-called associated elastic case has to be multiplied in order to obtain the plastic buckling stress. An approximate formula is presented for calculating the elastic buckling stress for combined shear and eccentric compression.

INTRODUCTION

THIS PAPER contains a continuation of the investigation on the plastic buckling of plates subject to nonhomogeneous stress distribution reported in reference 1. As explained more elaborately in that reference, the author's theory of plastic buckling[2–4] assumes that the shear (distortion) energy governs the plastic deformation and that the plastic part of the deformation occurs quasi-isotropically—that is, macroscopically in a similar way as the elastic deformation, but with a variable plastic modulus and with a Poisson's ratio equal to 0.5. Both these hypotheses are in good accordance with experiments.[5]

With incipient buckling of plates and shells, a state of stress with infinitely small stress components is superimposed on the original state of stress before buckling. In general, the ratios of the superimposed stress components will differ from those of the original stress components. This requires additional assumptions. The author's theory assumes that in the special case of plastic buckling the material behaves according to the so-called deformation theory (Hencky body), although it contains flow theory (Prandtl-Reuss body) as a special case. In deformation theory, it is assumed that the final strains are the same as if the stress components had increased from zero to their final values with constant ratios equal to these ratios in the final state of stress. Therefore, the final deviatory strain components are proportional to the final deviatory stress components. In flow theory, it is assumed that at any instant the increments of the deviatory plastic-strain components are proportional to the total deviatory stress components at that instant.

From the beginning[2] it was assumed that for the special case of buckling the material behaves according to deformation theory. Later tests by Kollbrunner,[6] Stüssi,[7] and the NACA[8] confirmed the author's theory,[9] as do also more recent experiments.[10–12] An explanation of why, in the case of buckling, materials like aluminum, magnesium, titanium, etc., where a given uniaxial stress entails a definite plastic strain, behave in accordance with deformation theory was given in references 1 and 9. It is due to the fact that with buckling, due to Shanley's principle of simultaneous action and also in connection with unavoidable eccentricities, the stresses from the original state of stress increase at the same time that the additional state of stress from the bending (buckling) action is superimposed, so that during the entire process the shearing stresses monotonically increase in practically all planes. As explained in reference 1, this behavior was confirmed directly by Feigen's experiments on tubes.[13]

In the present paper, first a long simply supported plate is considered, subject to combined shear and longitudinal bending in its plane. Using a method similar to that in reference 1 it would be possible to replace the governing partial differential equation by ordinary finite difference equations, but the presence of shear stresses makes it difficult to satisfy the boundary conditions at the edges $y = 0$ and $y = b$ (see Fig. 1). This may be demonstrated by considering the case of shear in the elastic range. In that case (see Fig. 1), the differential equation of the plate is[14]

$$N[(\partial^4 w/\partial x^4) + 2(\partial^4 w/\partial x^2 \partial y^2) + (\partial^4 w/\partial y^4)] - 2t\tau_{xy}(\partial^2 w/\partial x \partial y) = 0 \quad (1)$$

where N is the flexural rigidity of the plate. With

$$w = Ye^{i\alpha x} \quad (2)$$

where Y is a function of y only and $i = (-1)^{1/2}$, Eq. (1) is transformed to

$$Y^{IV} - 2\alpha^2 Y'' + \alpha^4 Y - 2i\alpha(t\tau_{xy}/N)Y' = 0 \quad (3)$$

where a prime denotes a differentiation with respect

Received April 13, 1956.

† This investigation was carried out (1953–1954) at Cornell University under the sponsorship and with the financial assistance of the Office of Ordnance Research of the U.S. Army. Most of the numerical calculations were done by Mohammed Y. Lalee, graduate student. The author wishes to express his appreciation for the valuable cooperation of all concerned.

* Professor of Structural Engineering.

to y. This equation can be written in the form of a finite difference equation. The boundary conditions at $y = 0$ and $y = b$ are now $Y = 0$ and $d^2Y/dy^2 = 0$. Using the method of finite differences, with pivotal points as shown in Fig. 1, for example, for point 0 these boundary conditions are transformed to $Y_0 = 0$ and $Y_{-1} = -Y_1$ (and, using second-order differences, also $Y_{-2} = -Y_2$). However, owing to the oblique nodal lines that occur in shear buckling, an imaginary extension of the plate outside the support $y = 0$ leads to the dashed nodal lines for negative values of y, so that Y_{-1} would not be equal to $-Y_1$ (see Fig. 1). Therefore, no good convergence can be expected in this case.

Indeed, a spacing $h = b/3$ of the pivotal points, which, from Table 1 of reference 1 in the case of bending, and by using second-order differences, gave an error of only +2 per cent, in the present case leads to a buckling stress coefficient $k = 6.43$, against an exact value of 5.35. Hence the error is here +20 per cent. The condition $Y_{-1} = -Y_1$ would be approximately satisfied if oblique coordinates y_0 in the general direction of the nodal lines were used (see Fig. 2). As a matter of fact, with oblique coordinates x_0 and y_0, where $\tan \varphi = 1/\sqrt{2}$ (see Fig. 2), and using 3 spacings ($h_0 = b_0/3$), one finds $k = 5.64$, or an error of only 5.5 per cent. However, in the case of plastic buckling under combined bending and shear, the direction of the oblique nodal lines is not known beforehand. Therefore, it was more convenient to use the energy method.

(As in the case of bending or eccentric compression, dealt with in reference 1, one has to begin with assuming a certain stress distribution. In the present case this stress distribution is not directly obvious. It will be considered in the next section.)

Subsequently, formulas are derived for the plastic and elastic buckling stresses for combined shear and bending as well as for combined shear and eccentric compression, which expressions are evaluated for special cases. Finally, design formulas are developed for the plastic reduction factor, with which the elastic buckling stress for the so-called associated case has to be multiplied in order to obtain the plastic buckling stress. In this connection the stress distribution for the associated case is determined, and design formulas are given for the elastic buckling stress for combined shear and eccentric compression.

A paper on the buckling of clamped plates, clamped flanges and hinged flanges under nonhomogeneous stress distribution will appear under the title given in reference 26.

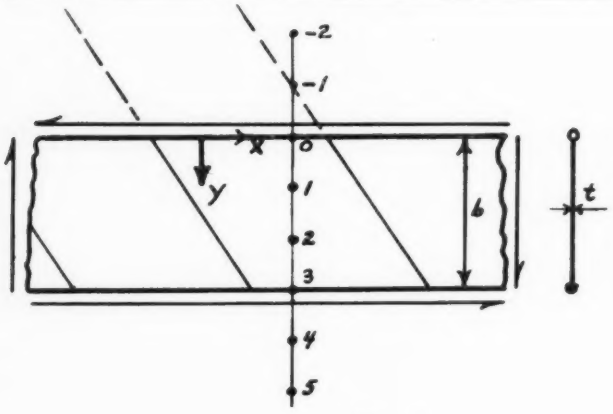

Fig. 1

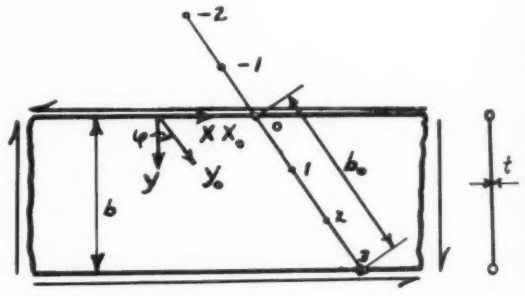

Fig. 2

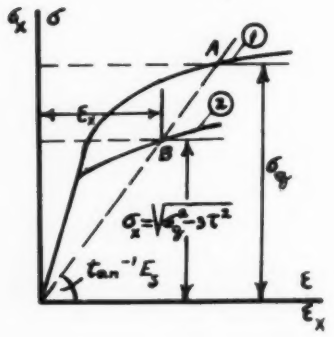

Fig. 3

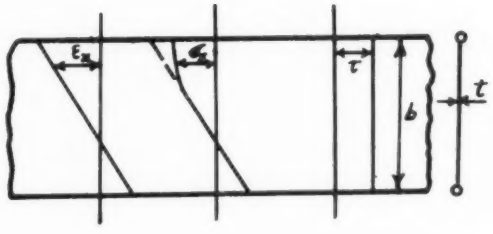

Fig. 4

FIG. 1. Plate subjected to shear, using rectangular coordinates. FIG. 2. Plate subjected to shear, using oblique coordinates. FIG. 3. $\sigma_x - \epsilon_x$ diagram without (curve 1) and with (curve 2) simultaneous shear. FIG. 4. Plate subjected to combined eccentric compression and shear.

Stress Distribution Prior to Buckling

The more general case of combined shear and eccentric compression will be considered first. Since only σ_x and τ_{xy} differ from zero, Poisson's ratio does not enter into the calculations, so that it is not necessary to split the strains into elastic and plastic ones. Hence, ϵ_x can be expressed as

$$\epsilon_x = \sigma_x / E_s \tag{4}$$

where E_s is the secant modulus. Further, at any point σ_x and τ_{xy} (hereafter denoted as τ) are connected by the condition of plasticity

$$\sigma_x^2 + 3\tau^2 = \sigma_q^2 \tag{5}$$

where σ_q is the equivalent uniaxial stress.

With a stress-strain diagram for uniaxial loading as given by curve 1 in Fig. 3, at an arbitrary point A, with a stress $\sigma = \sigma_q$, the secant modulus has a definite value E_s. Hence, with a given shear stress τ (see Fig. 4), with the same secant modulus E_s, from Eq. (5) the stress σ_x is equal to $\sqrt{\sigma_q^2 - 3\tau^2}$, so that point B in Fig. 3 determines a point of the stress-strain relation between σ_x and ϵ_x. Other points are found in a similar way. This results in the curve 2 in Fig. 3 as the $\sigma_x - \epsilon_x$ relation belonging to a given shear stress τ. Therefore, after assuming a constant shear stress (see Fig. 4), from Fig. 3 the $\sigma_x - \epsilon_x$ relation is known, so that, with an assumed linear ϵ_x distribution, the distribution of σ_x is directly known.

From reference 1 the form of the stress-strain diagram has practically no influence on the resulting critical edge stress, expressed as a function of the condition at the edge. Therefore, for the sake of convenience, the idealized stress-strain diagram of mild steel, as sketched in Fig. 5, will be used for the subject problem. For the case of combined bending and shear considered now, the stress distribution is sketched in Fig. 6. In the two plastic regions, where $d > y_1 > 0$ or $b > y_1 > b - d$, from Eq. (5), where now σ_q is equal to the yield stress σ_{ys}, the normal stress is

$$\sigma_{xp} = \sqrt{\sigma_{ys}^2 - 3\tau^2} \tag{6}$$

In Fig. 6 y_1 denotes the orthogonal coordinate, in contrast with the oblique coordinate y that will be used later. At a distance $y_1 = d$ (see Fig. 6) below the upper edge—that is, at the boundary between the elastic and plastic regions—$\epsilon_x = \sigma_{xp}/E$, where E is the elastic modulus. Hence, at any distance y_1 in the upper plastic region, from Eq. (4) and Fig. 6,

$$\epsilon_x = (\sigma_{xp}/E_s) = \left\{[(b/2) - y_1]/[(b/2) - d]\right\}(\sigma_{xp}/E) \tag{7}$$

from which

$$E_s = [(b - 2d)(b - 2y_1)]E \tag{8}$$

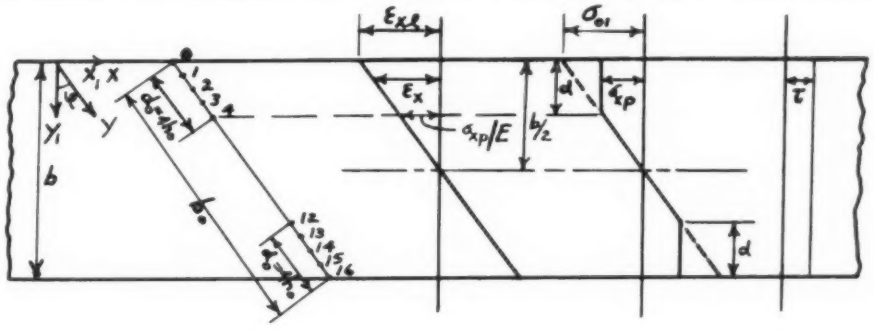

Fig. 6

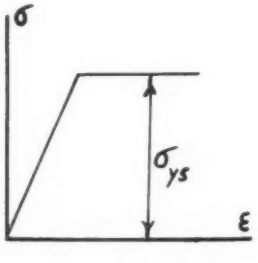

Fig. 5

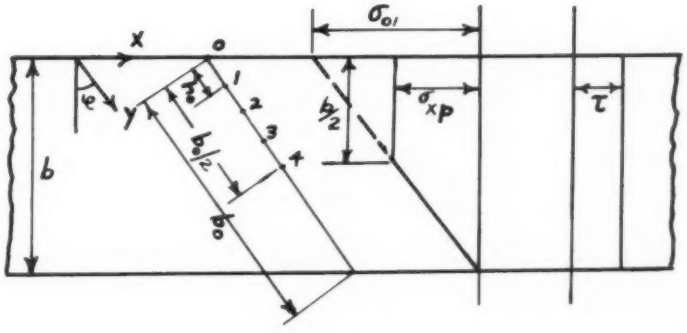

Fig. 7

FIG. 5. Stress-strain relation used in computations. FIG. 6. Plate subjected to combined bending and shear. FIG. 7. Plate subjected to special case of combined shear and eccentric compression.

From symmetry with respect to the neutral plane this also determines the values of E_s in the lower plastic region. Hence, with known values of E_v and $E_t = 0$, the plastic reduction coefficients in the theory of plastic plate buckling can be calculated at any point.

Derivation of a Formula for the Plastic Buckling Stress for Combined Shear and Bending

Using oblique coordinates x and y (see Fig. 6) as was done in reference 15 in the case of combined shear and longitudinal compression, the buckling deflection may be approximated very well by

$$w = K_0 Y \sin \pi x/a \tag{9}$$

where

$$Y = \sum_{n=1}^{3} K_n \sin (n\pi y/b_0) \qquad \text{(where } K_1 = 1) \tag{10}$$

so that only three terms of the series are considered. Further, b_0 is the oblique plate width in Fig. 6. Owing to the arbitrary term K_0 in Eq. (9), K_1 in Eq. (10) may be equated to one. From Eq. (59) of reference 15, the internal work at incipient plastic buckling is, for one half-wave length a in the X-direction,

$$V_i = \frac{1}{2} I \int_0^a \int_0^{b_0} [F_1(\partial^2 w/\partial x^2)^2 \cos\varphi + F_2(\partial^2 w/\partial x^2)(\partial^2 w/\partial x \partial y) + F_3(\partial^2 w/\partial x \partial y)^2/\cos\varphi + F_4(\partial^2 w/\partial x^2)(\partial^2 w/\partial y^2)/\cos\varphi + F_5(\partial^2 w/\partial x \partial y)(\partial^2 w/\partial y^2)/\cos^2\varphi + F_6(\partial^2 w/\partial y^2)^2/\cos^3\varphi]\, dxdy \tag{11}$$

where φ is the slope angle of the oblique coordinate Y (see Fig. 6), and

$$\left.\begin{aligned} F_1 &= C_{11} - 4C_{13}\alpha + 2(C_{12} + 2C_{33})\alpha^2 - 4C_{23}\alpha^3 + C_{22}\alpha^4 \\ F_2 &= 4[C_{13} - (C_{12} + 2C_{33})\alpha + 3C_{23}\alpha^2 - C_{22}\alpha^3] \\ F_3 &= 4(C_{33} - 2C_{23}\alpha + C_{22}\alpha^2) \\ F_4 &= 2(C_{12} - 2C_{23}\alpha + C_{22}\alpha^2) \\ F_5 &= 4(C_{23} - C_{22}\alpha) \\ F_6 &= C_{22} \end{aligned}\right\} \tag{12}$$

$$\alpha = \tan\varphi \tag{13}$$

C_{11}, C_{12}, etc. are plastic reduction coefficients which have been defined in reference 15 and will be further discussed below.

From reference 15 the external work for a half wave a in the X-direction is

$$V_e = (1/2)t \int_0^a \int_0^{b_0} \{\sigma_x(\partial w/\partial x)^2 \cos\varphi - 2\tau[(\partial w/\partial x)(\partial w/\partial y) - (\partial w/\partial x)^2 \sin\varphi]\}\, dxdy \tag{14}$$

Insertion of Eq. (9) into Eq. (11) and carrying out the differentiations, as well as the integration in the X-direction, leads to

$$V_i = (\pi^4/4ab^2) K_0^2 I \int_0^{b_0} \psi dy \tag{15}$$

where

$$\psi = (1/\beta^2) F_1 Y_1 \cos\varphi + (F_3 Y_3 + F_4 Y_4)/\cos\varphi + \beta^2 F_6 Y_6/\cos^3\varphi \tag{16}$$

Y_1, Y_3, Y_4, and Y_6 are the nondimensional values

$$Y_1 = Y^2; \quad Y_3 = (b^2/\pi^2)(Y')^2; \quad Y_4 = -(b^2/\pi^2) YY''; \quad Y_6 = (b^4/\pi^4)(Y'')^2 \tag{17}$$

where a prime denotes differentiation with respect to y and

$$\beta = a/b_0 \tag{18}$$

Splitting the internal work into that in the elastic and plastic regions, Eq. (15) may be written in the form

$$\left.\begin{aligned} V_i &= \frac{\pi^4}{4ab^2} K_0^2 I \left[\int_0^{d_0} \psi_p\, dy + \int_{d_0}^{b_0 - d_0} \psi_e dy + \int_{b_0 - d_0}^{b_0} \psi_p\, dy\right] \\ &= \frac{\pi^4}{4ab^2} K_0^2 I \left[\int_0^{b_0} \psi_e dy - \int_0^{d_0} (\psi_e - \psi_p) dy - \int_{b_0 - d_0}^{b_0} (\psi_e - \psi_p) dy\right] \end{aligned}\right\} \tag{19}$$

where ψ_e and ψ_p represent ψ from Eq. (16) in the elastic and plastic domain, respectively, and d_0 is the oblique distance d_0 shown in Fig. 6.

Carrying out the differentiations and the integration in the X-direction, Eq. (14) leads to

$$V_e = \frac{\pi^2 t}{4a} K_0^2 \int_0^{b_0} Y^2(\sigma_x \cos\varphi + 2\tau \sin\varphi) dy \tag{20}$$

where Y^2 is the same function as Y_1 in Eq. (17). In the elastic region, from Fig. 6,

$$\sigma_x = [1 - (2y/b_0)]\sigma_{01} = [1 - (2y/b_0)]\,[b_0/(b_0 - 2d_0)]\sigma_{xp} \tag{21}$$

while in the plastic regions $\sigma_x = \sigma_{xp}$, where σ_{xp} is given by Eq. (6). With the notation

$$\sigma_{xp}/\tau = \gamma \tag{22}$$

from Eqs. (20) and (21) in the elastic region, the external work is

$$V_{ee} = \frac{\pi^2 t}{4a} K_0^2 \tau_{xy} \int_{d_0}^{b_0 - d_0} \left[\gamma \frac{b_0}{b_0 - 2d_0} \left(1 - \frac{2y}{b_0}\right) \cos\varphi + 2\sin\varphi \right] Y^2\, dy \tag{23}$$

and the external work in the plastic regions is

$$V_{ep} = \frac{\pi^2 t}{4a} K_0^2 \tau_{xy} \left[(\gamma\cos\varphi + 2\sin\varphi) \int_0^{d_0} Y^2 dy + (-\gamma\cos\varphi + 2\sin\varphi) \int_{b_0 - d_0}^{b_0} Y^2\, dy \right] \tag{24}$$

Hence, the total external work is

$$V_e = V_{ee} + V_{ep} = \frac{\pi^2 t}{4a} K_0^2 \tau_{xy} \left\{ \gamma\cos\varphi \left[\int_0^{d_0} Y^2 dy - \int_{b_0 - d_0}^{b_0} Y^2 dy + \frac{b_0}{b_0 - 2d_0} \int_{d_0}^{b_0 - d_0} Y^2 dy - \frac{2}{b_0 - 2d_0} \int_{d_0}^{b_0 - d_0} y Y^2 dy \right] + 2\sin\varphi \int_0^{b_0} Y^2 dy \right\} \tag{25}$$

The condition $V_i = V_e$ yields, from Eqs. (19) and (25),

$$\tau = \frac{\pi^2 I}{b_0^2 t} \frac{\displaystyle\int_0^{b_0} \psi_e dy - \int_0^{d_0} (\psi_e - \psi_p) dy - \int_{b_0 - d_0}^{b_0} (\psi_e - \psi_p) dy}{\left(\gamma \frac{b_0}{b_0 - 2d_0}\cos\varphi + 2\sin\varphi\right) \displaystyle\int_0^{b_0} Y^2 dy - \frac{\gamma\cos\varphi}{b_0 - 2d_0} \left[2d_0 \int_0^{d_0} Y^2 dy + 2(b_0 - d_0) \int_{b_0 - d_0}^{b_0} Y^2 dy \right] - \frac{2\gamma\cos\varphi}{b_0 - 2d_0} \displaystyle\int_{d_0}^{b_0 - d_0} y Y^2 dy} \tag{26}$$

where the expression within the braces in Eq. (25) is written in a somewhat different way. From Eqs. (10), (16), and (17), in Eq. (26),

$$\int_0^{b_0} \psi_e\, dy = (b_0/2)\,[(1/\beta^2)F_1(1 + K_2^2 + K_3^2)\cos\varphi + (F_3 + F_4)(1 + 4K_2^2 + 9K_3^2)/\cos\varphi + \beta^2 F_6(1 + 16K_2^2 + 81K_3^2)/\cos^3\varphi] \tag{27}$$

Here F_1, F_3, F_4, and F_6 are given by Eq. (12), where the C coefficients now refer to the elastic range and are given by Eq. (64) of reference 15, so that

$$\left.\begin{aligned} C_{11} = C_{22} &= E/(1 - \nu^2); \quad C_{12} = \nu E/(1 - \nu^2) \\ C_{33} &= E/[2(1 + \nu)]; \qquad C_{13} = C_{23} = 0 \end{aligned}\right\} \tag{28}$$

where ν is Poisson's ratio in the elastic range. The other two integrals in the numerator of Eq. (26) have to be evaluated numerically, since in the plastic region ψ can hardly be expressed in a convenient form. They were evaluated by Simpson's rule, so that, from Fig. 6, for example, the second integral becomes

$$\int_0^{b_0} (\psi_e - \psi_p) dy = (h_0/3)[(\psi_e - \psi_p)_0 + 4(\psi_e - \psi_p)_1 + 2(\psi_e - \psi_p)_2 + 4(\psi_e - \psi_p)_3 + (\psi_e - \psi_p)_4] \tag{29}$$

Here the subscripts 0 to 4 refer to the pivotal points 0 to 4 in Fig. 6 and h_0 is the oblique spacing of these points. The third integral in the numerator of Eq. (26) practically does not require any additional computations, since all terms are either equal to those for the symmetrically situated points in the upper plastic region or equal and opposite to them.

Evaluation of the Plastic Buckling Stress for a Special Case

Eq. (26) was evaluated for the case that the height d of the plastic regions in Fig. 6 is $d = b/4$, so that also $d_0 = b_0/4$. It was further assumed that, in Eq. (22), $\gamma = \sigma_{xp}/\tau = \sqrt{3}$.

In Eq. (29) ψ_e and ψ_p are given by Eq. (16), where F_1 to F_6 follow from Eq. (12). For ψ_e the C coefficients are given by Eqs. (28). For ψ_p the C coefficients are defined by Eqs. (47), (50), and (51) of reference 15. For the special case considered, where $\sigma_x/\tau = \sqrt{3}$ and $\sigma_y = 0$, Eqs. (66) of reference 15 apply. In the present case $E_t = 0$, so that special care must be taken in calculating the C coefficients in order to eliminate E_t. This leads to the formulas for the C coefficients:

$$\left.\begin{aligned} C_{11} &= [-(1 - 2\nu)/(8E) + 15/(8E_s)]/\Delta \\ C_{12} &= [(1 - 2\nu)/E + 3/(2E_s)]/\Delta \\ C_{13} &= -[(1 - 2\nu)/(8E) + 3/(8E_s)]\sqrt{3}/\Delta \\ C_{22} &= [-(1 - 2\nu)/E + 3/E_s]/\Delta \\ C_{23} &= [(1 - 2\nu)\sqrt{3}/(4E)]/\Delta \\ C_{33} &= [(1 - 2\nu)/(4E) + 3/(8E_s)]/\Delta \\ \Delta &= 9/(4E_s^2) + 9(1 - 2\nu)/(8EE_s) - 5(1 - 2\nu)^2/(8E^2) \end{aligned}\right\} \tag{30}$$

E_s in these formulas is determined by Eq. (8), which, using the oblique distances and with $d_0 = b_0/4$, can be written as

$$E_s = [(b_0 - 2d_0)/(b_0 - 2y)]E = [b_0/2(b_0 - 2y)]E \tag{31}$$

The ratios E_s/E and the C coefficients were calculated for the points 0, 1, 2, 3, and 4 in Fig. 6. They also apply for the points 16, 15, 14, 13, and 12, respectively. Hence, the integrals in the numerator of Eq. (26) can be evaluated. In the integrals in the denominator, where now $d_0 = b_0/4$, everything is known, so that they can be integrated directly. In this way, τ can be calculated from Eq. (26) for given values of the angle φ and of $\beta = a/b_0$. This leads to an expression of τ in terms of K_2 and K_3. To find the actual buckling stress τ_{cr}, the values of φ, β, K_2, and K_3 have to be chosen such as to make τ a minimum.

The most convenient way for calculating the minimum buckling stress τ_{cr} was to evaluate Eq. (26) for 3 different values of $\alpha = \tan\varphi(\alpha = 0.4006, 0.5002$, and $0.6000)$ and with each value of α for 3 different ratios β ($\beta = 0.8$, 0.9, and 1). This leads for each of these nine combinations to an expression of τ in terms of K_2 and K_3, where K_2 and K_3 were determined from the conditions $\partial\tau/\partial K_2 = \partial\tau/\partial K_3 = 0$. For example, for $\alpha = 0.6$, $\beta = 0.9$, one obtains, from Eq. (26),

$$\tau = \frac{3.535 + 19.236K_2^2 + 67.467K_3^2 - 3.472K_3}{0.514 + 0.514K_2^2 + 0.514K_3^2 + 0.946K_2 + 0.855K_2K_3} \frac{\pi^2 EI}{b_0^2 t} \tag{32}$$

The conditions $\partial\tau/\partial K_2 = \partial\tau/\partial K_3 = 0$ yield $K_2 = 0.1746$, $K_3 = 0.0338$, so that from Eq. (32) $\tau = 5.8168\,\pi^2EI/(b_0^2t)$. Since $b_0 = b/\cos\varphi$ and $EI = (1 - \nu^2)N$ (see Fig. 6), this gives

$$\tau = 5.8168(1 - \nu^2)(\cos^2\varphi)\pi^2N/(b^2t) = 3.8922\pi^2N/(b^2t) \tag{33}$$

In a similar way the values τ for other combinations of α and β are obtained. The values k in the formula

$$\tau = k\pi^2N/(b^2t) \tag{34}$$

for the nine combinations are given in Table 1. The values k_{min} for each value of α, given in the last column of Table 1, were obtained by determining the equation of the parabola for k, as a function of β that passes through the three known points for $\beta = 0.8$, 0.9, and 1, and finding its minimum. In the same way, from these three values k_{min} the minimum value of k as a function of α was obtained. It is $k = 3.8495$. Hence, for the case of Fig. 6, with $d_0 = b_0/4$ and $\sigma_{xp} = \tau\sqrt{3}$,

$$\tau_{cr} = 3.85\pi^2N/(b^2t), \qquad (\sigma_{xp})_{cr} = 6.67\pi^2N/(b^2t) \tag{35}$$

TABLE 1

Buckling Stress Coefficients k			
α	β	k	k_{min}
0.4006	0.8	4.2077	
0.4006	0.9	3.9479	3.93
0.4006	1.0	4.0227	
0.5002	0.8	3.9227	
0.5002	0.9	3.8718	3.86
0.5002	1.0	4.0623	
0.6000	0.8	4.3070	
0.6000	0.9	3.8922	3.85
0.6000	1.0	3.9723	

Elastic Buckling Stress for Combined Shear and Bending

Analogous to what was done in reference 1 the elastic buckling stress was calculated for the case that, in terms of σ_{xp}, the bending stresses are those belonging to the same edge strains as occur in the plastic case above—that is, from Fig. 6, assuming edge stresses $\sigma_{xe} = \sigma_{01} = 2\sigma_{xp} = 2\tau\sqrt{3}$. The buckling stress τ follows from Eq. (26) by the substitution $d_0 = 0$, so that

$$\tau = \frac{\pi^2 I}{b_0^2 t} \frac{\int_0^{b_0} \psi_e dy}{(\gamma\cos\varphi + 2\sin\varphi)\int_0^{b_0} Y^2 dy - (2\gamma\cos\varphi/b_0)\int_0^{b_0} yY^2 dy} \tag{36}$$

The numerator is given by Eq. (27), where F_1 to F_6 follow from Eq. (12) and the C coefficients (for the elastic range) are given by Eqs. (28). In the denominator

$$\int_0^{b_0} Y^2 dy = (b_0/2)(1 + K_2^2 + K_3^2) \tag{37}$$

$$\int_0^{b_0} yY^2 dy = (b_0^2/4)[1 + K_3^2 + K_2^2 - (64/9\pi^2)K_2 - (192/25\pi^2)K_2K_3] \tag{38}$$

In a similar way as in the above plastic case it was found that the elastic buckling stresses are

$$\tau_{cr} = 4.72\pi^2N/(b^2t) \qquad \text{and} \qquad (\sigma_{xe})_{cr} = 2\tau\sqrt{3} = 16.35\pi^2N/(b^2t) \tag{39}$$

For the same case from reference 16 a critical stress $\tau_{cr} = 4.58\pi^2N/(b^2t)$ is obtained, so that for this case the present method gives a result that is 3 per cent too high. This discrepancy is sufficiently small, since a similar discrepancy will appear in the plastic buckling stress and only the ratio of these two stresses is of present interest.

Plastic Buckling Stress for Combined Shear and Eccentric Compression

With the data used for evaluating the case of Fig. 6, with $d_0 = b_0/4$, it is easy also to calculate the case of combined shear and eccentric compression sketched in Fig. 7, where $\sigma_{xp}/\tau = \gamma = \sqrt{3}$. It is obvious that all E_s and C values for the points 0, 1, 2, 3, and 4 in Fig. 6 also obtain for the points 0, 1, 2, 3, and 4 of Fig. 7. In the present case, however, the spacing $h_0 = b_0/8$, instead of $b_0/16$ in Fig. 6. Eqs. (15), (16), (17), and (20) for V_i and V_e also apply. Instead of Eq. (21), in the elastic region

$$\sigma_x = 2[1 - (y/b_0)]\sigma_{xp} \tag{40}$$

Hence, using Eq. (22), the external work in the elastic region is

$$V_{ee} = (\pi^2 t/4a)K_0^2\tau \int_{b_0/2}^{b_0} \{2\gamma[1 - (y/b_0)] \cos\varphi + 2\sin\varphi\} Y^2 dy \tag{41}$$

and for the plastic part it is

$$V_{ep} = (\pi^2 t/4a)K_0^2\tau(\gamma\cos\varphi + 2\sin\varphi) \int_0^{b_0/2} Y^2 dy \tag{42}$$

Equating the sum of V_{ee} and V_{ep} to the total internal work from Eq. (15) leads to the expression

$$\tau = \frac{\pi^2 I}{b_0^2 t} \frac{\int_0^{b_0} \psi_e dy - \int_0^{b_0/2} (\psi_e - \psi_p) dy}{2(\gamma\cos\varphi + \sin\varphi) \int_0^{b_0} Y^2 dy - \gamma\cos\varphi \int_0^{b_0/2} Y^2 dy - (2\gamma/b_0)\cos\varphi \int_{b_0/2}^{b_0} y Y^2 dy} \tag{43}$$

In a similar way as for the above cases τ_{cr} was calculated for the case of Fig. 7, with $\gamma = \sigma_{xp}/\tau = \sqrt{3}$, with the following result:

$$\tau_{cr} = 1.758\pi^2 N/(b^2 t), \qquad \sigma_{xp} = 3.045\pi^2 N/(b^2 t) \tag{44}$$

Elastic Buckling Stress for Combined Shear and Eccentric Compression

As far as known to the writer no data are available for the elastic buckling stress for combined shear and eccentric compression. It can be calculated with the present approximate method. For the case of Fig. 8, with the same edge strains ϵ_{xp}, as expressed in σ_{xp}, as in the plastic case of Fig. 7, $\gamma = \sigma_{xe}/\tau = 2\sqrt{3}$ and

$$\sigma_x = \sigma_{xe}[1 - (y/b_0)] = \gamma\tau[1 - (y/b_0)] \tag{45}$$

Hence, from Eq. (20),

$$V_e = (\pi^2 t/4a)K_1^2\tau \int_0^{b_0} \{\gamma[1 - (y/b_0)] \cos\varphi + 2\sin\varphi\} Y^2 dy \tag{46}$$

Equating this to the internal work V_i from Eq. (15), one obtains

$$\tau = \frac{\pi^2 I}{b_0^2 t} \frac{\int_0^{b_0} \psi_e dy}{(\gamma\cos\varphi + 2\sin\varphi) \int_0^{b_0} Y^2 dy - (\gamma/b_0)\cos\varphi \int_0^{b_0} y Y^2 dy} \tag{47}$$

Using Eqs. (27), (37), and (38) this leads to

$$\tau_{cr} = 1.99\pi^2 N/(b^2 t), \qquad (\sigma_{xe})_{cr} = 6.93\pi^2 N/(b^2 t) \tag{48}$$

Approximate Formula for the Elastic Buckling Stress Under Shear and Eccentric Compression

Expressing the distribution of σ_x (see Fig. 9) by the formula

$$\sigma_x = \sigma_{xe}[1 - \alpha(y_1/b)] \tag{49}$$

(y_1 is measured perpendicular to the edge; see Fig. 6) in the case of the preceding section $\alpha = 1$. If the shear stress is zero (in this case $\alpha = 1$), a plate behaves about in the same way as if it is subjected to an equally distributed compressive stress ($\alpha = 0$) of the average value $\sigma_{xe}/2$ of σ_x. The buckling stress coefficient k from Eq. (34) for the edge stress σ_{xe} is here 7.81 (reference 17). Hence for the average stress $\sigma_{xe}/2$ this coefficient k is 3.905, while for an equally distributed stress it is 4, or only 2 per cent more. Therefore, also in combination with a loading by shear stress, a plate under an eccentric compression with $\alpha = 1$ may be assumed to behave about in the same way as under combined shear and equally distributed compressive stress ($\alpha = 0$). For the latter case, from reference 18, the critical combination of σ_x and τ is given by the parabola

$$(\tau/\tau_{ocr})^2 + (\sigma_x/\sigma_{xocr}) = 1 \tag{50}$$

where τ_{ocr} or σ_{xocr} are the critical stresses if τ or σ_x act alone. As was shown in reference 19 this parabolic

relation means that the so-called reduced compressive stress is governing for buckling.

On the other hand, for combined shear and bending ($\alpha = 2$) the following relation holds sufficiently accurately (see reference 20):

$$(\tau/\tau_{ocr})^2 + (\sigma_{xe}/\sigma_{xeocr})^2 = 1 \qquad (51)$$

where τ_{ocr} or σ_{xeocr} are the critical stresses if only stresses τ or only stresses σ_x (with the same parameter α) are acting. As may be seen from Fig. 3 of reference 16 this relation is conservative. No exact data are available on the elastic buckling stress for combined shear and eccentric compression. A good approximation may be obtained by a relation between τ/τ_{ocr} and $\sigma_{xe}/\sigma_{xeocr}$ that, for $\alpha = 0$ and 2, reduces to Eqs. (50) and (51), respectively, and from the above, for $\alpha = 1$, differs only slightly from Eq. (50). This is accomplished by the relation

$$(\tau/\tau_{ocr})^2 + \tfrac{1}{4}[1 - (\alpha^5/32)]\,(\sigma_{xe}/\sigma_{xeocr}) + (\alpha^5/32)\,(\sigma_{xe}/\sigma_{xeocr})^2\tfrac{1}{4} = 1 \qquad (52)$$

For the case of the preceding section, where $\sigma_x = 2\tau\sqrt{3}$, from page 361 of reference 14, $\tau_{ocr} = 5.36\,\pi^2 N/(b^2 t)$, and, from reference 17, $\sigma_{xeocr} = 7.81\pi^2 N/(b^2 t)$. Then Eq. (52) yields

$$\tau_{cr} = \tau = 1.95\pi^2 N/(b^2 t), \qquad \sigma_{xecr} = \sigma_{xe} = 6.75\pi^2 N/(b^2 t) \qquad (53)$$

This is in excellent agreement with Eq. (48), since comparison at the end of the section "Elastic Buckling Stress for Combined Shear and Bending" of the elastic buckling stresses for that somewhat related case with

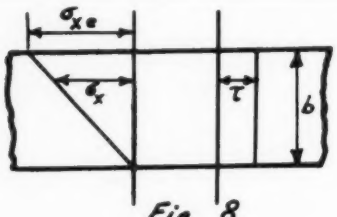

Fig. 8

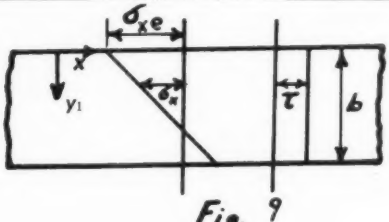

Fig. 9

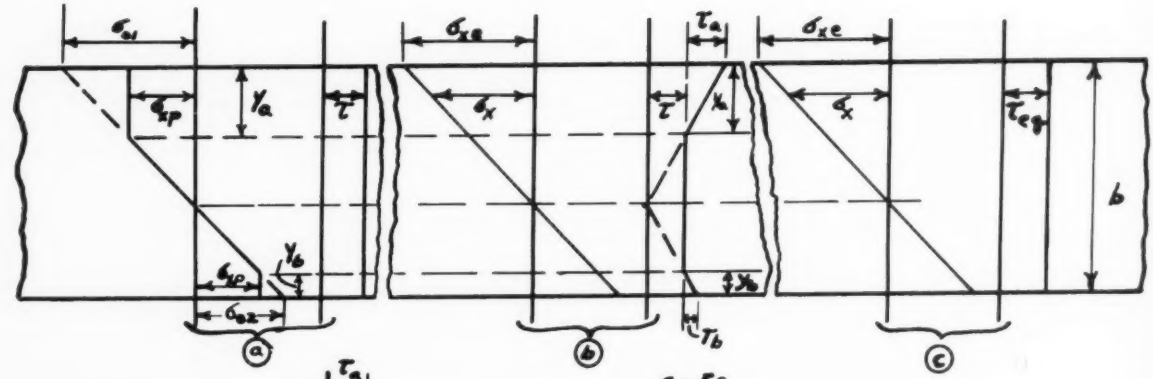

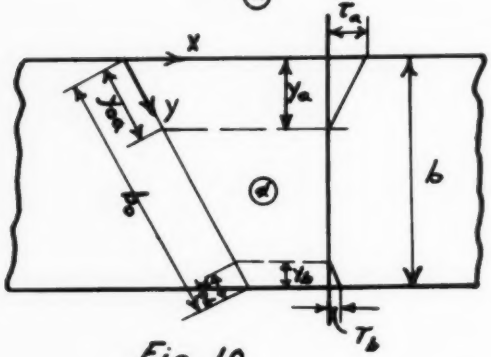

Fig. 10

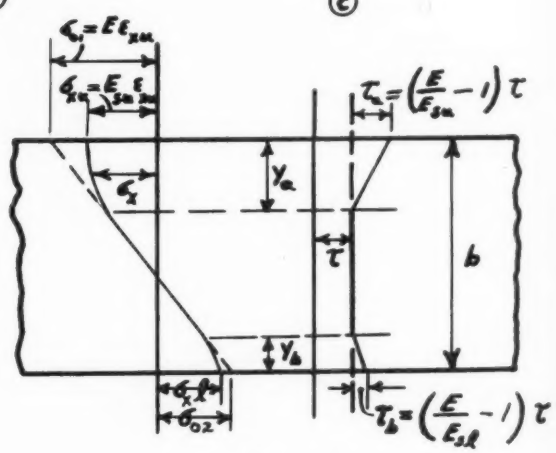

Fig. 11

FIG. 8. Plate subjected to special case of combined elastic shear and eccentric compression. FIG. 9. Plate subjected to general case of combined elastic shear and eccentric compression. FIG. 10. Comparison of plastic case and associated elastic case. FIG. 11. Determination of associated elastic case for materials with smooth stress-strain diagram.

those from reference 16, showed that the present energy method yields values that are about 3 per cent too high.

The Associated Elastic Case

In the section entitled, "Simple Way of Understanding Equation (22)," of reference 1, it is shown for the case of eccentric compression, with α not much smaller than 2, that in the plastic range, the deflecting forces acting upon the buckling plate are E_s/E times the deflecting forces for the elastic case with the same edge strains. With that loading also the restraining forces in the plastic case were about E_s/E times those in the associated elastic case, so that, if equilibrium exists in the elastic case, it will also exist in the plastic case. This resulted in a plastic reduction factor equal to the ratio $(E_s/E)_u$ at the upper edge. *In other words, this meant that the critical edge strain ϵ_{xc} for plastic buckling was equal to that for elastic buckling.*

Also in the present case an elastic stress distribution can be found where the stresses at any point are E/E_s times those for the plastic case. This will be called the *associated elastic case.* For the general case of combined shear and eccentric compression, as sketched in Fig. 10a, the associated elastic case is given in Fig. 10b. The edge stress σ_{xe} is equal to the edge stress σ_{01} that would occur if, with the same edge strains as in the plastic case, the plate would have been elastic—that is,

$$\sigma_{xe} = \sigma_{01} = (E/E_{su})\sigma_{xp} \tag{54}$$

where E_{su} is the secant modulus at the upper edge. Similarly, the shear stress at the upper edge is $\tau_e = \tau + \tau_a = (E/E_{su})\tau$, so that

$$\tau_a = [(E/E_{su}) - 1]\tau = [(\sigma_{01}/\sigma_{xp}) - 1]\tau \tag{55}$$

In the same way, at the lower edge,

$$\tau_b = [(E/E_{sl}) - 1]\tau = [(\sigma_{02}/\sigma_{xp}) - 1]\tau \tag{56}$$

where E_{sl} is the secant modulus at the lower edge. *Hence the stress distribution in the associated elastic case, for the normal as well as for the shear stresses, is the distribution that would occur if, with the same strain distribution as in the plastic case, the plate would remain elastic.*

Consequently, in the plastic case (see Fig. 10a), the deflecting forces, $-t\sigma_x(\partial^2 w/\partial x_1^2)dx_1dy_1$ and $2t\tau(\partial^2 w/\partial x_1\partial y_1)dx_1dy_1$, exerted upon any plate element tdx_1dy_1 are E_s/E times those in the associated elastic case (see Fig. 10b), provided that the deflection w has the same shape in both cases. However, owing to the presence of shear stresses, the restraining forces will be reduced more than in the ratio E_s/E with respect to those in the associated elastic case. Therefore, from the above, the plastic reduction factor $\eta_{sc} = \sigma_{xp}/\sigma_{xe}$ with respect to the associated case will be less than $(E_s/E)_u = E_{su}/E$ and can be expected to be about between $(E_s/E)_u$ and the *smallest* of the plastic reduction factors η_s and η_c for pure shear only and eccentric compression only, or

$$E_{su}/E \geqslant \eta_{sc} \geqslant \quad \textit{smallest} \text{ of } \eta_s \text{ and } \eta_c \tag{57}$$

This requires first finding σ_{xe} for the associated elastic case in Fig. 10b, which can be done by replacing the varying shear stress by an equivalent constant shear stress τ_{eq}, so that the associated elastic case in Fig. 10b is equivalent to the case of Fig. 10c. To express τ_{eq} in terms of τ, τ_a, τ_b, y_a, and y_b in Fig. 10b the external work done by the deflecting forces in the cases of Figs. 10b and 10c will be compared, in a similar way as is done in the writer's method of split rigidities.[21, 22] Only the shear stresses differ. They cause deflecting forces D on an element tdx_1dy_1, where x_1 and y_1 are orthogonal coordinates (see Fig. 6) of

$$D = 2t\tau(\partial^2 w/\partial x_1\partial y_1)dx_1dy_1 = 2t\tau[(\partial^2 w/\partial x\partial y) - (\partial^2 w/\partial x^2)\sin\varphi]dxdy \tag{58}$$

Here x and y are oblique coordinates (see Figs. 6 and 10d). With a deflection as given by Eq. (9) the work done by the deflecting forces on a part of the plate between two nodal lines and between $y = 0$ and $y = y_{0a}$ (Fig. 10d) is

$$V_c = \frac{1}{2}\int_0^a\int_0^{y_{0a}} Dw = \int_0^a\int_0^{y_{0a}} t\tau w\left(\frac{\partial^2 w}{\partial x\partial y} - \frac{\partial^2 w}{\partial x^2}\sin\varphi\right)dxdy$$
$$= (\pi^2/2a)t\sin\varphi\int_0^{y_{0a}} \tau Y^2 dy \tag{59}$$

Hence the constant shear stress τ_c that is equivalent to (does the same external work as) the triangular stress distribution with edge stress τ_a in Fig. 10d is

$$\tau_c = \int_0^{y_{0a}} \tau Y^2 dy \Big/ \int_0^{b_0} Y^2 dy \tag{60}$$

τ_c was first calculated by assuming Y in the form of Eq. (10), using average values of K_2 and K_3 as found in the previous calculations. To obtain a more simple expression, Y then was assumed to vary parabolically, so that

$$Y = 4K[(y/b_0) - (y/b_0)^2] \tag{61}$$

It was found that the result was in satisfactory accordance with the more accurate result using Eq. (10). With the triangular stress distribution (see Fig. 10d)

$$\tau = \tau_a[1 - (y/y_{0a})] \tag{62}$$

and using Eq. (61), Eq. (60) yields, with the substitution $y_{0a}/b_0 = y_a/b$ (see Fig. 10d),

$$\tau_c = [(y_a/b)^5 - 3(y_a/b)^4 + 2.5(y_a/b)^3]\tau_a \tag{63}$$

Hence, the shear stress distribution in Fig. 10b is equivalent to a constant shear stress in Fig. 10c of

$$\tau_{eq} = \tau + [(y_a/b)^5 - 3(y_a/b)^4 + 2.5(y_a/b)^3]\tau_a + [(y_b/b)^5 - 3(y_1/b)^4 + 2.5(y_1/b)^3]\tau_b \tag{64}$$

where τ_a and τ_b are given by Eqs. (55) and (56). For materials with a diagram like mild steel the distances y_a and y_b are the widths of the upper and lower plastic regions, as shown in Fig. 10. For materials with a smooth stress-strain diagram y_a and y_b should be measured up to the points where the proportional limit can be assumed to be reached, as shown in Fig. 11. Also then the shear stress distribution in the associated elastic case can be assumed to vary linearly over the distances y_a and y_b. From Fig. 11 and Eqs. (55) and (56), Eq. (64) may be written more generally as

$$\tau_{eq} = \tau\{1 + [(y_a/b)^5 - 3(y_a/b)^4 + 2.5(y_a/b)^3][(\sigma_{01}/\sigma_{xu}) - 1] + [(y_b/b)^5 - 3(y_b/b)^4 + 2.5(y_b/b)^3][(\sigma_{02}/\sigma_{xl}) - 1]\} \quad (65)$$

Determination of the Plastic Reduction Factor for the Cases Investigated

In the case of combined shear and bending, computed in the foregoing, in Fig. 6 the distance $d = b/4$, so that $\sigma_{01} = 2\sigma_{xp}$. Hence, in Eq. (65),

$$y_a = y_b = b/4 \quad \text{and} \quad \sigma_{01}/\sigma_{xu} = \sigma_{02}/\sigma_{xl} = \sigma_{01}/\sigma_{xp} = 2$$

This yields $\tau_{eq} = 1.0566\tau$. Further, in the equivalent associated elastic case (Fig. 10c),

$$\sigma_{xe} = \sigma_{01} = 2\sigma_{xp} = 2\tau\sqrt{3}$$

so that the ratio $\sigma_{xe}/\tau_{eq} = 3.28$. From reference 16 this gives

$$\sigma_{xe} = 15.27\pi^2N/(b^2t)$$

From Eq. (35) the buckling stress for the pertinent plastic case is

$$\sigma_{xp} = 6.67\pi^2N/(b^2t)$$

Since it was found from Eq. (39) that for a similar elastic case the present method gives results that are about 3 per cent too high, it may be concluded that the actual value of σ_{xp} is about $6.50\ \pi^2N/(b^2t)$. Hence, the plastic reduction factor for this case, where in Eq. (49) $\alpha = 2$, is $\eta_{sc} = 6.50/15.27 = 0.425$.

In the case of combined shear and eccentric compression, evaluated in the foregoing for the case $\alpha = 1$, from comparison of Figs. 7, 10b, and 11, $\sigma_{01}/\sigma_{xu} = \sigma_{01}/\sigma_{xp} = 2$. Further, $y_b = b/2$ and $y_b = 0$, so that from Eq. (65) in the equivalent associated elastic case (see Fig. 11c) $\tau_{eq} = 1.156\tau$. From Figs. 7 and 10 $\sigma_{xe} = \sigma_{01} = 2\sigma_{xp} = 2\tau\sqrt{3}$. Hence, in Eq. (52)

$$\tau = 1.156\tau,\ \sigma_{xe} = 2\tau\sqrt{3},\ \tau_{ocr} = 5.36\pi^2N/(b^2t)$$

and

$$\alpha = 1$$

From reference 17, for $\alpha = 1$,

$$\sigma_{xeocr} = 7.81\pi^2N/(b^2t)$$

Insertion of these data into Eq. (52) yields

$$\tau = 1.88\pi^2N/(b^2t)$$

Table 2
Plastic Reduction Factors

α	$(E_s/E)_u$	η_s	η_c	η_{sc}	$\eta_{sc}(67)$
2	0.5	0.425	0.50	0.425	0.432
1	0.5	0.425	0.465	0.453	0.443

so that the critical edge stress

$$\sigma_{xe} = 6.51\pi^2N/(b^2t)$$

From Eq. (44) for the pertinent plastic case,

$$\sigma_{xp} = 3.045\pi^2N/(b^2t)$$

so that, estimating its exact value 3 per cent lower,

$$\sigma_{xp} = 2.95\pi^2N/(b^2t)$$

This leads, for this case where $\alpha = 1$, to

$$\eta_{sc} = 2.95/6.51 = 0.453$$

Design Formula for the Reduction Factor

For both plastic cases that were computed ($\alpha = 2$ and 1), the ratio E_{su}/E at the upper edge (with the highest compressive strains ϵ_x) is 0.5, and $E_t/E = 0$. The reduction factor η_s for pure shear is given by Eq. (75) of reference 15 and is given graphically in Fig. 2 of reference 23, as a function of E_s/E and E_t/E. For $E_s/E = 0.5$ and $E_t/E = 0$, $\eta_s = 0.425$.

The reduction factor η_c for eccentric compression only is given by Eq. (22) of reference 1, where η_0 refers to pure compression. From Fig. 4 of reference 1 or Fig. 1 of reference 23, for $E_s/E = 0.5$ and $E_t/E = 0$, $\eta_0 = 0.43$. Hence, from Eq. (22) of reference 1, with $(E_s/E)_u = 0.5$ for $\alpha = 2$ and 1, $\eta_c = 0.5$ and 0.465, respectively. $(E_s/E)_u$, η_s and η_c are listed in Table 2. Also listed are the values $\eta_{sc} = 0.425$ and 0.453, obtained in the preceding section for $\alpha = 2$ and 1, respectively. Indeed, the values of η_{sc} are in accordance with expression (57). To find a design formula for η_{sc} it is remembered that, for the case of combined shear and homogeneous compression ($\alpha = 0$) from references 15 and 19, Eq. (27) of reference 19 applies, so that, with the present notation,

$$\eta_{sc} = (\gamma^2\eta_c + 3\eta_s)/(\gamma^2 + 3) \quad (66)$$

where $\gamma = \sigma_x/\tau$ and η_c and η_s refer to the same equivalent stress $\sigma_{eq} = \sqrt{\sigma_x^2 + 3\tau^2}$. Hence, a formula for η_{sc} has to be found that, for $\alpha = 0$, reduces to Eq. (66). Further, from Table 2, for $\alpha = 2$, η_{sc} should practically reduce to η_s, while, as shown above in connection with the development of Eq. (52), for $\alpha = 1$ it should differ only slightly from its value for $\alpha = 0$. This is accomplished by using the same fifth power of α as in Eq. (52), so that

$$\eta_{sc} = \{\gamma^2\eta_c + 3[1 + (1/4)\alpha^5]\eta_s\}/\{\gamma^2 + 3[1 + (1/4)\alpha^5]\} \quad (67)$$

where $\gamma = \sigma_{xu}/\tau$ and η_c and η_s refer to eccentric compression and shear for the same E_s and E_t as occur at the upper edge (with highest compressive stress) for the combined case. The values η_{sc} from Eq. (67)

are listed in Table 2 as η_{sc} (67). They are in good agreement with the actual values η_{sc} listed in the preceding column.

Comparison With Tests

No tests are available on plastic buckling under combined bending and shear. However, for pure compression the experimental values are in excellent agreement with theory. References to that effect have been given in the introduction and in reference 1. These results have been substantiated in reference 24. Hence, also for pure bending or eccentric compression the same good agreement may be expected to exist.

Buckling tests under pure shear have been published in reference 24 and 25. In Fig. 12 the dashed curve is the axial stress-strain curve for the aluminum alloy 24 S-O used in reference 25. Plotting the equivalent plastic buckling stresses $\sigma_{qp} = \tau_p \sqrt{3}$ from the author's theory versus $\sigma_{qe}/E = \tau_e \sqrt{3}/E$, where τ_e is the elastic buckling stress $\tau_e = \tau_p/\eta_s$, in a similar way as was done in Figs. 11, 12, and 13 of reference 9, the solid curve in Fig. 12 is obtained. The plastic reduction factors

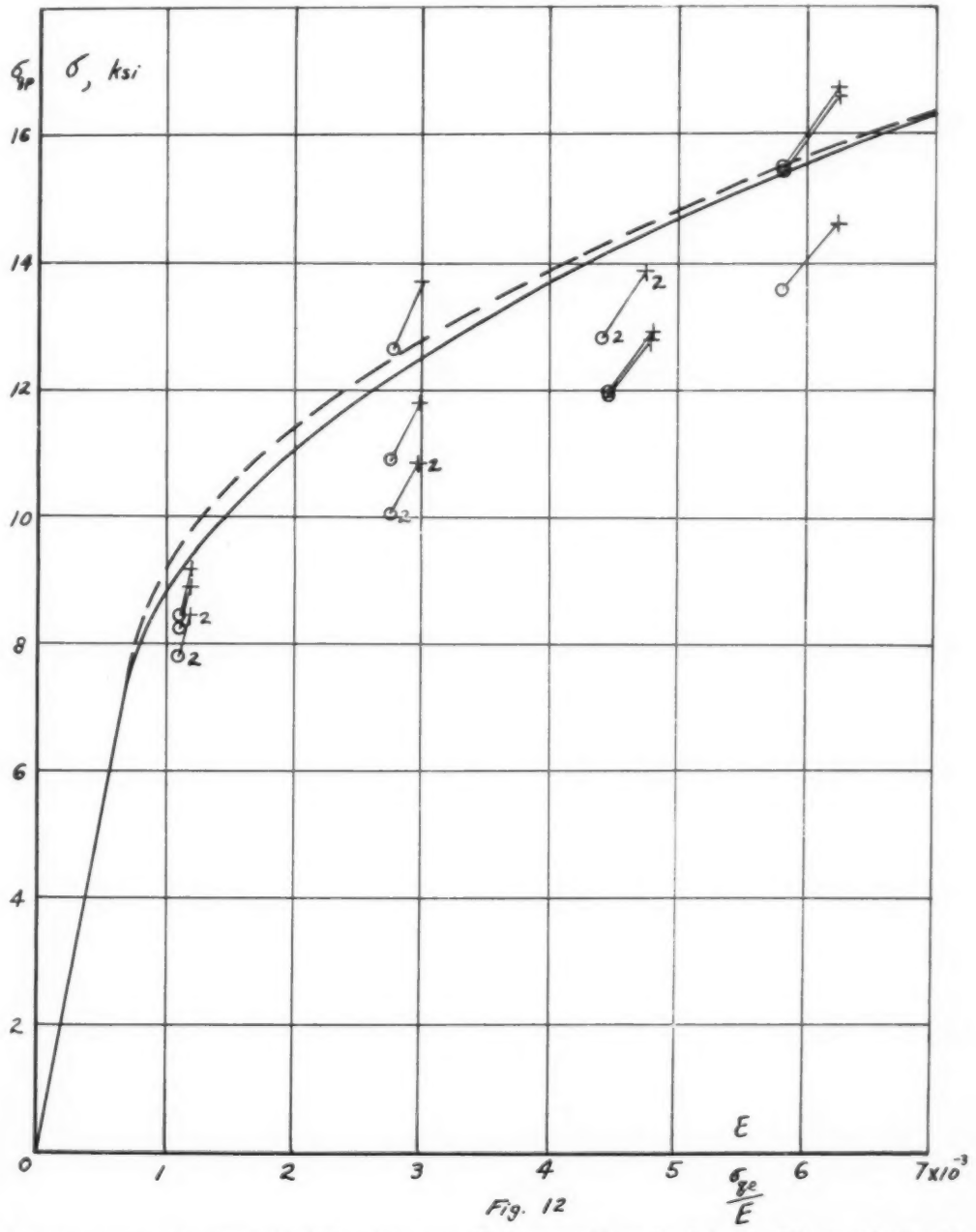

FIG. 12. Stress-strain diagram (dashed) and σ_{qp} vs. σ_{qe}/E diagram, with results of shear buckling tests by Gerard.

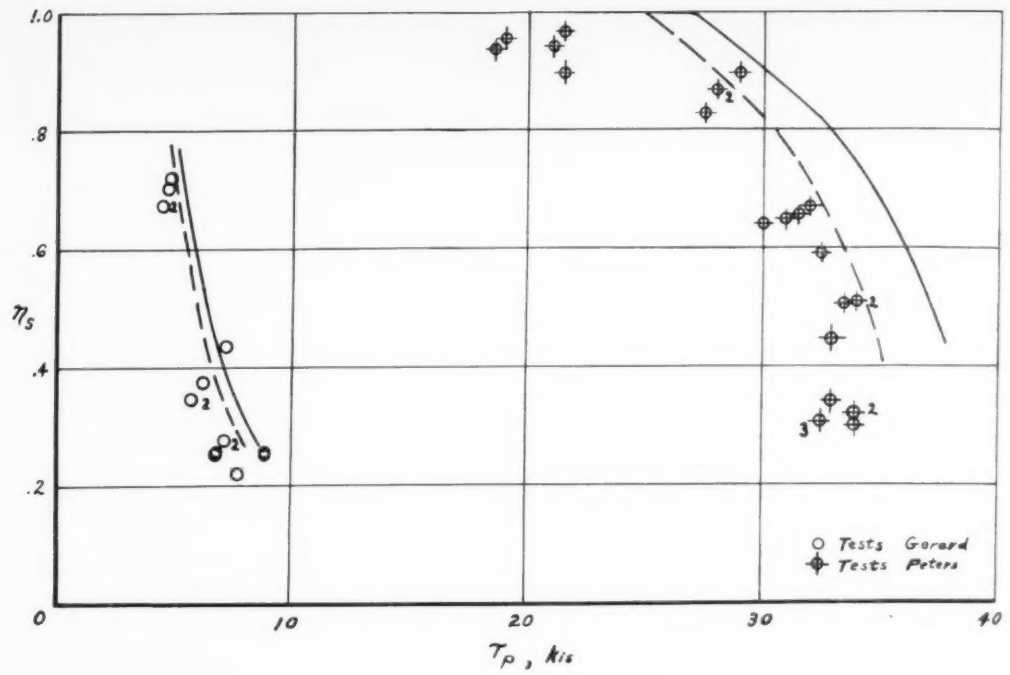

Fig. 13

FIG. 13. Diagram of plastic reduction factor η_s vs. plastic buckling stress in shear with test results by Gerard and Peters.

η_s used are those for a long plate under pure shear, as derived in reference 15 and plotted in reference 23.

From reference 25 the elastic buckling stress for the plates was $\tau_e = 6.7E(t/b)^2$. Plotting $\sigma_{qp} = \tau_p \sqrt{3}$ versus $\sigma_{qe}/E = \tau_e \sqrt{3}/E$ for the tests, where τ_p are the experimental buckling stresses, the small circles in Fig. 12 are obtained. There is considerable scatter, but two points are on and above the theoretical curve. In Fig. 13 for the same case the solid curve results from plotting the theoretical η_s values versus the plastic buckling stress τ_p, while the circles show the test results, where $\eta_s = \tau_p/\tau_e$.

In Fig. 13 also the theoretical reduction factor η_s for the material used in reference 24 has been plotted versus τ_p, again using η_s for a long plate under shear, resulting in the solid curve to the right. This curve is only slightly above that for a square plate, marked Ref. 7 and 7a, used in reference 24 in the corrected Fig. 5(b), given in Errata No. 1, NACA, Langley—8-2-54-825. The tests are presented by the crossed circles. Here the tests are all below the theoretical curve. Besides eccentricity, which causes also the elastic buckling stresses of about 20 ksi. to give η_s values below one, the reason for this discrepancy is apparently that the criterion of shearing energy, on which the writer's theory is based and which makes the equivalent axial stress σ_q equal to $\tau \sqrt{3}$, does not completely describe the behavior of the pertinent material in the region of pure shear. The actual behavior apparently deviates in the direction of the criterion of pure shear, where $\sigma_q = 2\tau$. To take this into account it is suggested η_s be calculated by assuming that a pure shear stress is equivalent to a compressive stress of the intermediate value

$$\sigma_q = \tau/0.535 = 1.87\tau \tag{68}$$

Hence, for finding η_s, one determines E_s and E_t from the uniaxial stress-strain diagram for $\sigma = 1.87\tau$ and reads η_s from Fig. 2 of reference 23 for the pertinent E_s/E and E_t/E ratios.

Using this value of σ_q the test points from reference 25 in Fig. 12 are indicated by crosses, so that in this way the theoretical curve is not too high. In Fig. 13, instead of the solid curves, the dashed ones are obtained, so that also here the agreement is satisfactory if one observes that for higher values of τ the average discrepancy is not greater than in the elastic range. Actually, for the three tests with highest discrepancy (circle denoted by 3), for $\tau = 33$ ksi., the theoretical buckling stress, as calculated in the proposed way, is 36 ksi., so that the discrepancy is only 8 per cent, while in the elastic range the discrepancy is maximum 10 per cent.

In accordance with Eq. (68), for calculating η_{sc} from Eqs. (66) and (67), η_c and η_s should be obtained from Eq. (22) of reference 1 and Figs. 1 and 2 of reference 23 for E_s and E_t belonging to the equivalent stress σ_i at the upper edge, determined by

$$\sigma_q^2 = \sigma_x^2 + (1.87\tau)^2 = \sigma_x^2 + 3.5\tau^2 \tag{69}$$

Investigation and Design of a Plate

A stress distribution is assumed, in the way explained in the section "Stress Distribution Prior to Buckling" of this paper. Let the normal edge stresses be σ_{xu} and σ_{xl} (see Fig. 11) and let the constant shear stress be τ.

Then one determines the associated elastic case. The normal stresses σ_x in this case follow directly from the normal strains in the plastic case as $E\epsilon_x$, where E is the elastic modulus. The edge stresses in this elastic case are σ_{01} and σ_{02} (see Fig. 11). The distances y_a and y_b in Fig. 11 are equal to the widths of the plastic regions, that is, where the stresses are above the proportional limit. Then in Eq. (65) all values are known, so that τ_{eq} for the equivalent elastic case (see Fig. 10c) can be calculated. The largest compressive edge stress for this case is $\sigma_{xe} = \sigma_{01}$. The buckling stresses τ_{eq} and σ_{xe} for this equivalent elastic case can be found from reference 16 if α in Eq. (49) is 2 (combined shear and bending). If α differs from 2 they are given approximately by Eq. (52), where $\tau = \tau_{eq}$ and τ_{ocr} and σ_{xocr} are the critical stresses if only τ or only σ_x (with the same parameter α) are acting. With the known ratio $\sigma_{xe}/\tau = \sigma_{xe}/\tau_{eq}$, Eq. (52) is solved for σ_{xe}. Then the actual critical edge stress σ_{xu} in the plastic case is $(\sigma_{xu})_{cr} = \eta_{sc}\sigma_{xe}$, where η_{sc} is given by Eq. (67). η_c and η_s in Eq. (67) are the plastic reduction factors for eccentric compression only and for pure shear, respectively, for the ratios E_s/E and E_t/E that prevail at the upper edge (where the compressive strain is largest). E_s and E_t are found from the uniaxial stress-strain diagram at the equivalent compressive stress σ_q from Eq. (69). For a stress distribution as in Fig. 10, $E_s = (\sigma_{xp}/\sigma_{01})E$ and $E_t = 0$. η_c is given by Eq. (22) of reference 1 where η_0 can be read from Fig. 1 of reference 23. η_s can be read from Fig. 2 of reference 23. Further, in Eq. (67), $\gamma = \sigma_{xu}/\tau$, where τ is the actual constant shear stress in the plastic case. If the value of $(\sigma_{xu})_{cr}$ is higher than the assumed edge stress σ_{xu} the plate is stable.

To find the required thickness for withstanding a given stress distribution, with an edge critical stress σ_{xu} one determines $(\sigma_{xu})_{cr}$ in the same way as explained above and expresses it in the form

$$(\sigma_{xu})_{cr} = \eta_{sc}k_c(\pi^2 N/b^2 t) = k_p(\pi^2 N/b^2 t) = 0.905k_p E(t/b)^2$$

where k_c is the buckling stress coefficient for the associated elastic case and k_p is the plastic buckling stress coefficient.

Hence the plate thickness required for an edge critical stress σ_{xu}, as assumed, is

$$t = 1.05(\sigma_{xu}/k_p E)^{1/2} b \qquad (70)$$

References

[1] Bijlaard, P. P., *Theory of Plastic Buckling of Plates and Application to Simply Supported Plates Subjected to Bending or Eccentric Compression in Their Plane*, ASME, Paper No. 55-A-8, Journal of Applied Mechanics, Vol. 23, No. 1, pp. 27–34, March, 1956.

[2] Bijlaard, P. P., *A Theory of Plastic Stability and Its Application to Thin Plates of Structural Steel*, Proc. Roy. Acad., Sci. Amsterdam, No. 7, pp. 731–743, 1938.

[3] Bijlaard, P. P., *Theory of the Plastic Stability of Thin Plates*, Publ. International Association for Bridge and Structural Engineering, Zürich, Vol. 6, pp. 45–69, 1940–41.

[4] Bijlaard, P. P., *Theory and Tests on the Plastic Stability of Plates and Shells*, Journal of the Aeronautical Sciences, Vol. 16, No. 9, pp. 529–541, 1949.

[5] Bijlaard, P. P., *Theory of Local Plastic Deformations*, Publ. International Association for Bridge and Structural Engineering, Zürich, Vol. 6, pp. 27–44, 1940–41.

[6] Kollbrunner, C. F., *Das Ausbeulen der auf einseitigen, gleichmässig verteilten Druck beanspruchten Platten im elastischen und plastischen Bereich*, Mitt. a. d. Institut fur Baustatik a. d. E. T. H., Zürich, Switzerland, No. 17, 1946.

[7] Bijlaard, P. P., Kollbrunner, C. F., and Stüssi, F., *Theorie und Versuche über das plastische Ausbeulen von Rechteckplatten unter gleichmassig verteiltem Langsdruck*, International Association for Bridge and Structural Engineering, Third Congress, Liège, Belgium, September, 1948, Preliminary Publication, pp. 119–128, 1948.

[8] Schuette, E. H., and McDonald, J. C., *Prediction and Reduction to Minimum Properties of Plate Compressive Curves*, Journal of the Aeronautical Sciences, Vol. 15, pp. 23–27, January, 1948.

[9] Bijlaard, P. P., *Theory and Tests on the Plastic Stability of Plates and Shells*, Journal of the Aeronautical Sciences, Vol. 16, No. 9, pp. 529–541, September, 1949.

[10] Pride, R. A., and Heimerl, G. J., *Plastic Buckling of Simply Supported Compressed Plates*, NACA TN 1817, April, 1949.

[11] Pride, R. A., *Plastic Buckling of a Simply Supported Plate in Compression*, Journal of the Aeronautical Sciences, Vol. 19, No. 1, pp. 69–70, January, 1952.

[12] Teodosiadis, R., Langhaar, H. L., and Smith, J. O., *Inelastic Buckling of Flat Plates*, First Midwestern Conference on Solid Mechanics, Engineering Experiment Station, University of Illinois, Urbana, Ill., April, 1953.

[13] Feigen, M., *Inelastic Behavior under Combined Tension and Torsion*, Proc. Second U.S. National Congress of Applied Mechanics, pp. 369–476, Ann Arbor, Michigan, 1954.

[14] Timoshenko, S., *Theory of Elastic Stability*, McGraw-Hill Book Company, Inc., New York, 1936.

[15] Bijlaard, P. P., *Analysis of the Elastic and Plastic Stability of Sandwich Plates by the Method of Split Rigidities—II*, Journal of the Aeronautical Sciences, Vol. 18, No. 12, pp. 790–796, 829, December, 1951.

[16] Johnson, A. E., and Buchert, K. P., *Critical Combinations of Bending, Shear, and Transverse Compressive Stresses for Buckling of Infinitely Long Flat Plates*, NACA TN 2536, 1951.

[17] Kollbrunner, C. F., *Present Situation in Switzerland with Regard to Experiments on Buckling with Indication of the Buckling Values k*, 15th Internat. Congress of the Steel Information Centres, Brussels, October 5–9, 1953.

[18] Batdorf, S. B., and Stein, M., *Critical Combinations of Shear and Direct Stress for Simply Supported Rectangular Flat Plates*, NACA TN 1223, 1947.

[19] Bijlaard, P. P., *Analysis of the Elastic and Plastic Stability of Sandwich Plates by the Method of Split Rigidities—I*, Journal of the Aeronautical Sciences, Vol. 18, No. 5, pp. 339–349, May, 1951.

[20] Pflüger, A., *Stabilitätsprobleme der Elastostatik*, Springer-Verlag, Berlin, 1950.

[21] Bijlaard, P. P., *Analysis of the Elastic and Plastic Stability of Sandwich Plates by the Method of Split Rigidities—III*, Journal of the Aeronautical Sciences, Vol. 19, No. 7, p. 502, July, 1952.

[22] Bijlaard, P. P., and Fisher, G. P., *Column Strength of H-Sections and Square Tubes in Postbuckling Range of Component Plates*, NACA TN 2994, 1953.

[23] Krivetsky, A., *Plasticity Coefficients for the Plastic Buckling of Plates and Shells*, Journal of the Aeronautical Sciences, Vol. 22, No. 6, p. 432–435, June, 1955.

[24] Peters, R. W., *Buckling of Long Square Tubes in Combined Compression and Torsion and Comparison with Flat-Plate Buckling Theories*, NACA TN 3184, May 1954, with Errata No. 1, NACA, Langley—8-2-54-825.

[25] Gerard, G., *Critical Shear Stress of Plates Above the Proportional Limit*, Journal Applied Mechanics, Vol. 15, No. 1, pp. 7–12, March, 1948.

[26] Bijlaard, P. P., *Plastic and Elastic Buckling Stresses of Clamped Plates and Clamped and Simply Supported Flanges Subjected to Bending or Eccentric Compression in Their Plane*, Engineering Mechanics Division, ASCE (to be published).

Readers' Forum

BRIEF REPORTS of investigations in the aeronautical sciences and discussions of papers published in the JOURNAL are presented in this special department. Entries must be restricted to a maximum of 1,300 words or the equivalent of one JOURNAL page including formulas and illustrations. Publication is completed as soon as possible after receipt of the material. The Editorial Committee does not hold itself responsible for the opinions expressed by the correspondents.

Contents

The Interaction of a Reflected Shock Wave With the Boundary Layer in a Shock Tube.....HERMAN MARK 304

Automatic Control With Artificial Inertia...G. M. ANDREW 306

An Analytic Form of the Principle of Maximum Power .....CARLO RIPARBELLI 307

The Significance of Zero Shear Stress in the Pure Bending of a Wide Curved Bar.....
...BERNARD W. SHAFFER AND RAYMOND N. HOUSE, JR. 307

Further Remarks on the Collapse Pressures of Uniformly Loaded Spherical Shells.....BERTRAM KLEIN 309

Buckling Loads of Pin-Ended Fluid Columns.ERYK KOSKO 309

Effect of the Change in Thermal Stresses Due to Large Deflections on the Torsional Rigidity of Wings.....
.....JOSEF SINGER AND N. J. HOFF 310

Leading-Edge Temperature of a Flat Plate Subjected to Aerodynamic Heating.....A. E. BRYSON, BERNARD BUDIANSKY, AND GEORGE F. CARRIER 311

Vortex-Ring Cascade and a Conjectured Model of Transition to Turbulence.....C. S. HSU 313

Note on Tip-Bluntness Effects in the Supersonic and Hypersonic Regimes.....F. D. BENNETT 314

On the Couette Flow of a Compressible, Viscous, Heat-Conducting, Perfect Gas.....A. J. A. MORGAN 315

Inversion of the Prandtl-Meyer Relation for Specific-Heat Ratios of 5/3 and 5/4.....RONALD F. PROBSTEIN 316

Damping Due to Internal Flow.....
.....A. W. GILMORE AND T. L. KELLER 317

The Analytic Study of Laminar Boundary-Layer Stability in Free Convection.....J. E. PLAPP 318

Choking Flow in Curved Ducts.....F. F. EHRICH 319

The Interaction of a Reflected Shock Wave With the Boundary Layer in a Shock Tube†

Herman Mark*

Graduate School of Aeronautical Engineering, Cornell University, Ithaca, N.Y.

October 24, 1956

INTRODUCTION

IDEALLY, the reflection of a shock from the closed end of a shock tube provides a slug of stationary, high-temperature gas very useful for study in a number of important applications. In the real case, however, the presence of the walls of the tube will cause the build-up of a boundary layer in the flow following the initial shock wave. The existence of this growing boundary layer causes attenuation in the strength of the shock wave before reflection and adds complication to the simple picture of the reflected shock bringing the flow to rest. Investigations have been made to describe the viscous and thermal interactions of the flow with the walls of the tube[1] and to explain the effects of the presence of the wall on attenuation of the initial shock.[2] The purpose of the present note is to report some of the results of an analytical and experimental study, made at the Cornell University Graduate School of Aeronautical Engineering, of the interactions of the reflected shock with the boundary layer of the flow behind the initial shock and the effects of these interactions on the flow behind the reflected shock.

REGIONS OF INTERACTION

Given the Mach Number M_1 of the initial shock wave, the Mach Number M_3 of the ideal reflected shock wave may be calculated from the interesting relation

$$M_2 M_3 = 1 \tag{1}$$

where M_2 is the Mach Number of the flow behind the initial shock in the coordinate system moving with that shock (see reference 6, p. 153). If we examine the interaction phenomenon in a coordinate system moving with the reflected shock, the situation as presented in Fig. 1 is encountered.

u_4 is the velocity of the wall in the coordinate system we have chosen, and thus it is the velocity of a very small layer of fluid close to the wall. Since we are searching only for the boundaries of interaction regions, it is sufficient for this purpose to describe the entire boundary layer [in which the actual $M(y)$ is $> M_{BL}$ but $< M_3$] by a jet of fluid of Mach Number $M_{BL} \equiv u_4/a_1$. The use of sound speed associated with conditions 1 is based on the results of reference 1 wherein it has been shown that T^*, the temperature at the wall after the passage of the initial shock, can be very closely approximated by T_1. Thus we have

† This research was supported jointly by the United States Air Force through the Office of Scientific Research of ARDC and the Mechanics Branch of the Office of Naval Research. Reproduction in whole or in part is permitted for any purpose of the United States Government.

* The author is indebted to Prof. N. Rott for many helpful suggestions.

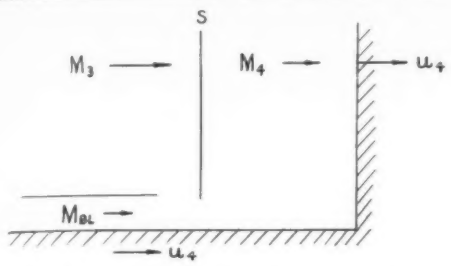

FIG. 1. Flow relative to the reflected shock S.

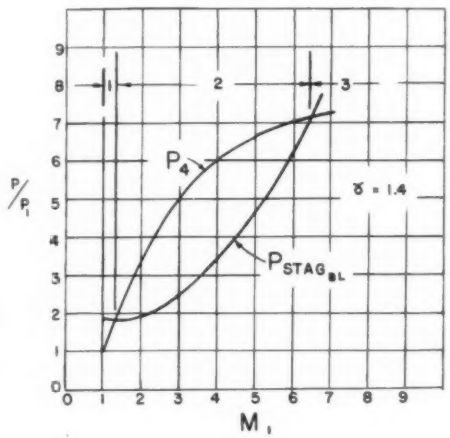

FIG. 2. Pressure ratios of the flow behind the undisturbed shock P_4 and the stagnation pressure of the boundary layer $P_{stag_{BL}}$ to the initial pressure P_1 plotted versus the Mach Number of the initial shock M_1.

$$M_{BL} = [2(\gamma - 1)M_1^2 + (3 - \gamma)]/(\gamma + 1)M_1 \qquad (2)$$

M_{BL} is then a function only of M_1 and γ.

By comparing the stagnation pressure of the boundary-layer fluid described by M_{BL} with the pressure behind the reflected shock at M_2 (Fig. 2) we can see that, in regions 1 and 3 of the Mach Number range, the stagnation pressure of the boundary layer exceeds the pressure behind the undisturbed shock. Thus we can expect the boundary layer to pass continuously under the foot of the shock and into the region behind reflection. We notice, however, that in region 2 of the Mach Number range the stagnation pressure of the boundary layer is exceeded by the pressure behind the undisturbed reflected shock. We cannot therefore expect a simple steady through flow of the boundary-layer fluid in this Mach Number range. Rather we expect that there will be a gathering up of this boundary-layer fluid in a region adjacent to the foot of the shock—i.e., the fluid which cannot proceed into the higher pressure region behind the reflected shock. Hess[3] has suggested a similar phenomenon in the interaction of shock waves with thermal boundary layers, and this has been investigated by Griffith and Bleakney.[4]

Fig. 3 is a representative photograph of the interaction that is observed at a value of M_1 ($M_1 = 2.15$) within region 2 of Fig. 2, and Fig. 4 is a schematic description of this interaction as constructed from many photographs of the phenomenon. The boundary-layer flow characterized by $M_{BL} > 1$ (such is the case if $M_1 > 2.00$) passes through a normal shock and then compresses subsonically to stagnation pressure. Associated with this compression is the diffusion angle of the flow boundary which can be seen quite clearly in Fig. 3 and which may be used to calculate with good accuracy the angle of the main "foot" of the interaction. The line extending rearward from the triple point is the boundary between that part of the main flow which has passed through the two oblique shocks of the pattern and that part of the main flow which has passed through the single normal shock. For $Re < \sim 900{,}000$, where

$$Re \equiv \tfrac{1}{2}\rho_u(u_3 - u_4)^2 x[1 + (u_1/u_4)]^{\frac{1}{2}}/\mu_u u_1$$

this flow picture grows as it gets further from the reflecting wall but remains geometrically similar—i.e., a quasi-steady or "conical" situation exists. At higher Reynolds Number, the picture gradually changes (presumably as the boundary layer becomes turbulent) until the interaction of Fig. 4 disappears. The resulting picture is that of a normal shock propagating along the tube with slight concavities forward at the walls of the tube. Doubtless this is the same interaction as that of Fig. 4 but of a much smaller scale and so not visible as such in the photograph. The upper limit of $Re \approx 900{,}000$ for the interaction of Fig. 4 was determined by two separate series of experiments. In the first series, Reynolds Number was varied by allowing only the distance from the reflecting wall to vary. In the second series all quantities were held constant, but the density was varied over an appropriate range. Although the Re for transition obtained from each of these two series was approximately the same ($\sim 900{,}000$) it is as yet not certain that Re as defined above is a universal constant for all shock strengths.

The interaction in the Mach Number ranges 1 and 3 of Fig. 2 is of the type similar to that described by Griffith[5] in discussing the interaction of shock waves with thermal boundary layers. In this case, the boundary layer can pass under the shock into the region behind reflection, and a steady flow (not considering the growth of the boundary layer) is possible. The interaction is of a much less violent nature, and the reflected shock is disturbed much less than in the case previously described. In the range of Re for which photographs were taken, the reflected shock appears to be, in fact, almost undisturbed. It was not possible to verify experimentally the boundary between regions 2 and 3 of Fig. 2 ($M_1 = 6.45$ for $\gamma = 1.4$) since γ falls for diatomic gases in this temperature range, and the boundary itself moves rapidly to higher Mach Numbers as γ falls. [As γ falls, the value for

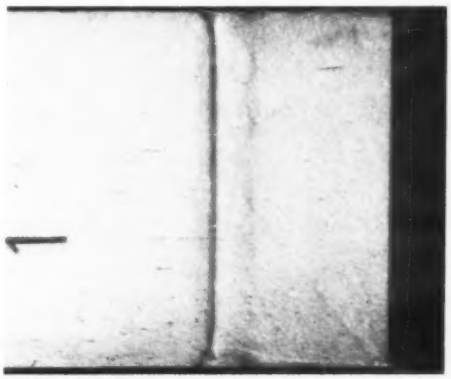

FIG. 3. Typical photograph of the interaction of region 2, Fig. 2, shortly after reflection (Re<900,000).

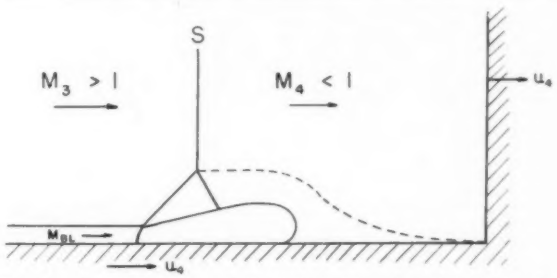

FIG. 4. A construction of the interaction of region 2, Fig. 2, shortly after reflection (Re<900,000).

the crossover M_1 goes approximately as $\sqrt{2}(\gamma - 1)^{-3/2}$.] Verification of the existence of region 3 and an experimental check on the boundary between regions 2 and 3 was possible, however, for gas mixtures of suitable γ and small γ variation. In the actual experiment, argon, only slightly diluted with air (resulting $\gamma = 1.62$), was used. The double-foot wedge interaction was obtained in region 2 for this gas mixture, but when the Mach Number was increased above the corresponding upper boundary of region 2 (Fig. 2) (and $Re < 900{,}000$), the mild interaction of region 1 reappeared.

Early publication of a detailed report of this investigation is intended.

References

[1] Rott N., and Hartunian, R. A., *On the Heat Transfer to the Walls of a Shock Tube*, Cornell Univ., Graduate School of Aeronautical Engineering Report [Contract AF 33 (038)-21406], November, 1955.

[2] Mirels, H., *Attenuation in a Shock Tube Due to Unsteady Boundary-Layer Action*, NACA TN 3278, August, 1956.

[3] Hess, R. V., *The Interaction of a Shock Wave with a Thermal Boundary Layer*, unpublished.

[4] Griffith, W. C., and Bleakney, W., *The Diffusion Analogy to Interaction of a Shock with a Thermal Boundary Layer*, Princeton Univ., Dept. of Physics, Tech. Report II-17 (NR061-020), January, 1955.

[5] Griffith, W. C., *Interaction of a Shock Wave with a Thermal Boundary Layer*, Journal of the Aeronautical Sciences, Vol. 23, No. 1, pp. 16–22, 66, January, 1956.

[6] Courant, R., and Friedrichs, K. O., *Supersonic Flow and Shock Waves*; Interscience Publishers, Inc., New York, 1948.

Automatic Control With Artificial Inertia*

G. M. Andrew
Missile Division, North American Aviation, Inc., Downey, Calif.

October 31, 1956

Summary

The behavior of a second-order system with built-in artificial inertia is analyzed and illustrated on the records from the analog computer.

Discussion

THE GENERAL TREND in servomechanisms is to get as fast a response of the system as possible. This being an orthodox case, there are special situations where the slow response of the system can be very beneficial. The analysis given in this paper applies to such cases.

To illustrate, consider roll stabilization of small missiles. They have hardly any inherent aerodynamic damping, thus they require an extremely fast servo; otherwise a large displacement would build up very rapidly. Increasing the rolling moment of inertia allows the servo to slow down and to do still a very satisfactory job by reducing the rolling displacement to a tolerable value.

As another example, take an airplane fuselage having a very slow first bending mode only slightly higher than the frequency of the aerodynamic pitching mode. By introducing a large artificial pitching moment of inertia, we can slow down considerably the aerodynamic mode well below the frequency of a critical aeroelastic mode in order to reduce the coupling. Thus a servo much slower than the aeroelastic mode can be used. The frequency interval between the servo frequency and first bending mode can be used for accommodation of a filter which prevents the danger of excitation of an aeroelastic mode.

The basic problem will be illustrated on the pitching motion of the airplane simplified to one degree of freedom.

The equation of motion of an uncontrolled airplane can be written in operational form (for initial conditions zero)

$$[s^2 + (M_{\dot\theta}/I)s + (M_\theta/I)]\theta(s) = 0 \qquad (1)$$

(for level flight $M_\theta = M_\alpha$) or

$$(s^2 + 2\zeta\omega_n s + \omega_n{}^2)\,\theta(s) = 0 \qquad (1a)$$

ω_n and ζ being the frequency and damping ratio of the pitching mode of the uncontrolled airplane.

When the airplane is controlled by an autopilot with ideal servo (instantaneous response), Eq. (1) shall be modified by a term on the right side of the equation

$$[s^2 + (M_{\dot\theta}/I)s + (M_\theta/I)]\theta(s) = (M_\delta/I)\delta(s) \qquad (2)$$

If we want to introduce artificial moment of inertia, the command signal for the elevator displacement can be written

$$\delta(s) = (-k_{\ddot\theta}\, s^2 - k_{\dot\theta} s - k_\theta)\,\theta(s) \qquad (3)$$

The first term in Eq. (3) represents artificial inertia, the second artificial damping, and the third artificial stiffness. Substituting Eq. (3) into Eq. (2) and rearranging yields

$$\{[1 + (M_\delta/I)k_{\ddot\theta}]s^2 + [(M_{\dot\theta}/I) + (M_\delta/I)k_{\dot\theta}]s + [(M_\theta/I) + (M_\delta/I)k_\theta]\}\theta(s) = 0$$

or

$$\{s^2 + [(M_{\dot\theta} + M_\delta k_{\dot\theta})/(I + M_\delta k_{\ddot\theta})]s + [(M_\theta + M_\delta k_\theta)/(I + M_\delta k_{\ddot\theta})]\}\theta(s) = 0 \qquad (4)$$

From Eq. (4) we can see that an airplane with autopilot can be compared to an uncontrolled system if the inertia term is increased by $(M_\delta k_{\ddot\theta})$, the damping term by $(M_\delta k_{\dot\theta})$, and the stiffness by $(M_\delta k_\theta)$.

In order to see the effect of an artificial inertia term, numerical values for a typical configuration were substituted into Eq. (2). In Eq. (3), $k_{\dot\theta}$ and k_θ were assumed zero; that yielded Eq. (4a) which was used in the analog computer. The recording of the computer runs for different values of $k_{\ddot\theta}$ are reproduced in this paper.

$$(D^2 + 9D + 40)\theta(t) = -(M_\delta/I)k_{\ddot\theta}\, D^2\theta(t) \qquad (4a)$$

Fig. 1 represents the case for which $k_{\ddot\theta} = 0$. Then gradually the artificial moment of inertia was added covering the following values: $k_{\ddot\theta} = 0.5$ (Fig. 2), 1.0 (Fig. 3), 1.5 (Fig. 4), 2.0 (Fig. 5), 3.0 (Fig. 6), 4.0 (Fig. 7), and 10.0 (Fig. 8). It can be seen clearly how a very nervous heavily damped system (Fig. 1) transforms gradually by artificial inertia into a slowly oscillating system (Fig. 8) having still a very satisfactory damping ratio (which could be increased if desired by increasing the rate gain $k_{\dot\theta}$).

The above system had an ideal servo. For a real servo, assume the response delayed by time T. We can evaluate this influence

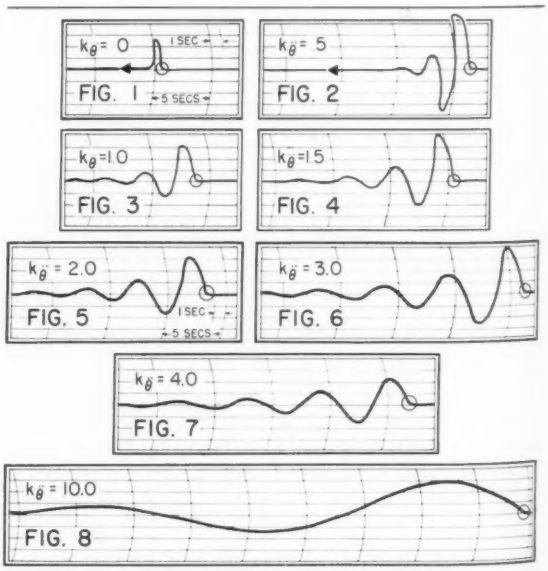

* Presented at the 9th Congress of Applied Mechanics, Brussels, Belgium, September, 1956.

by replacing, in Eq. (3), t by $(t - T)$ and taking the Laplace transformation for initial conditions zero. The time lag T changes Eq. (3) into Eq. (3a):

$$\delta(s) = (-k_{\ddot{\theta}}\, s^2 - k_{\dot{\theta}}\, s - k_\theta) e^{-sT} \theta(s) \qquad (3a)$$

Expanding e^{-sT} into series and taking only the first term yields

$$\delta(s) = (-k_{\ddot{\theta}}\, s^2 - k_{\dot{\theta}}\, s - k_\theta)\,(1 - Ts)\theta(s) \qquad (3b)$$

Substituting Eq. (3b) into Eq. (2) yields, after rearranging,

$$\left\{ s^2 + \frac{[M_{\dot{\theta}} + (1 - Ts)M_\delta k_{\dot{\theta}}]}{[I + (1 - Ts)M_\delta k_{\ddot{\theta}}]}\, s + \frac{[M_\theta + (1 - Ts)M_\delta k_\theta]}{[I + (1 - Ts)M_\delta k_{\ddot{\theta}}]} \right\} \theta(s) = 0 \qquad (5)$$

To evaluate the influence of the real servo and the system with artificial inertia, substitute $s = j\omega$ into Eq. (5). The vector signal $M_\delta k_{\ddot{\theta}}$ along the positive real axis now becomes complex, $(M_\delta k_{\ddot{\theta}} - j\omega T M_\delta k_{\ddot{\theta}})$ having a component along the negative imaginary axis $\omega T\, M_\theta k_{\ddot{\theta}}$. The vector signal is now inclined to the real axis at a lag angle $\psi = \tan^{-1}(-\omega T)$ and has the magnitude $M_\delta k_{\ddot{\theta}} \sqrt{1 + \omega^2 T^2}$.

An Analytic Form of the Principle of Maximum Power

Carlo Riparbelli
Convair, San Diego, A Division of General Dynamics Corporation
November 2, 1956

THE "principle of maximum power," outlined in heuristic form in reference 1,* can be formulated analytically as an extension of the principle of minimum energy of which the principle of minimum total potential energy as used in statics and Hamilton's principle are well-known forms.

Consider a mechanical system whose motion is defined in terms of a family of functions u, v, w (velocity components) of the coordinates x, y, z, t. The said functions are assumed to satisfy the conditions of continuity and the boundary conditions and to be defined through appropriate parameters by means of the extremum conditions

$$\delta \left\{ \iiiint \epsilon(u, v, w)\, dx\, dy\, dz\, dt \right\} = 0$$

$$\delta^2 \{\quad\} > 0$$

the integration being extended to the whole volume in the four dimensions x, y, z, t.

Let us now assume that none of the functions u, v, w depends on the variable t, while the system extends into the t direction. In other words, the distribution of u, v, w is the same at all the sections of the system orthogonal to t. The integration in dt is therefore immediate, and it can be extended to an arbitrary interval Δt, giving an arbitrary factor (which can be taken as a unit) to multiply the remaining integrals. The extremum condition can then be written

$$\delta \left\{ \iiint \epsilon(u, v, w)\, dx\, dy\, dz \right\} = 0$$

$$\delta^2 \{\quad\} > 0$$

and it does not contain the time anymore. The same way of reasoning is used, for instance, in the analysis by energy principles of the torsion of a bar of infinite length under Saint Venant's assumptions. In that case, only three coordinates are used. u, v, w are displacements, and the energy principle is applied to *a unit length* of the bar in the direction of its axis.

By applying the same deduction to a mechanical system in steady motion, the principle of maximum power is found, and its expression is the same as that of Hamilton's principle, provided that ϵ is all the transformable energy connected with the system, *including the energy introduced at every time unit* (that is, the power introduced × time unit, with minus sign) *and the energy dissipated at every time unit* (power dissipated × time unit, with plus sign). These signs are consistent with the form of a minimum given above to the extremum conditions.

The assumption that none of the parameters depends upon the time is justified if the motion is steady. It is seen, however, that the same conclusion is valid for a periodic motion, provided that the integral over the time is extended to any number of complete periods. Also, random motions can be included, provided the transformable energy connected with the system is known to be a constant in a statistical meaning, as in turbulent steady flows.

Consistently with the above deduction, the principle appears to be valid for linear and nonlinear systems.

REFERENCE

[1] Riparbelli, C., *A Principle of Maximum Power for Real Fluids in Steady Motion*, Readers' Forum, Journal of the Aeronautical Sciences, Vol. 23, No. 10, pp. 971, 972, October, 1956.

The Significance of Zero Shear Stress in the Pure Bending of a Wide Curved Bar†

Bernard W. Shaffer* and Raymond N. House, Jr.**
New York University, New York, and American Bosch Arma Corporation, Garden City, N.Y., Respectively
November 2, 1956

SUMMARY

A general solution is obtained for the displacements and strains within a wide curved bar made of an incompressible, perfectly plastic material subjected to zero shear stress. The solution, which is equally applicable for the elastic and plastic regions of the bar, shows that plane sections remain plane throughout the loading program.

INTRODUCTION

IN A RECENT PAPER, the authors have investigated the elastic-plastic stress distribution in a wide curved bar subjected to pure bending.[1] The analysis showed that during the bending process the shear stress across every radial section in the bar is equal to zero, even though part of the bar is within the plastic range. It is the objective of the current paper to interpret the significance of these results in order to shed some light on the displacement problem.

As in the case of the previous paper, the curved bar will be analyzed as a problem of plane strain. For the type of applied load being considered, the bending moment is the same in each radial cross section, and, consequently, the stress and strain distributions are functions of the radius r and not the angle θ.

The shear stress at each radial cross section is equal to zero in both the elastic and plastic regions of the bar.[1] Consequently, the shearing strain within the entire bar is also equal to zero. This follows from Hooke's Law which applies in the elastic domain and the Prandtl-Reuss Law[2] which applies in the plastic domain.

* An obvious error in the last equation in reference 1 should be corrected by dividing the energy term, instead of the two power terms, by the time factor (which can be taken as a unit).

† The results presented in this paper were obtained in the course of research sponsored by the Office of Ordnance Research, Department of the Army (Ordnance Corps) under Contract No. DA-30-069-ORD-1398, with New York University.

The authors wish to thank Dr. P. G. Hodge, Jr., and Dr. F. Lane for their valuable suggestions on an earlier draft of the current note.

* Associate Professor of Mechanical Engineering, New York University.

** Formerly, Instructor of Mechanical Engineering, New York University. Now, Senior Engineer, Project Research Department, American Bosch Arma Corporation.

In an attempt to find a closed solution of the problem and, therefore, one which may be relatively easy to apply, it will be assumed that the bar is made of a perfectly plastic material which is incompressible in both the elastic and plastic regions. This type of assumption has been used previously in finding the solution of other elastic-plastic problems with reasonable success.[2]

The Governing Equations

If the radial, circumferential, and longitudinal components of displacement are called u, v, and w, respectively, where the longitudinal component of displacement w is equal to zero because we are concerned with a problem of plane strain, then the expressions for strains in polar coordinates may be written[3, 4]

$$\epsilon_r = \partial u/\partial r, \quad \epsilon_\theta = (u/r) + (1/r)(\partial v/\partial \theta), \quad \epsilon_z = \partial w/\partial z = 0 \tag{1a}$$

$$\gamma_{r\theta} = (1/r)(\partial u/\partial \theta) + (\partial v/\partial r) - (v/r) \tag{1b}$$

For an incompressible material the mean normal strain[2]

$$e = (1/3)(\epsilon_r + \epsilon_\theta + \epsilon_z) \tag{2}$$

is equal to zero, and the displacement components, therefore, satisfy the differential equation

$$\partial v/\partial \theta = -u - r(\partial u/\partial r) \tag{3}$$

With the shearing strain $\gamma_{r\theta}$ equal to zero, we may write a second relationship between the displacement components—namely,

$$\partial u/\partial \theta = v - r(\partial v/\partial r) \tag{4}$$

Eqs. (3) and (4) constitute a system of simultaneous partial differential equations from which we may solve for the displacement components u and v. The solution would, of course, be subjected to the appropriate boundary conditions. Since there exists one point within the bar that neither translates nor rotates during the bending process, we may choose this point to be on the centroidal axis and write the boundary conditions as

$$u = 0, \quad v = 0, \quad \partial v/\partial r = 0, \quad \text{at } \theta = 0 \text{ and } r = r_0 \tag{5}$$

where r_0 is the radius of the centroidal axis.

The Displacements and Strains

When the applied load is a pure bending moment, the stresses and, consequently, the strains are independent of the θ coordinate. Thus, we may write, in view of Eq. (1a), that

$$\partial^2 u/\partial \theta \partial r = 0 \tag{6}$$

Consequently, should we differentiate Eq. (4) with respect to the variable r, we find that

$$r(\partial^2 v/\partial r^2) = 0 \tag{7a}$$

or

$$v = C_1(\theta) + C_2(\theta) r \tag{7b}$$

where $C_1(\theta)$ and $C_2(\theta)$ are functions of the variable θ. On the other hand, should we differentiate Eq. (4) with respect to the variable θ and introduce the expression for $\partial v/\partial \theta$ and $\partial^2 v/\partial r \partial \theta$ obtained from Eq. (3), we then find that

$$\partial^3 u/\partial \theta^3 = -(\partial u/\partial \theta) \tag{8a}$$

or

$$u = F(r) + G(r) \sin \theta + K_1(r) \cos \theta \tag{8b}$$

Upon comparing the expression for $\partial u/\partial \theta$ obtained from Eq. (8b) with the expression for $\partial u/\partial \theta$ defined in Eqs. (4) and (7b), we find that

$$C_1(\theta) = G(r) \cos \theta - K_1(r) \sin \theta \tag{9}$$

Obviously then, G and K_1 are constants, and Eqs. (9), (7b), and (8b) may be rewritten

$$v = -K_1 \sin \theta + G \cos \theta + C_2(\theta) r \tag{10a}$$

$$u = F(r) + K_1 \cos \theta + G \sin \theta \tag{10b}$$

The functions $F(r)$ and $C_2(\theta)$ may be evaluated by introducing Eqs. (10a) and (10b) into Eq. (3):

$$\partial C_2(\theta)/\partial \theta = -[F(r)/r] - [\partial F(r)/\partial r] \tag{11}$$

Each side of the resulting expression may be set equal to the constant $2B$, and the system of equations may then be solved to find that

$$C_2(\theta) = 2B\theta + K_3, \qquad F(r) = -[Br + (A/r)] \tag{12}$$

where A and K_3 are also constants. When these expressions are introduced into Eqs. (10a) and (10b), they become

$$v = 2Br\theta - K_1 \sin \theta + G \cos \theta + K_3 r \tag{13a}$$

$$u = -[(A/r) + Br] + K_1 \cos \theta + G \sin \theta \tag{13b}$$

The constants G and K_3, however, are equal to zero in view of the boundary conditions $\partial v/\partial r = 0$ and $v = 0$, when $\theta = 0$ and $r = r_0$, expressed in Eq. (5). Consequently, the components of the displacement may be written

$$v = 2Br\theta - K_1 \sin \theta \tag{14a}$$

$$u = -[(A/r) + Br] + K_1 \cos \theta \tag{14b}$$

The corresponding strains are, in view of Eqs. (1a) and (14)

$$\epsilon_r = (A/r^2) - B, \qquad \epsilon_\theta = -[(A/r^2) - B], \qquad \epsilon_z = 0 \tag{15}$$

Discussion of Results

An examination of the results obtained in the previous section shows that the terms $K_1 \cos \theta$ and $K_1 \sin \theta$ appear in the expressions for the displacement components u and v, respectively. These terms indicate a rigid body displacement of the entire bar parallel to the plane of symmetry. The remaining terms in Eq. (14a) show that the radial cross section rotates $\partial v/\partial r$ or $2B\theta$ about the center of curvature. Consequently, radial sections remain plane after deformation.

When the effect of $K_1 \cos \theta$ is temporarily neglected in examining the implication of Eq. (14b), it can easily be seen that the radial displacement u is constant whenever r is constant and, therefore, the surfaces of the bar remain cylindrical.

The previous discussion originated from the point of view that the coordinate system through the center of curvature remains fixed in space. Should we take a different point of view—namely, that the center of the bar remains fixed—then the displacement equations show that the center of curvature of the bar translates a distance K_1 parallel to the axis of symmetry and that each radial cross section rotates $2B\theta$.

These conclusions agree with what one might expect since, with pure bending, every radial cross section is a plane of symmetry and there is no variation of stress or strain with the angular coordinate.

The constants which appear in the displacement and strain equation can be evaluated in a more complete study of the elastic-plastic solution by using all the stress boundary conditions associated with the problem. Their numerical values will differ as the bar passes through the various stages of yielding.[1]

In conclusion, it may be stated that general expressions for displacements and strains were obtained directly from the conditions that the material is incompressible and that the shear stress is zero. These equations, which apply equally well in the elastic as well as the plastic regions of the problem, show that the curved bar will remain cylindrical and that planes will remain plane throughout its loading history.

References

[1] Shaffer, Bernard W., and House, Raymond N., Jr., *The Elastic-Plastic Stress Distribution Within a Wide Curved Bar Subjected to Pure Bending*, J. Appl. Mech., Vol. 22, pp. 305–310, September, 1955.

[2] Prager, W., and Hodge, P. G., Jr., *Theory of Perfectly Plastic Solids*, pp. 27–32, 95–110; John Wiley & Sons, Inc., New York, 1951.

[3] Wang, C. T., *Applied Elasticity*, pp. 52, 53; McGraw-Hill Book Company, Inc., New York, 1953.

[4] Timoshenko, S., and Goodier, J. N., *Theory of Elasticity*, 2nd Ed., pp. 65–66; McGraw-Hill Book Company, Inc., New York, 1951.

Further Remarks on the Collapse Pressures of Uniformly Loaded Spherical Shells

Bertram Klein
Chief of Stress, National Rocket Company, Culver City, Calif.
November 5, 1956

IN THE READERS' FORUM of October, 1956, Reiss[1] has reopened the subject of the buckling of spherical shells under external pressure.[2] An attempt is made to explain the apparent scatter in test data solely on the basis of sudden changes in the deflected shape of the shell with consequent cusps appearing in the buckling plot made according to new parameters. The effects of initial irregularities are not included.

First, let it be said that actual test data for this problem will show a sizable scatter even among shells of identical nominal dimensions. Such data were obtained by Tagowa of Tokyo and presented in a paper in the Transactions of the ASME of Japan about the year 1930. The author has seen this paper but unfortunately does not have a copy at present. Even though complete spheres were tested at the time, the scatter should be representative of what could be expected for shallow domes. On the basis of these facts, it is believed poor engineering practice to try to make an empirical curve go through nearly all test points as is attempted in Fig. 1 of reference 1. If the possible scatter in test data is of the order of magnitude of distances between cusps, these cusps may not exist in reality.

Consider next Fig. 3 of reference 1. It could be interpreted from the figure that, for a given R/t, the shell with the larger ρ, and hence β, is stronger. This conclusion is not physically feasible. Thus ρ in itself is not sufficient to define completely the problem; both R/t and β must be prescribed. It is believed, further, that after reaching a certain value the effect of β upon buckling is secondary. This conclusion is substantiated by Gerard and Becker[3] in a figure showing the buckling coefficient plotted vs. a parameter, Z, the plot of which on log-log paper resembles the plot of the buckling coefficient of cylinders in compression.

To settle the question once and for all, the author agrees that additional test data are needed. However, these tests should be conducted on sets of specimens of identical nominal dimensions to indicate the extent of the scatter of each point to be plotted, and on specimens with constant R/t but with varying β to determine the effect of β.

References

[1] Reiss, E. L., *On the Nonlinear Buckling of Shallow Spherical Domes*, Readers' Forum, Journal of the Aeronautical Sciences, Vol. 23, No. 10, pp. 973-975, October, 1956.

[2] Klein, B., *Parameters Predicting the Initial and Final Collapse Pressures of Uniformly Loaded Spherical Shells*, Readers' Forum, Journal of the Aeronautical Sciences, Vol. 22, No. 1, pp. 69, 70, January, 1955.

[3] Gerard, G., and Becker, H., *Instability Data Prepared for the NACA, Part V—Shells;* New York University Press, New York, April, 1955.

Buckling Loads of Pin-Ended Fluid Columns

Eryk Kosko
Assistant Chief Stress Engineer, Avro Aircraft Limited, Malton, Canada
November 15, 1956

DESIGN CURVES for hydraulic jacks subjected to compressive loads were recently given by Forray,[1] based on formulas derived by Hoblit.[2] In the writer's opinion, these formulas lead to appreciable errors when applied to a jack in which the maximum compressive load occurs when the jack is partially retracted.

In Hoblit's derivation, the jack is replaced by a stepped spring-column—i.e., a column composed of the full-length cylinder to which the outside portion of the piston rod is connected by means of a rotary spring; the spring is made to provide the same elastic restraint as that afforded by the inner portion of the piston rod, considered as a beam simply supported at the piston end and at the gland. The cylinder is thus assumed to carry the axial load over its entire length so that the possibility of the piston rod buckling within the cylinder is completely excluded; nor is any allowance made for the destabilizing effect that this portion of the rod may have on the remaining structure. On the other hand, the part of the cylinder which overlaps the piston rod does not, in reality, carry any axial stresses and should not be considered capable of buckling. Of these two effects, the former is generally the more important—at least when the piston rod is relatively flexible. The assumption of the spring-column leads then to an overestimation of the buckling load—i.e., to unconservative results.

A more satisfying model is obtained when assuming the axial load carried by the piston rod over its entire length, while the cylinder portion extending from gland to piston is stressed only in bending. With the notations of Fig. 1, the deflected shape of the column looks somewhat like Fig. 2(a), while the corresponding bending moments in the various members are represented by the hatched areas in Fig. 2(b). In this scheme, the flexural stiffness of the cylinder and the beam-column stiffness of the rod overlap over the common portion CD. Assuming the cylinder and the piston rod to have uniform section properties—EI_1 and EI_2, respectively—over their lengths, it is possible to represent the centerline deflections of portion AC of the cylinder and BD of the rod as arcs of sine curves, portion CD of the cylinder as an arc of a cubic elastica, while the overlapping part of the rod is governed by a beam-column equation. These expressions contain altogether seven arbitrary constants which must be so adjusted as to make the various deflections and slopes compatible at the points of contact C and D. No restraint against relative rotation at these points needs be assumed as this would only introduce an unnecessary complication and possibly affect the buckling load in an unconservative manner.

Elimination of the arbitrary constants leads to the buckling equation

$$[1 - (1/3)\,(\alpha_1 d)^2 + \alpha_1 d \cot(\alpha_1 a)] \cdot \alpha_2 d[\cot(\alpha_2 d) + \cot(\alpha_2 b)] = 1$$

where the lengths a, b, and d are as defined by Fig. 1 (the meaning of a is different from reference 1) and where $\alpha_1 = (P/EI_1)^{1/2}$, $\alpha_2 = (P/EI_2)^{1/2}$. The above equation serves to determine values of the parameters, and thereby of the critical load P_{cr}, at which equilibrium is possible in a deflected shape different from a straight line.

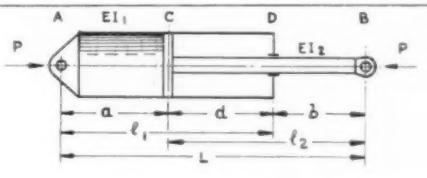

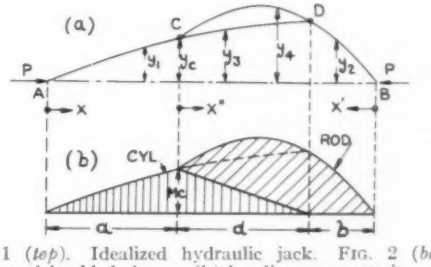

FIG. 1 (*top*). Idealized hydraulic jack. FIG. 2 (*bottom*). (a) Assumed buckled shape; (b) bending moments in cylinder and rod.

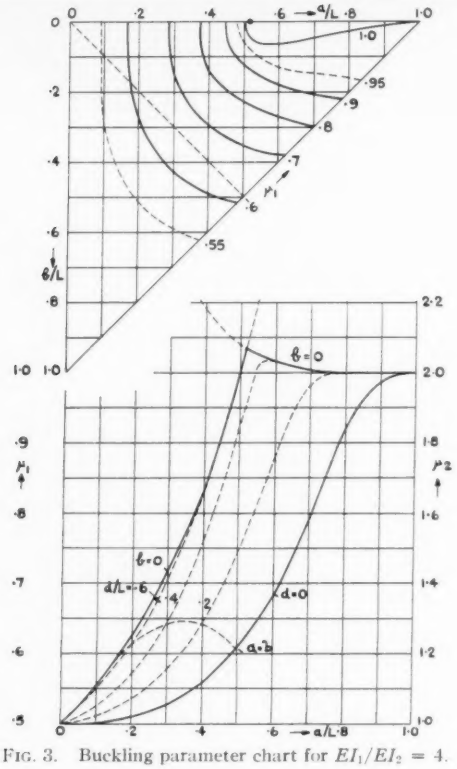

FIG. 3. Buckling parameter chart for $EI_1/EI_2 = 4$.

A full discussion of this equation and of its solution is contained in reference 3; this includes the various limiting cases in which one of the lengths a, b, or d becomes vanishingly small or the cylinder becomes infinitely rigid. Numerical results are presented there for several values of the ratio EI_1/EI_2 in the form of charts of which Fig. 3 is a sample. In the lower part, the buckling parameter $\mu_1 = \alpha_1 L/\pi$ (equal to the ordinate $L\sqrt{P/EI_1}$ of Forray's diagrams divided by π) is presented as a function of the geometric ratios a/L and d/L. The upper part is a contour map for constant values of this same parameter. The critical load is obtained as $P_{cr} = \pi^2\mu_1^2 EI_1/L^2$.

Although different from Eq. (5) of reference 1, the buckling equation above requires for its solution only slightly more work. In the limiting case $d = 0$, both reduce to an equation applicable to a stepped column

$$\alpha_1 \cot(\alpha_1 a) + \alpha_2 \cot(\alpha_2 b) = 0$$

As a further contribution, reference 3 shows how to make allowance for nonlinear elasticity of the material. The effects of transverse loading and of initial imperfections such as misalignment, pin friction, etc., are also considered. Finally, a similar approach for the analysis of landing-gear oleopneumatic legs is indicated.

Unfortunately, lack of time has not permitted to obtain numerical results which would cover as wide a range of stiffness ratios as Forray's charts. This is the reason why publication has not been considered to date.

REFERENCES

[1] Forray, M. J., *Buckling Loads of Pin-Ended Fluid Columns*, Readers' Forum, Journal of the Aeronautical Sciences, Vol. 23, No. 10, pp. 972, 973, October, 1956.

[2] Hoblit, F., *Critical Buckling Loads for Hydraulic Cylinders*, Product Engineering, pp. 108–112, July, 1950.

[3] Kosko, E., *The Compressive Instability of a Hydraulic Jack*, Avro Aircraft Limited, Stress Report Gen/1090/5 August, 1955.

Effect of the Change in Thermal Stresses Due to Large Deflections on the Torsional Rigidity of Wings*

Josef Singer and N. J. Hoff
Research Fellow, and Head, Department of Aeronautical Engineering and Applied Mechanics, Respectively, Polytechnic Institute of Brooklyn, Brooklyn, N.Y.

November 7, 1956

IN REFERENCE 1, an approximate analysis was presented of the reduction in torsional rigidity and of the torsional buckling of thin wings in consequence of thermal stresses. As the calculations were based on a small-deflection theory, indefinitely large deformations were predicted under any finite torque when the temperature reached a critical value. In reality, the thermal stresses do not remain constant but decrease when the deformations increase. This reduction in thermal stresses results in deformations that remain finite at all temperatures as long as the applied loads are finite.

The thermal stresses denoted in reference 1 by $\sigma_x = Rf(y)$ were the stresses arising in a wing of large aspect ratio in consequence of the condition that plane sections perpendicular to the spanwise (x) direction remain plane after heating. When the displacements w perpendicular to the plane of the wing are finite, they give rise to strains of a magnitude $(1/2)(\partial w/\partial x)^2$ in the plane of the wing and therefore modify the thermal stresses. In reference 1, the deflections were assumed to be given by $w = kxy$, with k the angle of twist per unit length. Then the strain caused by the finite deformations is $(1/2)k^2y^2$. Since no force is applied to the end of the wing, this strain must be accompanied by an average shortening of the wing to ensure a zero resultant spanwise force. The average shortening ϵ_0 is

$$\epsilon_0 = \left(1\Big/\int_{-b}^{b} h\,dy\right)\int_{-b}^{b} h(1/2)k^2y^2\,dy \tag{1}$$

where h is the thickness of the wing at y. Hence the thermal stress of the large-deflection theory can be given as

$$\sigma_x = Rf(y) - (E/2)k^2\left[y^2 - \left(1\Big/\int_{-b}^{b} h\,dy\right)\int_{-b}^{b} hy^2\,dy\right] \tag{2}$$

If a virtual displacement increasing k to $k + \delta k$ is undertaken, the work done by the applied torque M is

$$\delta W_M = M2a\,\delta k \tag{3}$$

where $2a$ is the span of the wing. In reference 1 the shortening of the horizontal projection of the distance between the end points of a spanwise fiber of the wing was given as

$$\Delta a = k^2 a y^2 \tag{4}$$

Consequently, the work done by the fictitious edge stresses σ_x during the virtual displacement is

$$\delta W_\sigma = \int_{-b}^{b} h\sigma_x\,\delta\Delta a\,dy = (2aRIk - EaKk^3)\,\delta k \tag{5}$$

where

$$I = \int_{-b}^{b} hy^2 f(y)\,dy \quad \text{and} \quad K = \int_{-b}^{b} h[y^4 - (2\epsilon_0/k^2)y^2]\,dy \tag{6}$$

If the wing is in equilibrium, the sum of the work $\delta W_M + \delta W_\sigma$ must be equal to the change in the strain energy U stored in the wing. One obtains from reference 1

$$\delta U = 2a\,k\,GC\,\delta k \tag{7}$$

where GC is the torsional rigidity according to St. Venant. Finally, the condition of equilibrium can be stated as

$$GC - RI + (1/2)EKk^2 = M/k = GC_{eff} \tag{8}$$

* Excerpt from a thesis submitted to the Polytechnic Institute of Brooklyn in partial fulfillment of the requirements for the degree of Doctor of Aeronautical Engineering. The work was carried out under contract AF33(616)-3214 sponsored by the Aeronautical Research Laboratory of the Wright Air Development Center of the U.S. Air Force.

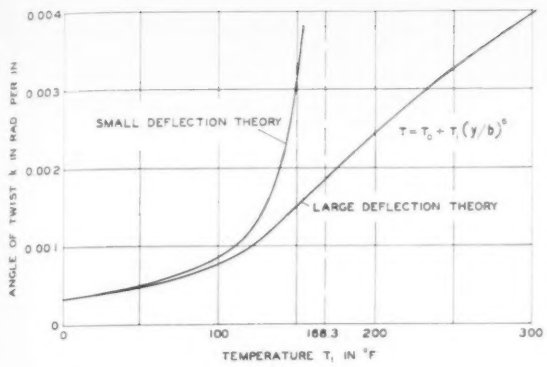

FIG. 1. Angle of twist per unit length of wing under applied torque, $M = 400$ in. lbs.

where GC_{eff} is the apparent, or effective, torsional rigidity of the wing in the presence of the given thermal stresses and at the rotation k. When $k = 0$, the effective torsional rigidity of reference 1 is obtained. Increasing rotations k stiffen the wing in proportion to k^2.

When the thermal stresses and the torque M are given, the angle of twist k can be computed from Eq. (8) through solution of a cubic. The finite deformations of the wing under thermal stresses exceeding the critical values of the small-deflection theory and in the absence of an applied torque M can be obtained from Eq. (8) if M is set equal to zero. The solution for k is

$$k = \{(2\,GC/EK)\,[(R/R_{cr}) - 1]\}^{1/2} \tag{9}$$

where R_{cr} is the critical value of R according to the small-deflection theory of reference 1—namely $R_{cr} = GC/I$.

Fig. 1 presents numerical values computed for a wing of constant thickness $h = 1/4$ in. (flat plate) when the chord $2b$ is 20 in. The temperature distribution is given by $T = T_0 + T_1 \times (y/b)^6$; the material constants are $E = 29 \times 10^6$ psi, $\alpha = 7.5 \times 10^{-6}$ °F.$^{-1}$, and Poisson's ratio $\nu = 0.3$; and the applied torque $M = 400$ in.lbs. The alleviating effect of the large deflections can be clearly seen in the Figure.

REFERENCE

[1] Hoff, N. J., *Approximate Analysis of the Reduction in Torsional Rigidity and of Torsional Buckling of Solid Wings under Thermal Stresses*, Readers' Forum, Journal of the Aeronautical Sciences, Vol. 23, No. 6, pp. 603, 604, June, 1956.

Leading-Edge Temperature of a Flat Plate Subjected to Aerodynamic Heating

A. E. Bryson, Bernard Budiansky, and George F. Carrier
Division of Engineering and Applied Physics, Harvard University, Cambridge, Mass.
November 8, 1956

SYMBOLS

M = Mach Number
Pr = Prandtl Number
T_∞ = free-stream temperature
T_e = equilibrium temperature = $T_\infty\{1 + r[(\gamma - 1)/2]M^2\}$
T_i = initial equilibrium temperature
T_f = final equilibrium temperature
a = velocity of sound in air
c_m = specific heat of plate material
h = heat-transfer coefficient, for isothermal plate in laminar flow, at a distance δ from leading edge [see Eq. (18)]
k_a = thermal conductivity of air
k_m = thermal conductivity of plate material
p = transform variable
r = recovery factor (= 0.85 for laminar boundary layer)
s = transform variable
t = time
t^* = rise time (time to achieve 63 per cent of ultimate temperature increase)
x = distance from plate leading edge
δ = plate thickness
γ = ratio of specific heats
θ = temperature parameter [= $(T_f - T)/(T_f - T_i)$]
ν = kinematic viscosity
ξ = nondimensional plate coordinate [see Eq. (3)]
ρ_m = mass density of plate material
τ = nondimensional time variable [see Eq. (4)]

INTRODUCTION

THE EFFECT of chordwise heat conduction is often neglected in the analysis of the transient aerodynamic heating of airfoil skins, and little error is incurred by this neglect when the chordwise variations of temperature and heating rate are small. At the leading edge, however, the usual boundary-layer assumptions imply that an infinite heat-transfer coefficient governs the convective heating rate. If chordwise conduction is suppressed, this infinite heat-transfer coefficient forces the leading edge to attain the current equilibrium temperature with zero time lag. The purpose of the present note is to provide a more realistic basis for the estimation of leading-edge airfoil temperatures by incorporating the influence of conduction in the analysis of a semi-infinite flat plate of constant thickness subjected to a sudden increase of forward speed. The convective heat transfer is assumed to take place through a laminar boundary layer on one side of the plate, and temperatures are assumed constant through the plate thickness.

FORMULATION OF THE PROBLEM

The governing differential equation is taken as

$$(\rho_m c_m \delta)\,(\partial T/\partial t) = k_m \delta(\partial^2 T/\partial x^2) + h\delta^{1/2}\int_{\bar{x}=-0}^{x} \frac{d[T_e(t) - T(\bar{x}, t)]}{(x - \bar{x})^{1/2}} \tag{1}$$

where the left-hand side represents the rate of heat storage per unit length of plate, and the two terms on the right-hand side represent, respectively, the heating rates per unit length due to conduction in the plate and convective heating from the laminar boundary layer. The convective heating term, derived in reference 1, takes approximate account of the fact that the plate temperature is nonuniform.

We shall assume that for $t < 0$ the plate is at the uniform temperature T_i equal to the equilibrium temperature corresponding to its initial Mach Number; at $t = 0$ the plate is instantaneously accelerated to a higher Mach Number. We now let

$$\theta = (T_f - T)/(T_f - T_i) \tag{2}$$

where T_f is the equilibrium temperature corresponding to the final Mach Number. We also introduce the nondimensional independent variables

$$\xi = \pi^{1/3}\epsilon^{2/3}\,(x/\delta) \tag{3}$$

$$\tau = \pi^{2/3}\,\epsilon^{1/3}\,(ht/\rho_m c_m \delta) \tag{4}$$

where the nondimensional parameter ϵ is defined by

$$\epsilon = h\delta/k_m \tag{5}$$

Then, since $T_e(t)$ in Eq. (1) may be replaced by T_f for $t \geq 0$, Eq. (1) may be reduced to

$$\theta_\tau = \theta_{\xi\xi} - (1/\sqrt{\tau})\int_{\bar{\xi}=-0}^{\xi} \frac{d\theta(\bar{\xi}, \tau)}{(\xi - \bar{\xi})^{1/2}} \tag{6}$$

for $\tau \geq 0$.

The initial condition on $\theta(\xi, \tau)$ is

$$\theta(\xi, 0) = 1 \tag{7}$$

and one boundary condition is

$$\theta_\xi(0, \tau) = 0 \tag{8}$$

which stipulates that there be zero heat flux through the plate

cross section at the leading edge. We shall also make use of the requirement that $\theta(\xi, \tau)$ remain bounded as ξ becomes infinite.

Solution for Leading-Edge Temperature

Let $\bar{\theta}(s, \tau)$ represent the Laplace transform with respect to ξ of $\theta(\xi, \tau)$; then, from Eqs. (6) and (8),

$$s^2\bar{\theta} - s\theta(0, \tau) - \bar{\theta}_\tau - \sqrt{s}\bar{\theta} = 0 \tag{9}$$

Now, let $\bar{\theta}^*(s, p)$ be the Laplace transform with respect to τ of $\bar{\theta}(s, \tau)$; then, from Eqs. (9) and (7),

$$s^2\bar{\theta}^* - s\theta^*(0, p) - [p\bar{\theta}^* - (1/s)] - \sqrt{s}\bar{\theta}^* = 0 \tag{10}$$

where $\theta^*(0, p)$ is the Laplace transform with respect to τ of $\theta(0, \tau)$. Then

$$\bar{\theta}^*(s, p) = s[\theta^*(0, p) - (1/s^2)]/(s^2 - \sqrt{s} - p) \tag{11}$$

The following argument is now presented for the determination of $\theta^*(0, p)$, the inversion of which would provide the desired leading-edge temperature history:

Consider the inversion with respect to s of $\bar{\theta}^*(s, p)$ by means of contour integration in the complex s-plane; in this inversion process, p is regarded as a positive real number. Now, for all real, positive p, the equation

$$s^2 - \sqrt{s} - p = 0 \tag{12}$$

has precisely one root in the right half of the complex s-plane. Consequently, it must be true that the equation

$$\theta^*(0, p) - (1/s^2) = 0 \tag{13}$$

has the identical root; for, if this were not so, $\bar{\theta}^*(s, p)$ would have a pole in the right half s-plane, with the result that $\theta^*(\xi, p)$, would become infinite for $\xi \to \infty$; but this would violate the requirement that $\theta(\xi, \tau)$ be bounded. Hence

$$\theta^*(0, p) = 1/q \tag{14}$$

where q is the positive real root of

$$q - q^{1/4} - p = 0 \tag{15}$$

Now, let $g = (p/q) - 1 = -q^{-3/4}$ and $\beta = -p^{-3/4}$; then

$$g/(1 + g)^{3/4} = \beta$$

and we may write

$$g = \sum_{n=1}^{\infty} a_n\beta^n$$

where the coefficients are given by residue theory as

$$a_n = \operatorname*{Res}_{\beta=0} [g(\beta)/\beta^{n+1}] = \operatorname*{Res}_{g=0} [g\beta'(g)/\beta(g)^{n+1}] = \Gamma[(3n/4) + 1]/n!\Gamma[2 - (n/4)]$$

Hence

$$\theta(0, p) = (1/q) = (1/p) + (g/p) = (1/p) + \sum_{n=1}^{\infty} (-1)^n p^{-[(3n/4)+1]} \{\Gamma[(3n/4) + 1]/n!\Gamma[2 - (n/4)]\}$$

Finally, term-by-term inversion gives

$$\theta(0, \tau) = 1 + \sum_{n=1}^{\infty} \frac{(-1)^n \tau^{3n/4}}{n!\Gamma[2 - (n/4)]} \tag{16}$$

for all values of τ.

An asymptotic expression for $\theta(0, \tau)$ for large values of τ, found by the method of steepest descent, is given by

$$\theta(0, \tau\tau) \cong (32/\sqrt{6\pi})\,(e^{-3\tau/4^{4/3}}/\tau^{3/2}) \tag{17}$$

Numerical Results

The results obtained from Eq. (16) for $(1 - \theta) = (T - T_i)/(T_f - T_i)$ are plotted against the time parameter τ in Fig. 1. It is seen from this Figure that 63 per cent—i.e., $1 - (1/e)$—of the ultimate temperature increase takes place in a time $t^* =$

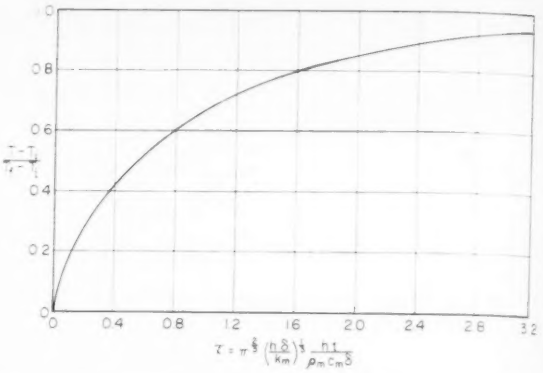

FIG. 1. Temperature history at the leading edge of a heat-conducting flat plate.

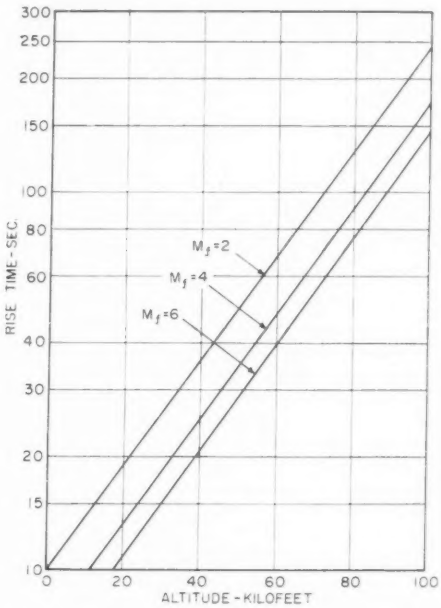

FIG. 2 Rise time at the leading edge of a 1/10-in. steel plate vs. altitude and Mach Number. (Rise time = time to 63 per cent of final temperature increase.)

$0.40(k_m/h\delta)^{1/3}(\rho_m C_m \xi/h)$. For illustrative purposes, Fig. 2 shows a plot of the rise time t in seconds versus altitude, for various Mach Numbers, for the case of a 1/10-in. steel plate. In the preparation of Fig. 2, the formula used for h was

$$h = (0.332)\,(k_a/\delta)\,(Ma\delta/\nu)^{1/2}\,(Pr)^{1/3}\,f(M) \tag{18}$$

and the variation of $f(M)$ with Mach Number was taken from reference 2. Since h is proportional to $\delta^{-1/2}$, it follows that t^* is proportional to $\delta^{4/3}$; for other thicknesses, therefore, multiply the rise time shown in Fig. 2 by $(10\delta)^{4/3}$; for aluminum multiply the rise time by 1.12.

It may be remarked that the present results for plates heated from one side may be applied approximately not only to airfoil skins but also to solid wings having blunted leading edges if δ is taken as half the leading-edge thickness.

References

[1] Bryson, A. E., *Note on Aerodynamic Heating with a Variable Surface Temperature*, Quart. Appl. Math., Vol. X, No. 3, October, 1952.

[2] Howarth, L. (Ed.), *Modern Developments in Fluid Dynamics—High Speed Flow*, p. 418, Oxford, 1953.

Vortex-Ring Cascade and a Conjectured Model of Transition to Turbulence

C. S. Hsu
Department of Engineering Mechanics, University of Toledo, Toledo, Ohio
November 12, 1956

Introduction

In the study of turbulence the mechanism which governs the transition from instability to full turbulence has not yet been clearly understood nor has the development of a tripped transition. It is the purpose of this note to report an interesting vortex-ring cascade phenomenon observed and to present a conjectured model of transition to turbulence. The model seems particularly suited for phenomena of tripped transition.

Vortex-Ring Cascade

The writer's attention was first drawn to the fact that a smoke ring, under suitable conditions, can reproduce smaller vortex rings. However, due to the highly turbulent condition of the air, it is difficult to ascertain the details of the phenomenon. The dye drop in water technique of generating rings was found to be much more instructive. Figs. 1(a)–1(d) form a sequence of pictures showing the development of a vortex-ring cascade.

This phenomenon can easily be observed by simply letting a dye drop enter a quiet body of fluid. The development can be briefly traced as follows. The entering dye drop will first form a vortex ring. Neglecting the viscous diffusion, a vortex ring, by itself, will move with a certain translational velocity and maintain its size. However, if the dye has a density slightly different from that of the fluid, a gravity force due to the density difference will be acting on the dye filament. Let us suppose a heavier dye for definiteness. Under this gravity force the ring will be accelerated downward and will expand in size owing to the Magnus effect. As the vortex ring moves down, some parts of it become distorted as shown in Fig. 2(a). These parts gradually move away from the plane of the ring, drawing the filament with them. Eventually a number of smaller offspring vortex rings will form and lie in planes, displaced away from that of the mother ring. The number of the offspring rings is not definite, probably because of the variation of the original rings. As many as ten have been observed. The new vortex rings generated will repeat the same process, as shown in Fig. 1(d). Thus, the writer believes that this is a genuine cascade phenomenon.

The same phenomenon exists if lighter dye is used. In that case, all the offspring rings will be displaced upward above the original ring. The original ring could also be generated by suddenly ejecting the dye through an opening of a tube which is submerged in the fluid. In general, the phenomenon is most favorably produced when the direction of translation of the original ring coincides with the direction of the force acting on the filament.

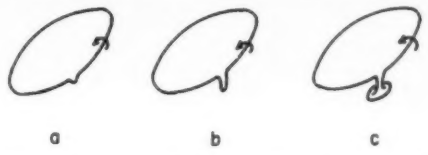

Fig. 2. Generation of an offspring ring from the mother filament.

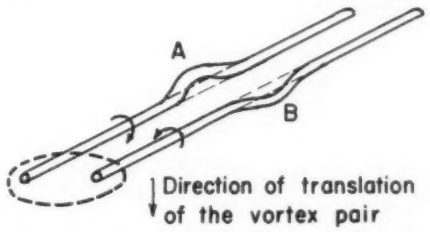

Fig. 3. Conjectured instability of a vortex pair under three-dimensional disturbances.

This phenomenon seems to originate from instability under some infinitesimal disturbances. As a matter of fact, it is found that the quieter the body of fluid is, the better and more symmetrical pattern of the phenomenon can be observed. The fundamental element in the instability mechanism is believed to be the force acting on the filament—in this case due to density difference. No generation of smaller rings was observed when dye with the same density as that of the fluid was used. The vortex motion of the original ring is essential to form the filament but is probably incidental to the basic mechanism of instability although its presence might modify the instability criterion. A mathematical analysis to prove the instability and to find the instability criterion is being attempted. The instability observed here is somewhat similar to that of a fluid layer heated from below and to the Taylor instability of fluid between two rotating cylinders. The complication in the present problem is that the undisturbed motion is not steady as in the other two cases.

One possible conjecture about the instability is that the vortex pair, attached and generated by the filament as the filament moves relatively to the fluid under the force acting on it, grows and becomes unstable under three-dimensional disturbances. If the pair is disturbed as shown in Fig. 3, the disturbed parts

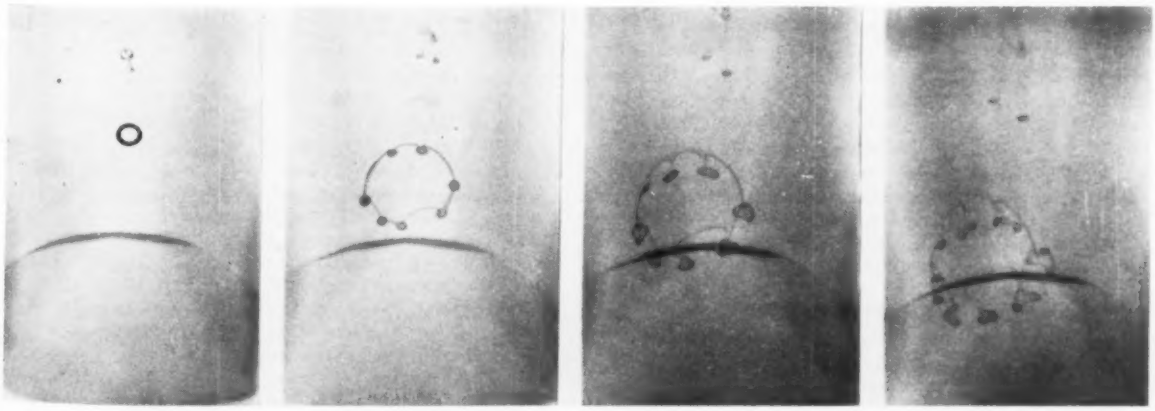

Figs. 1(a)–1(d) (*left to right*). A sequence of pictures showing the development of a vortex-ring cascade.

A and B, under suitable conditions such as a proper ratio of the distance between the pair filaments to the filament core size, may move forward with a greater velocity than the general translational velocity of the vortex pair. This relative motion will facilitate the increasing of the vorticity of the disturbed parts, resulting in even a greater relative velocity with respect to the vortex pair, and will eventually lead to the formation of a new vortex ring.

A Model of Transition to Turbulence

The cascade phenomenon described in the last section suggests a plausible model of transition to turbulence. Let us replace the dye filament by a vortex filament made of the same fluid as that surrounding it. Assume that the body of fluid has a shear motion. Furthermore, suppose that this vortex filament is not convected freely but has a relative motion with respect to the shear flow. Due to this relative motion, the vortex filament will experience some force acting on it and will be forced to accelerate through the fluid. Thus we have a situation analogous to the one described in the previous section except that here the acceleration is a result of the interaction of the shear flow and the vortex rather than that of the density difference. If the instability mechanism is also valid here, this vortex filament, under suitable conditions, will generate smaller vortex rings. These new filaments will, in turn, be acted upon and distorted by either the general shear flow or flows due to other vortex filaments and, if conditions are favorable, will continue the cascade process. After several cycles vortex rings of different sizes will be distorted and oriented in somewhat random fashion, resulting in a turbulent condition.

The essential relative motion between the vortex filament and the shear flow is not inconceivable. Let us consider the case of tripped transition or transition due to roughness. At low Reynolds Numbers a curved vortex filament will be generated and will be attached to the roughness. As the Reynolds Number increases beyond a certain value, a part of the filament will be at first dislodged and then stretched and moved away from the wall by the shear flow. Disregarding the viscous diffusion, a vortex filament coming from a highly retarded flow region could be expected to have a relative motion with respect to the surrounding shear flow. This relative motion can manifest itself, in an idealized case, by the velocity discontinuity at the interboundary which is actually the source of vorticity for the new rings to be generated just as the nonhomogeneity of density is the source of vorticity in the dye-ring cascade. To maintain such a source of vorticity, it is probably necessary to have a shear motion with increasing velocities away from the wall.

For investigating the transition phenomena it seems that there is a need of a basic unit process upon which a chain reaction or a cascade reaction, can be built up. Under certain favorable flow conditions this chain reaction will be triggered, and so enters the turbulence. The model just described meets this requirement. Some well-known features of transition may be interpreted with this model in mind.

In some instances, it is conceivable that the cascade has started, but, after a few cycles, it lacks the necessary conditions to continue. The flow will revert back to laminar flow. This may account for the turbulent burst spots which do not lead to turbulence as observed by Emmons.

In the cascade process, each generation occupies a larger territory than the preceding one. In a shear flow, starting from a turbulent spot, this cascade will sweep out a wedge-shaped turbulent region. This is in line with the observation made by Emmons with a water table and with the well-known transverse contamination first observed by Charters.

Transition is probably too complicated a phenomenon to be explained by any one single physical mechanism. The ring cascade observed is so interesting that the writer was tempted to make this conjectured model. Whether it is relevant or not as a transition mechanism remains to be seen.

Note on Tip-Bluntness Effects in the Supersonic and Hypersonic Regimes

F. D. Bennett
Ballistic Research Laboratories, Aberdeen Proving Ground, Md.
November 19, 1956

In a recent letter,[1] M. H. Bertram presents some data on flows at $M = 6.85$ around 10° half-angle cones with blunted tips. Since the demarcation between the supersonic and hypersonic regimes is not sharp and since one expects hypersonic flows to be generally similar to those at lower Mach Numbers—especially where viscous effects do not predominate throughout the entire field of interest—it is of some value to compare Bertram's results with those obtained by Giese and Bergdolt[2] for 15° half-angle cones at $M = 2.45$. Following the observation by Charters and Stein[3] that drag coefficient measurements on blunted cones imply a Reynolds Number effect, Giese and Bergdolt study the convergence to conical flow of the perturbed flow about a cone with truncated tip. They employ the Mach-Zehnder interferometer and the conical flow criterion[4] as analytical tools.

The first point of comparison may be made in connection with Bertram's observation that the main shock wave undergoes an inflection some 20–25 tip diameters from the nose. He ascribes this inflection to an overexpansion at the tip. Definite optical evidence that such an overexpansion takes place is not obvious from Bertram's schlieren pictures. On the other hand, in Fig. 3 of Giese and Bergdolt's paper and in Fig. 4 of the Charters-Stein report, the overexpansion is clearly marked by the presence of a shock wave emanating from a point slightly behind the corner formed by the truncation. According to the discussion given by these authors (reference 2, pages 1395–1396, and reference 3, pages 17–19), the flow at the blunted tip separates while traversing the corner, turns too far in passing over the separated region, and is both compressed and turned back to parallelism with the cone surface by the shock.

As is well known,[5] any interior shocks in the flow about a supersonic projectile must ultimately merge either with the main head wave or with the principal shock from the wake. For truncated cones, the truncation or secondary shock clearly must merge with the main front shock. Thus we may say that the flow behind the main shock is turned away from the axis upon passage through the secondary shock and that this occurs at points further and further back from the tip as the main shock is approached. Finally, the secondary shock merges gradually with the main shock in a pseudo-conical, triple-shock intersection. Beyond this point the main shock will have slightly increased slope in order to turn the flow as much as the two shocks together turn it before the intersection. Furthermore, the main shock will ultimately approach the slope characteristic of the conical flow to which the perturbed flow converges. Hence one would expect a rapid change toward higher values upon measuring shock angle through the intersection region. This is substantially what Bertram finds. The intersection occurs about 13.5 tip diameters behind the vertex of the detached, main shock in Giese and Bergdolt's Fig. 3. Considering that larger Mach Number and smaller cone angle will tend to displace the intersection rearward, we have support for the assumption that Bertram's inflection point is actually a triple-shock intersection of the type just described.

For other truncation diameters in the $M = 2.45$ series, the intersection of main and secondary shocks occurs between 13 and 16 tip diameters behind the foremost point on the main shock. As the truncation diameter decreases, the flow perturbation decreases and so also does the optical effect of the secondary shock until all three vanish for the perfect cone. While for small truncations the attached shock is difficult to distinguish by eye, its effect is very noticeable in the conicity plot where it causes a large bump in the curves representing traces near the nose (cf. Fig. 11 of reference 2).

Remeasurement of the original photographs shows that the ratios of shock detachment distance to truncation diameter for

the $M = 2.45$ series lie between 0.33 and 0.38. The 1-mm. truncation length interferogram was excluded on account of the large error of the measurement (approximately ±17 per cent). Fig. 5 of reference 2 cannot be relied upon for this ratio because of what appears to be scale error made in locating the intersection of the shocks with the axis. Interferograms of cylinders at $M = 2.65$, 0.2 Mach Number higher than the mean for the truncated cones, were available to the writer. Shock stand-off to cylinder diameter ratios were 0.30 and 0.32 for two cases.

The reduced interferograms of Figs. 14 and 15 of reference 2 show a density variation at the surface in the same direction as Bertram's C_p variation but much sharper near the tip. Densities up to twice those characteristic of the cone are found at the truncation corner. These fall rapidly through a steep gradient to values lower than conical within one fifth of a tip diameter or less and then rise more gradually as far as the data extend toward the shoulder.

In Fig. 14 of reference 2 the weak secondary shock is indicated by close isopycnals for $\rho/\rho_1 = 1.20$ and 1.30. The region shown in Fig. 15 of reference 2 lies entirely ahead of the second shock whose attachment point would lie just behind the 0.80 isopycnal. The low-density region is relatively more than twice as large as that of Fig. 14. Thus, the existence of a Reynolds Number effect is evident upon comparison of the density fields alone.

Considering that the highest tip Reynolds Number obtained by Bertram is nearly a factor of 10 smaller than that of Giese and Bergdolt and that the scale effect is quite small even for their 3- and 6-mm. truncation lengths, it is not surprising that Bertram does not find any appreciable Reynolds Number effect.

References

[1] Bertram, M. H., Readers' Forum, *Tip-Bluntness Effects on Cone Pressures at $M = 6.85$*, Readers' Forum, Journal of the Aeronautical Sciences, Vol. 23, No. 9, pp. 898–900, September, 1956.

[2] Giese, J. H., and Bergdolt, V. E., *Interferometric Studies of Supersonic Flows about Truncated Cones*, J. Appl. Phys., Vol. 24, p. 1389, 1953. See also BRL Report No. 830, September, 1952, for more complete isopycnal charts.

[3] Charters, A. C., and Stein, H., *The Drag of Projectiles with Truncated Cone Headshapes*, BRL Report No. 624, March, 1952.

[4] Giese, J. H., Bennett, F. D., and Bergdolt, V. E., *A Simple Interferometric Test for Conical Flow*, J. Appl. Phys., Vol. 21, p. 1226, 1950.

[5] Whitham, G. B., *The Flow Pattern of a Supersonic Projectile*, Commun. on Pure and Appl. Math., Vol. 5, p. 301, 1952.

On the Couette Flow of a Compressible, Viscous, Heat-Conducting, Perfect Gas

A. J. A. Morgan
President, AER, Inc., Pasadena, Calif.

November 19, 1956

THE PURPOSE of this note is to provide the background for a generalization of some of the results given for the problem considered in references 1 and 2. The problem is that of determining the steady laminar flow of a compressible, viscous, heat-conducting, perfect gas or fluid, influenced by both gravity and buoyancy body forces, between two infinite horizontal plates. The lower plate is stationary, and the upper plate is in translation along its length with a speed U_0^* in the direction of the positive x-axis. The origin of the axes is placed at the stationary plate so that the x-axis coincides with this plate and the positive y-direction is upward, towards the moving plate.

From the above formulation of the problem, it is seen that all quantities characterizing the flow will be functions of y only and that the only nonzero velocity component is in the x-direction. Let starred quantities, with and without a subscript 0, refer, respectively, to conditions at the moving plate and at any point y between the two plates. Further, let T^*, U^*, p^*, ρ^*, μ^*, and k^* denote, respectively, the absolute temperature, x-velocity component, static pressure, density, viscosity, and heat conductivity within the gas. Then a corresponding set of dimensionless quantities can be defined by the equations

$$T^* = TT_0^*, \quad U^* = uU_0^*, \quad p^* = pp_0^*, \quad \rho^* = \rho\rho_0^*$$
$$\mu^* = \mu\mu_0^*, \quad k^* = kk_0^*, \quad y = \eta h$$

where h is the distance between the two plates.

Now, under our formulation, the continuity equation is identically satisfied and, in terms of the above-defined dimensionless variables, the partial differential equations for the conservation of momentum and energy[3] reduce to

$$(d/d\eta)\,[\mu(du/d\eta)] = 0 \tag{1}$$

$$(dp/d\eta) = -2K\rho + K \tag{2}$$

$$(d/d\eta)\,[k(dT/d\eta)] + 2\sigma^2\mu(du/d\eta)^2 = 0 \tag{3}$$

with the equation of state for a perfect gas, $p^*/\rho^*T^* = p_0^* \div \rho_0^*T_0^*$, taking the form

$$p/\rho T = 1 \tag{4}$$

where

$2\sigma^2$ = $(\gamma_0 - 1)P_{r_0}M_0^2$
P_{r_0} = Prandtl Number at moving plate = $\mu^*(T_0^*)c_p^*(T_0^*)/k^*(T_0^*)$
M_0 = Mach Number at moving plate = $U_0^*/\sqrt{\gamma_0 RT_0^*}$
$c_{p_0}^*$ = $c_p^*(T_0^*)$ = value of specific heat at constant pressure at moving plate, a function of absolute temperature
$c_{v_0}^*$ = $c_v^*(T_0^*)$ = value of specific heat at constant volume at moving plate, a function of absolute temperature
γ_0 = $c_{p_0}^*/c_{v_0}^*$
a_0 = speed of sound at moving plate = $\sqrt{\gamma_0 p_0^*/\rho_0^*}$ = $\sqrt{\gamma_0 RT_0^*}$
g = acceleration due to gravity
R = gas constant
K = $gh\rho_0^*/p_0^*$ = $\gamma_0 gh/a_0^2$

Note that the values of σ and K are only dependent on the values of the properties of the fluid at the moving plate. Furthermore, Eqs. (1)–(4) hold when μ, k, $c_p = c_p^*/c_{p_0}^*$, and $c_v = c_v^*/c_{v_0}^*$ are arbitrarily assigned differentiable functions of T. In fact, because of the nature of the simplifications introduced by our problem, $c_p(T)$ and $c_v(T)$ do not even appear in Eqs. (1)–(4); hence, these equations may be considered to hold when the Prandtl Number varies from point to point within the fluid.

The boundary conditions for the problem are taken as

$$u(\eta = 0) = 0, \quad u(\eta = 1) = 1, \quad T(\eta = 0) = T_0, \quad T(\eta = 1) = 1 \tag{5}$$

Following reference 2, on integrating Eq. (1) we obtain

$$\mu(du/d\eta) = C_1 \tag{6}$$

where C_1 is a constant. Upon substituting this result into Eq. (3), it can be written as

$$(d/d\eta)\,[k(dT/d\eta)] = -2\sigma^2C_1(du/d\eta) \tag{7}$$

so that an integration of this equation gives

$$k(dT/d\eta) = C_2 - 2\sigma^2C_1u \tag{8}$$

Now, departing from the method of reference 2, on dividing Eq. (8) by Eq. (6) and integrating the resulting equation, we have†

$$(C_2/C_1)u - \sigma^2u^2 + C_3 = \int_1^T [k(\zeta)/\mu(\zeta)]d\zeta \equiv F(T) \tag{9}$$

where C_2 and C_3 are constants. Since the boundary conditions of Eq. (5) can also be expressed as $T(u = 0) = T_0$ and $T(u = 1) = 1$, the evaluation of the constants in Eq. (9) gives $C_2 = \sigma^2C_1 - F(T_0)C_1$ and $C_3 = F(T_0)$. Hence, Eqs. (8) and (9) can be written as

$$k(dT/d\eta) = [\sigma^2(1 - 2u) - F(T_0)]C_1 \tag{10}$$

$$F(T) = \sigma^2u(1 - u) + (1 - u)F(T_0) \equiv \omega(u) \tag{11}$$

† From the kinetic theory of gases we can conclude that $[k(T)/\mu(T)] \times a\,c_v(T)$. Hence, if $T_0 = 1$ and $C_v^*(T) = \text{const.}$, Eq. (7) of reference 2 will (for most real gases and over some temperature ranges) hold up to a constant multiplying factor.

The ratio of heat transfer to skin friction is obtained on dividing Eq. (10) by Eq. (6). At $\eta = 0$, where $u = 0$, this ratio becomes

$$\kappa(0) \equiv \tfrac{1}{2}\,[k(dT/d\eta)]/[\mu(du/d\eta)]\big|_{\eta=0} = \sigma^2 - F(T_0) \quad (12)$$

which holds for arbitrarily assigned differentiable $\mu(T)$, $k(T)$, $c_p(T)$, and $c_v(T)$ *under* the boundary conditions of Eq. (5). Thus, the result given in reference 2 has been generalized since there Eq. (12), with $F(T_0)$ omitted, was shown to hold when $\mu(T) = k(T) = T$, $c_p = K_1$, and $c_v = K_2$ or when $\mu = K_3$, $k = K_4$, $c_p = K_1$, and $c_v = K_2$, $K_1, \ldots, K_4$ being constants.

Eq. (12) reveals several interesting properties of the flow under consideration: (1) This equation (even at $\eta \neq 0$) is independent of K, which characterizes the gravity effect; thus, the ratio of heat transfer to skin friction, $\kappa(\eta)$, is unaffected by gravity. (2) Because $c_v(T)$ is a monotonically increasing function of T, the integrand of Eq. (9) (see footnote) and $F(T)$ must also have this property; hence, there is a value of the prescribed temperature, $T_0 > 1$, at the stationary plate for which the quantity $\sigma^2 - F(T_0)$ vanishes. Thus, there is a value of $T_0 > 1$ for which $\kappa(0) = 0$ or, alternately, for which there is no heat transfer from the stationary plate. (3) If $\bar{\kappa}(0) = \sigma^2 = \kappa(0)$ when $T_0 = 1$, we note that $\kappa(0) < \bar{\kappa}(0)$ when $T_0 > 1$ and $\kappa(0) > \bar{\kappa}(0)$ when $T_0 < 1$. (4) The dependence of $\kappa(0)$ on the properties of the fluid between the two plates is evidenced only through the term $F(T_0)$, whose value is known once $\mu(T)$ and $k(T)$ have been assigned.

By inverting Eq. (11) (graphically or analytically) it is possible to obtain an expression for T as a function of u, say

$$T = F^{-1}(\omega(u)) \equiv g(u)$$

But, since $\mu(T)$ is a known function of T, Eq. (6) can be integrated to yield

$$C_1\eta + C_4 = \int_0^u \mu(g(\xi))d\xi \equiv \bar{F}(u) \quad (13)$$

where, upon imposition of the boundary conditions of Eq. (5),

$$C_1 = \int_0^1 \mu(g(\xi))d\xi = \bar{F}(1) \qquad C_4 = 0 \quad (14)$$

Again, by a graphical or analytical inversion of Eq. (13), u can be exhibited as a function of η—that is,

$$u = \bar{F}^{-1}(C_1\eta) \quad (15)$$

so that T can also be found as a function of η.

It now remains to determine p as a function of η. By use of Eq. (4), Eq. (2) can be written as

$$(dp/d\eta) + 2[K/T(\eta)]p = K \quad (16)$$

The solution to this equation can be found on letting $p = v(\eta)w(\eta)$, where $w(\eta)$ satisfies the homogenous counterpart of Eq. (16); it is

$$p(\eta) = CK\left\{\exp\left[-2K\int_0^\eta \frac{d\xi}{T(\xi)}\right]\right\}\left\{\int_0^\eta \exp\left[2K\int_0^\xi \frac{d\xi}{T(\xi)}\right]d\xi\right. \quad (17)$$

where C is a constant that can be evaluated on setting $p = 1$ at $\eta = 1$. Eq. (17) is a slight generalization of one of Illingworth's[4] results. The expression for $\rho(\eta)$ is now obtained from Eq. (4)—that is, $\rho(\eta) = p(\eta)/T(\eta)$.

The expressions for the four unknowns in our problem $u(\eta)$, $T(\eta)$, $p(\eta)$, and $\rho(\eta)$, *under* the boundary conditions of Eq. (5), have been obtained without specifying the functional forms of $\mu(T)$, $k(T)$, $c_p(T)$, and $c_v(T)$; hence, they hold for arbitrary Prandtl Number. Admittedly, once the functional dependence of these quantities on temperature has been specified, numerical integrations may be required to exhibit the solutions in explicit form.

References

[1] De Groff, H. M., *On Viscous Heating*, Readers' Forum, Journal of the Aeronautical Sciences, Vol. 23, No. 4, pp. 395, 396, April, 1956.

[2] De Groff, H. M., *Comments on Viscous Heating*, Readers' Forum, Journal of the Aeronautical Sciences, Vol. 23, No. 10, pp. 978, 979, October, 1956.

[3] Goldstein, S. (Ed.), *Modern Developments in Fluid Dynamics*, Vol. II, Chap. XIV; The Clarendon Press, Oxford, 1950.

[4] Illingworth, C. R., *Some Solutions of the Equations of Flow of a Viscous Compressible Fluid*, Proceedings, Cambridge Philosophical Society, Vol. 46, p. 469, 1950.

Inversion of the Prandtl-Meyer Relation for Specific-Heat Ratios of 5/3 and 5/4*

Ronald F. Probstein

Associate Professor, Division of Engineering, Brown University, Providence, R. I.

December 3, 1956

RECENT WORK[1] has indicated the general usefulness of determining airfoil characteristics by the so-called shock-expansion method, in which the surface pressure distribution on the airfoil is computed by calculating the conditions directly behind the airfoil associated with a uniform shock generated by a wedge equal to the leading-edge angle, followed by an isentropic Prandtl-Meyer expansion. In particular, the approach has proved to give excellent results at hypersonic speeds. However, in the usual form in which the Prandtl-Meyer relation is written, the turning angle is expressed as a function of the incident Mach number M and the specific-heat ratio γ. In this case, the local Mach Number (or pressure) on the body surface can only be expressed implicitly as a function of the body shape, with the result that in general it is not possible to determine analytically such properties as optimum airfoil design, etc.

For a constant specific-heat ratio, the Prandtl-Meyer relation is usually written in the form

$$\nu = \sqrt{(\gamma+1)/(\gamma-1)}\,\tan^{-1}\left[\sqrt{M^2-1}\times\sqrt{(\gamma-1)/(\gamma+1)}\right] - \tan^{-1}\sqrt{M^2-1} \quad (1)$$

where ν is the turning angle. It is the purpose of the present note to show that for two practically important values of γ an analytic inversion of Eq. (1) can be carried out. To the author's knowledge, these inversions have not been pointed out previously.

By setting $\lambda^2 = (\gamma+1)/(\gamma-1)$ and $\alpha = \sqrt{M^2-1}/\lambda$, Eq. (1) becomes

$$\nu = \lambda\,\tan^{-1}\alpha - \tan^{-1}\lambda\,\alpha \quad (2)$$

If λ is assumed to take on only positive integer values, then for

$$\lambda = 1, 2, 3, 4, \ldots, n, \ldots, \infty$$

γ is, respectively,

$$\gamma = \infty, 5/3, 5/4, 17/15, \ldots, (n^2+1)/(n^2-1), \ldots, 1$$

Now from the addition formula for the arctangent

$$\tan^{-1}x \pm \tan^{-1}y = \tan^{-1}[(x \pm y)/(1 \mp xy)]$$

and it follows directly from Eq. (2) that for λ integer a polynomial in α of order $(\lambda+1)$ will be obtained. Since a solution in terms of roots exists only up to the fourth degree, then in general an analytic inversion of Eq. (2) is possible only for values of $\lambda = 1, 2$, or 3.† However, the case $\lambda = 1$ ($\gamma = \infty$) is physically unreal so that the two remaining cases for which Eq. (1) could in principal be inverted are $\lambda = 2$ ($\gamma = 5/3$), and $\lambda = 3$ ($\gamma = 5/4$).

Before carrying out the inversion it should be noted that both of these values of γ are of practical interest. For example, $\gamma = 5/3$ corresponds to a monatomic gas. It has already been shown[2] that aerodynamic testing at hypersonic Mach Numbers can be

* This note is an outgrowth of a broad program of theoretical research on hypersonic flow sponsored by the Aeronautical Research Laboratory, Wright Air Development Center, USAF, under Contract AF33(616)-2798. The author wishes to thank Prof. Boa-Teh Chu of the Division of Engineering, Brown University, for many interesting discussions.

† If λ is expressed as the rational fraction m/n, where $m > n$, it can be shown that the degree of the equation which is obtained in the quantity $n\alpha$ is $m + n$ and that no other simple analytic inversions can be found.

accomplished in helium, and recently Mueller[3] has found, by utilizing the shock-expansion method, that a correlation exists between the force coefficients measured in a helium tunnel and the equivalent data in air. Clearly then, for the shock-expansion-type of pressure distribution, analytic expressions could be determined for the forces acting on airfoils, utilizing an inverted form of the Prandtl-Meyer equation. Another example for which the value of γ might be approximately 5/3 is at ultra-high flight speeds where the shock wave is very strong and where the dissociated gas between the body and the shock wave is "frozen" at the equilibrium composition behind the wave because the atomic recombination rates are very slow. For this frozen case where the shock wave is sufficiently strong so that all the molecules are dissociated into atoms, the effective value of γ is also equal to 5/3. On the other hand, if the recombination rates are very fast and the gas reaches a state of thermodynamic equilibrium, then, at temperatures from approximately 3,400°R. to 4,600°R. (at 1 atmosphere), the mean specific-heat ratio would vary from about 1.28 to 1.22. Under such conditions an average value for γ of about 5/4 would be appropriate. Still another example of where $\gamma = 5/4$ is applicable is to be found in the conditions existing in the nozzle section of a rocket motor, where hot gases are expanded from the combustion chamber. Clearly, many more aerodynamic applications can be found.

For the case of $\gamma = 5/3$ the inversion of Eq. (1) is quite straightforward and may be accomplished by setting $\nu = 2\theta$ and $\sqrt{M^2 - 1} = \tan 2\beta$. This leads to the relation $\tan(\theta + \beta) = (1/2)\tan 2\beta$, from the expanded form of which one finds $\tan\beta = [\tan(\nu/2)]^{1/3}$. The Mach Number can then be expressed in terms of $\tan\beta$ by expanding $\tan 2\beta$, giving the following relation for $M = M(\nu)$ with $\gamma = 5/3$:

$$M = \{1 + [\tan(\nu/2)]^{2/3}\}/\{1 - [\tan(\nu/2)]^{2/3}\} \qquad (3)$$

From the above equation, the maximum turning angle given by $M = \infty$ is seen to be $\nu_{max} = \pi/2$.

The method of inversion for $\gamma = 5/4$ is the same as used previously, where, however, in this case one sets $\nu = 3\theta$ and $\sqrt{M^2 - 1} = \tan 3\beta$. From this definition of β the following relation for M is found by expanding $\tan 3\beta$:

$$M^2 = (\xi^2 + 1)^3/\xi^2(\xi^2 - 3)^2$$

where $\xi = \cot\beta$. However, the solution for $\beta = \beta(\nu)$ is not quite as simple as before since the relation $\tan(\theta + \beta) = (1/3)\tan 3\beta$ leads to a quartic in ξ of the form

$$\xi^4 - 2\xi^2 - (8/3)\mu\xi - (1/3) = 0$$

where $\mu = \cot\theta = \cot(\nu/3)$. The root of the quartic which is sought may be determined by utilizing the fact that the maximum turning angle associated with $M = \infty$ is $\nu_{max} = \pi$. Thus, the coefficient of the ξ term is always negative since $\mu \geq 1/\sqrt{3}$. On solving the given quartic for ξ, the relation for M, with $\gamma = 5/4$, is found to be

$$M = \{[(\psi + 3)/[\psi + (3/2)]\}^{1/2}\,[(\psi + 3)/(\psi - 3)]$$

where

$$\psi = \left[\frac{\eta^3 + 1}{\eta + 1}\right]^{1/2} + \left\{(\eta + 1)\left[(2 - \eta) + \left(\frac{\eta^3 + 1}{\eta + 1}\right)^{1/2}\right]\right\}^{1/2} \qquad (4)$$

$$\eta = [3\cot^2(\nu/3) - 1]^{1/3}$$

References

[1] Eggers, A. J., Jr., Syvertson, C. A., and Kraus, S., *A Study of Inviscid Flow About Airfoils at High Supersonic Speeds*, NACA TR 1123, 1953.

[2] Bogdonoff, S. M., and Hammitt, A. G., *Fluid Dynamic Effects at Speeds From $M = 11$ to 15*, Journal of the Aeronautical Sciences, Vol. 23, No. 2, pp. 108–116, 145, February, 1956.

[3] Mueller, J. N., *Conversion of Inviscid Normal-Force Coefficients in Helium to Equivalent Coefficients in Air For Simple Shapes at Hypersonic Speeds*, NACA TN 3807, October, 1956.

Damping Due to Internal Flow

A. W. Gilmore* and T. L. Keller**

University of Colorado, Boulder, Colo., and Grumman Aircraft Engineering Corporation, Bethpage, N.Y., Respectively

December 7, 1956

Symbols

$C_{M_{(\dot\theta d/2V)}}$	=	dimensionless damping derivative
d	=	reference length
F	=	force
l_1	=	distance from the center of rotation to the duct entrance (positive downstream)
l_2	=	distance from the center of rotation to the duct exit (positive downstream)
M	=	moment
S	=	area
t	=	time
V	=	velocity
x	=	distance to fluid element from center of rotation
$\dot\theta$	=	rate of rotation $d\theta/dt$ of the duct
ρ	=	density of fluid

Subscripts

0	=	free-stream conditions
R	=	reference
e	=	entrance effect
c	=	Coriolis effect
IF	=	total internal-flow effect

Introduction

Because of the increasingly large mass-flow rates being handled by internal-flow engines as flight speeds are increased (e.g., supersonic ram-jets), the question of the contribution of the internal flow to the total aerodynamic damping has become of interest.

This paper derives an expression for the additional damping coefficient due to internal flow based upon considerations of the change in flow angle of the air as it enters the tube and on the Coriolis effect on the fluid within the tube. The relations obtained apply to both straight and curved ducts when the distances are measured in straight lines from the center of rotation. An expression is also presented for the percentage contribution to the total damping from the flow of fuel along the duct length.

Analysis

Damping Due to Flow Entry

The following assumptions are made: (1) Changes in direction of the air entering the duct occur abruptly at the duct entrance. (2) Fluid velocities within the tube are not affected by rotation—that is, centrifugal forces in the flow direction are neglected.

The air entering the duct is given a velocity increment $-\dot\theta l_1$ normal to the duct centerline. The normal force developed at the duct entrance due to this velocity increment will be equal to the rate of change of momentum of the entering air and can be expressed as the product of the mass-flow rate and the velocity increment. Thus

$$F_e = -\rho SV(\dot\theta l_1) \qquad (1)$$

The damping moment developed by this force acting about the center of rotation is

$$M_e = -\rho SV\dot\theta l_1^2 \qquad (2)$$

We may also express this moment in terms of the conventional damping coefficient, reference area, and length:

$$M_e = (1/2)\rho_0 V_0^2 S_R d(\dot\theta d/2V_0) C_{M_{(\dot\theta d/2V_0)_e}} \qquad (3)$$

From the principle of continuity the mass-flow rate must be constant within a given stream tube. Thus

$$\rho SV = \rho_0 S_0 V_0 = \rho_0 V_0 S_R(S_0/S_R) \qquad (4)$$

* Assistant Professor, Department of Aeronautical Engineering.

** Research Engineer.

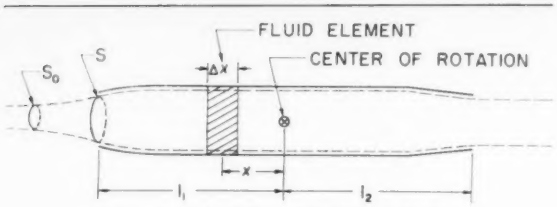

FIG. 1. Typical flow stream through duct.

Combining Eqs. (2), (3), and (4) we obtain

$$C_{M_{(\dot{\theta}d/2V_0)_c}} = -4(S_0/S_R)\ (l_1/d)^2 \tag{5}$$

where S_0/S_R is defined as the "capture area ratio."

Damping Due to Coriolis Effect on Fluid Within the Tube

Referring to Fig. 1 we see that the force exerted on the wall of the tube by a fluid element of volume Sdx may be expressed as the Coriolis force on a particle which is moving with respect to a rotating coordinate system:

$$\Delta F_c = 2\rho S \Delta x V\dot{\theta} \tag{6}$$

Then the net moment developed by the fluid contained in the tube may be determined by summing over the tube length the product of the Coriolis force on each fluid element and the distance from the element to the center of rotation:

$$M_c = \int_{l_1}^{l_2} -xdF_c = \int_{l_1}^{l_2} -2\rho SV\dot{\theta}xdx \tag{7}$$

But since $2\rho SV\dot{\theta}$ is constant,

$$M_c = [-2\rho SV\dot{\theta}(x^2/2)]_{l_1}^{l_2} = -2\rho SV\dot{\theta}[(l_2^2/2) - (l_1^2/2)] \tag{8}$$

Then defining the M_c in terms of the reference areas, length, and moment coefficient we obtain in a manner analogous to the previous case

$$C_{M_{(\dot{\theta}d/2V_0)_c}} = -4(S_0/S_R)\ [(l_2/d)^2 - (l_1/d)^2] \tag{9}$$

Total Damping Moment Contributed by Internal Flow Through Duct

The total moment coefficient due to the entrance and Coriolis effects is

$$C_{M_{(\dot{\theta}d/2V_0)_{IF}}} = -4(S_0/S_R)\ (l_2/d)^2 \tag{10}$$

This relation applies to both straight and curved ducts when l_2 is measured in a straight line from the center of rotation.

It has been tacitly assumed throughout that no fluid other than that in the external stream tube flows through the duct. This, of course, ignores the effect of any fuel addition. If it is desired to include the effects of fuel addition, the damping should be increased by a percentage equal to

$$[1 - (l_3/l_2)^2]\ (F/A) \cdot 100 \tag{11}$$

where l_3 is the straight-line distance from the fuel supply to the center of rotation, and F/A is the fuel-air ratio.

The Analytic Study of Laminar Boundary-Layer Stability in Free Convection

J. E. Plapp
Assistant Professor of Mechanical Engineering, The Rice Institute, Houston, Tex.
December 17, 1957

IF, IN A FLUID of infinite extent, a stationary semi-infinite flat plate is held isothermal at a temperature different from that of the fluid far from the plate, a free-convection flow can be expected to become established when a body force field such as that of gravity is present. When the plate is warmer than the fluid and the component of the body force vector parallel to the plate is directed toward the leading edge, the flow will proceed along the plate away from the leading edge as a boundary layer as shown in Fig. 1. A similar type of flow occurs when the plate is cooler than the fluid and the component of the body force parallel to the plate is directed away from the leading edge. Both the boundary-layer thickness and the maximum velocity in the boundary layer increase with increasing distance from the leading edge. In Fig. 1, F is the body force vector, and ξ and η are nondimensional coordinates measured parallel and perpendicular, respectively, to the plate. Experience has shown that such flows are initially laminar and become turbulent after the fluid has proceeded some distance away from the leading edge.

By means of an interferometric technique, observations[1] have been made of instability waves preceding transition in such free-convection flows. These instability waves are similar to the Tollmien-Schlichting waves of the forced-convection boundary layer in that they proceed in the direction of flow and are amplified with the eventual establishment of the turbulent regime. Lately, an attempt[2] has been made by the author under the direction of W. D. Rannie of California Institute of Technology to treat the stability of these laminar free-convection flows analytically. The method of small oscillations was used to derive the following two equations, which are descriptive of the essentially parallel flow of a fluid with properties other than density taken to be constant:

$$(\bar{u} - c)(\varphi'' - \alpha^2\varphi) - \bar{u}''\varphi + (i/\alpha R)(\varphi'''' - 2\alpha^2\varphi'' + \alpha^4\varphi) + (f/\alpha R)\ (ib_1 s' - \alpha b_2 s) = 0 \tag{1}$$

$$(\bar{u} - c)s - \bar{\theta}'\varphi + (i/\sigma\alpha R)(s'' - \alpha^2 s) = 0 \tag{2}$$

where

- $\bar{u}$ = nondimensional mean-flow velocity component parallel to plate, a function of η
- c = nondimensional phase velocity of disturbance
- φ = complex amplitude of a disturbance stream function equal to $\varphi(\eta)e^{i\alpha(\xi - c\tau)}$, in which α is the wave number of the disturbance and τ is nondimensional time
- f = a constant fixed when σ is specified
- R = Reynolds Number based on maximum velocity in boundary layer and boundary-layer thickness at a given distance from the plate leading edge
- b_1 = cos ω, ω being defined in Fig. 1
- b_2 = sin ω
- s = complex amplitude of temperature disturbance function equal to $s(\eta)e^{i\alpha(\xi - c\tau)}$
- θ = nondimensional mean temperature of fluid, a function of η
- σ = Prandtl Number of fluid

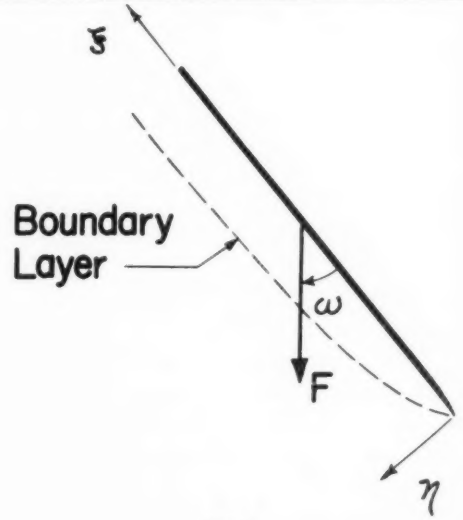

FIG. 1.

Primes denote differentiation with respect to η.

Eq. (1) differs from the well-known Orr-Sommerfeld stability equation by the presence of the last term, which is due to buoyant forces resulting from the interaction of the body force field with density perturbations. Since these density perturbations are considered to arise from temperature fluctuations, this last term of Eq. (1) provides coupling with Eq. (2), which is a disturbance energy equation.

Obtaining solutions of these equations and applying appropriate boundary conditions can in general, for a given flow, be expected to determine an indifference curve in the α-R plane which separates pairs of values of α and R corresponding to amplified oscillations from those corresponding to damped oscillations. Practically, however, performing this process is very difficult; all except possibly the two simplest of six approximate methods which have been developed for doing this on the bases of various simplifying assumptions would require the use of extensive high-speed computing facilities for their application.

One of the two simplest methods of solution was used to construct indifference curves for free convection in air. The curves which were obtained indicated correctly that the flow is laminar near the leading edge of the plate and that it can become turbulent only after proceeding some distance along the plate. However, the quantitative agreement with observations[1] was considerably poorer than had been anticipated apparently because of computational limitations and inadequacies in assumptions.

It is hoped that extensions of both experimental and analytic investigations of laminar flow stability in free convection can be made in the future.

References

[1] Eckert, E. R. G., and Soehnghen, E., *Interferometric Studies on the Stability and Transition to Turbulence of a Free-Convection Boundary Layer*, Proceedings of the General Discussion on Heat Transfer, 11th–13th September, 1951, pp. 321–323; Institution of Mechanical Engineers, London, 1951.

[2] Plapp, J. E., *I Laminar Boundary Layer Stability in Free Convection, II Laminar Free Convection with Variable Fluid Properties*, Ph.D. Thesis, California Institute of Technology, 1957.

Choking Flow in Curved Ducts

F. F. Ehrich
Advisory Engineer, Aviation Gas Turbine Division, Westinghouse Electric Corp., Kansas City, Mo.

December 24, 1956

Symbols

C_F = ratio of curved duct flow to choking flow in a straight duct
F = a function of t
j = an integer
k = perfect gas specific heat ratio
M = Mach Number
m, n = integers
r = radial distance from center of curvature of duct
t = ratio of static to stagnation temperature
T = temperature
V = gas velocity
ρ = gas density

Superscript

$*$ = sonic condition

Subscripts

p = pressure side of the passage
s = suction side of the passage
0 = stagnation condition
max = maximum value

Introduction

Various analyses[1] have been carried out to evaluate the choking-flow coefficient in a passage due to the curvature of the passage. These treatments were, of necessity, approximate in form using various linearizations and simplifications for the curvature of the streamlines and the perfect-gas relationships.

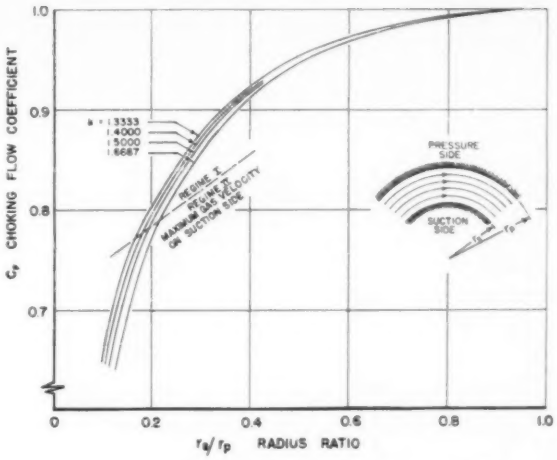

Fig. 1. Choking-flow coefficients in curved passages.

The following is an exact solution for a very special class of problem. The analysis treats the case of constant-width passages whose sides are circular arcs with a common center of curvature. The gas is assumed to have uniform stagnation properties and a simple free-vortex velocity profile.

General Equations

The basic parameter of interest is the ratio of flow in the channel with free-vortex velocity distribution to the flow in a straight channel with choked flow:

$$C_F = \int_{r_s}^{r_p} \rho V\, dr \Big/ \int_{r_s}^{r_p} \rho^* V^*\, dr = [1/(r_p - r_s)] \int_{r_s}^{r_p} (\rho/\rho^*)\,(V/V^*) dr \quad (1)$$

The various conventional substitutions for perfect gases with uniform stagnation conditions give

$$(V/V^*) = M^* = [(1 - t)\,(k + 1)/(k - 1)]^{1/2} \quad (2a)$$

$$(\rho/\rho^*) = [t(k + 1)/2]^{1/(k-1)} \quad (2b)$$

where $$t = T/T_0 = 1 - M^{*2}[(k - 1)/(k + 1)] \quad (2c)$$

and the free-vortex assumptions imply

$$M^* = M_p^* r_p/r \quad (3a)$$

$$r_s/r_p = M_p^*/M_s^* = [(1 - t_p)/(1 - t_s)]^{1/2} \quad (3b)$$

Then the integral may be reduced to the form

$$C_F = \{M_p^*/[1 - (r_s/r_p)]\}\ [(k + 1)/2]^{1/(k-1)} \times \int_{t_s}^{t_p} \frac{t^{1/(k-1)}\, dt}{2(1 - t)} \quad (4)$$

This expression is integrable in closed form only if the exponent $1/(k - 1)$ is equal to a rational fraction (n/m) or, for practical purposes, only if $m = 2$. Therefore, the only permissible values of the specific-heat ratio are

$$k = 1 + (2/n) \qquad n = 1, 2, 3, 4 \ldots \quad (5)$$

This is no severe limitation since the entire range of interesting values of k can still be covered in detail. By coincidence, this criterion for integration is identical to the theoretical estimation of k in the molecular theory of gases, with n equalling the number of molecular degrees of freedom.

The value of the integral is then, for n odd,

$$C_F = \{M_p^*/[1 - (r_s/r_p)]\}\ [(k + 1)/2]^{1/(k-1)} \times \left\{ -\sum_{\substack{j=1 \\ \text{odd}}}^{n} (t^{j/2}/j) + \operatorname{arctanh}(t^{1/2}) \right\}_{t_s}^{t_p} \quad (6a)$$

and, for n even,

$$C_F = \{M_p^*/[1 - (r_s/r_p)]\}\ [(k+1)/2]^{1/(k-1)} \times \left\{ - \sum_{\substack{j=2 \\ \text{even}}}^{n} (t^{j/2}/j) - (1/2)\ln(1-t) \right\}_{t_s}^{t_p} \quad (6b)$$

Maximum Flow

The maximum flow that the passage can pass is defined by the requirement

$$\partial C_F/\partial M_p^* = 0 \quad (7)$$

which results in the relation

$$C_{F\,max} = \{M_p^*/[1 - (r_s/r_p)]\}\ [(k+1)/2]^{1/(k-1)}\ \{t^{1/(k-1)}\}_{t_s}^{t_p} \quad (8)$$

Actual computation requires the simultaneous solution of Eqs. (6) and (8). This is possible to accomplish in a straightforward manner by obtaining solutions to the relationship

$$F(t_p) = F(t_s) \quad (9a)$$

where, for n odd,

$$F(t) = \left[t^{1/(k-1)} + \sum_{\substack{j=1 \\ \text{odd}}}^{n} (t^{j/2}/j) - \operatorname{arctanh}(t^{1/2}) \right] \quad (9b)$$

or, for n even,

$$F(t) = \left[t^{1/(k-1)} + \sum_{\substack{j=2 \\ \text{even}}}^{n} (t^{j/2}/j) + (1/2)\ln(1-t) \right] \quad (9c)$$

and substitution in Eqs. (2a), (3b), and (6a) or (6b).

Regime I on Fig. 1 indicates the solution that this computation sequence yields for various values of specific-heat ratio. No solution is possible beyond this regime by the foregoing type of analysis because the maximum velocity of the gas is reached at the suction side of the channel. Beyond this limiting situation (in Regime II), the limiting flow is given by Eq. (1) with maximum velocity at the suction side equivalent to

$$t_s = 0 \quad (10)$$

Reference

[1] Huppert, M. C., and MacGregor, C., *Comparison Between Predicted and Observed Performance of Gas Turbine Stator Blade Designed for Free Vortex Flow*, NACA TN 1810, April, 1949.

...Calculated and Observed Flutter Characteristics of a Helicopter Rotor Blade

(*Continued from page 290*)

For nontrivial solution of Eqs. (A-2) to exist, the determinant of the coefficients of β_1 and θ_1 must equal zero. This determinant has a real and an imaginary part, each of which therefore has to be identically equal to zero. Two equations are thus obtained in terms of $1/\Omega_f^2$ and ω_f/Ω_f. These equations are solved for the flutter speed, Ω_f, and the frequency ratio, ω_f/Ω_f. The resulting value of $k = \omega_f(c/2)/\Omega_f(3/4)R$ is compared with the assumed value, and, if agreement is not obtained, the process is repeated for another value of k. The convergence is very rapid and, after some experience, is usually obtained in about two iterations.

References

[1] Brooks, George W., and Sylvester, Maurice A., *The Effect of Control Stiffness and Forward Speed on the Flutter of a 1/10 Scale Dynamic Model of a Two-Blade Jet-Driven Helicopter Rotor*, NACA TN 3376, April, 1955.

[2] Scanlan, Robert H., and Rosenbaum, Robert, *Introduction to the Study of Aircraft Vibration and Flutter*, The Macmillan Company, New York, 1951.

[3] Theodorsen, Theodore, *General Theory of Aerodynamic Instability and the Mechanism of Flutter*, NACA Report 496, 1949.

[4] Timoshenko, S., *Vibration Problems in Engineering*, 2nd Ed., D. Van Nostrand Company, Inc., New York, 1947.

[5] Goland, Leonard, and Perlmutter, A. A., *A Comparison of the Calculated and Observed Flutter Characteristics of a Helicopter Rotor Blade Having Both Control System and Blade Flexibility*, Aeronautical Engineering Department, Report No. 333, Princeton University, December, 1955.

[6] Gessow, Alfred, and Meyers, Garry C., Jr., *Aerodynamics of the Helicopter*, The MacMillan Company, New York, 1952.

[7] Perlmutter, Abraham Adolf, *The Effects of a Spanwise Variation of the Section Shear Center Position on the Flutter Characteristics of a Helicopter Blade*, Aeronautical Engineering Department, Report No. 350, Princeton University, May, 1956.

An Authorized Binding for
Journal of the Aeronautical Sciences

Arrangements have been made by the Institute of the Aeronautical Sciences for members and subscribers to have their Journals bound carefully and economically. Simply write for details to:

Publishers' Authorized Bindery Service

5809 West Division St. Chicago 51, Ill.

$t^{1/2}$)] (9b)

$- t$)] (9c)

is computa-
-heat ratio
regoing type
s reached at
ng situation
with maxi-

(10)

Predicted and
r Free Vortex

pter Rotor,

oduction to
illan Com-

namic In-
96, 1949.
, 2nd Ed.,

parison of
Helicopter
Flexibility,
3, Prince-

ynamics of
952.
ise Varia-
haracteris-
partment,

ll.